KAUNAS UNIVERSITY OF TECHNOLOGY

MONIKA MAKŪNAITĖ

INVESTIGATION OF TISSUE ENDOGENOUS PULSATIONS FOR ULTRASOUND ELASTOGRAPHY

Doctoral dissertation
Technological Sciences, Electrical and Electronic Engineering (T 001)

Kaunas, 2021

This doctoral dissertation was prepared at Kaunas University of Technology, Biomedical Engineering Institute, during the period of 2017–2021.

Scientific Supervisor:
Dr. Rytis JURKONIS (Kaunas University of Technology, Technological Sciences, Electrical and Electronic Engineering, T 001).

Scientific Advisor:
Assoc. Prof. Dr. Alberto RODRIGUEZ MARTINEZ (Miguel Hernandez University of Elche, Spain, Technological Sciences, Electrical and Electronic Engineering, T 001).

The dissertation was edited by: English language editor Brigita Brasienė (Publishing House *Technologija*), Lithuanian language editor Aurelija Gražina Rukšaitė (Publishing House *Technologija*)

Dissertation Defence Board of Electrical and Electronic Engineering Science Field:
Prof. Dr. Arminas RAGAUSKAS (Kaunas University of Technology, Technological Sciences, Electrical and Electronic Engineering, T 001) – **chairperson**;
Prof. Dr. Olivija GUSTIENĖ (Lithuanian University of Health Sciences, Biomedical Sciences, Medicine, M 001);
Prof. Dr. Jose Maria Sabater NAVARRO (Miguel Hernandez University of Elche, Spain, Technological Sciences, Electrical and Electronic Engineering, T 001).
Prof. Dr. Renaldas RAIŠUTIS (Kaunas University of Technology, Technological Sciences, Electrical and Electronic Engineering, T 001);
Prof. Dr. Algimantas VALINEVIČIUS (Kaunas University of Technology, Technological Sciences, Electrical and Electronic Engineering, T 001).

The official defence of the dissertation will be held at 1 p.m. on 10th of January, 2022 at the online meeting of Dissertation Defence Board of Electrical and Electronic Engineering Science Field at Kaunas University of Technology Dissertation defence hall.

Adresas: K. Donelaičio g. 73-404 Kaunas LT-44249, Lietuva.
Tel. (+370) 37 300 042; faks. (+370) 37 324 144; el. paštas doktorantura@ktu.lt

Doctoral dissertation was sent on 10th of December 2021.
The doctoral dissertation is available on the internet http://ktu.edu and at the library of Kaunas University of Technology (K. Donelaičio St. 20, 44239 Kaunas, Lithuania).

KAUNO TECHNOLOGIJOS UNIVERSITETAS

MONIKA MAKŪNAITĖ

AUDINIŲ ENDOGENINIŲ PULSACIJŲ TYRIMAS ULTRAGARSINEI ELASTOGRAFIJAI

Daktaro disertacija
Technologijos mokslai, elektros ir elektronikos inžinerija (T 001)

Kaunas, 2021

Disertacija rengta 2017–2021 m. Kauno technologijos universiteto Biomedicininės inžinerijos institute.

Mokslinis vadovas:
doc. dr. Rytis JURKONIS (Kauno technologijos universitetas, technologijos mokslai, elektros ir elektronikos inžinerija, T 001).

Mokslinis konsultantas:
doc. dr. Alberto RODRIGUEZ MARTINEZ (Elčės Migelio Hernandeso universitetas, Ispanija, technologijos mokslai, elektros ir elektronikos inžinerija, T 001).

Disertaciją redagavo: anglų kalbos redaktorė Brigita Brasienė (leidykla „Technologija“), lietuvių kalbos redaktorė Aurelija Gražina Rukšaitė (leidykla „Technologija“)

Elektros ir elektronikos inžinerijos mokslo krypties disertacijos gynimo taryba:
prof. dr. Arminas RAGAUSKAS (Kauno technologijos universitetas, technologijos mokslai, elektros ir elektronikos inžinerija, T 001) – **pirmininkas**;
prof. dr. Olivija GUSTIENĖ (Lietuvos sveikatos mokslų universitetas, biomedicinos mokslai, medicina, M 001);
prof. dr. Jose Maria Sabater NAVARRO (Elčės Migelio Hernandeso universitetas, Ispanija, technologijos mokslai, elektros ir elektronikos inžinerija, T 001).
prof. dr. Renaldas RAIŠUTIS (Kauno technologijos universitetas, technologijos mokslai, elektros ir elektronikos inžinerija, T 001);
prof. dr. Algimantas VALINEVIČIUS (Kauno technologijos universitetas, technologijos mokslai, elektros ir elektronikos inžinerija, T 001).

Disertacija bus ginama viešame Elektros ir elektronikos inžinerijos mokslo krypties disertacijos gynimo tarybos posėdyje 2022 m. sausio 10 d. 13 val Kauno technologijos universiteto Disertacijų gynimo salėje.

Adresas: K. Donelaičio g. 73-403, 44249 Kaunas, Lietuva.
Tel. (370) 37 300 042; faks. (370) 37 324 144; el. paštas doktorantura@ktu.lt

Disertacija išsiųsta 2021 m. gruodžio 10 d.
Su disertacija galima susipažinti interneto svetainėje http://ktu.edu ir Kauno technologijos universiteto bibliotekoje (K. Donelaičio g. 20, 44239 Kaunas).

TABLE OF CONTENTS

ABBREVIATIONS

ASA − angular spectrum approach
AUC – area under curve
BM − block matching
CCA − common carotid artery
CSD − cross-sectional distensibility
CVD − cardiovascular diseases
FM − feature matching
FWHM − full width at half maximum (of point spread function)
IMT − *intima-media* thickness
KZK − Khokhlov-Zabolotskaya-Kuznetzov
LOKI − longitudinal kinetics
MAE − mean absolute error
MCS − mean scatterer spacing
MSE − mean squared error
NRMSE − normalized root mean squared error
OF − optical flow
PSF − point spread function
PW − pulse wave
PWV − pulse wave velocity
RF – radiofrequency
ROC − receiver-operating characteristic
ROI − region of interest
SNR − signal-to-noise ratio
TMM − tissue-mimicking material
US − ultrasound
USE − ultrasound elastography
VVI − velocity vector imaging

INTRODUCTION

Relevance of the research

Cardiovascular diseases (CVDs) are the main cause of human death worldwide. Every year, more people die from this disease than any other. In 2019, the latest year for which the worldwide statistics are calculated, globally, 18.6 million people died from CVDs, which reflects a 17.1 % increase over the past decade [1]. In fact, 42.1 % of the leading cause of death attributable to the CVDs was coronary heart disease [1], and atherosclerosis is the major cause of this disease. Global cardiovascular deaths are predicted to reach 23.6 million by 2030 [2]. Stroke, one of the several possible outcomes of CVD, represents the second cause of mortality and the sixth cause of permanent disability [3,4]. Therefore, the prediction of cardiovascular events towards efficient patient treatment is the major public health issue [5,6,7,8,9]. Atherosclerosis, the underlying pathological mechanism, is a chronic and systemic vascular disease, often referred as a "silent killer", because its progression and evolution is tremendously complex and rather unpredictable, leading to an exceedingly high number of fatal events, occurring without any precautionary signs [10]. Generally, in the long term, atherosclerotic arterial affection is not noticeable; however, the general signs of this illness develop only after the onset of complications: thickening of the *intima-media* complex, narrowing of the lumen or its thrombosis, and/or loss of elasticity [11]. Atherosclerosis causes heart attacks, strokes, peripheral arterial diseases, all of which are called CVDs, and myocardial infarction and stroke are described as the final stage of atherosclerosis [12].

Arterial stiffness is an independent predictor of cardiovascular events, and it is analyzed to assess the cardiovascular risk [13,14,15]. *Intima-media* thickness (IMT), pulse wave velocity (PWV), and cross-sectional distensibility (CSD) are the most commonly used risk markers for the arterial stiffness evaluation in clinical practice [16,17,18,19]. Unfortunately, the clinical potential of these traditional risk markers as the screening test remains limited [20]. It is difficult to evaluate the risk of CVDs in patients under the age of 50, especially in the absence of specific individual CVDs risk factors or anamnesis. As a result, assessing the likelihood of developing a disease and, if necessary, starting drug treatment is challenging [13].

Nonetheless, it has been proven that mechanical changes (i.e., longitudinal and radial motion of the arterial wall) appear much earlier than significant anatomical changes (i.e., IMT) of the arterial wall [12]. In recent years, radial motion has been widely studied and become a parameter, describing the mechanical properties of the arterial walls. Becoming an informative, non-invasive parameter, radial motion helps to investigate cardiovascular diseases and determine the elasticity of arterial walls. The longitudinal motion has not received such recognition, unlike the radial motion of the arterial wall. Compared with the radial motion, it was believed that the longitudinal motion during the heart cycle was negligible. However, using modern ultrasound scanners, it has been noticed that the *intima-media* complex during the heart cycle moves in the radial as well as longitudinal directions [21,22]. It has been observed that as the radial motion, the longitudinal motion of the arterial wall has the

same amplitude and reaches about one millimeter [23]. Furthermore, the clinical investigations have linked longitudinal motion of the common carotid artery (CCA) to the risk factors and CVDs [24,25]. The previous studies have shown a relationship between the arterial stiffness, CVDs, and the decrease in longitudinal motion [12]. Even though the longitudinal motion amplitude is linked to the CVDs, the determinants of phases of longitudinal motion remain unknown [16].

Within the context of CVD risk assessment, the motion of arterial tissues during the cardiac cycle is important, as mechanical deformation represents vessel elasticity and is putatively inversely related to the arterial stiffness, an independent indicator of all-cause mortality and morbidity [26]. The arterial tissue motion during the cardiac cycle consists of radial (artery wall motion perpendicular to the blood flow), longitudinal (*intima-media* complex motion in parallel with the blood flow) motions, and circumferential strain. Using several motion tracking techniques, the motion of the arterial tissue from the sequences of ultrasound (US) radiofrequency (RF) signals or images has been analyzed and summarized by Rizi et al. in [27].

Currently, the available ultrasound elastography (USE) techniques can be classified into two major groups, according to the measured physical quantity, i.e., 1) strain imaging, 2) shear wave imaging [28]. Both these groups of methods use an external source of stress. Nevertheless, an internal source of deformation or so-called endogenous motion in the tissue induced by heartbeat and vascular activity could be used in the elasticity measurement [29,30,31].

Methods, based on the endogenous motion detection, are not applied in clinical practice these days. Firstly, these methods should be carefully studied and investigated. Due to this, the computational ultrasound imaging could be used to simulate US RF signals or B-scan images from measurements, using algorithms that are dedicated to this purpose. The most popular simulation software packages [32,33,34] are CREANUIS [35] (based on Khokhlov-Zabolotskaya-Kuznetzov (KZK) equation) for nonlinear propagation and simulation of harmonic imaging and Field II [36] (based on Huygens principle and hybrid digital-analytic method), which gained a wide application since the publication of the model in 1991 [37] and software package in 1996 [38]. The popularity of Field II lies in a considerable flexibility to accommodate a wide range of transducers, beamforming options, and imaging possibilities. It is still a powerful and evolving tool for the simulation of various scanning and focusing modalities as well as a whole echoscopy mechanism, including scattering in the tissues and organs [39]. Although there are a lot of Field II applications described in many articles, only a few publications deal with the quantitative comparison of simulation and experiment evaluating uncertainties [40,41].

The motion of the carotid artery wall has been modeled by many authors. Gemignani et al. [42] simulated radial motion as Sawtooth function, while Solomon et al. [43], as triangular function. As reported by Deng et al. [44], they proposed a geometric model of a common carotid artery (CCA), where the dynamic scatterers model is constructed by moving the positions of the scatterers, according to the synthesized pulse wave (PW). The PW is estimated from the *in vivo* RF signals of the vessel wall by using a 1-D normalized cross-correlation (NCC) algorithm, based on

the echo tracking. For the motion in the radial direction, Hu et al. [45] proposed an isotropous pulse model with elasticity to describe the relationship between the radial displacement and blood pressure. However, neither of the previous studies considers the longitudinal motion of the artery together with the radial and longitudinal motions slope deep into the tissue. It was done by Stoitsis et al. [46], simulating the radial motion as pulse function, which parameter values were determined based on the experiments with *in vivo* data. The longitudinal motion was modeled as a sinusoidal function, because there is no conclusive information about the mathematical modeling of this motion. Based on a similar *in vivo* examination, the spatial dependence of radial and longitudinal motions, which are independent of the axial position, was incorporated as well.

The longitudinal motion, a new, non-invasive parameter for elasticity measurement, is still not fully exploited for evaluating the cardiovascular risk; therefore, it has a lot of potential. Moreover, computational ultrasound imaging must deal with the quantitative comparison of simulation and experiment, evaluating uncertainties before the simulation of US RF signals or B-scan images, for the development of methods of endogenous motion detection. All these facts raise a scientific-technological problem and a hypothesis.

Scientific-technological problem and hypothesis

Methods, based on the endogenous motion detection, are not applied in the clinical practice these days. First, these methods should have three "in" steps before a wide usage: 1) approach justification *in-silico* to understand, develop, and verify the method, 2) testing *in-vitro* to optimize, double-check, and validate the pilot results, and finally, 3) certification *in-vivo* to fine-tune and confirm the reliability of the proposed method. Therefore, an unsolved scientific problem exists: how to identify the accuracy of motion tracking algorithms before applying the methods based on the endogenous motion detection in clinical practice.

The working hypothesis is formulated that the computational ultrasound imaging and digital 3D artery model can be used for the identification of the accuracy of motion tracking algorithms to detect the endogenous motion, induced mainly by the blood pulsation in vessels, which are associated with tissue elasticity (or stiffness) evaluation and early detection of atherosclerosis. The hypothesis is verified by the investigation results of methods for radial and longitudinal motion detection accuracy.

Research object

The research is based on the development and investigation of the algorithms for the simulation of common carotid artery wall motion for early diagnosis of atherosclerosis.

The aim of the research

The aim of this doctoral thesis is to develop and investigate the ultrasound radiofrequency signals-based algorithm for common carotid artery wall motion simulation, associated with the early diagnosis of atherosclerosis.

The objectives of the research

To achieve the aim, the following objectives were formulated:

1. To develop and investigate a virtual scanning simulation, adequate to the physical ultrasonic scanning;
2. To create a 3D artery model, capable to reproduce the biomechanical behavior of human CCA for the simulation of US RF signals;
3. To investigate and evaluate the accuracy of the proposed motion detection algorithms by using simulated CCA US RF signals;
4. To investigate the capability to differentiate arteries by motion slope profiles;
5. To collect US RF data from healthy volunteers and patients at increased risk of CVD group, investigate and compare the motion parameters between two different populations.

Scientific novelty

In this doctoral thesis, a quantitative evaluation of the main resolution uncertainties that are arising in digital US linear scanning simulation by Field II and comparing them with physical phantom's scanning results was done. This leads to the conclusions on quantitative uncertainties of the point spread function (PSF) and resolution in the elevation plane by using standard phantoms.

A dynamic 3D artery model, capable of reproducing realistic dynamic RF signals of pulsating human blood vessels, surrounded by viscoelastic tissue, was developed.

Practical significance

Quantitative ultrasound imaging allows simulating raw RF signals that are adequate to those obtained from the real ultrasonic scanning.

The proposed dynamic 3D artery model allows simulation for 3D deformation elastography, development and verification of elastography algorithms, 3D elastography experiments, and feasibility studies.

The approaches provided in this thesis were developed and used in support of the following project "Investigation of radiofrequency based ultrasonic strain elastography algorithms (ELASTUS)". No.: S-MIP-19-8; the work was funded by the Research Council of Lithuania in the frame of the Researchers group project, 2019–2022.

The statements presented for the defense

1. Virtual scanning simulation that is adequate to the physical ultrasonic scanning was developed. Digital scanning shows a good agreement with the physical one: full width at half maximum (FWHM) estimates of PSF in the axial and lateral directions are according to the practical estimates with a discrepancy of less than 12 % and 16 %, correspondingly.
2. A 3D artery model that is capable of reproducing the biomechanical behavior of human CCA for the simulation of US RF signals has been

created. The echoscopy simulation shows that the artery model represents A, B and M-mode image structure like *in vivo* artery wall. The evaluated simultaneous radial and longitudinal motion of the virtually scanned 3D structure over a single pulse is visually almost indistinguishable from the generated motion pattern.

3. The accuracy of the proposed motion detection algorithms, using simulated CCA US RF signals, was investigated. The results demonstrate that a variety of accuracy evaluation parameters for radial and longitudinal motion detection are capable to access error as well as evaluate the dissimilarities between the estimated and theoretical motion signals.
4. The capability to differentiate arteries by motion slope profiles was investigated. The results demonstrate that the variety of slope profiles of radial and longitudinal motions that define different elasticity tissues may be used for the differentiation of healthy volunteers and at-risk patients.
5. The US RF data from healthy volunteers and patients at increased risk of CVD group was collected; the motion parameters of two different populations were calculated, and the diagnostic ability of those parameters to diagnose patients with and without the atherosclerosis was evaluated. The highest sensitivity of the proposed time and frequency domain parameters has displacement of 0.77 and spectral spread of 0.86. The velocity and spectral centroid were assigned as parameters with the highest specificity resulting in 0.88 and 0.71, correspondingly.

Approval of the results

In total, the results of the dissertation were published in 9 publications, of which 5 articles were published in the Journals of the Master List of Thomson Reuters Web of Science (with impact factor). The results were presented in 2 international and 1 national scientific conferences: World Congress on Medical Physics and Biomedical Engineering (IUPESM 2018), 2019 IEEE International Ultrasonics Symposium (IUS), and Bioateitis: gamtos ir gyvybės mokslų perspektyvos 2019. In 2020, a doctoral scholarship, granted by the Research Council of Lithuania, was received. In 2019 and 2020, PhD Students Scholarships for Achievements, granted by KTU, were received.

Structure of the doctoral thesis

The dissertation consists of an introduction, 3 chapters, general conclusions, summary, a list of references, a list of publications and conferences of the author, and 2 appendixes. The thesis consists of 152 pages, 54 figures, 4 tables, 21 formulas, and 175 references. The content of the thesis is organized as follows: Chapter 1 describes the CCA anatomy and histology, longitudinal motion of the artery wall, currently proposed digital artery models, adequate simulation of the real ultrasound echoscopy, and algorithms for artery wall motion tracking. Chapter 2 presents the CCA US examination, developed modeling and verification of a digital simulation of physical US scanning, created digital artery model, and developed RF US signals post-

processing algorithms. Chapter 3 shows the experimental results of modeling, investigation of motion detection accuracy, and *in vivo* radial motion parametrization. Chapter 4 is dedicated to general conclusions.

1. OVERVIEW OF THE MOTION OF COMMON CAROTID ARTERY AND APPROACHES TO THE MOTION DETECTION

1.1. Common carotid artery anatomy and histology

The left common carotid artery CCA originates in the neck from the aortic arch in the thorax, while the right common carotid artery, from the bifurcation of the brachiocephalic trunk. The left and right common carotid arteries in the thorax extend on both sides of the throat and go through the superior thoracic aperture to the neck where enters the carotid triangle (see Figure 1.1.). This triangle is situated at the front of the neck and bounded by the sternocleidomastoid muscle, omohyoid muscle, and the posterior belly of the digastric muscle [47].

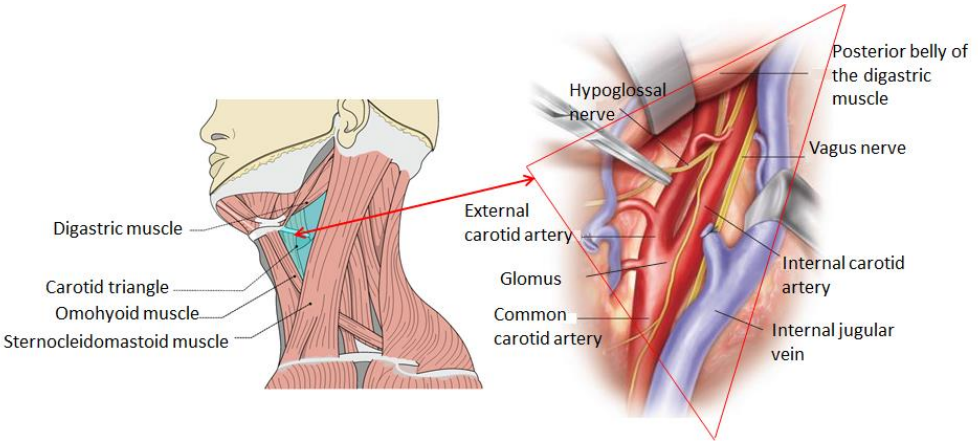

Figure 1.1. Anatomy of the common carotid artery; the left side of the neck is represented (adapted from [48])

The main contents of the carotid triangle are made up of the common carotid artery, the hypoglossal and vagus nerves, and the internal jugular vein. At the level of the superior margin of the thyroid cartilage or at the level of the fourth cervical vertebra (C4), the common carotid arteries split into the external and internal carotid arteries [49]. The carotid artery is close enough to the outer skin to press down on it and feel the carotid artery pulse. It is one of the larger arteries that the throb of the artery, as the walls distend or widen, could be felt with each heartbeat.

The histological structure of the CCA wall consists of three layers (see Figure 1.2.) [17,50]:

- The innermost layer is called the *tunica intima*. This layer is composed of endothelial cells. A membrane composed of an elastic fiber, which is called the *internal elastic lamina*, separates the inner layer from the middle layer.
- The middle layer is called *tunica media.* It is mainly composed of longitudinal smooth muscle cells, surrounded by connective tissue. The combination of the inner and middle layers is called the *intima-media* complex.
- The outermost layer is called the *tunica adventitia*. This layer is composed of connective tissues, mostly collagen fibers.

Finally, the outer layer gradually extends into the surrounding connective tissue.

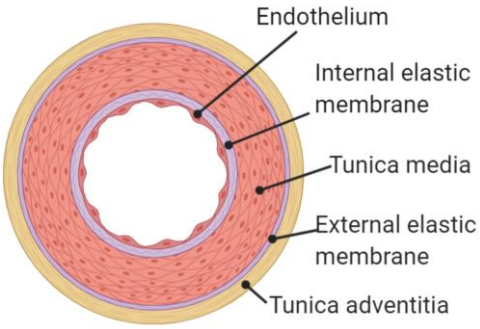

Figure 1.2. Histological structure of the common carotid artery

1.2. Longitudinal motion of the artery wall

During systole, ventricular contraction ejects blood into the major arteries, resulting in the expansion of the arteries, while during diastole, when ventricles are relaxed, the elastic walls of the blood vessels return to their initial position, thus pushing the blood to the periphery. In addition, the pulsating blood flow is caused by the radial expansion of the arteries; most arteries (carotid, brachial, popliteal arteries) have a longitudinal motion, i.e., movement parallel to the blood flow, which characterizes vascular elasticity. It has been assumed that longitudinal motion is negligible, compared with the diameter change or radial motion. However, using modern ultrasound scanners, it has been noticed that *intima-media* complex during the heart cycle move in both radial and longitudinal directions [21,22]. The longitudinal motion of the arterial wall has been observed to have the same amplitude as the radial motion and reaches around one millimeter [23].

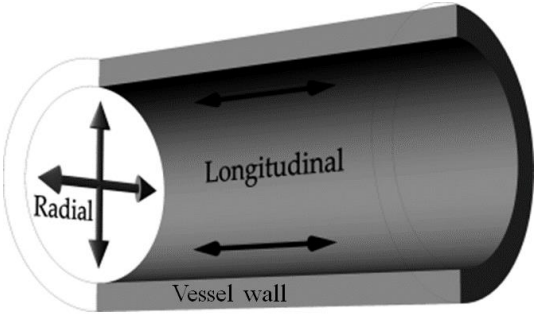

Figure 1.3. A schematic figure of a vessel showing the directions of the longitudinal and radial motions (adopted from [22])

Distinct multiphasic bidirectional longitudinal motion of the *intima-media* complex could be observed during the cardiac cycle (see Figure 1.4.). The first antegrade motion (1) (i.e., motion in the direction of the blood flow) of the *intima-media* complex is observed at the beginning of systole. Later, still in systole, the first retrograde motion (2) (i.e., motion in the opposite direction of the blood flow) of this

complex appears. During diastole, the second antegrade motion (3) of the *intima-media* complex follows, and finally, it gradually returns to its original position (4). The first antegrade longitudinal motion (1) and the distension of the artery started almost simultaneously. The retrograde longitudinal motion (2) starts almost the same time as positive and second antegrade motion (3), as the negative slope of the diameter. The direction of blood flow in the artery is antegrade throughout the length of systole and diastole, and the longitudinal motion is of the same magnitude as the diameter change [21].

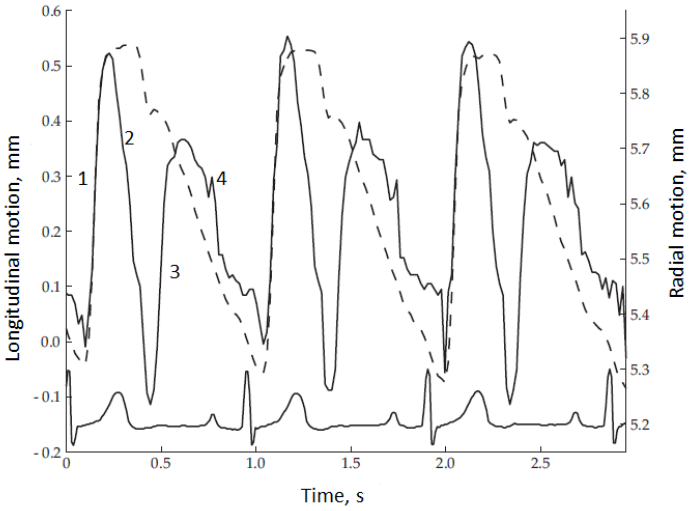

Figure 1.4. CCA longitudinal motion of the *intima-media* complex (—) and radial motion (- - -) in relation to the electrocardiogram (bottom trace); the numbers (1, 2, 3, 4) indicate the phase of longitudinal motion during the cardiac cycle; longitudinal motion is of the same magnitude as the diameter change; note the pattern of multiphasic longitudinal motion: retrograde motion during late systole (2) and second antegrade motion during diastole (3) (adapted from [21])

Cinthio et al. [21] supported by Nillson et al. [51] has shown that the *adventitia* layer of the artery wall had the same basic pattern of longitudinal motion, but the magnitude of the motion is smaller than that of the *intima-media* complex, thus demonstrating the presence of previously unknown substantial shear strain, and thus shear stress intramurally. In demarcation between the *media* and *adventitia* layers (likely at the external elastic lamina, which is a layer of elastic connective tissue, lying between the above mentioned two layers) (see Figure 1.2.), it seems that there occurs the largest longitudinal shearing, and thus shear strain. To sum up, it seems that the *media* and the *adventitia* slide against each other at the *external elastic lamina* (see Figure 1.5.).

Later, this phenomenon was named by Zahnd et al. [52] as “longitudinal kinetics” (LOKI), a cyclic shearing motion of the arterial wall when the *intima-media* complex moves with respect to the *adventitia* layer, parallel to the direction of the blood flow during the cardiac cycle. LOKI was observed in the abdominal aorta, carotid, brachial,

popliteal arteries. The studies have shown that the parameter of "longitudinal kinetics" reflects the stiffness of the arteries and the presence of cardiovascular risk factors [21,52].

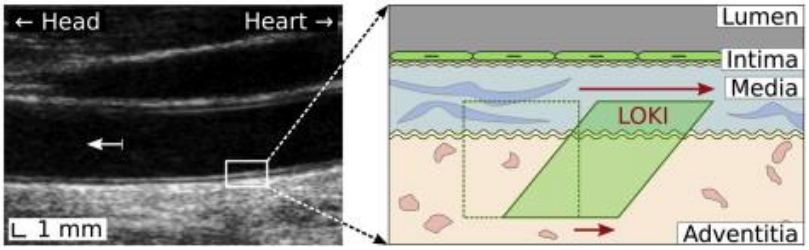

Figure 1.5. Longitudinal B-mode ultrasound image of a healthy CCA *in vivo* (*left*); the direction of the blood flow in the lumen is indicated by the white arrow; LOKI occurring within the concentric layers of the wall during the heartbeat (*right*); please note that the tissue motion obeys a multiphasic and bidirectional pattern in both retrograde and antegrade directions during the cardiac cycle, source: Zahnd et al. [52]

The geometry of the walls of blood vessels is affected by the blood flowing through them. The elastic arteries (aorta, pulmonary arteries) have a "shock-absorbing" function that allows them to maintain a relatively constant pressure, gradient despite the constant pumping action of the heart, making the flow of pulsating blood from the heart continuous [53].

During systole, when the left ventricle contracts, blood is pushed out from the heart into the circulatory system. The ejected blood expands the elastic walls of the blood vessels, and thus the blood vessels accumulate a portion of the blood ejected by the heart. During diastole, when the left ventricular valve closes, the walls of the blood vessels contract, pushing the blood away. This causes an arterial pressure wave to travel through the arteries, called a pulse pressure wave. This wave travels through the arteries at a much higher rate than the speed of blood particles. The PW depends on the elasticity of the artery wall, causing almost simultaneous flow of blood in the arteries [54].

Despite the fact that the arteries expand in the radial direction, as they propagate in a pulse pressure wave, the longitudinal motion of the arterial walls is observed as well. As already mentioned, the longitudinal motion of arterial walls has been considered negligible or absent for a long time. The longitudinal motion was first observed by Lawton and Greene (1956), who performed studies with the abdominal aorta [55]. Later, the results were confirmed by Patel et al. (1961) in studies with the thoracic aorta [56]. Longitudinal movement of the thoracic aorta was very small, and diaphragm movements during the respiration were thought to be mainly the result of the onset of longitudinal arterial wall motion. The subsequent studies have shown that the inner layers of the arterial walls, i.e., *intima-media* complex, move in the radial as well as longitudinal directions during a pulse wave propagation [57]. It was thought that breathing causes longitudinal movement of the arterial walls. However, much more reproducible longitudinal movement of the artery wall was observed when patients were asked to hold their breath during the examination [23].

Another factor that would affect the longitudinal movement of the artery wall is the shear stress caused by the shear strain, when the *intima-media* complex of the vessel moves more than the outer layer of the vessel [58]. Artery wall shear stress is dependent on the blood viscosity and the blood velocity gradient at the vessel wall (wall shear rate). As the blood velocity increases, the shear rate increases as well. Later studies have shown that there is no correlation between the longitudinal motion and the wall shear rate, and thus the wall shear stress [59].

The cardiac cycle consists of systole and diastole, during which the blood pressure in the blood vessels changes. Normally, systolic blood pressure is 120 mmHg, and diastolic blood pressure is 80 mmHg [53]. The studies have shown that adrenaline can significantly increase the longitudinal movement of the artery wall, and during systole, the longitudinal movement of the intima-media complex can increase by more than 200 % at the highest blood pressure levels, as compared to the baseline [15]. Moreover, the administration of drugs that increase the heart rate and blood pressure (such as norepinephrine) has an effect on the increased longitudinal movement of the artery wall [58].

Recent studies have shown that the longitudinal motion of the carotid artery is progressively attenuated along the length of the artery, as it is located away from the heart. As an obvious decrease in the amplitude of motion along the carotid artery exists, it is quite clear that the cardiac factors can affect the amplitude of longitudinal motion in the wall of the carotid artery. However, no studies have been performed to directly measure the influence of the cardiac mechanics on the longitudinal motion [52].

It has been hypothesized that there is simultaneity between the timing of retrograde longitudinal motion and left ventricular mechanics, and the timing of anterograde longitudinal motion and the local blood flow events at the carotid artery. The studies have shown that there is no difference in time between the peak blood velocity and peak anterograde motion. However, in terms of time, a difference was obtained between the time at peak retrograde longitudinal motion and the time of peak apical and basal rotations of the left ventricle. The amplitude studies revealed a strong correlation between the peak retrograde longitudinal motion and peak basal rotation of the left ventricle, but no correlation between the apical rotation or basal septal longitudinal motion. The researchers concluded that there is a temporal relationship between the anterograde longitudinal motion of the carotid artery wall and blood velocity. Meanwhile, the retrograde longitudinal motion in terms of time and amplitude is related to the rotation of the left ventricle, but not to the longitudinal septal displacement, as originally hypothesized. The determinants of the phases of longitudinal motion remain unknown, despite the preliminary evidence of a link between the longitudinal motion and cardiovascular health [16].

1.3. Review of the digital dynamic artery models

The literature on the digital dynamic artery models shows a variety of approaches, and the motion of the carotid artery wall has been modeled by many authors. Gemignani et al. [42] simulated the artery as a cylinder and radial motion, as

Sawtooth function. Synthetic images were obtained by using the Field II ultrasound simulation program. Within the volume of the phantom, 100 000 scatterers were randomly distributed, and strong scatterers were placed to simulate the boundaries. The images were made by simulating 13 MHz linear array probe with 192 elements. Only several parameters were presented for B-mode imaging and ultrasonic probe simulation, which is a limitation of this study. In total, 100 images were created to simulate five cardiac cycles. The main purpose of this simulation was to estimate the accuracy of the algorithm in assessing the diameter by using the absolute error parameter.

Another solution is presented by Solomou et al. [43] where artery radial motions had a triangular function. In this approach, the synthetic images were based on the clinical structure of the CCA, and the grayscale median levels for each area, i.e., blood, *intima-media* layer, *adventitia*, were proposed. Nonetheless, realistic B-Mode ultrasound videos of the artery were generated by using MATLAB based simulation procedure instead of Field II. Speckle noise in ultrasound videos was applied by using a random distribution with a noise variance from 0.01 to 0.06. The simulated video consisted of 120 images, which correspond to three cardiac cycles. The mean squared error was used to compare the result of automated and manual measurements of the CCA diameter.

As reported by Deng et al.[44], they proposed a geometric model of CCA where a blood vessel was represented as a concentric cylinder (see Figure 1.6.).

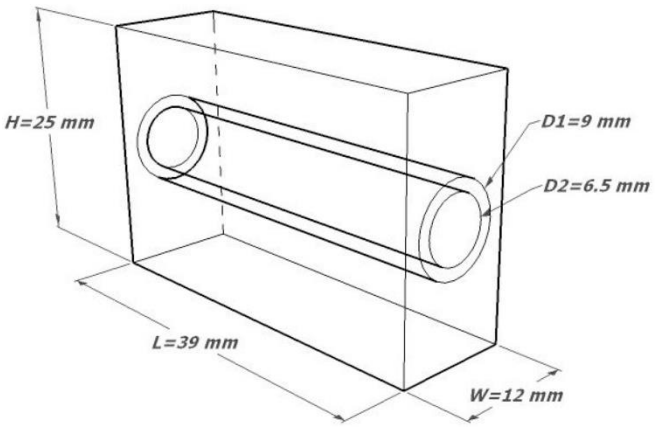

Figure 1.6. Geometric model of a segment of the CCA, source: Deng et al. [44]

The scatterers in the artery model were randomly distributed within the volume of the model, and the amplitudes of the scatterers followed Gaussian distribution. The intensity of the scatterers of the blood flow was set to zero, while the vessel walls were set to five times the intensity of the surrounding tissue. Even though the above mentioned studies do not take into account the number of scatters per resolution cell (resolution cell is the minimum volume that can be extracted by the imaging system [60]), Deng et al. did include it. What is more, the parameters of the B-mode imaging and ultrasonic probe that are used in the ultrasound simulation based on the Field II

program were presented in detail, for example, center frequency 10 MHz, sampling frequency 100 MHz, frame rate 1333 Hz, ultrasound velocity 1540 m/s, etc. The motion in the dynamic scatterer model of the artery is constructed by moving the positions of the scatterers, according to the synthesized PW. The PW is estimated from the *in vivo* RF signals of the vessel wall by using a 1-D NCC algorithm based on the echo tracking. The artery model was proposed to provide a realistic data source for the validation pulse wave velocity (PWV) estimation algorithms. In order to quantitatively verify the effectiveness of the simulation model, the normalized root mean squared error (NRMSE) was used to compare the estimated and preset PWV.

For the motion in the radial direction, Hu et al. [45] proposed an isotropous pulse model with elasticity to describe the relationship between radial displacement and blood pressure. For the motion in the axial direction, the longitudinal motion of *intima-media* complex was extracted from a healthy subject and directly used to get a realistic simulation of pulsatile motion in the longitudinal direction. Hu et al. suggested that in order to obtain the values of parameters of scatterers distributions, including the shape parameter, density, and intensity, for arterial layers and blood, the envelope signals, simulated from different configurations of scatterers distribution, could be compared with those from different kinds of tissue of CCA *in vivo* through a statistical analysis, and this seems an innovative approach. As Deng et al. [44], Hu et al. used detailed parameters of the B-mode imaging and ultrasonic probe in the ultrasound simulation based on the Field II program. The artery model was proposed for the validation of two-dimensional wall motion and blood velocity estimation algorithms.

However, neither of the previous studies considers the radial and longitudinal motions slope deep into the tissue. To the author's best knowledge, very few publications can be found in literature that addresses the issue of artery motion slope. It was done by Stoitsis et al.[46]. The radial motion was defined in a piecewise fashion by using pulse function, which parameter values were determined based on the experiments with *in vivo* data. The longitudinal motion was modeled as a sinusoidal function, because there is no conclusive information about the mathematical modeling of this motion. Based on a similar *in vivo* examination, the spatial dependence of radial and longitudinal motions, which are independent of the axial position, was incorporated as well. Later, Golemati et al. [61] proposed to use a pulse function to model the radial motion as well as longitudinal. Function parameters were accessed during the experiment with real data, but only five subjects were incorporated into this investigation. Such a small sample of subjects is not sufficient to describe the pulse function parameters. Moreover, there is a large variety of longitudinal motion patterns between the individuals [58,62,63], making longitudinal motion modeling difficult.

1.4. Adequate simulation of the real ultrasound echoscopy

The US imaging is the most widely used imaging modality in clinical practice due to its low cost, non-ionizing nature, noninvasiveness, and real-time imaging. The US imaging technologies are continuously evolving. A lot of imaging advancements are related to the processing and parametrization of raw RF echoscopy signals,

opening new possibilities in tissue elastography, quantitative imaging, and parametric mapping of quantitative tissue parameters, valuable for differential diagnostics.

A powerful tool for further developments and modifications is modeling and simulation of all echoscopy processes, especially in the RF domain. This *in silico* approach potentially allows simulating new concepts, methods, and implementations, which are unavailable in a clinical environment and even in laboratory experiments. However, the success decisively depends on the quantitatively evaluated adequacy of simulation to the real echoscopy situation. Therefore, the simulation method and quantitative evaluation of involved simulation uncertainties are highly important. The general method of uncertainty quantification in simulation models proposed in [64] is based on consecutive forward uncertainty propagation (from the system under simulation towards the output of the system model) and the backward uncertainty quantification (consecutive evaluation uncertainty components from system model output to the real system). In the simulation uncertainty components are related to the models of multi-element transducer and beamforming, the US wave propagation and 3D field, backscattering, and speckle formation in nonhomogeneous tissue, transmit-receive mode, RF data acquisition, and preprocessing. Therefore, echoscopy deals with complex interlinked modeling and simulation tasks and requires reliable simulation methods and software tools.

The adequate modeling of US wave propagation in the biological tissue involves solving the nonlinear KZK equation, which can be derived as the parabolic approximation to the Westervelt equation [65]. The direct solution of equations is quite complicated and limited to directional wave propagation. From the KZK equation, computational resource-saving K-wave model and angular spectrum approach (ASA), which are based on some simplified assumptions of linearity and space invariance of PSF [66,67,68], were derived. These methods, balancing between the adequacy and needed computational resources, are used for the US field modeling and simulation of the wave propagation in tissue [69], but not directly applicable for the transmit-receive scanning of scattering media by multi-element transducer arrays.

The most popular simulation software packages are CREANUIS [35] (based on KZK equation) for nonlinear propagation and simulation of harmonic imaging and Field II [36] (based on Huygens principle and hybrid digital-analytic method), which gained a wide application since the publication of the model in 1991 [37] and software package in 1996 [38]. The popularity of Field II lies in considerable flexibility to accommodate a wide range of transducers, beamforming options, and imaging possibilities. It is still a powerful and evolving tool for the simulation of various scanning and focusing modalities as well as the whole echoscopy mechanism, including scattering in the tissues and organs [39]. Scanning by a linear array transducer, simulated by both Field II (as a reference) and ASA, shows that Field II is effective in the simulation of the US field generated by the transducer, while ASA in nonlinear propagation [70]. The comparison of several new resources-saving simulation tools for fast simulation of the US data has shown [71] that the methods, based on the principle of convolving a set of point scatterers with a PSF, do not simulate the process of US field and beam formation and interaction in echo mode, in

contrast to Field II. The simulations of plane wave images made with Field II, using wire phantom and a tissue-mimicking phantom, having anechoic cysts [72], have shown a high value of simulation, which could be applied for the optimization of imaging.

Digital models of tissues and organs are as well components of *in silico* echoscopy and sources of simulation uncertainty. Nonhomogeneous tissue is usually simulated by discrete digital phantoms, based on the small scatterers distributed in space. The proper setting of scatterer maps is essential to the realistic resulting image of the ultrasonic wave interference (speckle) pattern [73]. Mean scatterer spacing (MCS) for different tissues was reviewed in [74], showing a potential to simulate tissue microstructure by fitting the MCS parameter. The scatterer maps as well could be generated from the real images by solving the inverse-problem of US speckle formation [75].

The most simulation results are for the case of linear scanning transducer arrays. The articles mainly use Field II simulation results as a reference for the analysis of some US imaging development, without prior assessment of simulation adequacy. Although there are a lot of Field II applications described in many articles, only a few publications deal with a quantitative comparison of simulation and experiment evaluating uncertainties. The brief comparison of Field II simulation and experimental results provided on wire images was presented in [40,41,76].

As reported by Pham et al. [41], in order to validate the simulated PSF, physical wire phantom was used. In both, physical experiments and digital simulation, 10 MHz linear array transducer was used. The simulated wire phantom was adequate to the measured one, i.e., the positions of the point scatterers were the same as in the measured wire phantom: 41.8 mm, 51.7 mm, 61.6 mm, and 71.6 mm away from the transducer in the axial direction. The discrepancy between the FWHM of the measured and simulated resolutions were 6.7 %, 0.6 %, 0.1 %, and 10.4 % in the lateral direction and 17 %, 15 %, 16.7 %, and 21 % in the axial direction, respectively.

The same methodology as Pham et al. [41] used Mattausch and Goksel [40]. The difference between the parameters was that Mattausch and Goksel used the 6.6 MHz linear array transducer for the measurement and simulation, instead of 10 MHz as Pham et al. [41]. The positions of the point scatterers were the same as in the measured wire phantom: 40.4 mm, 60 mm, 86.6 mm away from the transducer in the axial direction. The error between the FWHM of the measured and simulated resolutions were 0 %, 6.3 %, and 0.5 % in the lateral direction and 6.5 %, 12.4 %, and 4.9 % in the axial direction, correspondingly.

Another group of researchers [76] obtained wire phantom images by both 35 MHz linear array and Field II simulation of the array. The measured −6dB lateral width at the wire targets was 175 μm, 165 μm, 200 μm, 260 μm, while the simulated −6dB lateral width by Field II was 155 μm, 165 μm, 175 μm, 245 μm, accordingly. The comparison of the Field II simulation and experimental results was presented without a quantitative assessment of adequacy.

The quantitative results of simulation and dealing with experimental verification of such simulations are presented further when the other types of arrays were incorporated into the research. Phased array lateral PSF width at 60 mm depth was

simulated with Field II for 5 MHz frequency by [77], and FWHM was 1.4 mm, without the experimental verification of this result, since the experiments were provided with a curvilinear array transducer. Field II simulations performed for a 3.5 MHz phased array with a focal depth at 30 mm and spatial resolution were quantified by measuring the lateral FWHM width in resolution target phantom [78]. The simulated resolution (FWHM) with the phased array at focal depth was 1.01 mm lateral and 0.6 mm axial. However, the simulations were not verified, since compared with the experimental results of curvilinear array transducer of 3.1 MHz. Simulated lateral FWHM, which is found minimal at the focal distance, is almost twice wider in the near field (1.5 mm at 1 cm) or far field (2.41 mm at 5 cm). Field II calculation results were obtained for point reflector at a distance of 2d, where d is the length of the phased array with 64 elements [79]. At the frequency of 3.5 MHz and the distance of 2d, the FWHM of the lateral main lobe obtained about 2 degrees of angle, without experimental verification of this result.

With the Field II simulation of phased 1.75D array, it was shown that the beam width in the elevation direction (or scanning slice thickness) has a significant influence on the B-image contrast reproduction [80]. This was shown by the experimental contrast verification with a phantom of spherical inclusions, but no verification of quantitative beam width estimates in the elevation direction was provided. The experimental analysis of elevation beam width profiles that were made for the freehand ultrasound calibration purposes has shown the importance of scanning slice thickness for linear-array transducer calibration accuracy [81], but no results for linear array were provided, and there were no digital simulations. The improvement of ultrasound transducer radiation beam profile was verified by hydrophone scanning of the pressure field [82], but not simulated. Thus, a quantitative comparison of linear array simulation with an experiment, including the analysis of resolution in elevation direction, remains limited.

The problem of simulation adequacy is especially crucial for the USE, where tissue displacements could be extremely small, and the resolution in strain estimation is important [83]. For example, Field II could be used for static US images as well as pulsating carotid artery simulation [46]. It is as well effective in combination with a convolution-based method [84], which shows the potential of 3D moving scatterers and tissue deformation modeling, using the finite element method and then the corresponding pre-/post-deformation RF signals comparison, using Field II [85,86]. Despite the very wide use of Field II simulation software, the remaining problem that is relevant for the development of new imaging modalities, including USE, is a quantification of simulation uncertainty, especially for the sector scanning. An adequate simulation of tissue deformations would open a way for more rapid development of the USE, which enables differential tissue diagnostic [28,87], including the use of the endogenous motion of tissue, induced by the cardiovascular activity, where experiments are limited because of technical and principal constraints [31].

1.5. Motion tracking algorithms

The motion tracking algorithms that are described in this section have been published in "Carotid Wall Longitudinal Motion in Ultrasound Imaging: An Expert Consensus Review" [27].

"Since the initial evaluation of carotid wall longitudinal motion in humans *in vivo* [22,88], an increasing number of motion tracking techniques have been designed to address this task [61,89]. Several challenges inherent to either ultrasound imaging (e.g., speckle noise and artifacts) or vessel physiologic behavior (e.g., abrupt motion patterns) must be considered for reliable motion tracking. As a result, specialized and advanced methodologies were gradually developed to specifically extract longitudinal motion."

1.5.1. Wall motion extraction based on the B-mode images

The B-mode is the most well-known representation of ultrasound imaging: this modality, characterized by a specific grayscale speckle pattern, is used to represent structural information that can be interpreted visually on the scanner monitor. Three major motion-tracking approaches are used to extract the motion from B-mode ultrasound image sequences: block matching (BM), optical flow (OF), and feature matching (FM). These techniques and the related studies, focusing on longitudinal motion, are listed in Table A1.1 in Appendix A1 and discussed thereafter.

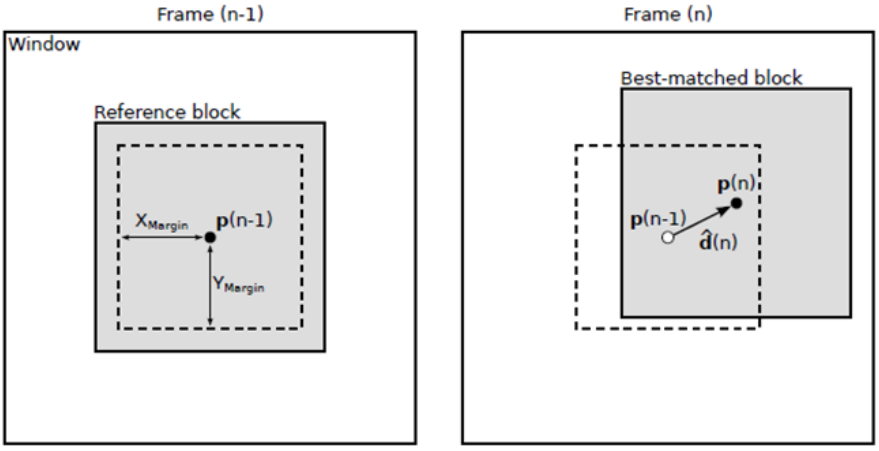

Figure 1.7. Block matching schematic diagram: the displacement $\hat{\boldsymbol{d}}(n)$ corresponds to the motion from the reference block centered on the point $\boldsymbol{p}(n-1)$ to the location of the best matched block centered on the point $\boldsymbol{p}$(n) between the $(n-1)$st and the nth frames; the search window corresponds to the whole investigated neighborhood defined by the maximal displacement margins $[X_{Margin}, Y_{Margin}]$, delimited by the dashed square, source: Zahnd et al.[19]

Block matching. BM is a conventional technique in the field of motion estimation and is widely used to perform speckle tracking in image sequences.

The general underlying principle (see Figure 1.7) is to find within the (n + 1)st image the most probable location of a target region, denoted as the reference pattern, from the nth image. The estimation is performed either by minimizing a difference metric with operators, such as the sum of the squared differences, or maximizing the similarity metric with operators, such as the normalized cross-correlation. Among the most critical parameters are the size of the analyzed speckle pattern and the size of the maximal authorized displacement (i.e., the "block" and the "search window," respectively).

The strategies directly based on the traditional BM have been successfully applied to assess the longitudinal motion. In an early study [88], the extracted motion waveforms were rather coarse, likely because of a large block size and no sub-pixel interpolation. However, the obtained reproducible and well-defined patterns contributed to the feasibility of *in vivo* examinations. The BM method known as "echo tracking," using a small block size (originally defined as a 0.7 × 0.7 mm^2 region), enabled accurate tracking of salient speckles in carefully acquired images [23]. Nevertheless, the reduced block sizes are unlikely to provide robust results in general routine clinical scans, where the image quality is often poor.

Adaptive BM approaches were introduced to tackle the issue of speckle decorrelation across time. Such approaches generally correspond to the mathematical model, involving a control scheme as well as an evolution scheme, capable of representing the expected temporal motion and compensating for tracking errors. The Kalman filter was exploited to model the temporal changes in the location of the target block [90,91] as well as in its gray levels [19,90,91] during the cardiac cycle.

The BM approach, based on the consideration of two previous frames (as opposed to only one in the classic techniques), was proposed to increase the tracking robustness [92]. Adding one extra reference block in a BM scheme was proposed to use different reference blocks [92], where, the actual pixel values of the previous frame were used, as opposed to Kalman-based methods, where the reference block was predicted. A more advanced method was proposed later, involving an affine block motion model, able to consider the rotation and scaling of the tracked pattern, in addition to the rigid translation [61]. A scheme based on luminance optimization was proposed as well to take into consideration the progressive variations of pixel values across the time and maximize the matching potential [63].

A non-linear state-space approach based on the elasticity model of the carotid wall and including H1 filter was further proposed and adapted to carotid wall motion estimation [93,94,95]. The major benefit of these approaches is their ability to deal with noisier data and provide robust and accurate tracking results when a conventional BM approach would likely fail.

The combined use of multiple blocks was investigated in several studies. These approaches are based on the following principle: at a given time step, the motion is independently estimated with a series of adjacent or partly overlapping blocks, and the resulting motion is obtained via the averaging of all contributions. The rationale for multiblock matching is to increase the robustness by diminishing the influence of any single block that may fail. Such approaches include five [25], six [96], or sixteen [97]

blocks. A method that is based on the consideration of multiple frames per estimation and a parabolic sub-sample interpolation in high-frame-rate cine loops (1300–1500 Hz) was developed further [98]. Several advanced search strategies, initially introduced in RF imaging [99,100], were successfully applied in B-mode imaging to improve the computation time, such as a coarse-to-fine interpolation scheme [25] and a sparse-to-dense tracking scheme [92].

Going one step further, the extraction of a dense motion field was recently addressed [101]. In this case, the temporal motion across the full width of the image is estimated by placing a block in each column (typically, > 350). A combinatorial analysis scheme based on dynamic programming is used to simultaneously extract the motion of each block (as opposed to one after the other), while enforcing motion rules and enabling fast computational times. The results from this study enabled the assessment of the degree of motion homogeneity across the length of the vessel.

Optical flow. OF consists of determining the velocity field across different temporal frames [102]. The fundamental difference between OF and BM is the adoption of the Eulerian paradigm (i.e., motion is evaluated through a static window) instead of the Lagrangian scheme (i.e., motion is evaluated by dynamically following the target). Complex motions that are involving rotations and deformations are usually captured better via OF-based approaches than BM [103].

Applied in the context of carotid longitudinal motion, OF has been successfully used in several studies [61,104,105], as listed in Table A1.1 in Appendix A1. It was reported that the general waveform shape of the wall motion was different when extracted by BM and OF, although their peaks occurred at the same time instants of the electrocardiogram signal [106]. The maximum velocity and extracted motion in the radial and longitudinal direction were reported to be greater when using BM [106]. The estimated wall motion on the same B-mode images by OF and BM in the radial direction were reported to be more similar compared with those in the longitudinal direction [106]. In the presence of either Gaussian or speckle noise, it has been reported that the weighted least-squares OF outperforms the BM, particularly in poor quality images that are typically observed in clinical populations [61].

Feature matching. An original approach based on automatic extraction of several salient image regions was recently introduced [107]. The detectors, such as scale-invariant feature transform, speeded-up robust features, and maximally stable extremal regions, were used to identify the target points. The main advantage of this approach is its robustness, because only salient points are considered for tracking and are re-selected at each time step. Moreover, this method has potential to be fully automatic, because regions are determined by the above mentioned descriptors. Additionally, shear strain evaluation in different anatomic layers is possible as well by using the FM via the tracking of points, located in different anatomic layers, offering a similar potential for depth-specific shear evaluation as provided by certain BM approaches [108,109]. However, a generally encountered drawback of FM approaches is the constant re-selection of target points and the averaging of their respective motion vectors, making both precise single-point and full dense-field motion estimation impossible.

1.5.2. Wall motion extraction based on the RF signals

Tracking methodologies based on RF signals were introduced in 1985 to estimate the radial motion via the autocorrelation approach [110]. As opposed to B-mode imaging, RF-based motion tracking involves the computation of the phase shift (i.e., in the frequency domain) between two subsequent time steps to determine the corresponding spatial displacement. In fact, the acquisition and export of RF signals usually necessitate research-oriented scanners, as this functionality is generally not available in clinical devices. An overview of the approaches that were developed towards the carotid wall motion estimation is provided in Table A1.2 in Appendix A1 and detailed thereafter.

Concerning small interframe displacements, a BM based method has been developed in an iterative manner [98]. Phase-based estimation on RF signals has been applied on phantom and *in vivo* carotid for simultaneous wall motion and flow estimation [111,112,113,114]. Phase-sensitive methods have recently been applied for 2-D motion estimation, using 2D frequency spectra of RF echo signals, using the complex analytical signal, obtained by modulating the ultrasonic field [115] by the Hilbert transform [116,117,118,119] or the wavelet transform [120,121]. The Hilbert transform was repeatedly used to generate a complex analytical signal from RF data, using correlation-based estimators [116]. In line with a similar approach, phase correlation and subsample interpolation were successfully applied [122]. Fourier-based methods [123,124,125] were introduced as well. A paired 1D and 2D motion estimation technique with shifted cross-spectra developed to assess the phase shift was put forward and exhibited an increased accuracy with a smaller spatial window than conventional 2D motion estimators [116]. One advantage of Fourier-based approaches is their intrinsic ability to achieve sub-pixel accuracy without the need for spatial interpolation, which can result in greater accuracy, compared with speckle tracking in B-mode [126,127]. It was reported that the 2D phase-sensitive method [127] outperformed the BM method in terms of accuracy (bias errors and standard deviations) in motion estimation at a high frame rate that was realized by parallel beamforming [126]. This is especially important along the longitudinal direction of the artery, because the image across this axis is generally coarser than the radial counterpart.

The approach, relying on synthetic aperture imaging, was specifically designed as an unconventional beamforming strategy to generate a pressure field with a controlled carrier frequency in the transverse direction [115]. This real-time technique, referred to as “US tagging” (in reference to the principle of magnetic resonance imaging tagging), consists of the transmission of an unfocused wave, subsequently received with a dynamic quadratic focusing combined with dynamic apodization [119,128]. Building upon the potential offered by such marked signals, a local phase-based OF method was devised for subpixel estimation [129] and was applied *in vivo* in the context of longitudinal motion on so-called RF-2-D images [20]. A similar approach, leveraging high-frame-rate imaging (10 kHz), was introduced as well [117], bridging the gap between the association of longitudinal motion and PWV. For 2-D velocity vector estimation of tissue motion, plane wave imaging has been used along with transverse oscillation and efficient frequency domain estimator [117]. It is

noteworthy that unitary displacements, greater than half of the signal wavelength (be it determined by the carrier frequency along the radial direction or the synthetic aperture along the longitudinal direction), cannot be ascertained via phase-tracking methods, because they fall under the effect of aliasing [116,129], therefore justifying the demand for a sufficiently high frame rate.

Inspired by the field of computer vision, an approach known as "motion video amplification" was proposed to magnify the tiny and subtle deformation of the vessel wall in B-mode ultrasound carotid image sequences [130]. While large-scale deformations are not amplified, low-amplitude deformations within the vessel wall (such as longitudinal motion, radial motion, deformation caused by the passage of the pulse wave) are substantially magnified up to a factor of 1000 and can be easily perceived by the naked eye. This technique opens up new possibilities for the evaluation of complex motion patterns, such as the small phase W and phase X displacements described under the Characterization Based on Directional Wall Displacements. Moreover, this technique requires the acquisition of high-frame-rate sequences (> 2500 Hz) that are available on only a limited number of research-oriented ultrasound systems.

1.5.3. Available tools

The velocity vector imaging (VVI) software platform (VVI, Research Arena 2; TomTec Imaging Systems GmbH, Unterschleissheim, Germany) is a commercially available tool that was used to investigate the association of longitudinal motion with cardiovascular risk in human and mouse [18,24,131]. This technique, initially designed to measure the heart dynamics, involves the positioning of a multisegment horseshoe-shaped skeleton in the image, using 20 control points in total. When applied to the carotid artery, one segment (approximately 5 mm long) can be positioned on a region of interest in the intima-media complex. Most importantly, the VVI displays the measured temporal trajectory together with the corresponding motion amplitude, but does not support any export of the time series for the finer analysis. Despite relevant clinical findings [18,24,131], a thorough evaluation of the tracking performance [19] revealed poor accuracy and reproducibility, while being tedious and time consuming because of substantially large amount of manual operations that are required to run VVI.

The MyLab desktop analysis software (Esaote, Firenze, Italy) is a commercially available tool that was used to extract longitudinal shear values [132]. However, although this technique was specifically designed for the ultrasound carotid data, the quantitative reports of the tracking performance *per se* are not publicly available to the best of the authors' knowledge.

The CAROLAB software platform [133] is a freely available (available at: https://www.creatis.insa-lyon.fr/carolab/) tool that has been put forward to analyze the ultrasound image sequences of the carotid artery. The motivation behind CAROLAB is to encapsulate several previously published and thoroughly validated methodologies for wall segmentation [134] and motion estimation [19,101] within the efficient graphical user interface.

A web-based platform named CAROTID that integrates motion-based computer-aided diagnosis functionalities for patients with carotid atherosclerosis has been developed [135].

1.6. Conclusions of the 1st chapter

1. Atherosclerosis is a chronic disease of the arterial wall that is not noticeable until the atherosclerotic plaques build up. However, it has been proven that significant changes in the mechanical properties of arterial walls occur much earlier than the anatomical changes. The longitudinal motion of the arterial wall, a parameter reflecting the mechanical properties of the arterial wall, described as a bidirectional motion of the *intima-media* complex, is parallel to the blood flow during the cardiac cycle. Although the longitudinal movement of the carotid artery wall is associated with cardiovascular health, the determinants of longitudinal motion remain unknown.
2. The motion of the carotid artery wall has been modeled by many authors. Nonetheless, in order to model a dynamic 3D artery model, many parameters must be incorporated, i.e., scatterers amplitude, number of scatterers per resolution cell, radial and longitudinal motions amplitude and waveform, motions slope deep into the tissue, etc. However, most of the previous studies do not take into account all of the above mentioned parameters. Therefore, a new artery model, capable of reproducing a realistic dynamic 3D artery model, surrounded by viscoelastic tissue, is necessary.
3. Since digital simulation is increasingly important for the US imaging and elastography developments, a quantitative assessment of uncertainties, involved by all interrelated components of the simulation process as well as revealing the possible factors, causing those uncertainties, remains a problem. Besides, a quantitative comparison of simulation with an experiment, including the analysis of resolution in axial, lateral, and elevation direction, remains limited.
4. A number of motion tracking algorithms are proposed for radial and longitudinal motion detection. Some of them are freely or commercially available for the investigation of longitudinal motion. However, none of them is applied in clinical practice these days. Firstly, these methods should be carefully investigated before a wide usage.

2. DEVELOPED APPROACHES FOR SIMULATING ARTERY AND SURROUNDING TISSUE PULSATION AND ACCURACY EVALUATION OF THE MOTION DETECTION

This section is organized as follows: subsection "Carotid artery ultrasound examination" presents the ultrasonic scanner used in *in vivo* examination, scanning preset, CCA examination methodology, study population, and estimated radial and longitudinal motion signals that are used in the motion modeling. After this, the subsection "Modeling and verification of a digital simulation of physical US scanning" outlines digital scanning simulation and modeling of digital resolution phantoms, adequate to the physical scanning and phantoms. When digital scanning is presented and *in vivo* radial and longitudinal motion signals are estimated, a digital model of the artery and real *in vivo* signals that are used in it are proposed for the simulation of sequential US data. Finally, subsection "RF ultrasound signals post-processing algorithms" is devoted to both motion tracking algorithms and their testing with model data, and *in vivo* signal processing and parametrization to compare two groups, i.e., healthy volunteers and at-risk patients.

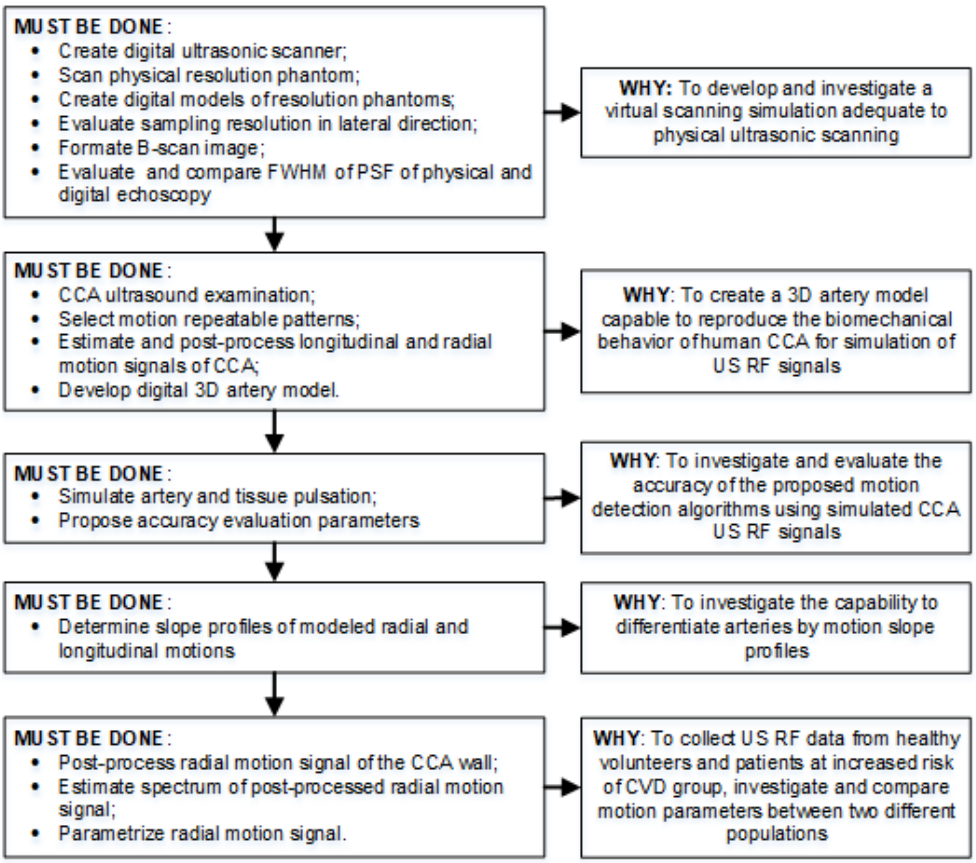

Figure 2.1. Schematic diagram illustrating the workflow structure

In order to highlight the purpose of the performed experiments, the schematic diagram illustrating the workflow structure is given (see Figure 2.1.), representing what was done and why.

2.1. Carotid artery ultrasound examination

2.1.1. Physical ultrasonic scanner

Research dedicated ultrasonic scanner Ultrasonix SonixTouch (Analogic Ultrasound, Canada), equipped with a linear array probe (L14-5/38), was used for data collection during the *in-vivo* examination of CCA. The US scanner is capable to open access to the RF signals and control scanning algorithms. The main parameters of the US scanning and RF signals digitization were as follows: frequency of US waves – 13.3 MHz, transmit focal single depth – 1.5 cm, scanning depth – 2.5 cm, frame rate – 52 Hz, number of frames – 629, number of post-beamformed scanning lines – 640, scanning sector – 50 %, sampling frequency 40 MHz, ADC resolution 16 bits. The data, US RF signals, and B-mode image sequences were stored in a cine-loop as consecutive frames for the later offline analysis in MATLAB R2018b (The MathWorks, Inc., Natick, USA).

In the axial direction, the RF signal sampling resolution is 19.25 μm (when the speed of sound waves is 1540 m/s), while in the lateral direction, the sampling resolution is dependent on the preselected line density. The sampling resolution in lateral direction was evaluated throughout the experiment where a special phantom, made [136] using a fishing line, was used. Later, the evaluated sampling resolution in the lateral direction was used in digital ultrasonic scanner simulation B-scan formation (see 2.2.1. subsection).

A picture of the phantom is given in Figure 2.2. a. The monofilament fishing line of small diameter was wounded on the screw thread at equal distances (L = 1.25 mm) and serve as point target reflectors (see Figure 2.2. b). Since the diameter of the fishing line is d = 0.1 mm only, it can be considered as a point target reflector, and the recorded image of the reflector is a PSF, which can be used to evaluate the spatial resolution of an ultrasonic scanning system.

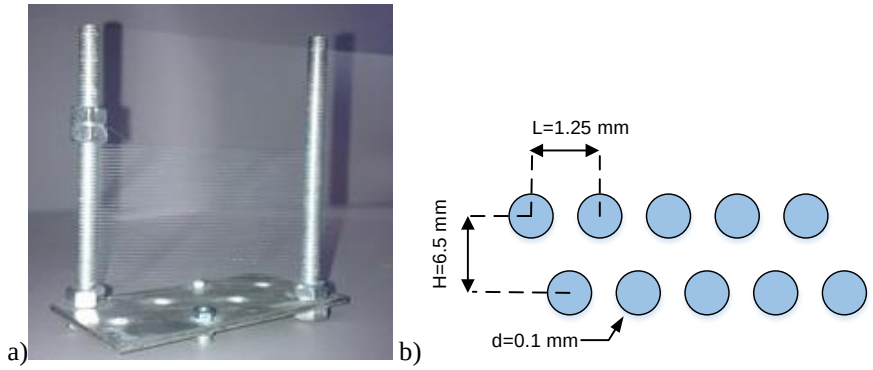

Figure 2.2. Special phantom made using a fishing line (a), cross-section structure of the phantom (b)

The phantom was placed in a container of distilled water and scanned, maintaining the main parameters of the US scanning; only the scanning depth was changed from 2.5 to 3.5 cm. By scanning the stretched threads with a linear array probe (L14-5/38) whose scanning plane is perpendicular to threads, a cross-sectional view of the threads was obtained. The acquired B-scan image of the point targets is presented in Figure 2.3. a, while the single line of the phantom image, crossing point targets laterally, is provided in Figure 2.3. b.

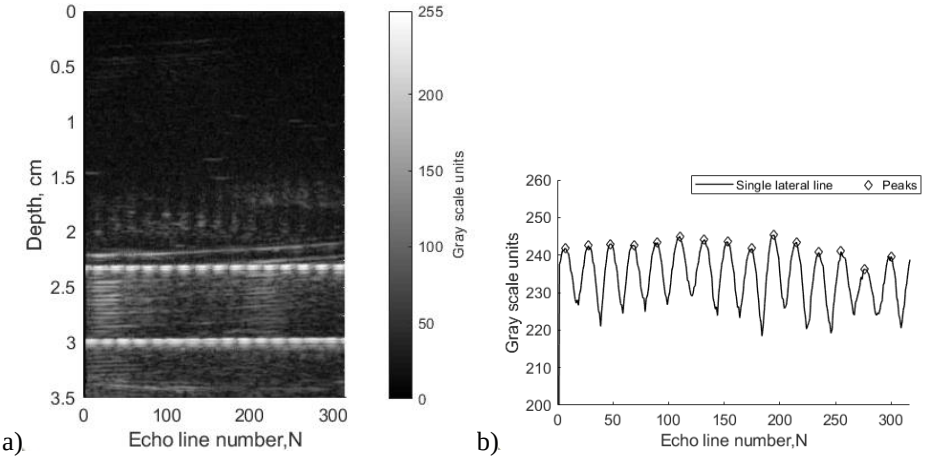

Figure 2.3. Evaluation of sampling resolution in lateral direction, using a special phantom, made by using a fishing line: the B-scan image of the point targets (a) and single lateral line of the B-scan image with seen point targets and preselected peaks, whose position was used for the evaluation of sampling resolution in the lateral direction (b)

Using a single line of the B-scan image and preselected peaks, the distances between adjacent point targets (peaks) were detected, i.e., 20.36 ± 0.48 post-beamformed scanning lines. The sampling resolution in the lateral direction was calculated by dividing the distance between point targets (L = 1.25 mm) of a detected number of post-beamformed scanning lines between two adjacent point targets, i.e., 20. It has been found that the sampling resolution in the lateral direction is 0.0625 mm.

2.1.2. CCA ultrasound examination methodology

Thirty young healthy volunteers (21 females, 9 males) and twenty-eight older at-risk patients (10 females, 18 males) were involved in this study (see Table 2.1.). As assessed by a written questionnaire, healthy subjects had no cardiovascular risk factors, while the older subjects had a high risk of cardiovascular disease and participated in the preventive program of CVD [137].

The clinical data were collected at the Lithuanian University of Health Sciences Hospital, Department of Cardiology, during May–October, 2018. The study was approved by the Kaunas Region Biomedical Research Ethics Committee (2018-08-02, No. BE-2-51, Kaunas, Lithuania). Every participant provided a written

consent to participate in the study and allowed the usage of the obtained US RF signal and B-mode image sequences under the principle of confidentiality.

Table 2.1. Characteristics of the subjects

	Young volunteers (n = 30)	**At-risk patients (n = 28)**
Age (year)	28.03 ± 9.01	50.00 ± 6.24
Height (cm)	174.60 ± 6.11	172.68 ± 9.60
Weight (kg)	73.43 ±11.76	92.54 ± 16.03
Body mass index (kg/m2)	24.02 ± 3.35	30.91 ± 3.69

Two cardiology physicians performed the acquisition of US RF signal and B-mode image sequences of the radial and longitudinal motions of CCA. Before the examination, all volunteers were asked to rest in the supine position for at least 15 min. During the US data registration, the volunteers were lying in the supine position, stretching their necks and turning it 45 degrees to the right or left, depending on the examined neck side. Both right and left CCA were scanned, since the artery motion amplitude does not depend on the echoscopic neck side [18]. The measurements of the longitudinal and radial motions of the CCA were performed 2–3 cm proximate to the bifurcation during at least two full heart cycles. In order to avoid motion artifacts, an ultrasonic transducer was mounted in a stationary holder that was attached to the couch. The sequences of US RF signals and B-mode images were recorded by volunteers holding their breath for about 10–15 seconds [16,19,21,25].

All analyses were performed by using a Clinical scanner Ultrasonix SonixTouch (see Physical ultrasonic scanner). During the examination, no pressure was applied to the transducer, i.e., it is not pressed against the neck not to deform the artery. The ultrasound examination of the artery was started at the root of the neck by moving the transducer towards the head cranially along the course of the artery. Initially, the ultrasound transducer was held across the CCA to monitor the transverse image of the artery (see Figure 2.4.).

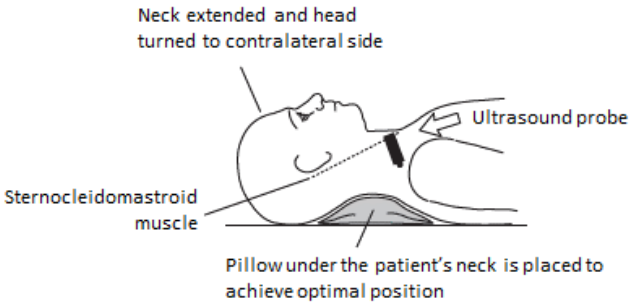

Figure 2.4. An ultrasound probe in the transverse position (adopted from [138])

The sternocleidomastoid muscle can be used as a reference point. Following these instructions, the location of the splitting of the CCA into the internal and the

external arteries was found, or the signs of vascular disease were observed (e.g., thickening of the artery wall). This results in a transverse section of the artery (see Figure 2.5.) [138].

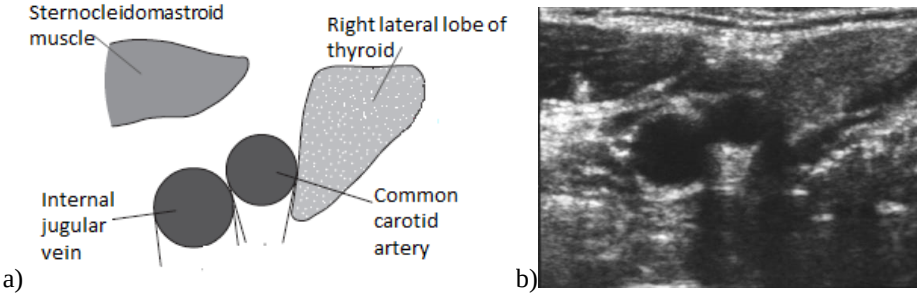

Figure 2.5. Transverse section of the CCA: a) structured and b) real; scanned the right side of the neck (adapted from [138])

By capturing the location of the CCA, the ultrasound transducer was rotated 90 degrees clockwise to image a longitudinal view of the artery. The internal and external carotid arteries are in different planes. Therefore, when a bifurcation of the CCA was found, the lower part of the probe was kept over the CCA, and the upper part was rotated through small angles to image the internal and external carotid arteries separately [138]. A representative ultrasound image, identifying the carotid artery in a longitudinal direction, is given in Figure 2.6.

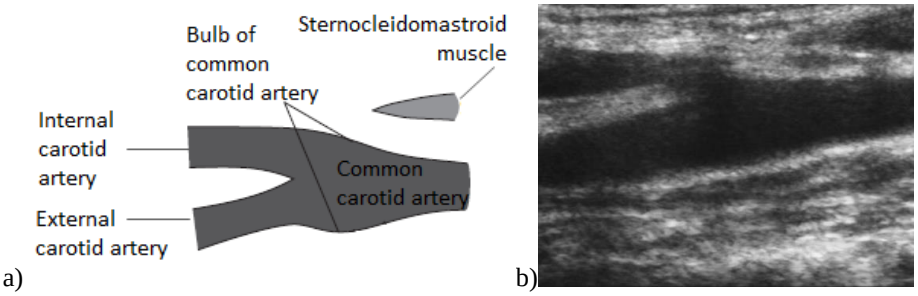

Figure 2.6. Longitudinal section of the CCA: a) structured and b) real; scanned the right side of the neck (adapted from [138])

In order to ensure that the CCA US RF signals and B-mode image sequences were of acceptable quality, both longitudinal movements had to be clearly visible along the preselected segment of the arterial wall, and CCA walls had to appear as double-line patterns [21]. When an acceptable view of the CCA was seen on the ultrasound scanner screen, the cardiology physician unhanded the transducer, and the subjects were asked to hold their breath for about 10–15 seconds until the data sequences were recorded. Finally, all sequences were stored digitally and transferred to a computer for the further analysis with MATLAB R2018b (The MathWorks, Inc., Natick, USA).

2.1.3. Selection of motion repeatable pattern

The sonography of tissue motion in-vivo is challenging. The quality thresholding of *in-vivo* ultrasound data is the first step in the analysis. Au et al. [139] proposed to average the four consequent heart cycles for representative measurement of motion in CCA. The author noticed that the indices of variability were reduced when two to four heart cycles were used. When more than four heart cycles were averaged, any improvements in indices of variability were not observed. This indicates that there is no need to record more than four heart cycles. According to these recommendations, the subjects, presenting low-quality data sequences (motion artifacts due to the patient motion, unclear *intima-media* complex in B-mode ultrasound image sequences, etc.) or having less than four full heart cycles, were rejected from the study.

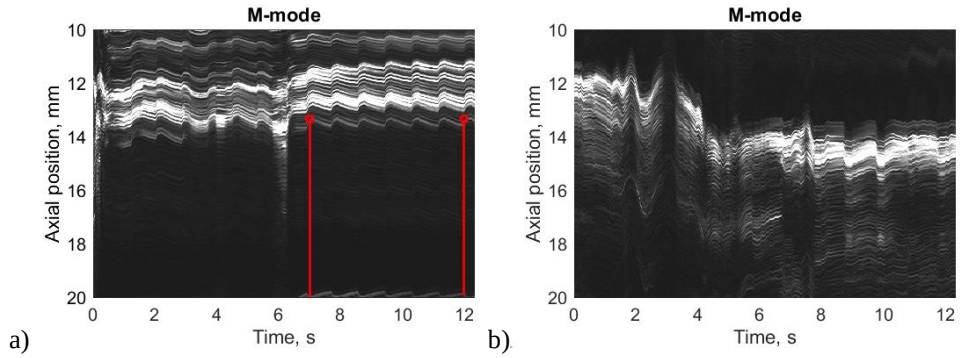

a) b)

Figure 2.7. High-quality data (a) vs. low-quality data (b) of CCA; red stems in (a) indicate the time interval, which was used for further analysis

The data quality assessment was performed based on the visual inspection of one ultrasonic scan line (A-mode) in the M-mode of each subject. The echoscopic line covered both the proximal and distal walls of the CCA.

The ultrasound line displayed in M-mode clearly showed which time interval is corrupted by the motion artifacts, which interval is qualitative, and how many full repetitive cardiac cycles there are in the latter interval. After visual inspection, eight healthy volunteers and four at-risk patients were excluded from the study, and the qualitative time intervals of each subject were manually preselected for further analysis.

2.1.4. Estimation and post-processing of longitudinal and radial motion signals of CCA

The methodology described in this section has been published in "Ultrasonic Parametrization of Arterial Wall Movements in Low and High-Risk CVD Subjects"[140].

For this study, CAROLAB software was used to estimate the longitudinal and radial motions of CCA [133,134]. This software is used for the analysis of ultrasound B-mode image sequences and assesses both longitudinal and radial motions with a

speckle-tracking approach that is based on the BM method [19]. The main point of the BM framework is to detect the motion *d(n)* between two consequent frames by comparing pixel blocks of consecutive images *I(n-1)* and *I(n)*. The motion corresponds to the displacement between the center point *p(n-1)* of the reference block and the center point *p(n)* of the best-matched block. This results in the shift of the center point *p(n)* between images *I(n-1)* and *I(n)*. Pixel block alignment in the images *I(n-1)* and *I(n)* takes place only within the search window, i.e., in the defined maximum margin around the center point of the reference and best-match blocks. After summing up all the displacements *d(n)* that were received, the *p(n)* point motion trajectory is estimated. In order to cope with the issue of speckle decorrelation, a pixel-wise Kalman filter is used to update the reference block [19].

A region of interest (ROI), containing a well-contrasted speckle pattern of the distal vessel wall for longitudinal and radial motion evaluation, was chosen in the first B-mode sequence frame of a qualitative time interval. A kernel of the ROI was selected manually with the size of 3 × 0.5 mm. The estimated signals of longitudinal and radial motion were saved for further post-processing in MATLAB R2018b (The MathWorks, Inc., Natick, USA).

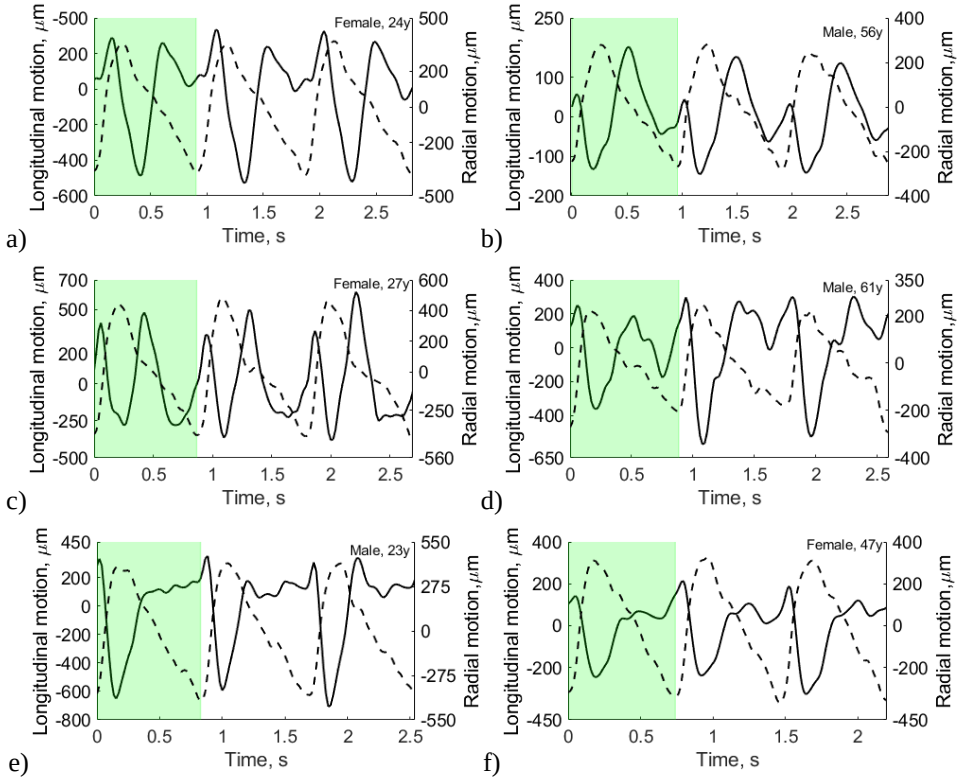

Figure 2.8. *In vivo* radial (dashed line) and longitudinal (solid line) motions of CCA of different ages, illustrating different patterns of longitudinal motions: a), c), e) young volunteers and b), d), f) at-risk patients; the preselected periods (green shadowed area) were used to model artery and tissue pulsation

Motion signals were then filtered with a band-pass IIR filter ($f_{pass\text{-}lower}$ = 0.5 Hz and $f_{pass\text{-}higer}$ = 8 Hz, filter order 2nd) and detrended, subtracting the mean or the best-fit line (in the least-squares sense) from the resulting signal. After this, three consequent heart cycles were selected manually in time. Only one heart cycle (see the green shadowed area in Figure 2.8. for an example) was used in motion modeling, especially since other periods are quasi-periodic with the cardiac cycle.

2.2. Modeling and verification of digital simulation of physical US scanning

Quantitative evaluation and comparison of digital US scanning with physical US scanning is needed for adequate digital US echoscopy simulation. FWHM of PSF was used as the main parameter for the determination of the image resolution and discrepancy evaluation between the physical and digital US scanning.

In ultrasonography, the spatial resolution of an ultrasound beam can be divided into three dimensions: 1. axial resolution (along the axis of the ultrasound beam, Z-axis), 2. lateral resolution (perpendicular to the axis of the ultrasound beam, X-axis), and 3. elevation resolution (the width of the ultrasound beam, Y-axis) [141]. According to these three dimensions of spatial resolution, the adequacy was assessed by comparing the digital simulation of the US scanning with physical US scanning.

2.2.1. Digital ultrasonic scanner and B-scan formation

A digital ultrasonic scanner, based on a physical ultrasonic scanner (see subsection 2.1.1.), was simulated by using the Field II package for MATLAB [36,142]. In order to reach the adequacy between experiments and simulation results, the parameters of a physical scanner Ultrasonix SonixTouch and linear array probe L14-5/38 were identified and incorporated into the Field II program. The height and width of the array elements, kerf, pitch, number of elements, and elevation lens focus were found in the Transducer Specification Sheet [143] of the linear array probe. The speed of sound, transmit focal depth, element excitation, etc. were identified from the physical ultrasonic scanner.

In order to increase the accuracy of the simulation, e.g., elevation lens focus, apodization in the *YZ* plane, the physical elements must be divided into the sub_X by sub_Y mathematical elements. This could be done by changing the number of physical element sub-division in *x* and *y* directions and investigating the influence on the pressure field of the simulated transducer.

The evaluation of the number of physical element sub-division in *x* and *y* directions was started by calculating the pressure field when sub_X and sub_Y were 1 and 1, accordingly. As it can be seen from Figure 2.9., the element sub-division in the *y*-direction is not sufficient; the side lobes are observed in the pressure field in *YZ* plane.

In order to identify the sufficient number of element sub-division in the *y*-direction, when side lobes amplitude would be 30 dB lower, compared to the main lobe amplitude, the main lobe and side lobe patterns at 15 mm axial distance from the pressure field in YZ plane were investigated. For the visual representation of the dependence of the side lobes amplitude to the number of sub-divisions in the *y*-direction, Figure 2.10. is given. From this figure, it can be seen that when the number

of element sub-division in the *y*-direction is from 1 to 8, the side lobes amplitude is from -17.48 dB to -28.86 dB, correspondingly. When the number of element sub-division in the *y*-direction is 9 or more, the side lobes amplitude is lower than -30 dB. It is worth noting that the simulation time of a single ultrasound RF frame in the Field II program is dependent on the volume of the model, the number of scatterers, or in this instance, the number of element sub-division.

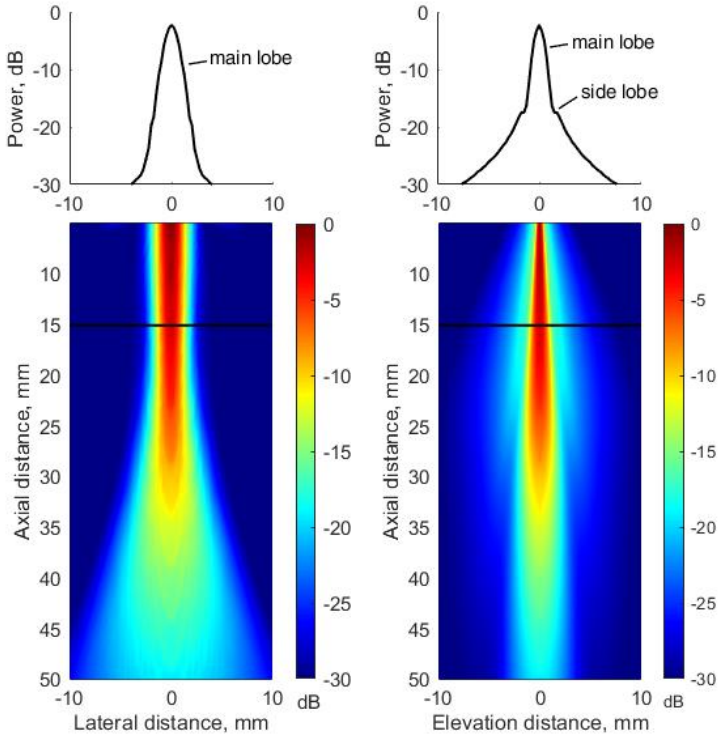

Figure 2.9. Simulation of linear array transducer pressure field in the XZ plane (left) and YZ plane (right); black lines at 15 mm axial distance depict the position from where the main lobe and side lobe patterns are taken and represented above the corresponding pressure field; sub-divisions in the x-direction and y-direction were the same and equal to 1

In concordance with this statement, it was decided to use the lowest number of element sub-division in the *y*-direction, i.e., 9, and in this way optimize both apodization in *y*-direction and simulation time of single or sequence of ultrasound RF frames.

A similar analysis as presented above was done. In this case, the main lobe and side lobe patterns at 15 mm axial distance from the pressure field were investigated in the XZ plane. Figure 2.11. indicates that the number of element sub-divisions in the *x*-direction does not influence the side lobes amplitude, and in all cases, it is lower than -30 dB.

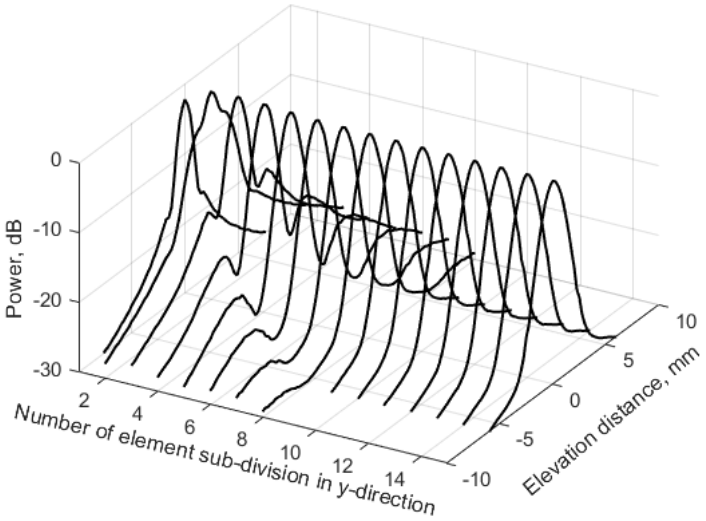

Figure 2.10. Representation of the main lobe and side lobe patterns at 15 mm axial distance from the pressure field in YZ plane when a different number of sub-divisions in the *y*-direction of the element was used in the simulation

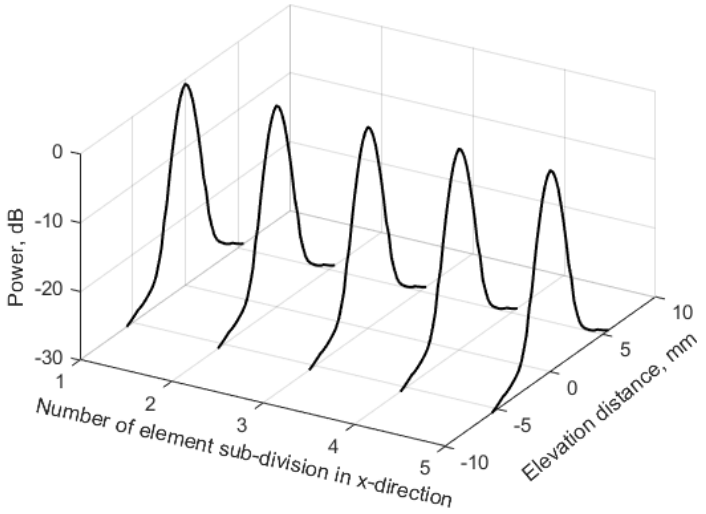

Figure 2.11. Representation of the main lobe and side lobe patterns at 15 mm axial distance from the pressure field in XZ plane when a different number of element sub-divisions in the x-direction was used in the simulation

Summing up the above given results, it was decided to divide the physical elements into the $sub_X = 1$ by $sub_Y = 9$ mathematical elements. The simulation result of linear array transducer pressure field in *XZ* and *YZ* planes with corresponding physical element sub-division is presented in Figure 2.12. The illustration confirms the fact that the determined number of physical element sub-division in the *x* and *y*

direction is sufficient to model appropriate apodization in both *XZ* and *YZ* planes and suppress side lobe amplitude lower than -30 dB.

Finally, the parameters that were used to simulate scanning with linear array transducer are listed in Table 2.2.

Table 2.2. Parameters of virtual scanning with Field II

Parameter	Value
Array type	Linear array
Transducer center frequency	5 MHz
Number of physical elements	128
Element excitation	Hanning-modulated sinusoid of two cycles
Height of element	4 mm
Width of element	0.279 mm
Kerf	0.025 mm
Pitch	0.304 mm
Element sub-division in x-direction	1
Element sub-division in y-direction	9
Elevation lens focus	16 mm
Transmit focal distance	15.5 mm
F-number in transmit	3
F-number in receive	1.7
Apodization	Hanning
Sampling frequency	40 MHz
Speed of sound	1540 m/s
Assumed frequency-dependent attenuation	0.5 dB/cm/MHz@ 3.5 MHz

The simulated B-scan image consists of 317 echo lines, the distance between two adjacent echo lines was 0.0625 mm, and the image width was 19.8 mm.

In order to obtain the same formation of the B-scan image in both physical and digital scanning, it was chosen to load registered (i.e., physical scanning) and modeled (i.e., digital scanning) US RF signals into MATLAB R2018b (The MathWorks, Inc., Natick, USA). Then, the B-scan formation consists of the following steps: 1. RF signals envelope detection; 2. log-compression from 0 to -70 dB.

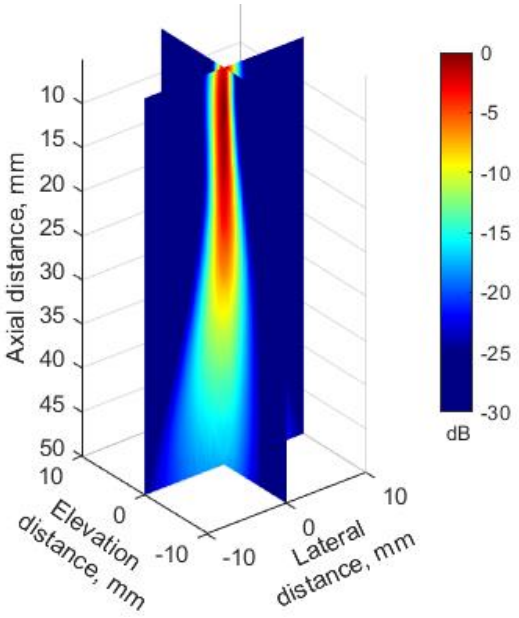

Figure 2.12. Simulation of linear array transducer pressure field in XZ and YZ planes; the element sub-divisions in the x-direction and y-direction were 1 and 9, accordingly

2.2.2. Physical resolution phantoms

For the echoscopy experiments, two ATS Laboratories Inc. physical phantoms were used: Model 549 General & Small Parts phantom (physical wire phantom) [144] and Model 538NH Beam Profile & Slice Thickness phantom (physical slice thickness phantom) [145]. Figure 2.13. shows which areas of the physical phantoms were used for the evaluation of axial, lateral, and elevation resolutions.

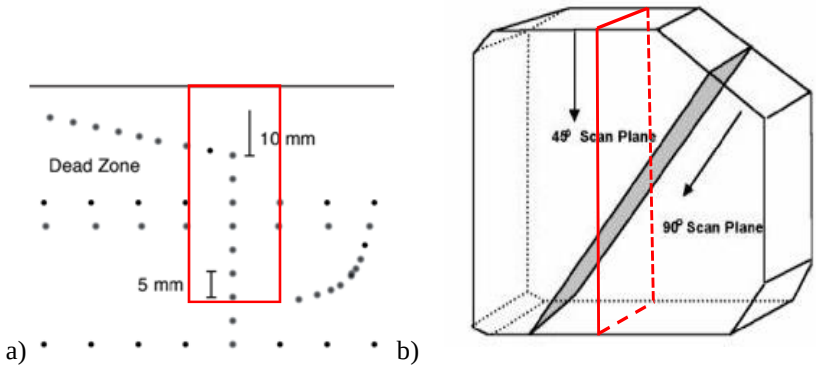

Figure 2.13. Structure of ATS Laboratories Inc. Phantoms: a) Model 549 (physical wire phantom) and b) Model 538NH (physical slice thickness phantom) with preselected scanning areas shown (adapted from [144,145])

Physical wire phantom was used for the assessment of axial and lateral resolutions, while physical slice thickness phantom was used for the assessment of elevation resolution. B-scan slice thickness or beam width in the elevation plane was evaluated, according to the method pioneered by Goldstein and Madrazo [146], and updated later [147].

According to the technical passport of the phantom, as a point targets in the physical wire phantom are monofilament Nylon wires with a diameter of 0.05 mm. The spacing between wires is 10 mm. In the physical elevation plane phantom, there is no information about the plane characteristics, i.e., material, thickness.

During the echoscopy of physical phantoms, physical ultrasonic scanner parameters were set the same as in subsection 2.1.1., except scanning depth, which was set to 4 cm.

2.2.3. Digital models of resolution phantoms

Digital models of resolution phantoms that are described in this section have been published in "Main Uncertainties in the RF Ultrasound Scanning Simulation of the Standard Ultrasound Phantoms" [34].

In order to create a digital model of resolution phantom, a 3D scattering map should be created, which is defined by the scatterer positions, scattering strength, and the number of scatters. A 3D scattering map of digital models of resolution phantoms was generated, according to the structure of physical wire and elevation plane phantoms (see subsection 2.2.1.).

A 3D scattering map defines the medium, which will be scanned with modeled linear array transducer. Firstly, the number of scatterers within the volume of the digital model is defined, according to the corresponding resolution cell of the physical ultrasonic transducer [41] and the volume of the digital model. The resolution cell is the minimum volume that can be extracted by the imaging system [60]. In order to model the fully developed speckle pattern of simulated ultrasound B-scan image, the number of scatterers in the resolution cell was equal to 10 [41,148,149]. A resolution cell is calculated by [148]:

$$resolution\ cell = \lambda \cdot N \cdot FWHM_{lat} \cdot FWHM_{azi}; \quad (1)$$

where λ is the wavelength, N is the number of cycles in the pulse, $FWHM_{lat}$ and $FWHM_{azi}$ are FWHM laterally and azimuthally, respectively of the physical transducer PSF at the focus point.

The number of scatterers within the volume of the digital model was calculated by [148]:

$$number\ of\ scatterers = 10 \cdot \frac{volume\ of\ model}{resolution\ cell}. \quad (2)$$

Secondly, the number of scatterers was predefined, and they were randomly distributed within the volume of the model. The scattering strength of the scatterers followed a Gaussian distribution. The variance of the distribution for wire and plane modeling is determined by the backscattering cross-section of the particular object, i.e., from the real B-scan image of the physical phantom (see Figure 2.14). The

amplitude of the B-scan image is used to scale the variance [150]. The amplitude of the B-scan image, which is normalized from 0 to 255 and represents the brightness of each pixel, was used to scale the variance. In summary, the variance value used for wire modeling was 177.6, while for plane modeling, it was 132.

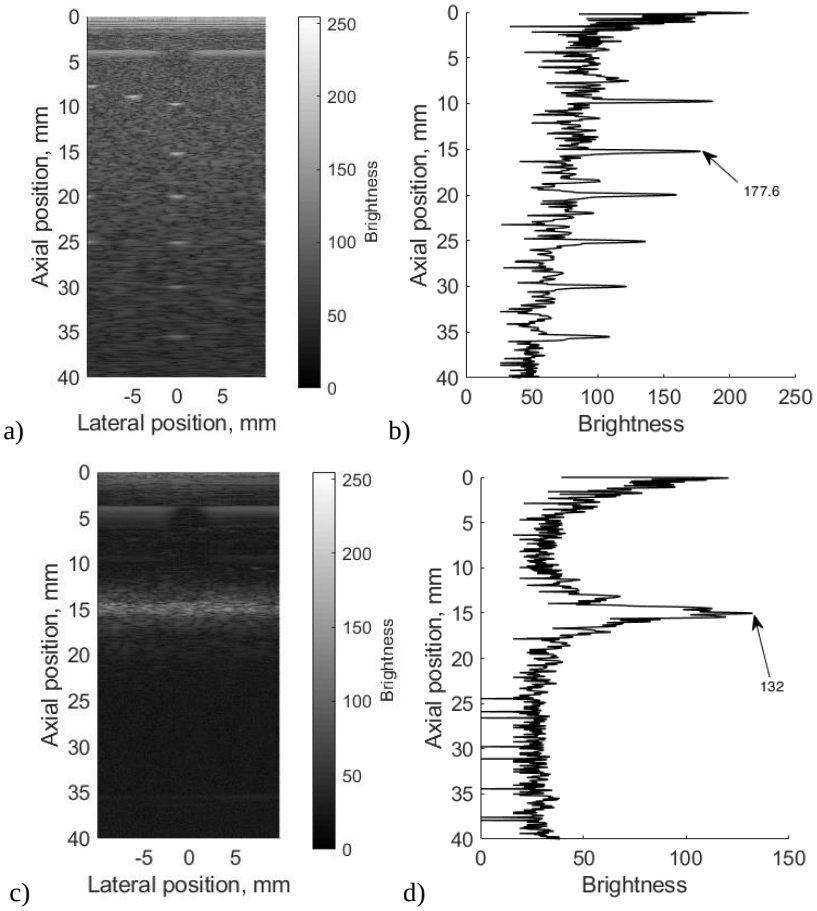

Figure 2.14. Determination of scatterers scattering strength in the digital phantoms: a) B-scan image of physical wire phantom, b) central echo line of B-scan image of physical wire phantom used for the assignment of variance value for the digital wire phantom, c) B-scan image of physical elevation plane phantom, and d) central echo line of B-scan image of physical elevation plane phantom used for the assignment of variance value for the digital elevation plane phantom

Digital wire phantom. The physical phantom, used for the resolution and PSF estimation, contains monofilament wires with a diameter of 0.05 mm [31]. However, PSF is correctly defined as a result of US wave reflection from the point scatterer, not from a wire. Therefore, the digital phantom that is containing point scatterers located at the same positions was designed (see Figure 2.15. a). The positions of seven scatterers were set from 10 mm every 5 mm to 40 mm away from the transducer in the axial direction. The variance value used for point scatterer modeling was 177.6.

Digital slice thickness phantom. Digital slice thickness phantom (see Figure 2.15. b) for the simulation of resolution parameters in the elevation plane (transverse to the plane of scanning) was designed following the physical phantom Model 538NH (see Figure 2.13. b). The model has a 45-degree inclined reflecting plane, simulated as a slice of scatterers. As there was no information about the plane characteristics, i.e., thickness, of a physical slice thickness phantom, it was decided that the thickness of the slice would be the same as monofilament wires diameter in the physical wire phantom i.e., 0.05 mm. The variance value used for the elevation plane modeling was 132.

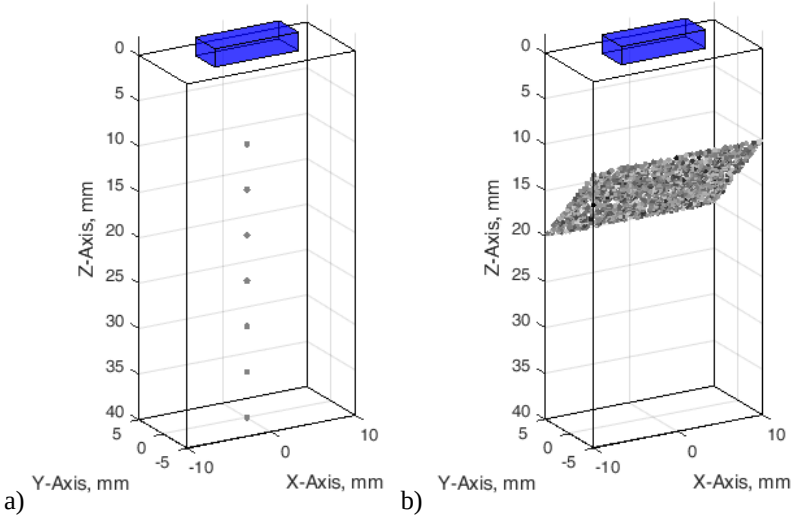

Figure 2.15. Configuration of digital phantoms: a) wire, b) slice thickness; the cuboids on the top of digital phantoms have marked the position of the digital ultrasound transducer

Since phantoms, like real tissues, have frequency-dependent attenuation, this feature was considered as well in the simulation. The initial attenuation parameters were taken from the phantom documentation.

2.3. Digital artery model

The materials and methods section is organized into four subsections, and each of them stands for the corresponding four stages of the proposed algorithm, as shown in Figure 2.16. The purpose of this algorithm flow is to show the input and output parameters and highlight the ability of the simulation algorithm to modify the input parameter in order to adapt it to a specific simulation task.

At Stage 1, the artery is modeled by the static scatterer distribution, accordingly to the vessel geometry and position. Subsequently, a static artery model is modified to the dynamic one by giving the radial and longitudinal motions to the 3D distributed scatterers of the artery (Stage 2). Moving scatterers were used to simulate the sequence of scanning US RF signals for one cardiac cycle (Stage 3). At Stage 4, US RF signals for consecutive cardiac cycles could be composed; noise and artifacts could be added, thus approaching a more realistic model for the application of chosen signal

processing algorithms. Finally, the processing of simulated US RF signals, motion estimation, comparison of motion detection results with artery and surrounding tissue pulsation data set in Stage 2 as a reference, relative errors of motion detection were estimated.

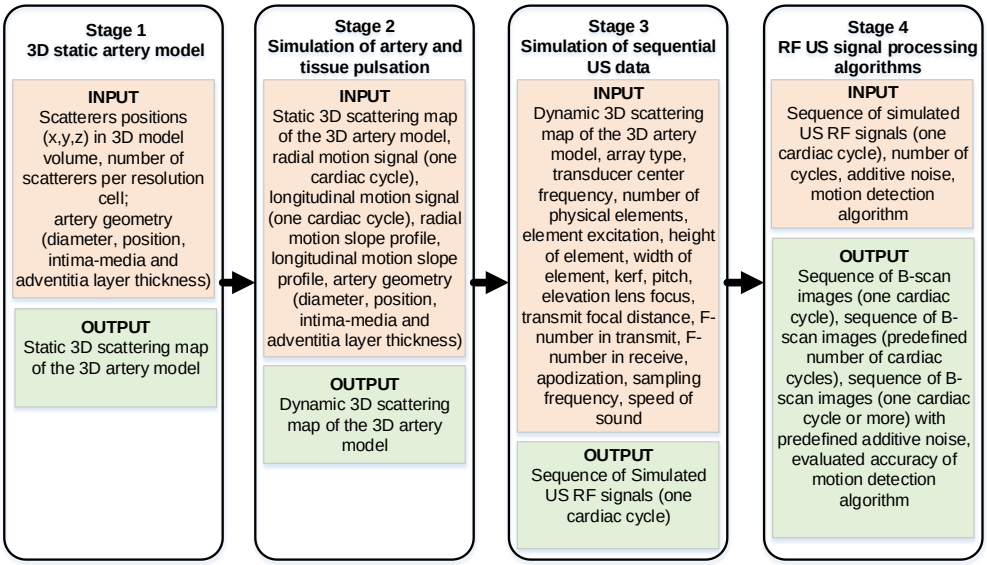

Figure 2.16. Overall simulation algorithm flow

2.3.1. 3D artery model

The artery was modeled by a 3D map of scatterers, which is defined by the scatterer number, positions, and scattering strength. A scattering map of the 3D artery model was generated, according to the histological structure of the CCA [17]. The geometry and structure of the artery model are shown in Figure 2.17. The structure consists of three layers (see subsection 1.1.).

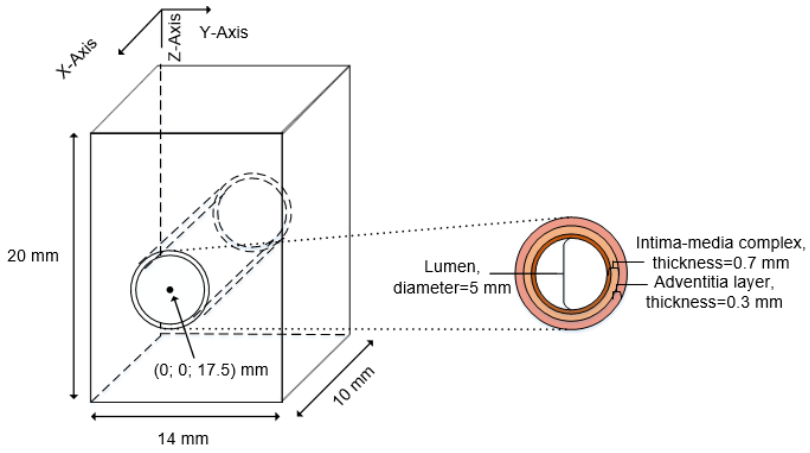

Figure 2.17. The general geometry of the artery model

The artery was modeled as three concentric pipes, which correspond to three layers of the artery wall, i.e., *tunica intima*, *tunica media*, and *tunica adventitia*, keeping geometric dimensions of layers close to the dimensions of the *in vivo* CCA. The following dimensions were chosen for an illustrative example: the lumen diameter was D_0 = 5 mm; the thickness of the *intima-media* complex was 0.7 mm; the thickness of the *adventitia* layer was 0.3 mm; the artery center is 17.5 mm deep from the surface (see Figure 2.17.).

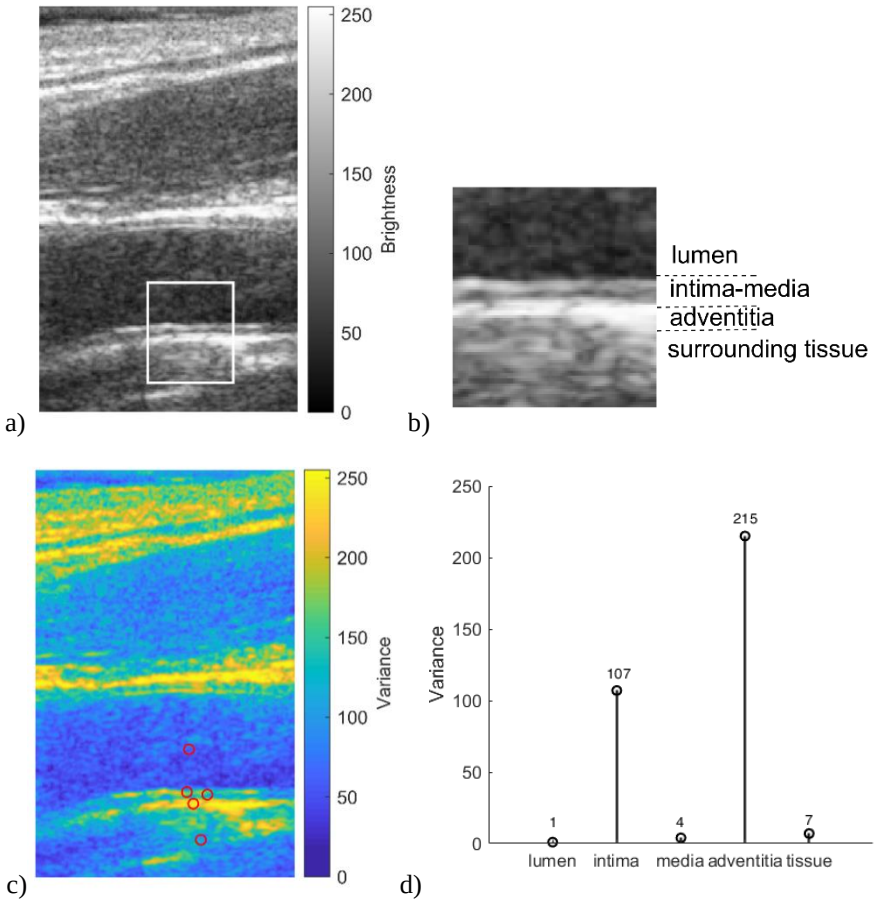

Figure 2.18. Determination of scatterers scattering strength in the artery model: a) B-scan image of CCA, b) detailed region (white rectangle in the B-scan image of CCA) of the distal wall with the lumen, the intima-media complex, the adventitia, and surrounding tissues, c) variance map of CCA with preselected points from where variance values are selected to use in the artery model and d) variance values assigned for a particular tissue of the artery model

The first step in simulation is to define the medium, in which scattering structures will be embedded and finally digitally scanned with modeled linear array transducer. The scatterers were randomly distributed within the volume of the artery model. The number of scatterers within the volume of the artery model is defined,

according to the corresponding resolution cell of the modeled linear array transducer [148]. A fully developed speckle pattern of simulated ultrasound B-scan image would be achieved if there were 10 scatterers per resolution cell [41]. Therefore, this constant was used in the calculation of the scatterer number in the artery model. The scattering strength of the scatterers followed a mean set to zero and the variance set according to the backscattering cross-section of a particular tissue [150], i.e., from the real *in vivo* B-scan image of CCA (see Figure 2.18.). The amplitude of the B-scan image, which is normalized from 0 to 255 and represents the brightness of each pixel, is used to scale the variance.

The scattering strength was attributed for each scatterer, according to its coordinates, i.e., if the scatterer belongs to the *intima* layer, its scattering strength was determined by the variance of the *intima* layer, etc. Finally, a 3D scattering map of the 3D artery model was generated (see Figure 2.19.).

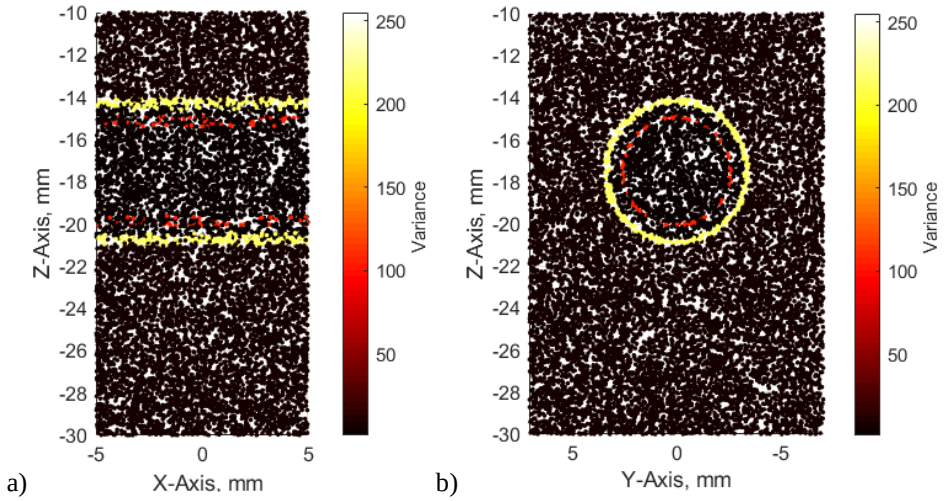

Figure 2.19. 3D map of scatterers at different viewpoints, representing the artery model: a) longitudinal, b) axial

Limitations of the 3D artery model. Blood flow, blood pressure were not incorporated into the 3D artery model. The main interest is to model determinate amplitude artery motion and evaluate the capability of motion tracking algorithms to detect it. The simulation of artery and tissue motion is presented in the next subsection.

2.3.2. Simulation of the artery and tissue pulsation

The main purpose was to model not a single B-mode ultrasound image but to simulate a sequence of B-mode images that would reflect radial and longitudinal motions of the artery and surrounding tissue. Since the simulation of a single ultrasound RF frame in the Field II program can take up to several hours (depending on the volume of the model and the number of scatterers), cardiac cycles are similar and quasi-periodic with heart rhythm, it was decided to model only one cardiac cycle of complex (longitudinal and radial) motion.

In vivo radial and longitudinal motion signals of CCA chosen for the simulation of artery and tissue pulsation were evaluated and presented in subsection 2.1.4.

As mentioned before, only one heart cycle (see the green shadowed area in Figure 2.20. a) as an example) was used in motion modeling. In order to cut out one cardiac cycle from motion signals, a rectangular window was used. The length of the motion signal segment depended on how long the heartbeat takes, and the beginning and the end of the segment were the moments of systole and diastole, correspondingly.

For the simulations, the amplitude of preselected and cut-out periods of longitudinal and radial motion signals were normalized, taking peak-to-peak amplitude in three levels: 0.5 mm, 0.75 mm, and 1 mm for young healthy volunteers, and 0.25 mm, 0.5 mm, and 0.75 mm for older at-risk patients. The time axis was not normalized.

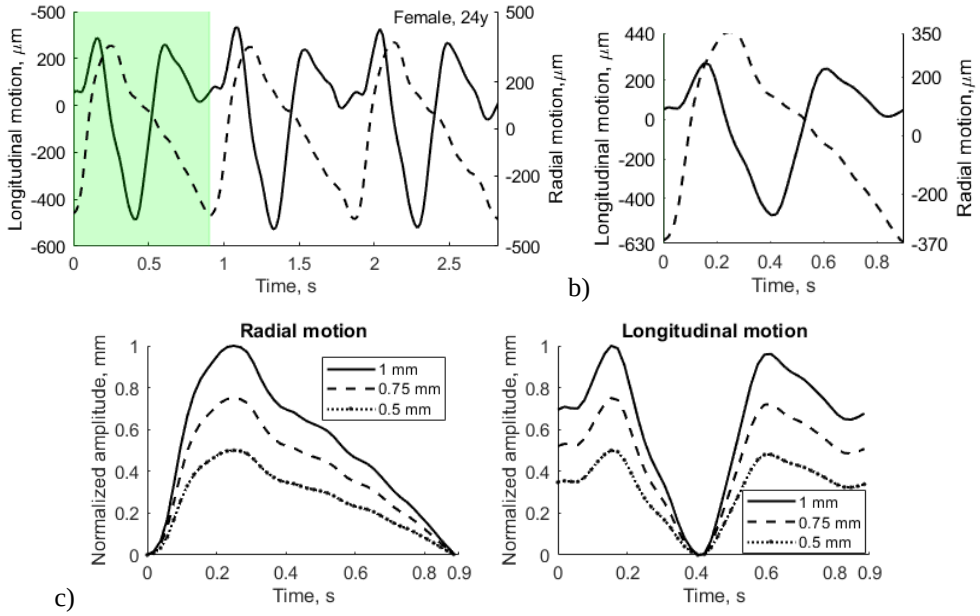

Figure 2.20. Motion signal post-processing for the simulation of artery and tissue pulsation: a) in vivo radial (dashed line) and longitudinal (solid line) motion signals of CCA with a preselected period (green shadowed area), which would be used to model artery and tissue pulsation, b) preselected heart cycle cut out from the motion signals, c) motion signal amplitude normalization in three levels

As reported by Golemati et al. [61], the radial and longitudinal motions *in vivo* are weakening away from the artery lumen and express the spatial dependence of displacements, which are defined as the exponential functions of the axial position. In order to simulate realistic *in vivo* artery motion, the motion slope deep into the artery wall and the surrounding tissues were incorporated into the artery model. According to Golemati et al. [61], $b_1 = -0.1722$ and $b_2 = -1.075$ express the slope of the radial and longitudinal motion amplitude of healthy volunteers, accordingly. However, there are no studies that propose a slope of the radial and longitudinal motion amplitude of at-

risk patients. Nonetheless, the previous studies have shown a relationship between the decrease in longitudinal motion of the CCA wall, arterial stiffness, and CVDs [12]. Taking that into account, the slope of motion's amplitude should be higher in modeling artery motion of at-risk patients. Thus, it was decided to use 1.5 times bigger b_1 and b_2 values for that purpose.

Table 2.3. Motion modeling parameters of the artery model

	Healthy volunteers	**At-risk patients**
Waveforms of motion signals	see Figure 2.8 a), c), e)	see Figure 2.8 b), d), f)
Radial and longitudinal motion amplitude, μm	1000, 750, 500	750, 500, 250
Slope of radial motion b_1	0.17	0.26
Slope of longitudinal motion b_2	1.08	1.62
Total:	9 cases	9 cases

The mechanical deformation of the arterial wall, consisting of two motions, was simulated in this stage: 1. radial motion and 2. longitudinal motion. Even though the scatterers are randomly distributed within the artery model volume, their coordinates and scattering strength (scatterer amplitudes) are available for the simulation algorithm as a static map. This static map is an input of the Stage 2 simulation where at each scatterer's coordinates, a definite magnitude (the increment motion signal for the next time moment) and nature (radial or longitudinal) displacement were added (see Figure 2.20. a). The scatterer's strength for a particular tissue was kept constant as assigned at the initiation of modeling.

Each step of the artery and the surrounding tissue pulsation simulation is explained in detail below, following a functional diagram of Stage 2 in Figure 2.21.

Step 1. Initially, the artery center of the artery model is set at 17.5 mm in depth (see Figure 2.17.). Before adding radial and longitudinal displacement to a particular scatterer, the coordinate system is centered at the artery center (coordinates (0; 0) are at the artery center). In the next steps, Cartesian and polar coordinates were used for longitudinal and radial scatterer's movement simulation, accordingly.

Step 2. Simulating radial motion component, before adding displacement to a particular scatterer, the Y and Z coordinates of scatterers were recalculated from Cartesian to polar. The scatterers that do not belong in static map to the artery lumen (diameter D_0 = 5 mm) are selected, and the radial displacement $d_{radial}(f)$ in the polar coordinate system was applied to each scatterer. Since the radial motion of the artery in the sequence of B-mode images is the sum of the motions of the proximal and distal artery walls (the motion of the proximal wall is equal to the motion of the distal wall), only the half of the displacement of radial motion is added in the artery model. The magnitude of the displacement of artery layers and surrounding tissues depends on the coordinates of the scatterers, i.e., the farther was the scatterer from the lumen radius, the lower magnitude of the displacement $d_{radial}(f)$ was added:

$$Slope_{radial} = \begin{cases} 1, & |y| = r_l \\ e^{b_1|y-r_l|}, & |y| > r_l \end{cases}; \quad (3)$$

where y is the radial position, $r_1 = 2.5$ mm is the initial lumen radius, b_1 expresses the slope of the radial displacement.

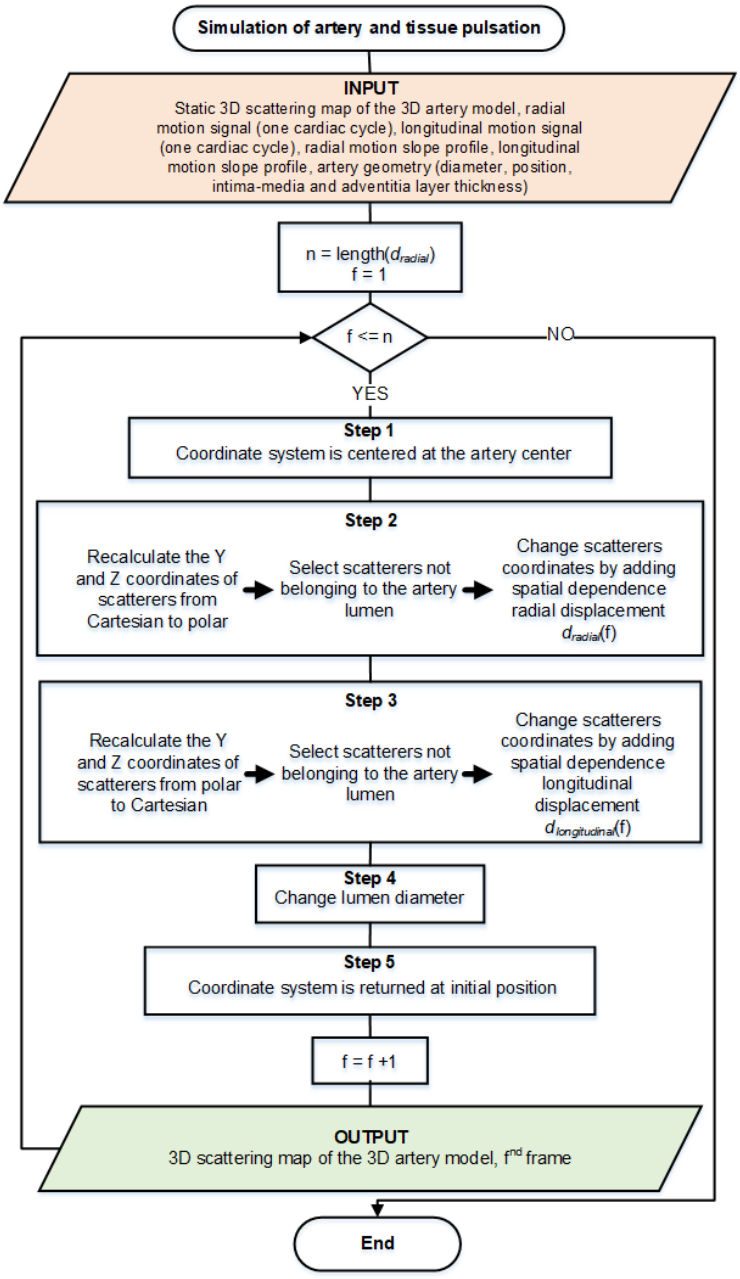

Figure 2.21. Functional diagram of Stage 2, simulation of the complex artery and tissue pulsation, where *f* corresponds to the currently analyzing frame number in the motion signal and *n* is the total number of such frames

In this way, the field of spatial-dependent radial displacements (see Figure 2.22.), propagating away from the artery lumen radially and declining in surrounding tissues, is modeled.

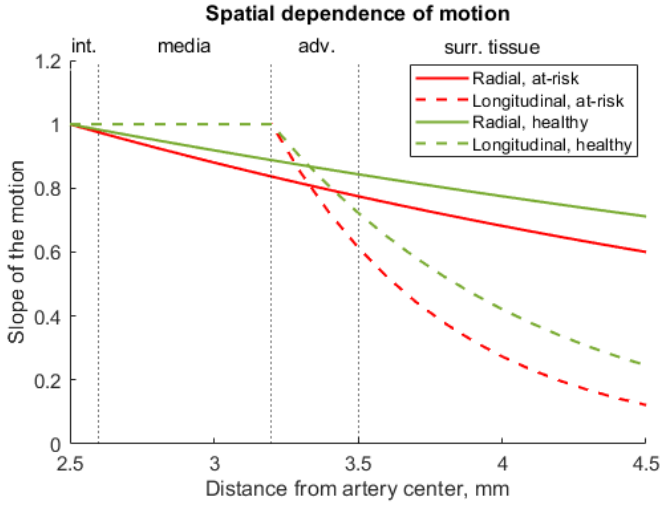

Figure 2.22. Spatial dependence of radial and longitudinal motions for healthy (slope of radial and longitudinal motions: $b_1 = 0.17$, $b_2 = 1.08$) and at-risk (slope of radial and longitudinal motions: $b_1 = 0.26$, $b_2 = 1.62$) subjects; the amplitude of radial motion is greatest at the surface of the artery (2.5 mm) and decreases exponentially into the surrounding tissues; the amplitude of longitudinal motion is greatest at the *intima-media* complex (at 2.5–3.2 mm), decreases significantly into the adventitia layer (3.2–3.5 mm), and finally, the longitudinal motion amplitude is negligible in the surrounding tissues

Step 3. After adding the radial displacement, the coordinates of the scatterers were converted again from polar to Cartesian coordinate system.

The scatterers that do not belong to the artery lumen in a static map (diameter $D_0 = 5$ mm) are selected, and longitudinal displacement $d_{longitudinal}(f)$ in the X–Z plane is added to each scatterer. Other studies [52,151] have demonstrated that the *intima-media* complex shows a larger longitudinal motion than the *adventitia* layer. Therefore, for scatterers that were outside the *intima-media* complex, i.e., *adventitia* layer and surrounding tissues, the longitudinal displacement was added with sloping, according to the distance from the artery center (see Figure 2.22.):

$$Slope_{longitudinal} = \begin{cases} 1, & r_l \le |y| \le r_{ma} \\ e^{b_2|y-r_{ma}|}, & |y| > r_{ma} \end{cases}; \quad (4)$$

where y is the radial position, $r_l = 2.5$ mm is the lumen radius, $r_{ma} = 3.2$ mm is the radius of the *media-adventitia* boundary, b_2 expresses the slope of the longitudinal displacement.

Step 4. In Step 2, the artery wall was displaced, the lumen diameter had changed; therefore, at each next frame of the sequence, the lumen was modeled as a cylinder with variable diameter:

$$D_{lumen}(f_2) = D_0 + d_{radial}(f_1), \quad (5)$$

where $D_{lumen}(f_2)$ – lumen diameter for the *2-nd* frame of the sequence, D_0 – lumen diameter (const.), $d_{radial}(f_1)$ – radial displacement between the two artery walls at the 1-*st* frame of the sequence.

Step 5. The coordinate system has returned to its initial position, i.e., 17.5 mm in depth. Thus, in each subsequent frame (f_2, f_3, etc.), the coordinates of the scatterers in the artery model were recalculated, and the lumen with varying diameter that yield all remaining frames of artery motion was modeled.

2.3.3. Simulation of sequential US data

Using Field II software [36,38], the RF ultrasound signals were simulated from a time sequence of scattering 3D maps of the artery model. While simulating RF signals, a model of linear array transducer was used. Field II parameters that are used to simulate scanning with linear array transducer are listed in Table 2.2. From the simulated US RF signals, the sequences of B-scan images were calculated. The example of the B-scan image is presented in Figure 2.23.

The resulting simulated B-scan image, in this case, consists of 160 echo lines, the distance between two adjacent echo lines was 0.0625 mm, and the image width was 10 mm. One cardiac cycle consisted of 43 image frames or more (frame rate: 52 frames per second), depending on cycle length. Several quasi-periodic cycles were compiled from the first one, while the analysis of the one cycle peculiarities was the main concern in this dissertation.

2.3.4. Simulated RF US signal processing algorithms and accuracy evaluation of the motion detection

From the simulated US RF data, the patterns of radial and longitudinal motion could be evaluated by using the chosen signal processing algorithms. Two algorithms were employed: one to estimate only radial motion, and one to estimate both radial and longitudinal motions. When the interest is in tissue properties, based on the motion only in one direction, a classical 1D cross-correlation is an option. The inter-frame radial motion of the artery and surrounding tissue was detected along the beamlines by using cross-correlation function, calculated between obtained RF signal segments and parabolic interpolation of the peak of the correlation function [30,152]. This method is presented in detail in subsection 2.4.1. In order to get radial motion, the integral of inter-frame radial motion must be calculated. An OpenOpticalFlow algorithm [153] was chosen to evaluate both radial and longitudinal tissue motions between the adjacent frames. This method is presented in detail in 2.4.1. The inter-frame displacements were later converted into the accumulated motions that are relative to the first frame.

The accuracy of motion detection was evaluated in the midline (i.e., a middle scanning line) for various axial positions, i.e., starting from 11 mm every 1 mm to 29 mm. The preselected points, where the accuracy of motion detection was evaluated, are depicted in Figure 2.23.

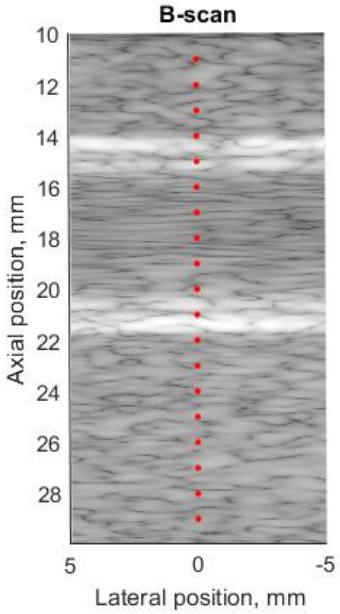

Figure 2.23. Simulated B-scan image of the artery model with preselected point (red dots) where the accuracy of motion detection algorithms was evaluated

When evaluating the accuracy of motion detection algorithms, it is important to know how much the observed motion corresponds to the predicted motion. For this purpose, different parameters were chosen. The first one is the mean absolute error (MAE), one of the simpler errors to understand, which corresponds to the average of absolute errors, i.e., it is the difference between the measured value and "true" value:

$$MAE = \frac{1}{N}\sum_{n=1}^{N}|y_e(n) - y_t(n)|; \quad (6)$$

where MAE – mean absolute error, $n = 1\ldots N$, N is the number of samples in motion signal, $y_e(n)$ – estimated motion, and $y_t(n)$ – theoretical motion. However, MAE is not standardized within a predefined range as the Pearson correlation coefficient, making it difficult to decide which value of the MAE is high and which is low. Moreover, the magnitude of the error depends on the amplitude of the signal.

The error criterion often uses an estimate of the mean squared error (MSE), which estimates the error between the estimated motion $y_e(n)$ and the theoretical motion $y_t(n)$:

$$MSE = \frac{1}{N}\sum_{n=1}^{N}(y_e(n) - y_t(n))^2; \quad (7)$$

where MSE – mean squared error, $n = 1\ldots N$, N is the number of samples in motion signal.

The disadvantage of such an estimate is that square units of error are obtained, and it is, therefore, difficult to evaluate the obtained error. Moreover, the value of the error depends on the amplitude of the motion. Therefore, it makes sense to normalize

the MSE estimate after subtracting the square root from the MSE estimate. The MSE is normalized to the standard deviation of the estimated motion σ_e:

$$NRMSE = \frac{\sqrt{MSE}}{\sigma_e}, \tag{8}$$

and the parameter evaluating the resulting error is called NRMSE. NRMSE = 0 describes the ideal similarity between the estimated and theoretical motions.

In addition to the NRMSE, the accuracy of the algorithms for motion detection was quantified by the Pearson correlation coefficient. The correlation coefficient evaluates the similarity between the estimated and theoretical, and it is easier to interpret. If there is an estimated motion y_e with a number of data points N and $\overline{y_e}$ – mean of y_e together with the theoretical motion y_t with a number of data points N and $\overline{y_t}$ – mean of y_t, then the correlation between these two motion signals is calculated according to the formula:

$$r = \frac{\sum_{n=1}^{N}(y_e-\overline{y_e})\cdot(y_t-\overline{y_t})}{\sqrt{\sum_{n=1}^{N}(y_e-\overline{y_e})^2\cdot\sum_{n=1}^{N}(y_t-\overline{y_t})^2}}. \tag{9}$$

The Pearson correlation coefficient r shows the strength of the similarity between the two signals. The values of the correlation coefficient vary within the range [-1; 1]. r = -1 indicates absolute opposite similarity, r = 0 means that the relationship between the two signals does not exist, r = 1 indicates absolute positive similarity. An important advantage of the correlation coefficient over the MSE parameter is that the correlation coefficient is automatically normalized within a predefined range. However, the correlation coefficient does not take into account the effect of changes in the constant component (DC component) and amplitude of the signal, only the morphological similarity of the signals. When estimating radial or longitudinal motion, a less accurate algorithm will evaluate a smaller amplitude of motion signal, although the partial morphological similarity would be maintained. Taking into account such a possibility, the Pearson correlation coefficient and NRMSE are important parameters to evaluate the accuracy of the motion detection algorithms.

2.3.5. Evaluation of slope profiles of radial and longitudinal motions

As mentioned before, radial and longitudinal motions *in vivo* are weakening away from the artery lumen and express the spatial dependence of displacements, which is defined as exponential functions of the axial position [61]. This concept was incorporated into the 3D artery model. The question was raised if it is possible to differentiate arteries, having a variety of motion amplitudes, and waveforms only by motion slope profile deep into the tissue.

For that purpose, the slope profiles of modeled radial and longitudinal motions were determined. The first step is to estimate both radial and longitudinal motion signals from simulated RF US signals at the preselected points as depicted in Figure 2.23. The algorithms for radial and longitudinal motion detection are presented in the 2.4.1. subsection. Then, the maximal values of radial and longitudinal motion signals

were found at the preselected axial positions. These values were normalized according to the initial radial and longitudinal motion amplitude in the 3D artery model (see Table 2.3.). For example, 1 mm longitudinal motion amplitude was incorporated into the 3D artery model. At the preselected axial position, the estimated peak-to-peak amplitude of the longitudinal motion signal is 0.96 mm. After normalization (0.96 mm/1 mm), the slope of the motion is 0.96. The same normalization procedure was done with all preselected points at different axial positions (see Figure 2.23.).

The slope profile evaluation was done with all the cases of modeled data, i.e., as a result, 18 estimated slope profiles (9 for radial motion and 9 for longitudinal motion) are for the healthy volunteer group and 18 (9 for radial motion and 9 for longitudinal motion) for the at-risk patient group. The mean values and standard deviations of slope profiles were calculated for healthy volunteers and at-risk patient groups for every preselected axial position.

2.4. RF ultrasound signal post-processing algorithms

2.4.1. Algorithms for radial and longitudinal motion detection

The methodology described in this subsection has been published in "Quantification of Endogenous Brain Tissue Displacement Imaging by Radiofrequency Ultrasound" [30].

The same ultrasonic RF signal processing algorithm was used for both the motion signal of a short segment of the RF signal and radial motion estimation of the CCA wall. Combining the classical 1D cross-correlation function, calculated between the obtained RF signal segments and parabolic interpolation of the peak of the function, the motion along the scanning line was estimated [30,152].

The cross-correlation lag between the segments at adjacent scanning frames f and $f+1$ represents the inter-frame estimate (velocity) of motion magnitude. The correlation peak was estimated as follows [152]:

$$C_f[n] = \max_{-T \le z \le T} \left[\mathcal{F}^{-1} \left\{ \mathcal{F} \left[w[z] \cdot S_f^*[z] \right] \cdot \mathcal{F} \left[w[z] \cdot S_{f+1}[z] \right] \right\} \right]; \qquad (10)$$

where S is the RF signal segment at a certain scanning line and scanning depth, $\mathcal{F}$ is the Fast Fourier transform, acquisition instance (frame number) $f = 1 \ldots F$, * the asterisk denotes the complex conjugate. The empirical threshold value T was set at ± 150 µm, w is the Hamming window function, $z = 1 \ldots Z$, Z is the number of samples of the RF, the signal segment (0.924 mm of six periods of US wave) used for the assessment of displacements, n is the correlation lag at the peak of the function. In order to prevent false peaks of the cross-correlation function, which occur when a secondary correlation peak exceeds the primary peak, the threshold is used. The threshold was set after analyzing the outcomes of the algorithm, the estimated motion signals. The tapering function was applied to suppress the leakage in the frequency domain and increase the probability of the right correlation peak detection. Nonetheless, when the tissue motion is higher than a quarter of the wavelength of the ultrasound echo data, the probability of identifying a false correlation peak increase. This results in large tracking errors that are known as "peak hopping" errors [154]. In

order to overcome these errors, it was decided to attribute "Not-a-Number" value to inter-frame motion that is higher than a quarter of the wavelength. Finally, the inter-frame estimate with integer accuracy of motion magnitude $IF\_motion_{integer}[f]$ was defined as follows:

$$IF\_motion_{integer}[f] = \Delta d \cdot C_f[n],]; \quad (11)$$

where $C_f[n]$ is the largest sample of the cross-correlation function, Δd is the RF signal sampling period (Δd = 19.25 μm).

Nevertheless, only at the integer sample level, the magnitude of the cross-correlation function can be estimated. A variety of approaches in the literature have been suggested to achieve sub-sample accuracy [155,156,157,158,159]. The fundamental concept behind these methods is to fit the (discretely estimated) magnitude of the function of cross-correlation into an underlying analytical function. Consequently, it is possible to analytically resolve the position of the true correlation peak [154] (see Figure 2.24.). Due to its efficiency and simple implementation, the parabolic interpolation [155] of the correlation peak was applied to obtain a sub-sample resolution of the inter-frame estimates of motion magnitude, since the estimated inter-frame estimate of motion magnitude had integer accuracy. The sub-sample accuracy of the inter-frame estimate of motion magnitude $IF\_motion_{sub}[f]$ was defined as follows [152]:

$$IF\_motion_{sub}[f] = \Delta d \cdot \frac{C_f[n-1]-C_f[n+1]}{2\cdot(C_f[n-1]-2\cdot C_f[n]+C_f[n+1])}; \quad (12)$$

where $C_f[n-1]$ and $C_f[n+1]$ are the nearest neighbors of the largest sample of cross-correlation function $C_f[n]$, f is the acquisition instance (frame number), $f = 1 \ldots F$.

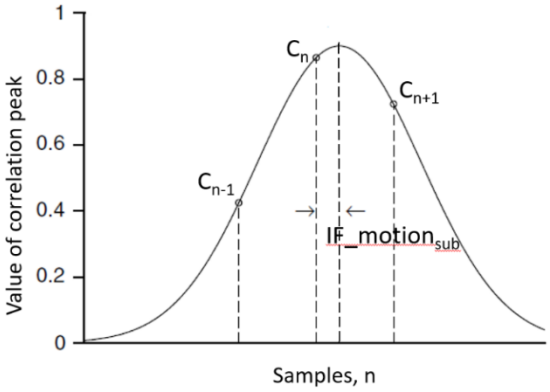

Figure 2.24. Interpolation of the correlation peak for sub-sample estimation

Finally, summing up both inter-frame estimates of motion magnitude with integer and sub-sample accuracies, the inter-frame motion *IF_motion* was estimated as follows:

$$IF\_motion[f] = IF\_motion_{integer}[f] + IF\_motion_{sub}[f]. \quad (13)$$

Since the distance is the integral of velocity, the motion signal relative to the transducer was calculated by the integral (cumulative sum) of the inter-frame motion signal.

The radial motion estimation of the CCA wall was done by using the cross-correlation functions and parabolic interpolation methods described above. In the case of the artery wall motion, the radial motion was detected in the ROI, which covered the proximal and distal walls of the artery (see Figure 2.25.). The width of ROI in all cases was 5 mm (81 echoscopic lines, lateral resolution 62.5 µm) while the height of ROI was 10 mm on purpose to cover both walls of the artery. The ROI was then divided equally into two parts: the top of the ROI (proximal arterial wall and upper part of the lumen) and the bottom of the ROI (distal arterial wall and lower part of the lumen). The cross-correlation and parabolic interpolation methods were then applied to the RF signal segments in the length of 5 mm in these two ROIs. After calculating the inter-frame motion for each echoscopic line, integrating them, and summing the top and bottom motion signals, the radial motion signals of the ROI were found (n = 81). Averaging these signals over time yielded an average signal of CCA wall motion in the 5 mm segment.

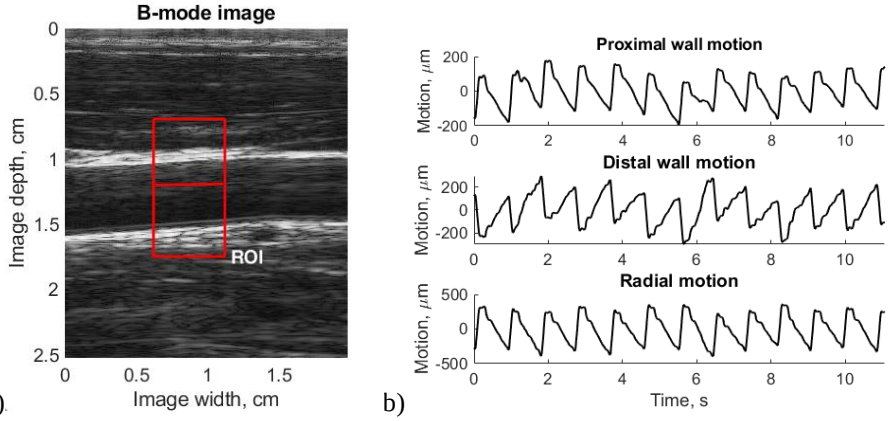

Figure 2.25. B-scan image with outlined ROI (a) and proximal, distal artery wall motion together with a total radial motion of the CCA wall (b); the motion detected in the upper and lower part of outlined ROI corresponds to the proximal and distal wall motion, accordingly; summing the proximal and distal motion signals, the radial motion signals of the ROI were found: 53 years old female

Intending to detect larger tissue motion, the main disadvantages of the 1D cross-correlation method become apparent: 1. motion only in the axial direction (along beamline) could be detected, 2. “peak hopping” error results if motion is higher than a quarter of the wavelength. In order to avoid the above mentioned 1D cross-correlation drawback, another motion detection algorithm could be used. One of those kind of algorithms, i.e., modern optical flow algorithms, which allow the estimation of motion in the plane, is more resistant to the rotation of the parts and can be used to evaluate both macro and micro level motion [154].

OpenOpticalFlow is an open-source optical flow program in MATLAB for the extraction of high-resolution velocity fields from various flow visualization images by Tianshu Liu [153] (freely available at: https://github.com/Tianshu-Liu/OpenOpticalFlow).

The simulated RF signals were normalized to 1, an envelope (Hilbert transformation) of simulated RF signals was presented in decibels, the resulting data stronger than –90 dB was normalized from 0 to 255 and then passed as an input for OpenOpticalFlow to identify the motion between adjacent frames. The parameters that are used for OpenOpticalFlow: size filter 4, Horn-Schunck estimator for the initial field $\lambda 1 = 120$, Liu-Shen estimator for the refined estimation $\lambda 2 = 3000$; these parameters were selected as an optimal combination after preliminary investigation within the size filter values from 1 to 30, $\lambda 1$ values from 1 to 1000, $\lambda 2$ from 100 to 10000 by comparing results with theoretical scatters movement and evaluating movement precision and smoothness. The inter-frame displacements were later converted into the accumulated motion relative to the first frame.

2.4.2. Post-processing of radial motion of the CCA wall

The post-processing of the radial motion signal of the CCA artery consist of three main steps:

- motion signal filtering;
- detection of the end of diastole moments in motion signal;
- detection of correlated periods.

Motion signals were filtered with a band-pass IIR filter ($f_{pass\text{-}lower}$ = 0.5 Hz and $f_{pass\text{-}higer}$ = 8 Hz, filter order 2nd) and then detrended, subtracting the mean or the best-fit line (in the least-squares sense) from the resulting signal. Then, the detection of diastolic moments in radial motion signal was done by calculating the second derivative of motion signal, i.e., acceleration signal, and searching for peaks spaced with at least 1 second time interval with a minimum peak height of 1/3 of the maximum value in the acceleration signal. The time interval between two adjacent peaks was chosen, according to that for the adults, the normal resting heart rate varies between 60 and 100 beats per minute, while the minimum peak height value was chosen experimentally. The peaks in the acceleration signal over time coincide with the diastolic moments [160,161] in the radial motion signal (see Figure 2.26.).

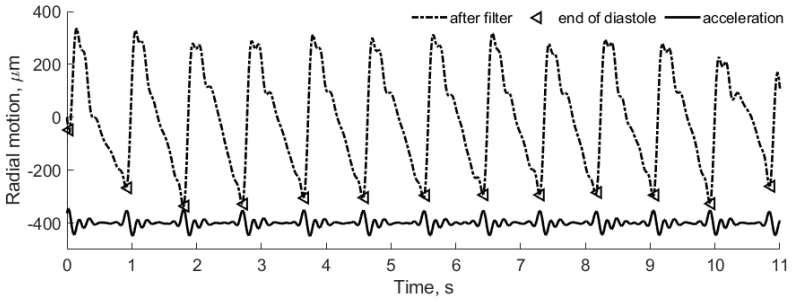

Figure 2.26. End of diastole detection in radial motion signal, according to the peaks in the acceleration signal: 53 years old female

The motion signal from the first to the last peak, found in the acceleration signal, was divided into separate periods, and those periods were aligned, according to the diastolic moments (see Figure 2.27. b).

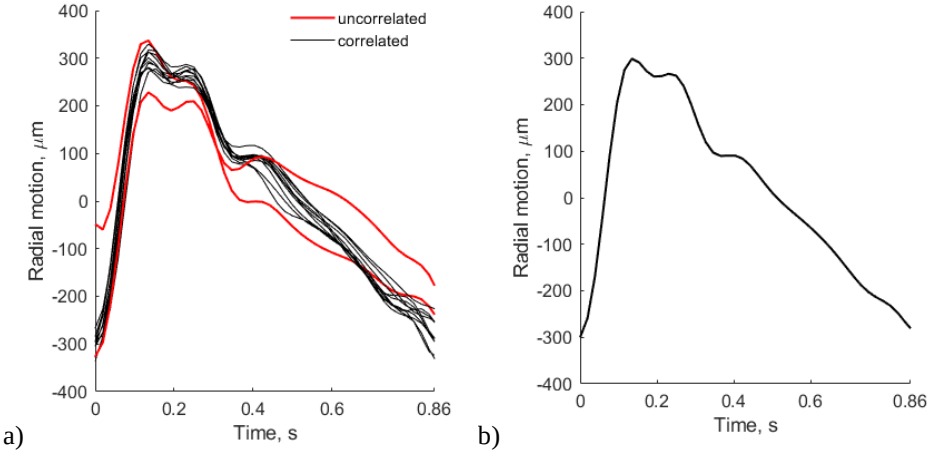

Figure 2.27. Detection of the average period for radial motion parametrization in time and frequency domain: a) periods of motion signal alignment, according to the end of diastole and detection of both correlated and uncorrelated periods and b) the average period of the radial motion signal: 53 years old female

The length of all periods was set equal to the shortest period in the motion signal as proposed in [162]. This gives a $\mathbf{P}[p \times l]$ matrix, where p is the number of periods, l is the period length. In the next step, the correlation coefficient matrix $\mathbf{R}[p \times p]$ between the motion signal periods was estimated, and the diagonal was removed, as it represents the autocorrelation result:

$$\mathbf{R} = \begin{bmatrix} 1 & R_{12} & R_{13} & & R_{1p} \\ R_{21} & 1 & R_{23} & \cdots & R_{2p} \\ R_{31} & R_{32} & 1 & & R_{3p} \\ & \vdots & & \ddots & \vdots \\ R_{p1} & R_{p2} & R_{p3} & \cdots & 1 \end{bmatrix}. \tag{14}$$

Then, the averaging was done to obtain a row vector $\mathbf{S}[1 \times p]$ with the mean of correlation coefficient in each column. Vector **S** indicates the period similarity. The periods were assumed similar, if the correlation coefficient value exceeded 0.95 [29,30,152]. Applying the threshold of 0.95, the periods that correlate less with the remaining periods were determined and excluded from the calculation of the average period of the radial motion signal. Meanwhile, similar periods were averaged over time, and the average period of the radial motion signal was obtained, which was used to parametrize motion in the time domain. Moreover, the spectrum estimation approaches were applied to detect the frequency domain parameters.

2.4.3. Spectrum estimation approaches

Fourier based power spectrum estimates are referred to as classical methods. The advantages, in comparison to the other methods, is that Fourier transform methods are most robust of the spectral estimators, require no assumptions about the origin or nature of the data, and accurately estimate the spectrum of the signal with noise, while usually, the spectrum is wanted of the noise-free signal. The modern approaches of the spectrum estimation are designed to overcome the distortions produced by the classical approach, are particularly effective if the data segments are short [163]. Therefore, in order to estimate the spectrum of the average period of the radial motion, as its length is about one second (normal heart rate is 60 beats/minute, the frame rate is 52 Hz, the average period of radial motion length is about 52 samples), it will be more constructive to use the modern approaches instead of the classical methods.

One of the classes of modern techniques is parametric or model based. In order to estimate the power spectrum, the parametric methods make use of a linear time-invariant model. The basic strategy of this approach is that the model is assumed to be driven by white noise. Then, the output of the model is compared with the input waveform, and the model parameters are adjusted for the best match between the model output and the waveform of interest. Finally, the spectrum is computed [163].

Autoregressive power spectral density estimate, Yule-Walker method and autoregressive power spectral density estimate, modified covariance method were selected and investigated in detail to choose a better approach and the optimal model order for the average period of radial motion signal spectrum estimation. Yule-Walker and modified covariance approaches to spectral estimation are implemented in the MATLAB R2018b (The MathWorks, Inc., Natick, USA) Signal Processing Toolbox (*pyulear, pmcov*). An investigation was carried out to determine the optimal model order. Firstly, a sinusoidal signal of 1 Hz, 1 s duration, and 52 Hz sampling frequency was modeled. Then, changing the model order from 1 to 20, the spectrum was computed by using *pyulear* and *pmcov* functions, and the maximal value of the spectrum was detected, reflecting the modeled sinusoidal signal frequency. The frequency dependence on model order is depicted in Figure 2.28.

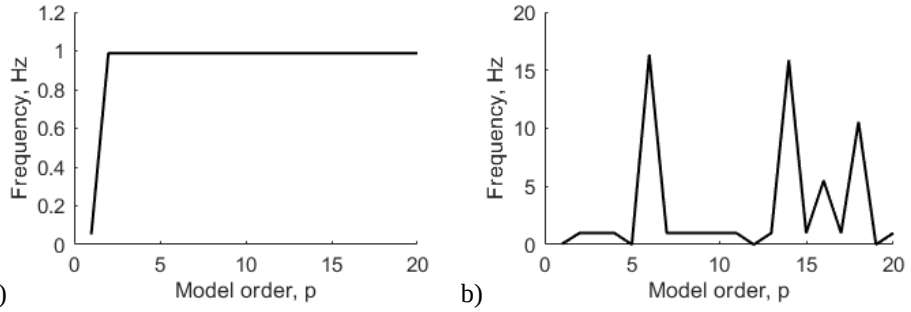

Figure 2.28. Frequency detection dependence on the model order: a) Yule-Walker method and b) modified covariance method

As follows from the figure shown above (see Figure 2.28.), the model order does not influence the detected frequency when the Yule-Walker method was used rather than the modified covariance. When the modified covariance approach was used, the detected frequency was highly similar to the frequency of the modeled signal. Going into deeper analysis, not only frequency dependence on the model order but both model order and signal-to-noise ratio (SNR) were investigated, choosing a better approach to compute the average period of the radial motion signal spectrum.

During the investigation of Yule-Walker and modified covariance methods for a capability to detect 1 Hz frequency, the model order was changed from 1 to 30, while the SNR of the modeled sinusoidal signal was from -5dB to 10 dB by every 1dB. If the maximal value of spectrum rounded to the nearest integer is equal to 1 Hz, then the result of model order and SNR combination is represented as green, otherwise as red (see Figure 2.29.).

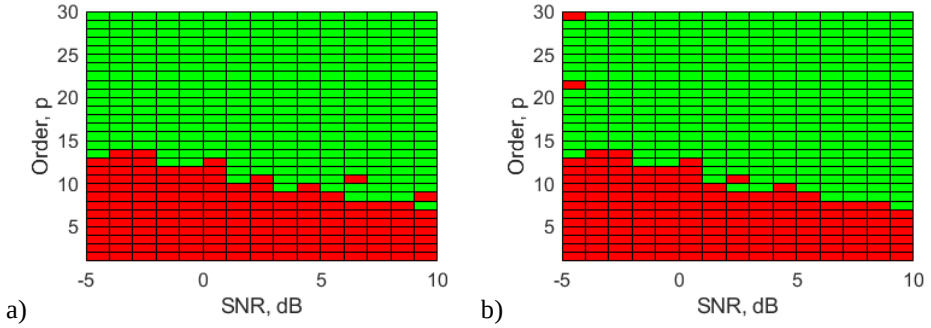

Figure 2.29. Frequency detection dependence on the model order and SNR: a) Yule-Walker method and b) modified covariance method

It can be seen from Figure 2.29 that Yule-Walker and modified covariance methods are capable to detect 1 Hz frequency when the model order is 14 or more, despite the SNR value. Taking into account these results, the model order was chosen to be constant and equal to 14 for the further analysis.

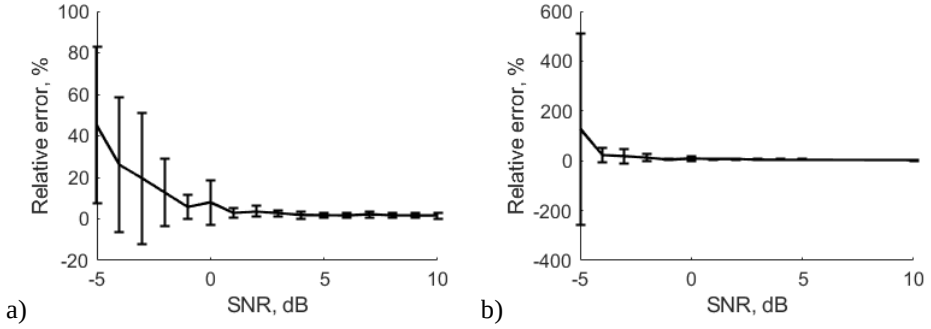

Figure 2.30. The relative error between modeled and detected frequency dependence on SNR: a) Yule-Walker method (model order const. = 14) and b) modified covariance method (model order const. = 14); error bar represents the mean and standard deviation of relative error (n = 40)

The relative error between modeled and detected frequency was evaluated when the model order was 14 and SNR was from -5dB to 10 dB by every 1dB. As it can be seen from Figure 2.30., the mean relative error is from 6 % to 45 % and 6 % to 127 % when Yule-Walker and modified covariance methods were used, correspondingly, and SNR is 0 dB or lower. If the SNR is higher than 0 dB, the mean relative error is from 1.6 % to 3.5 % and 2.3 % to 6.7 % when Yule-Walker and modified covariance methods were used.

Summing up all the above presented results, the Yule-Walker method was chosen for spectrum computation of the average period of the radial motion signal due to its robustness to detect modeled signal frequency against the modified covariance method.

2.4.4. Parametrization of the radial motion signals

The focus of the recent researches has been only on the longitudinal motion amplitude in different heart cycle phases. Predominantly, the measure of the first antegrade, the first retrograde, and the peak-to-peak amplitude of the longitudinal motion during the heart cycle was measured [21,164,165]. The entire longitudinal motion pattern (waveform) can be useful, even though the longitudinal motion amplitude is used, and can distinguish healthy volunteers from at-risk patients [164,166]. Moreover, different individuals are characterized by different longitudinal motion patterns [62,165]. To the best knowledge of the author of this dissertation, the frequency domain estimates for arterial wall motion were not tested in healthy controls and at-risk patients.

Therefore, time and frequency domain parameters were chosen for the parametrization of the average period of the radial motion signal (see

Table **2.4**.).

Table 2.4. Time and frequency domain parameters for the parametrization of the average period of radial motion signal

Time domain parameters	**Frequency domain parameters (in the range of 0–10 Hz)**
• Heart rate	• Sectral centroid
• Motion amplitude	• Spectral spread
• Velocity amplitude	• Spectral skewness
• Acceleration amplitude	• Spectral kurtosis

The peak-to-peak value of the average period of the radial motion signal was referred to as motion amplitude in the time domain. Taking the first and the second derivatives of the average period of the radial motion signal, the velocity and acceleration signals were calculated, and the peak-to-peak values of those signals were referred to as velocity and acceleration amplitudes in the time domain, correspondingly.

The length of all correlated periods of radial motion signal was determined, and the heart rate was estimated by:

$$BPM = \frac{FPS \cdot 60}{\frac{\sum_{n=1}^{N} L}{N}}; \quad (15)$$

where *BPM* are the beats per minute, *FPS* − frames per second (radial motion signal discretization in time), *L* − the length of the correlated period by samples, *n* = *1.N*, *N* is the number of correlated period in the radial motion signal.

The frequency domain parameters were evaluated from the power spectrum of the averaged period of radial motion signal and presented further (see Figure 2.31.).

Spectral centroid μ_1 characterizes the "center of gravity" of the spectrum [167]:

$$\mu_1 = \frac{\sum_{k=b_1}^{b_2} f_k s_k}{\sum_{k=b_1}^{b_2} s_k}; \quad (16)$$

where f_k is the frequency in Hz, corresponding to bin *k*, s_k is the spectral value at bin *k*, b_1 and b_2 are the band edges, in bins, over which to calculate the spectral centroid.

The spectral spread μ_2 is the standard deviation around the spectral centroid [167]:

$$\mu_2 = \sqrt{\frac{\sum_{k=b_1}^{b_2} (f_k - \mu_1)^2 s_k}{\sum_{k=b_1}^{b_2} s_k}}; \quad (17)$$

where f_k is the frequency in Hz, corresponding to bin *k*, s_k is the spectral value at bin *k*, b_1 and b_2 are the band edges, in bins, over which to calculate the spectral spread, μ_1 is the spectral centroid.

Spectral skewness μ_3 measures the symmetry around the spectral centroid [167]:

$$\mu_3 = \frac{\sum_{k=b_1}^{b_2} (f_k - \mu_1)^3 s_k}{\mu_2^3 \sum_{k=b_1}^{b_2} s_k}; \quad (18)$$

where f_k is the frequency in Hz, corresponding to bin *k*, s_k is the spectral value at bin *k*, b_1 and b_2 are the band edges, in bins, over which to calculate the spectral skewness, μ_1 is the spectral centroid, μ_2 is the spectral spread.

Spectral kurtosis μ_4 measures the flatness or non-Gaussianity of the spectrum around its centroid. Conversely, it is used to indicate the peakiness of a spectrum [167]:

$$\mu_4 = \frac{\sum_{k=b_1}^{b_2} (f_k - \mu_1)^4 s_k}{\mu_2^4 \sum_{k=b_1}^{b_2} s_k}; \quad (19)$$

where f_k is the frequency in Hz, corresponding to bin *k*, s_k is the spectral value at bin *k*, b_1 and b_2 are the band edges, in bins, over which to calculate the spectral kurtosis, μ_1 is the spectral centroid, μ_2 is the spectral spread.

The ability to discriminate healthy volunteers from at-risk patients of the above mentioned time and frequency domain parameters were evaluated by calculating and plotting receiver-operating characteristic (ROC) curves, evaluating area under curve

(AUC), and estimating sensitivity and specificity of proposed parameters. Sensitivity is defined as follows:

$$Sensitivity = \frac{TP}{TP+FN}; \tag{20}$$

where *TP* is the number of true positives and *FN* is the number of false negatives. Specificity is obtained by:

$$Specificity = \frac{TN}{TN+FP}; \tag{21}$$

where *TN* is the number of true negatives and *FN* is the number of false positives.

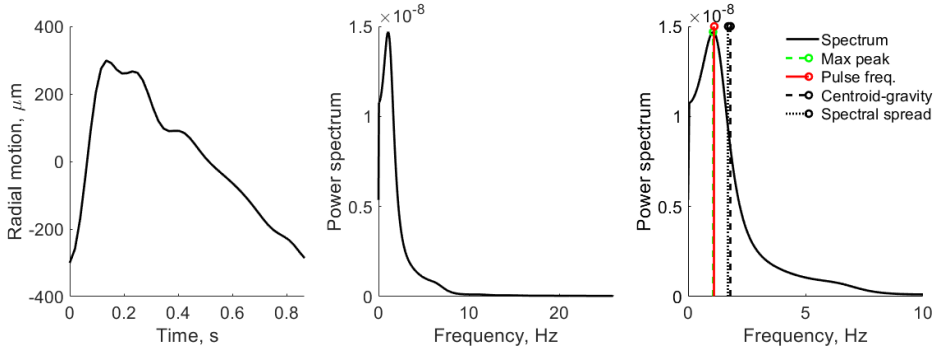

Figure 2.31. Averaged period of the radial motion signal in the time domain (left), averaged period of the radial motion signal in the frequency domain (middle), and spectrum with calculated frequency domain parameters in the range of 0–10 Hz (right): 53 years old female

2.5. Conclusions of the 2nd chapter

1. A virtual scanning simulation, adequate to the physical ultrasonic scanning, was developed. It is based on a comparison of axial, lateral, and elevation plane resolution between the physical scanning and digital simulation. An investigated virtual scanning could be used for the development and testing of complex echoscopy solutions in silico.
2. A 3D artery model, capable to reproduce the biomechanical behavior of human CCA for the simulation of US RF signals, was created. The model enables the evaluation of the artery geometry (artery diameter, intima-media complex thickness) and the amplitude, shape, and slope of elastic motions deep into the tissues. This opens possibilities for the development and validation of algorithms for the processing of RF signals or B-mode images, e.g., micro-motion tracking, elastography, etc.
3. The accuracy of the proposed motion detection algorithms, using simulated CCA US RF signals, was investigated and evaluated. This opens possibilities for further development and investigation of motion detection algorithm in vitro and endogenous motion detection application in clinical practice.
4. The parametrization of radial motion signals was proposed. It may prove valuable in risk stratification for the disease of atherosclerosis.

3. RESULTS

3.1. Fitting scanning model to physical PSF

The adequacy of the simulation depends on the conformance of the simulated ultrasound pulse shape to the experimentally measured one. The emitted ultrasound pulse model is 2 periods of 5 MHz oscillation, modulated by Hanning function. Figure 3.1. presents the pulse shape and frequency spectra of reflection from wire target, located 15 mm from the physical transducer and simulated by Field II and experimentally measured in the same position. The comparison shows a relatively good agreement (Pearson correlation coefficient between measured and simulated pulse-echo waves is 0.91, while between their spectrum, it is 0.98), since the results are influenced by the ultrasound diffraction and other propagation effects.

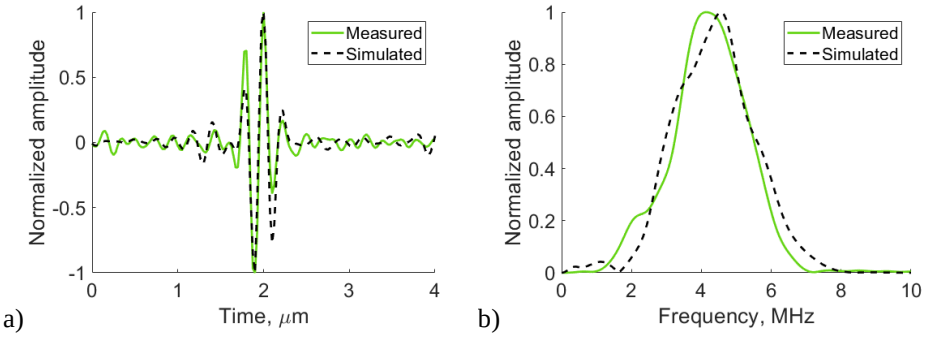

Figure 3.1. Comparison of measured physical and simulated digital a) pulse-echo waves reflected from wire targets at 15 mm depth (axial view) and b) their spectrum

Regardless of the good agreement of measured physical and simulated digital pulse-echo waves and their spectrum, it seems relevant to go deeper into the analysis, trying to ensure similarity between the experiment and simulation. Therefore, FWHM was used as a resolution parameter that quantitatively determines the axial, lateral, and elevation width of PSF of both measured physical and simulated digital phantoms.

The simulation of wire phantom, using the scanning parameters, shown in Table 2.2., was compared with the experimental scanning results and presented in Figure 3.2. PSF axial positions are compared by using a common axis of depth (see Figure 3.2.). Axial and lateral profiles of experimental and simulated PSFs are compared by using common normalized axes. The summary of the quantitative FWHM parameter comparison between experiment echoscopy and simulation is presented in Table 3.1. It shows that the average relative error of axial and lateral resolution is 11.6 and 15.2 %, accordingly. The results show some discrepancy in the lateral position of reflections from equidistant wires: the scatterers lateral positions in experimental echoscopy were exactly at 0 mm positions and varied between -0.13 mm and 0.06 mm. Hypothesizing, this could be due to the internal deformations that could occur in urethane rubber with embedded scattering wires, as the phantom was manufactured 10 years ago. Thus, the internal deformation influenced the average relative error of

axial and lateral resolutions, as PSF of experimental echoscopy and simulation were not exactly at the same positions.

Table 3.1. FWHM parameter comparison of experimental echoscopy and simulation

Experimental echoscopy				Simulation					
Scatterers axial position, mm	Scatterers lateral position, mm	Axial resolution, mm	Lateral resolution, mm	Scatterers axial position, mm	Scatterers lateral position, mm	Axial resolution, mm	Lateral resolution, mm	**Axial resolution relative error, %**	**Lateral resolution relative error, %**
9.8	-0.13	0.23	0.80	10.3	0.00	0.26	1.01	13.0	26.3
15.3	0.06	0.24	1.02	15.4	0.00	0.27	1.05	12.5	2.9
20.1	0.06	0.25	1.18	20.4	0.00	0.27	1.03	8.0	12.7
25.2	0.00	0.26	1.37	25.4	0.00	0.27	1.16	3.8	15.3
30.1	-0.06	0.24	1.46	30.4	0.00	0.29	1.29	20.8	11.6
35.6	-0.06	0.26	1.69	35.3	0.00	0.29	1.31	11.5	22.5
						Average, %		**11.6**	**15.2**

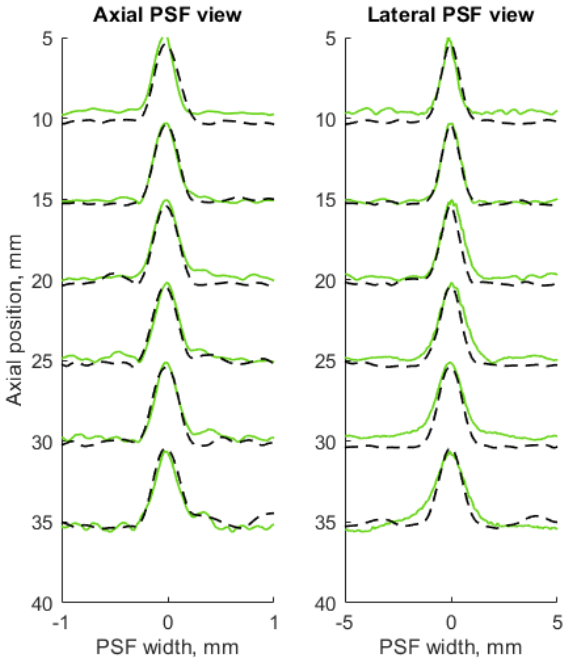

Figure 3.2. Comparison of the axial and lateral width of PSF: solid green line – experimental echoscopy of physical wire phantom, dashed black line – simulation of digital wire phantom; PSF amplitudes were normalized from 0 to 5

Figure 3.2. shows that the simulation results of the axial view of normalized PSF coincide better with the experiment than the lateral one, which is influenced by

difficult-to-account parameters of apodization, focusing, and other ultrasound diffraction effects.

Since PSF is the most important measure of resolution, a more detailed analysis in two dimensions is provided further (see Figure 3.3.). The axial dimension of PSF is influenced by the pulse duration and spectrum, which is quite similar both in simulation and experiment (see Figure 3.1.) and is much smaller than the lateral one. At a focal distance zone (z = 15 mm), the lateral dimension is smaller than at the far-field (z = 35 mm), but the simulation and experimental results presented in Figure 3.3. have a good agreement. There can be seen some peculiarities of both experimental and simulation results from the two-dimensional representation of PSF: an asymmetrical profile in the lateral direction in experimental echoscopy, while PSF of simulation data are symmetrical in axial and lateral directions. Moreover, the fact that the lateral peaking coordinate of simulated PSF has been observed centered at zero of the lateral position, while the experimental PSF profiles slightly deviate from this position.

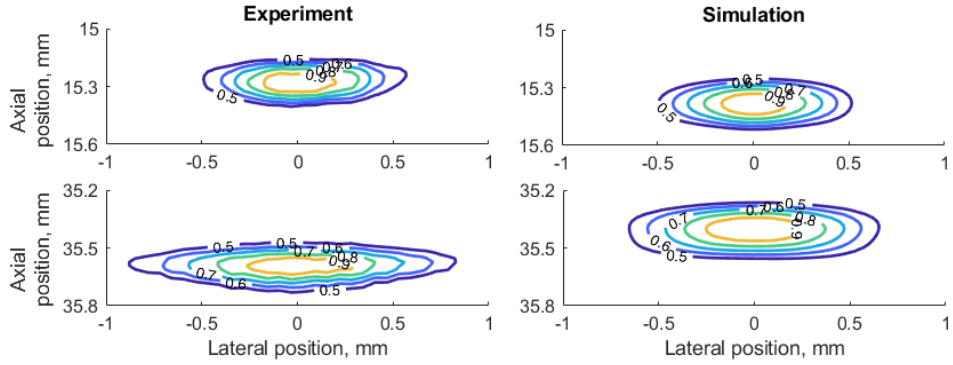

Figure 3.3. Comparison of PSF, using isoline diagrams of RF signals, reflected from targets, at approximately 15 and 35 mm: experimental echoscopy of physical wire phantom (left column) and simulation of digital wire phantom (right column); isolines presented at 0.1 intervals (from 0.5 to 0.9) of a normalized envelope of RF signals

Digital slice thickness phantom (see Figure 2.13. b) is used for the evaluation of scanning resolution in the elevation plane, perpendicular to the scanning plane. B-scan slice thickness or beam width in the elevation plane was evaluated, according to the method pioneered by Goldstein and Madrazo [146] and updated later [147]. In the physical experiment, the phantom with a 45° inclined scattering plane was used [145]. The distance of the B-scan central line intersection with the scattering plane was 15 mm, as observed in the scanner monitor, and RF signals were saved for B-scan formation. Using Field II software, the 45° inclined scattering plane phantom was modeled (see Figure 2.15. b), RF signals were simulated, and a corresponding B-scan image was composed. The experimental and simulated B-scan images of this case are presented in Figure 3.4., while the envelopes of the laterally averaged scanning lines were obtained from the inclined plane of physical and digital slice thickness

phantoms, Figure 3.5. The FWHM of the beam in the elevation plane was 1.21 mm in physical echoscopy, while in digital elevation phantom simulation, it was 1.38 mm.

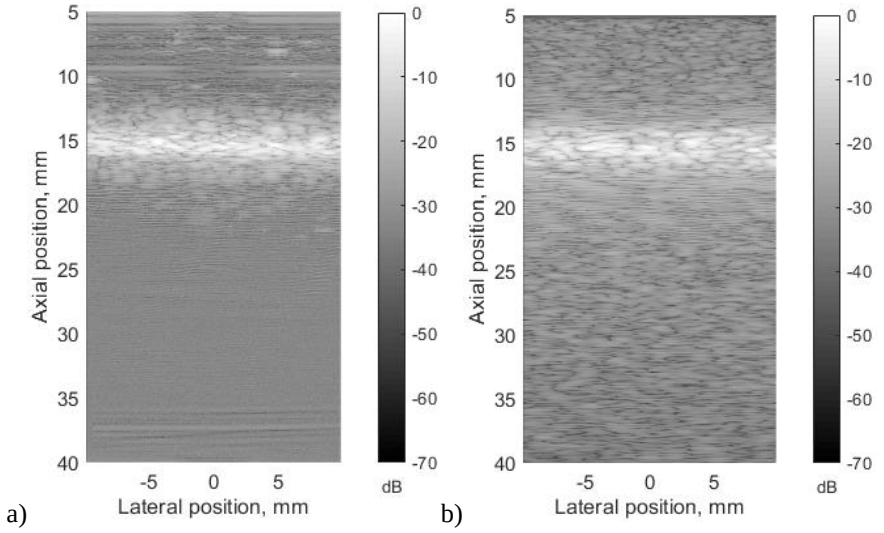

Figure 3.4. Comparison of slice thickness (elevation resolution) in a) physical and b) digital elevation phantoms B-scan images

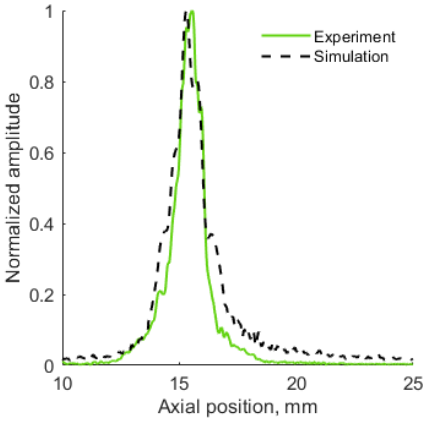

Figure 3.5. Comparison of elevation resolution along the laterally averaged scanning lines of physical echoscopy and digital elevation phantom simulation

The elevation resolution of physical echoscopy and simulation (see Figure 3.4. and Figure 3.5.) is in qualitatively good agreement (Pearson correlation coefficient is 0.97). In simulated and practical B-images (see Figure 3.4.) and envelopes of laterally averaged scanning lines along the axial scanning direction (see Figure 3.5.), the specular pattern is seen especially in the inclined plane zone, i.e., 15 mm. In sonography, the PSF width in the elevation plane usually is represented on the axis of axial distance [146,147]. According to the estimation methods, the widths of PSF in axial and elevation directions are inter-related. In the experiment case (see Figure 3.5.), the

FWHM of the beam in the elevation plane is 1.21 mm, and in the simulation case, it is 1.38 mm, i.e., the simulated beam width appears wider than the experimental one. Supposedly, this is due to the insufficient simulation accuracy of transducer aperture apodization in the elevation direction.

The final stage of echoscopy simulations is based on the wave scattering from randomly distributed scattering centers, representing tissue-mimicking material (TMM). Experimental and digital wire phantom B-scan images and central scanning line envelopes are compared in Figure 3.6.

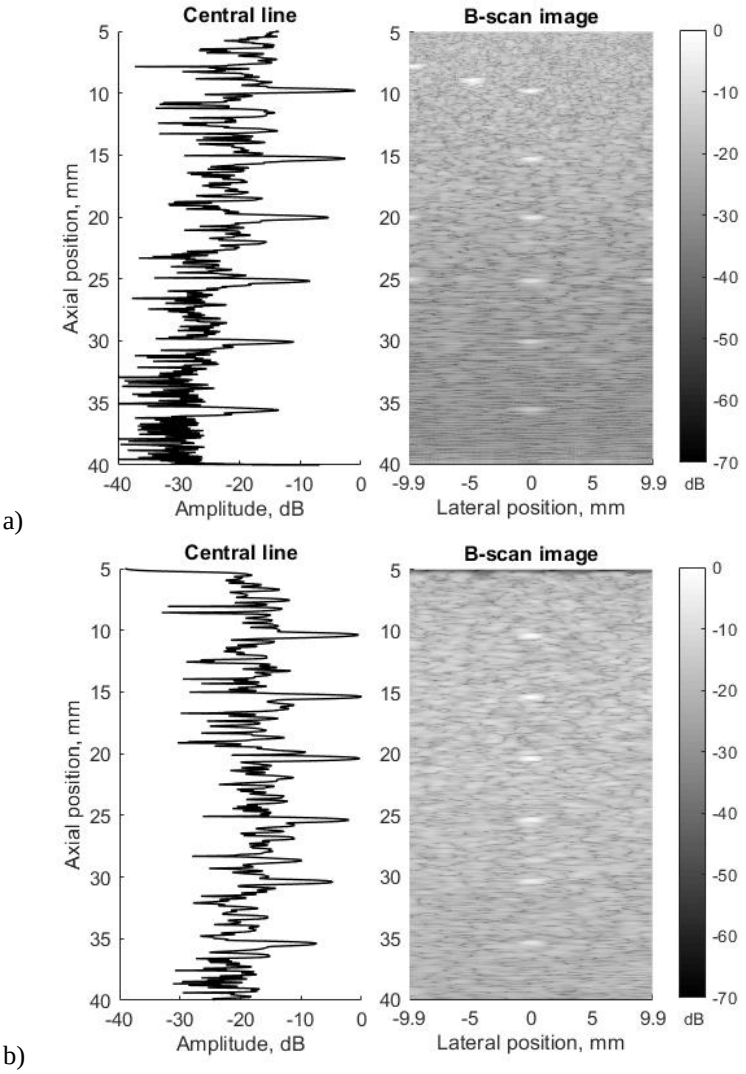

Figure 3.6. Comparison of scattering profile of point targets along the central echoscopy line and the whole B-scan images of a) measured US image of ATS Model 549 (physical wire phantom) b) simulated US image of digital wire phantom

It is worth mentioning that the B-scan image formation algorithm was common for both RF signals from physical scanner output and RF signals from modeling. Thus, the proprietary scanner image preparation is excluded from all cases of comparisons. The main difference is seen in the signal scattering from wire targets and background TMM, since the energy of ultrasound waves, reflected from the physical phantom wires, is unknown and difficult to simulate adequately. Moreover, the scattering in TMM of physical phantom is not identified in the available documentation, and the additional fitting of those parameters was out of the scope of the dissertation.

Discussion

The result shows a good agreement of digital simulation with the physical one. FWHM estimates in the axial direction are according to the practical estimates with a discrepancy of less than 12 %. The simulation results of the axial view of normalized PSF coincide better with the experiment than the lateral one, which is supposedly influenced by the difficulties to account in simulation parameters of apodization, focusing, and other ultrasound beamforming measures, taken by the scanner. The FWHM estimates in the lateral direction are according to the practical estimates with a discrepancy of less than 16 %.

A comparison of quantitative results with other researchers in Field II simulation of linear array scanning is quite difficult because of a limited number of articles that are dealing with experimental verification of such simulations. Thus, the obtained results are compatible with Pham et al. [41], who presented mean discrepancy between the FWHM of the measured and simulated resolutions that were less than 5 % and 18 % in the lateral and axial directions, respectively.

The limitations of the present research are related to the limited a *priory* knowledge of all parameters of the ultrasound transducer, beamforming, and standard phantoms as well as the ability to control the needed parameters of Field II software. A rather limited simulation accuracy of the lateral resolution is due to the lack of available information about the peculiarities of focusing and apodization both in transmit and receive modes. The apodization, especially in the elevation direction for 1D apertures is practically defined by transducer technology and difficult to specify.

The simulation of echoscopy is a multitask issue, because the outcome of real scanner, RF signals and quality of the B-scan image, is a result of many transformations, including those induced by the transducer, propagation in non-homogeneous media (tissue), focusing, apodization, filtering, and image presentation. In each stage of those transformations, the simulation uncertainties are related to insufficient knowledge of parameters to be used in the simulation model that is faced with them. The present results are an attempt to evaluate and discuss the main simulation uncertainties, which are important for the use of simulated data for the developments of imaging technologies.

3.2. Results of simulated RF US signals and images of artery model

In order to compare *in vivo* US data and *in silico* model data in more detail, they were presented in three different ultrasound modes: A, B, and M. Comparing the

experimental and modeled data, it has been found that in the A-mode, the echoes from the lumen-*intima* and *media-adventitia* boundaries are clearly visible in both cases. In B-mode cases, the artery walls are visible as a double-line pattern. In summary, the artery model has a structure like an *in vivo* arterial wall (see Figure 3.7. a and b).

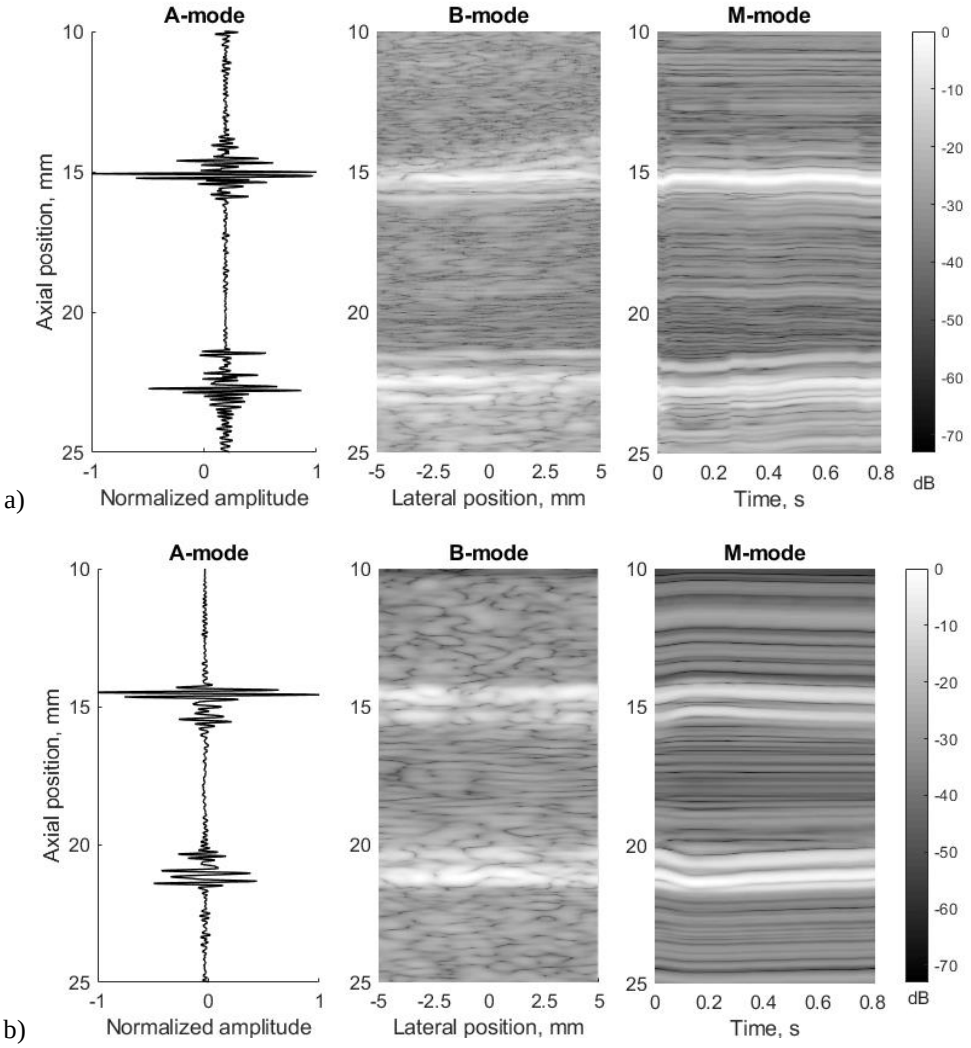

Figure 3.7. Comparison of RF signal form (A-mode, frame f_1, lateral position 0 mm), whole image (B-mode, frame f_1), and movement over time (M-mode), according to the artery: a) *in vivo* (23 years old female, motion amplitude was not normalized) and b) *in silico* model data (23 years old female, motion amplitude was normalized to 1 mm)

It is worth remembering that for the simulations, the amplitude of the preselected period of longitudinal and radial motion signals (see Figure 2.20. c) was normalized, taking peak-to-peak amplitude. In the example below (see Figure 3.7. b), the radial and longitudinal motions peak-to-peak amplitude was 1 mm. In the *in vivo*

case, radial and longitudinal motions peak-to-peak amplitude of the preselected period (see Figure 2.8. e) did not change and were 827 µm and 982 µ, accordingly. The time axis was not normalized. In M-mode, the movement of the artery model, according to the radial motion signal is seen (see Figure 2.8. e). Both the proximal and distal walls of the artery move according to the same pattern, only in the opposite direction (see Figure 3.7. b), and the motion amplitude of the distal and proximal walls is a radial motion divided by two as simulated. In the *in vivo* case, not so uniform motion pattern of both walls is seen (see Figure 3.7 a). Likely, the ultrasound transducer was not perfectly positioned at the center of the artery and 90-degree angle into the artery at the time of registration. It is not ruled out as well that the ultrasound transducer was pressed into the neck during the recording, which prevented the proximal wall of the artery from moving in the same pattern as the distal one.

Figure 3.8. depicts the B-mode images of the artery model at frames f_1 and f_9, where $f_9 = f_1 + 0.15$ s and $f_1 = 0$ s (frame rate was 52 frames per second). There is a 1000 µm motion difference between the proximal and distal walls, and the difference between B-mode images could be seen. However, a detailed analysis of RF signals at frames f_1 and f_9 shows a clear difference (see Figure 3.9.).

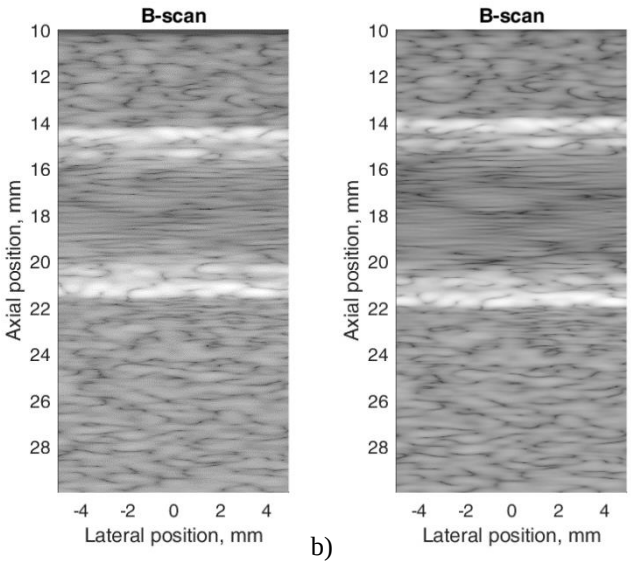

Figure 3.8. Simulated B-mode images of the artery model at certain frames of the sequence: a) $f_1$and b) f_9: 23 years old male, motion amplitude was normalized to 1 mm

A calculated radial displacement of the virtually scanned artery model at 3.91 mm and 5.1 mm away from the artery model center between frames f_1 and f_9 is 400 µm and 330 µm (as observed in Figure 3.9.). Even though the displacement at those depths was expected to be 390 µm and 320 µm, correspondingly, the expectation was based on the half radial motion 500 µm between these time instances and the theoretical healthy volunteer radial motion decrement 0.78 and 0.64 at the selected depths, accordingly (see Figure 2.22.).

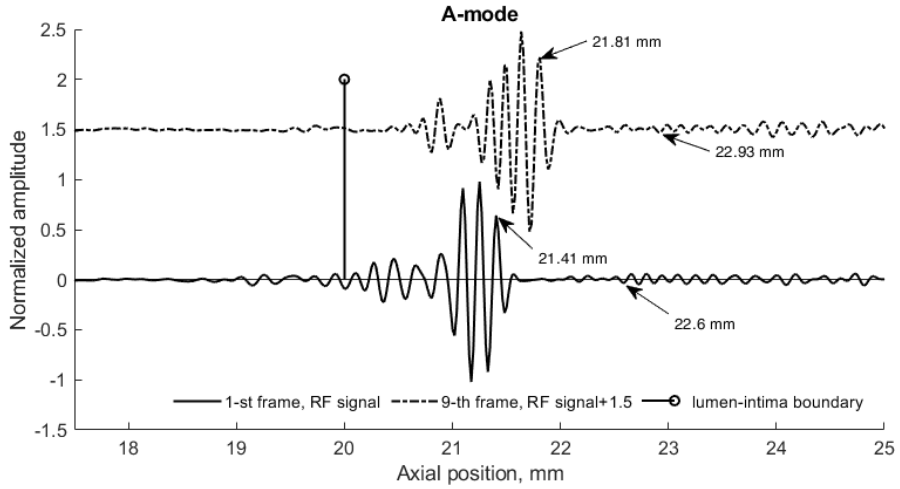

Figure 3.9. RF signals simulated by the model of a pulsating artery at frames f_1 and f_9, distal wall and surrounding tissues scattered RF signals (the artery center at 17.5 mm), depicting the radial wall displacement and its decrease in surrounding tissues: 23 years old male, motion amplitude was normalized to 1 mm

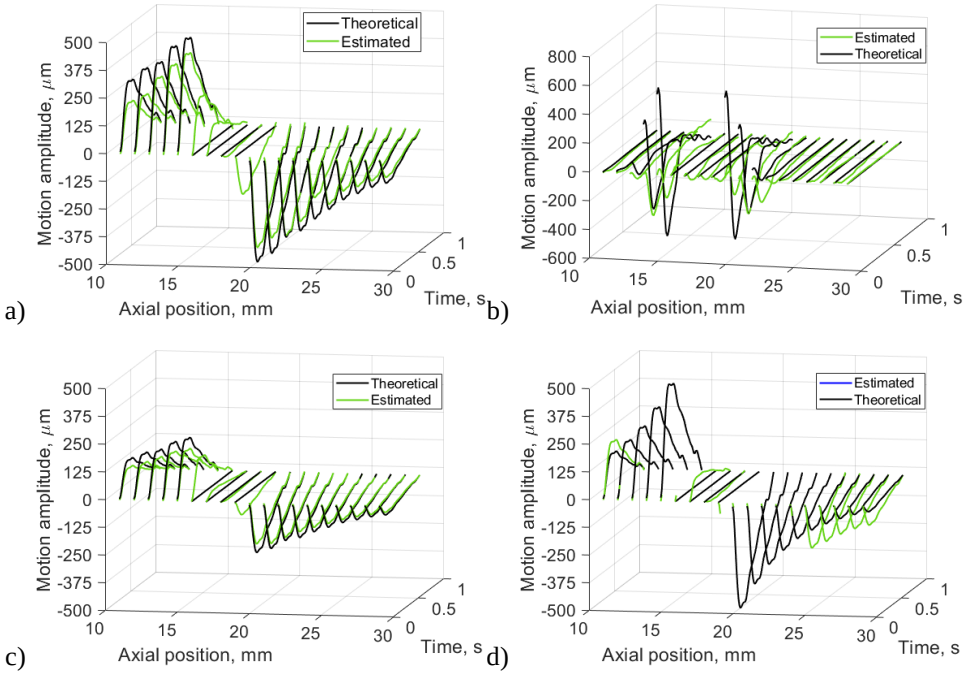

Figure 3.10. Motion of both proximal and distal wall of the artery and surrounding tissues: a) 1 mm peak-to-peak radial motion, estimated using OpenOpticalFlow, b) 1 mm peak-to-peak longitudinal motion, estimated using OpenOpticalFlow, c) 0.5 mm peak-to-peak radial motion, estimated using 1D cross-correlation, d) 0.5 mm peak-to-peak radial motion, estimated using 1D cross-correlation: 23 years old male

For comparison, the results, using 1D cross-correlation and OpenOpticalFlow algorithms, were presented (see Figure 3.10.). The further analysis of radial and longitudinal motions showed that the movements that were estimated from the simulated scanning frames match the initially defined motion pattern that were used for the modeling. Nonetheless, the 1D cross-correlation method is not capable to detect large inter-frame motion (higher than a quarter of the wavelength of the ultrasound echo data) due to "peak hopping" errors that result in a discontinuity of radial motion signals (see Figure 3.10. d).

Dynamic 3D artery model has similar radial and longitudinal motion patterns, amplitude, and decrement into the tissue as theoretically predefined motions, even though the estimated motion amplitude is negligibly lower than the theoretical one. It is important to note that the motion estimation from simulated US RF signals is highly dependent on the estimation algorithm that was applied. Therefore, the simulation errors cannot be attributed to the simulation method only.

Discussion

The echoscopy simulation shows that the artery model represents A, B and M-mode image structure like *in vivo* artery wall. The evaluated simultaneous radial and longitudinal motion of the virtually scanned 3D structure over a single pulse is visually almost indistinguishable from the generated motion pattern.

Besides, a radial and longitudinal motion slope away from the artery lumen or lumen-*intima* boundary was modeled. These results go beyond the previous reports [42,46] and show that the artery wall structure could be modeled in detail together with the longitudinal and radial artery wall motion signal shape and amplitude. Because there is no conclusive information about the mathematical modeling of longitudinal motion, this motion in the model was defined according to the data evaluated from *in vivo* experiments.

The limitation of this study is not verified *in vivo*, the slope of the longitudinal and radial motion deep into the tissue. For this moment, the slope is described by an exponential function, which parameters were chosen according to Stoitsis et al. [46]. Cinthio [21] evaluated such exponential function parameters from *in vivo* data, but in a limited study and only from a healthy subject. For a more accurate evaluation of slope, the artery diameter and compliance of the surrounding tissues should be concerned as well. With aging, the arterial stiffness increases [168]; thus, the motion slope should be evaluated in healthy as well as atherosclerotic patients to model different arterial stiffness.

The artery model, which uses both shape and amplitude of radial and longitudinal motion signals from real *in vivo* data, has not been proposed in the previous studies. Further investigations are necessary to evaluate and confirm the author's results [46] of the spatial dependence of radial and longitudinal motions *in vivo*.

3.3. Investigation results of methods for radial and longitudinal motion detection accuracy

For motion detection, two methods were chosen: 1. 1D cross-correlation for the detection of radial motion and 2. OpenOpticalFlow for both radial and longitudinal motion detection. The difference between these two approaches is obvious, i.e., OpenOpticalFlow deals better with large radial motion rather than 1D cross-correlation (see Figure 3.11. a and b).

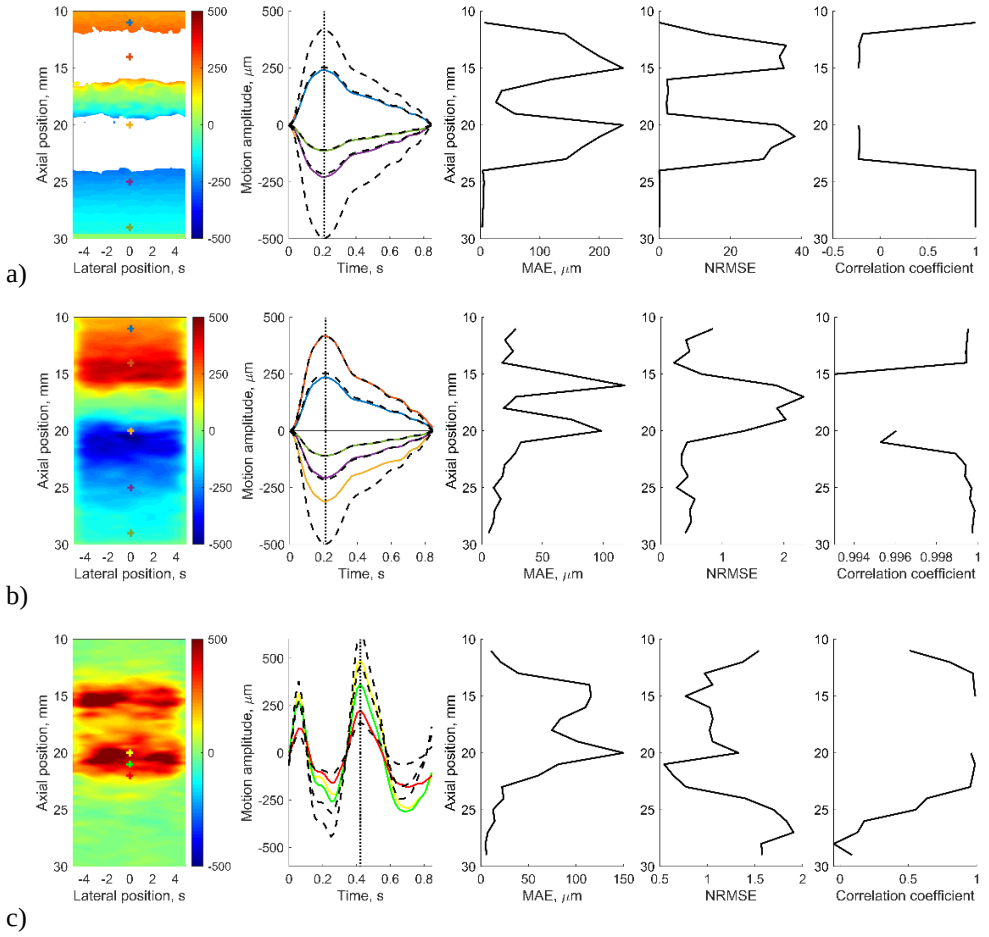

Figure 3.11. Investigation results of methods for radial and longitudinal motion detection accuracy: a) radial motion, 1D cross-correlation, b) radial motion, OpenOpticaFlow, and c) longitudinal motion, OpenOpticaFlow; the radial motion map in scanning plane with preselected points from where the estimated motion is taken and depicted together with the theoretical; there, the vertical dashed line corresponds to the time moment of maximal theoretical displacement; at this time moment, a motion map is depicted; finally, MAE, NRMSE, and Pearson correlation coefficient are evaluated in the midline of the motion map at the different axial positions, i.e., starting from 11 mm every 1 mm to 29 mm: 27 years old female, theoretical motion peak-to-peak amplitude is 1 mm

Inter-frame displacements are accumulated relative to the first frame resulting in motion. White areas in the motion map (see Figure 3.11. a) correspond to the regions where inter-frame motion is higher than a quarter of the wavelength, and there exist a probability to identify the false correlation peak, resulting in large tracking errors that are known as "peak hopping" errors. OpenOpticalFlow method is not faced with this issue; the motion map is smooth, without any discontinuity.

Large MAE values that are exceeding 150 μm (modelled motion amplitude was 1 mm) are seen at the boundary of the artery wall and lumen when longitudinal motion was detected with the OpenOpticalFlow method. This may be explained by that the longitudinal motion mainly are exhibited in *intima-media* complex, which thickness is only 0.7 mm, which causes difficulties in the detection of longitudinal motion in such small ROI. Nonetheless, the correlation coefficient shows a higher similarity between the estimated and theoretical motion signals at the artery wall (from 14 mm to 22 mm, according to the axial position) rather than in the surrounding tissues (from 10 mm to 14 mm and from 22 mm to 30 mm, according to axial position), where the relationship between the two motion signals is pure or does not exist.

The further analysis of MAE showed that great errors occur when 1D cross-correlation method was used for radial motion detection, and peak-to-peak motion amplitude is equal to or higher than 0.75 mm (see Figure 3.12. a). Once again, this is caused by the fact that the inter-frame motion was higher than a quarter of the wavelength, and there exists a probability to identify the false correlation peak, resulting in large tracking errors that are known as "peak hopping" errors. Nonetheless, for high values of peak-to-peak radial motion, the median values of MAE were found to be lower than 25 μm when the OpenOpticalFlow method was investigated. As may be seen below (see Figure 3.12. b), the median values of MAE were found to be lower than 25 μm when the OpenOpticalFlow method was investigated for a capability to detect longitudinal motion. Moreover, it could be seen that the average values of MAE are about 50 μm or lower and have a tendency to decrease when the detected motion amplitude is decreasing.

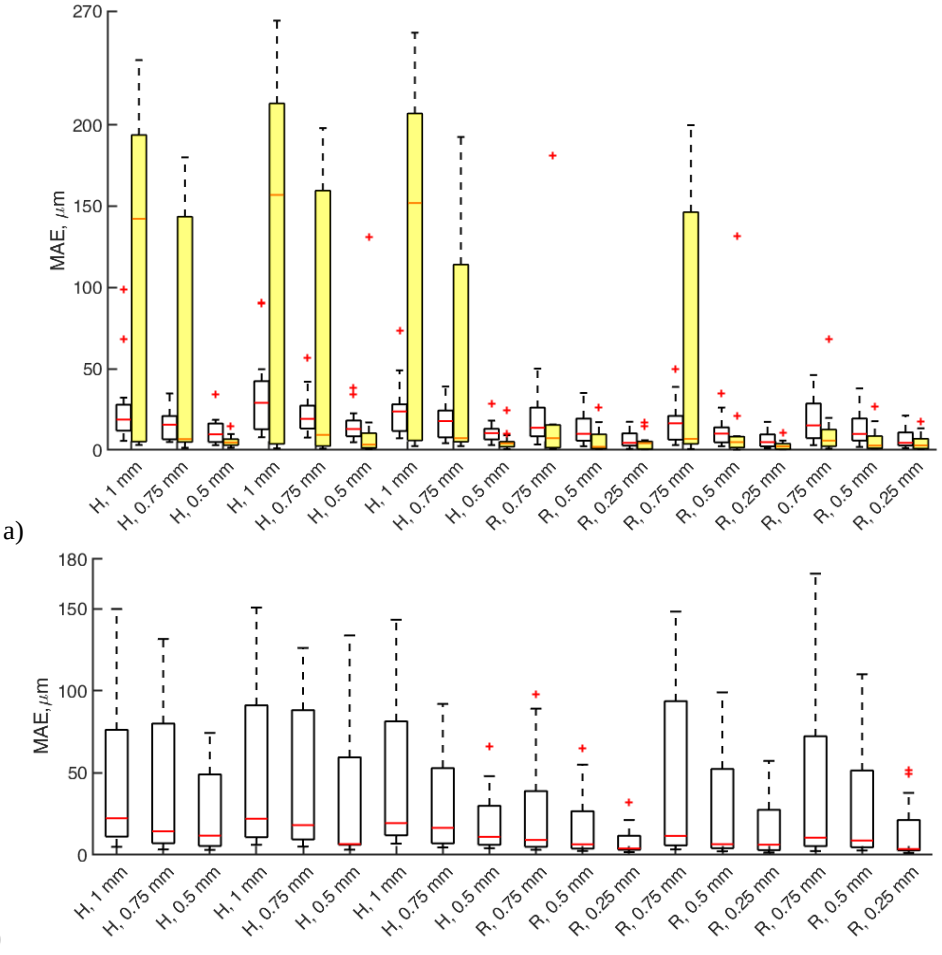

Figure 3.12. Box plots of MAE of estimated and theoretical motion signals, evaluated in the middle scanning line, starting from 11 mm every 1 mm to 29 mm: a) radial motion detection, b) longitudinal motion detection; white and yellow boxes correspond to 1D cross-correlation and OpenOpticalFlow methods, accordingly (n = 19); the median values are shown as a horizontal red line; the whiskers represent the minimum and maximum values; the outliers are indicated by red +, H – healthy volunteer, R – at-risk patient

Discussion

The results demonstrate that the variety of accuracy evaluation parameters for radial and longitudinal motions detection are capable to access error as well as evaluate the dissimilarities between the estimated and theoretical motion signals.

Nonetheless, the accuracy in motion tracking was examined by others and presented in APPENDIX A1. Some authors state that no quantitative evaluation of accuracy was introduced in their studies, while others use qualitative evaluation only. In contrast to these reports in the literature, there were studies where accuracy evaluation criteria mainly were the average absolute error. As stated by Zahnd et al.[19],

the average absolute error of longitudinal motion was 20 ± 19 μm, while the radial motion was 84 ± 107 μm, using Klaman-based block matching method for motion detection. Later, Zahnd et al.[101] proposed a dynamic block-matching approach for motion tracking and stated that the average absolute error of longitudinal motion was 150 ± 163 μm. In accordance with the results of previous studies, the average values of MAE of longitudinal motion lie between the results of Zahnd et al.[19,101]. Moreover, it is worth mentioning that only a few researchers groups incorporated *in silico* experiments in their studies [90,92]. Most of the accuracy evaluation studies are based on *in vivo* studies. There, the estimated motion was compared with manual tracing results, which were performed by experienced ultrasound physicians and considered as the ground truth. Therefore, the motion detection errors cannot be attributed to the motion detection method only. The errors can as well occur due to the manual tracing. Still, the motion detection approaches should be carefully investigated *in silico* and *in vitro* before testing *in vivo*.

The main limitation of the accuracy evaluation of motion detection is that the motion tracking approaches were not specialized to a specific motion, i.e., longitudinal motion, which demands particular solutions for motion tracking, as longitudinal motion exists mainly in *intima-media* complex and is negligible in the surrounding tissues.

Future investigations *in vitro* and *in vivo* are necessary to further investigate the methods for motion detection and suggest even more reliable approaches for that purpose.

3.4. Comparison of theoretical and estimated slope profiles of radial and longitudinal motions

The results show the spatial dependence of radial and longitudinal motions (see Figure 3.13.).

The amplitude of radial motion is greatest at the surface of the artery (16 and 20 mm) and decreases exponentially into the surrounding tissues; the amplitude of longitudinal motion is greatest at the artery wall (approximately at 16 mm and 20 mm), decreases significantly, and the longitudinal motion amplitude is negligible in the surrounding tissues. The apparent comparison between healthy volunteer (see Figure 3.13. a and c) and at-risk patient (see Figure 3.13. b and d) radial and longitudinal motion slope deep into the tissue is seen: more abrupt radial and longitudinal motion slope is observed with at-risk patient rather than healthy volunteer.

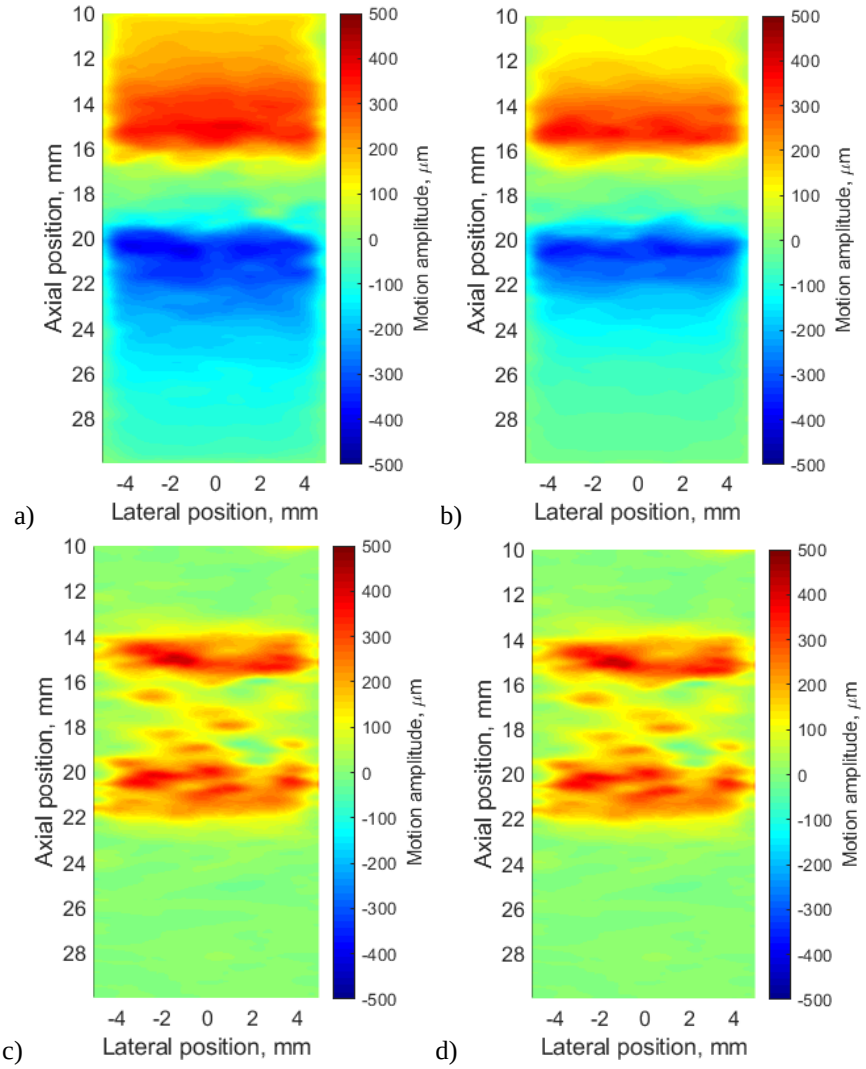

Figure 3.13. Motion maps of both proximal and distal wall of the artery and surrounding tissues, estimated using OpenOpticalFlow: a) radial motion and its slope deep into the tissue (motion amplitude 0.75 mm, b_1 = 0.17, 27 years old female), b) radial motion and its slope deep into the tissue (motion amplitude 0.75 mm, b_1 = 0.26, 56 years old male), c) longitudinal motion and its slope deep into the tissue (motion amplitude 0.75 mm, b_2 = 1.08, 27 years old female), d) radial motion and its slope deep into the tissue (motion amplitude 0.75 mm, b_2 = 1.62, 56 years old male)

Figure 3.14. depicts the spatial dependence comparison of radial and longitudinal motions of the distal wall of the artery and surrounding tissues between the theoretical and estimated values.

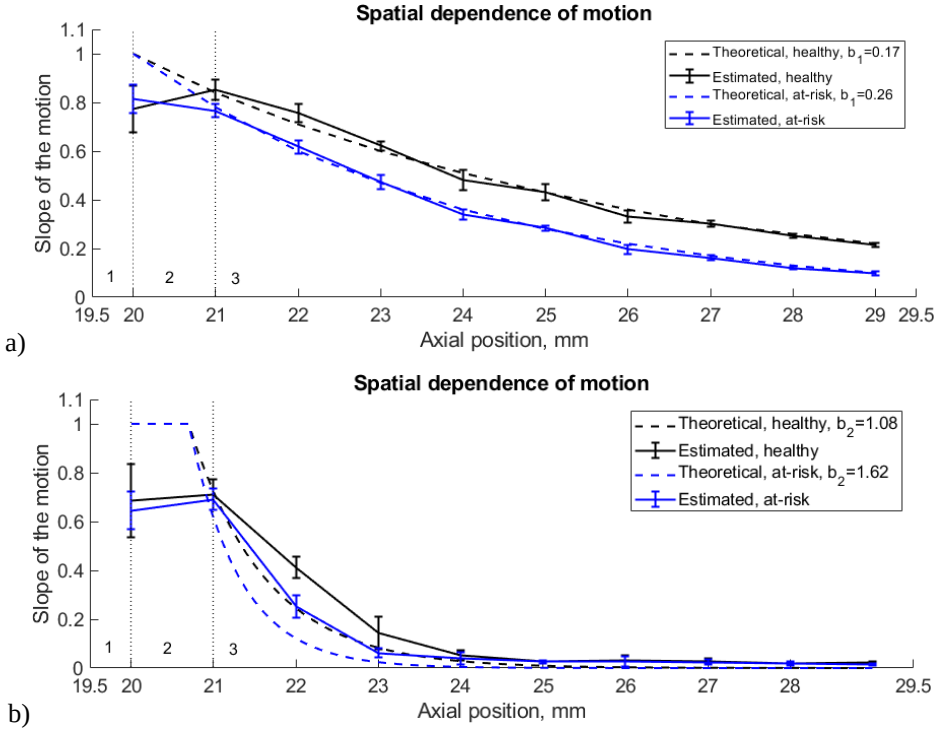

Figure 3.14. Spatial dependence comparison of radial and longitudinal motions of distal wall of the artery and surrounding tissues between theoretical values and estimated from OpenOpticalFlow algorithm of envelopes of simulated RF signals: a) radial motion slope in the artery wall and deep into the tissue, b) longitudinal motion slope in the artery wall and deep into the tissue; the error bars represent the mean (n = 9) and standard deviation (n = 9) of estimated values of slope profiles for healthy volunteer and at-risk patient groups for every preselected axial position; numbers 1, 2, and 3 in the graph corresponds to the lumen, artery wall, and surrounding tissues, respectively

There is a correlation between the theoretical and estimated slope profiles of radial motion in the surrounding tissues. However, such a good coincidence is not seen in the artery wall. This could be due to the insufficient number of preselected points in the artery wall where the slope profile was evaluated, i.e., only two axial positions at the boundary of the artery wall define the motion slope profile in the artery wall. The same number of preselected points was in the longitudinal motion slope profile definition in the artery wall. There, even more discrepancy between the theoretical and estimated slope profiles is seen (see Figure 3.14. b). What is more, the estimated profiles of longitudinal motion had a bias, relative to the theoretical ones, in the surrounding tissues. Despite the mismatch between theoretical and estimated profiles, especially in the case of longitudinal motion, it is capable to differentiate healthy volunteers and at-risk patients according to the slope profiles of radial and longitudinal motions.

Discussion

The results demonstrate that the variety of slope profiles of radial and longitudinal motions that defines different elasticity tissues may be used for the differentiation of healthy volunteers and at-risk patients.

Nonetheless, radial and longitudinal motion slope in the artery wall and surrounding tissues was modeled by others [61]; no artery motion maps or slope profiles were investigated in detail. Recently, several authors [30,31] have proposed motion maps of liver and brain tissues. Despite the clear difference between healthy and diseased tissues, according to the motion amplitude, the motion slope was not explored thoroughly. The results obtained in [169] suggest that the radial motion in tissue-mimicking phantoms with predicted Young modulus 10 kPa and 7kPa results in different motion amplitudes at the same axial position. Summing up, it was found that motion is dependent on the phantom elasticity, i.e., with the increase of phantom stiffness, the motion amplitude decreases.

The main limitation of the modeling result is that the slopes of radial and longitudinal motions were modeled by a limited study and only from a healthy subject [21], while the slope for at-risk patients was selected at random, i.e., 1.5 times bigger than for the healthy volunteers.

For a more accurate evaluation of the slope, the artery diameter should be concerned as well. With aging, the arterial stiffness increases [168], and the motion slope should be evaluated in healthy as well as atherosclerotic patients to model different arterial stiffness.

The tissue differentiation, according to the slope profiles of radial and longitudinal motions, has not been proposed in previous studies. Further investigations of motion slope dependence of tissue elasticity *in silico* and *in vivo* are necessary.

3.5. *In-vivo* results of the parametrization of radial motion signals

Time and frequency domain parameters that were used for the parametrization of radial motion signals of healthy volunteers and at-risk patients were used as inputs for plotting ROC curves that were used to evaluate the performance of binary classification algorithms. MATLAB R2018b (The MathWorks, Inc., Natick, USA) was used to perform this analysis.

Further on, the ROC curves are provided to evaluate the diagnostic performance of a proposed time and frequency domain parameters to discriminate the diseased cases from the normal ones. Figure 3.15. a) demonstrates that the heart rate parameters have poor ability to distinguish healthy volunteers from at-risk patients, as AUC is 0.63 (see Figure 3.15. a). Nonetheless, the radial motion displacement, velocity, and acceleration parameters have some predictive power, as AUC is about 0.8 (see Figure 3.15. b, c, and d).

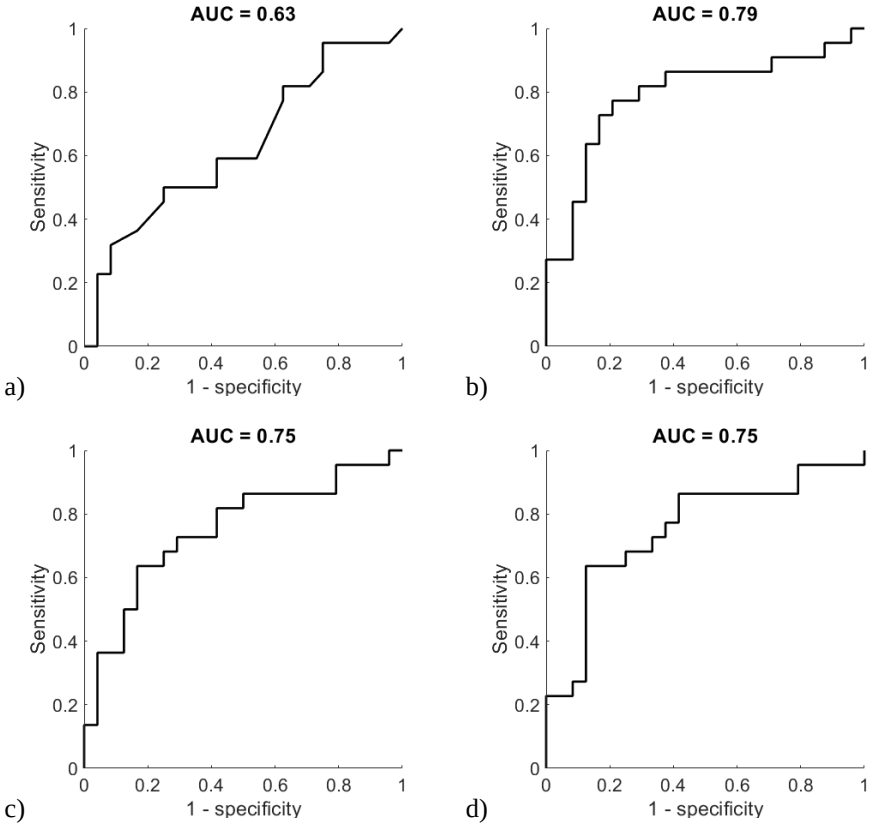

Figure 3.15. ROC curves of a) heart rate, b) radial motion displacement, c) velocity, and d) acceleration, proposed to compare their diagnostic performance in detecting atherosclerosis

Comparing the ability of frequency domain parameters (see Figure 3.16.) to detect at-risk patients, it has been found that the spectral centroid and spectral spread have fair ability to diagnose patients with and without the atherosclerosis, as AUC of the ROC curve of those parameters is about 0.7. The ROC curves of spectral skewness and spectral kurtosis have shown that these parameters have some predictive power to discriminate the diseased cases from normal ones, as AUC is 0.79 in both cases.

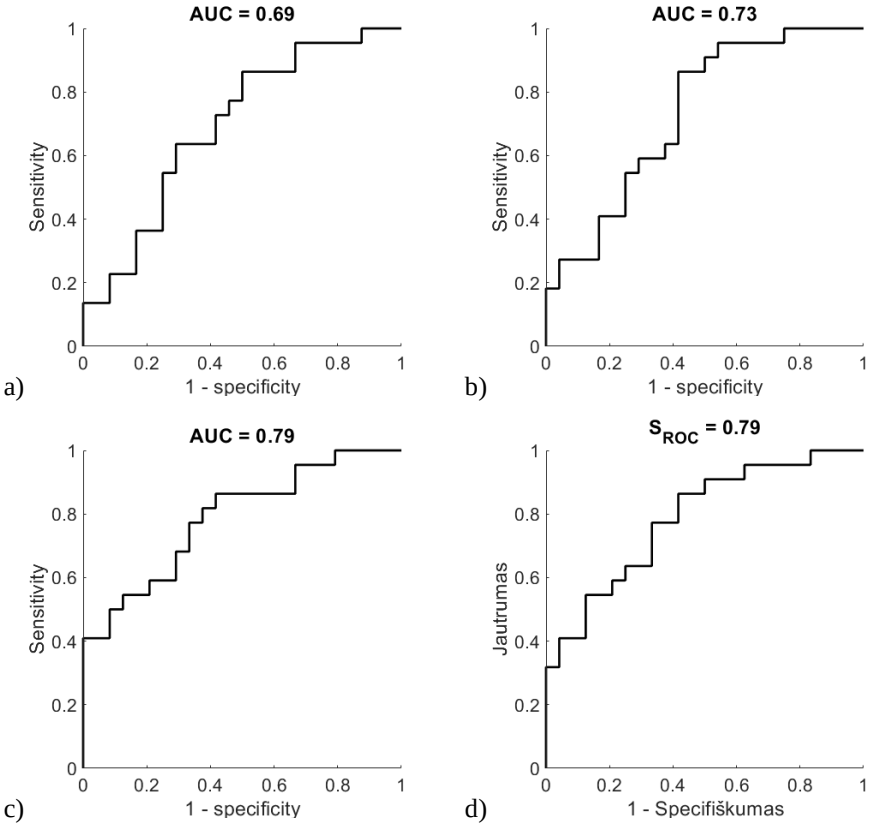

Figure 3.16. ROC curves of a) spectral centroid, b) spectral spread, c) spectral skewness, and d) spectral kurtosis, proposed to compare their diagnostic performance in detecting atherosclerosis

Table 3.2. Diagnostic value of time and frequency domain parameters in distinguishing healthy volunteers from at-risk patients

		Sensitivity	**Specificity**
Time domain parameters	Heart rate, BPM	0.50	0.63
	Displacement, µm	**0.77**	0.79
	Velocity, µm/s	0.64	**0.88**
	Acceleration, µm/s^2	0.73	0.71
Frequency domain parameters	Spectral centroid, Hz	0.64	**0.71**
	Spectral spread	**0.86**	0.58
	Spectral skewness	0.77	0.67
	Spectral kurtosis	0.77	0.67

The highest sensitivity of the proposed time and frequency domain parameters has displacement, i.e., 0.77, and spectral spread, i.e., 0.86. The velocity and spectral

centroid are assigned as parameters with the highest specificity, resulting in 0.88 and 0.71, correspondingly (see Table 3.2.).

Discussion

The results indicate that the proposed parametrization of radial motion signals is efficient for the differentiation of healthy volunteers and at-risk patients when radial motion displacement, velocity and acceleration spectral centroid, spectral spread, spectral skewness, and spectral kurtosis parameters are used.

The results of motion parametrization in the time domain are built on the existing evidence of [21,164,165] that healthy volunteers could be discriminated from at-risk patients by using the displacement parameter. However, most of the previous studies do not take into account the frequency domain parameters.

The current *in vivo* study was limited by CCA motion detection and parametrization only in the radial direction. The longitudinal motion evaluation requires a specific approach when dealing with three challenges described by Zahnd [19]. Firstly, there exists a low contrast in the longitudinal direction due to the anatomical structure of the artery (*intima-media* complex is characterized by homogeneous profile, i.e., a small variation of the image gray level along the wall). The second challenge is a small *intima-media* layer thickness of about 0.5 mm. Finally, the speckle decorrelation, i.e., the degrading phenomenon caused by out-of-plane movements, low echoes, tissue deformation, and movement artifacts, must be dealt with.

Further investigations are necessary to validate the conclusions that can be drawn from this study. New frequency domain parameters could be investigated in larger study population in the future to distinguish healthy subjects from at-risk patients.

3.6. Conclusions of the 3rd chapter

1. The result shows a good agreement of digital simulation with the physical one. FWHM estimates in the axial direction are according to the practical estimates with a discrepancy of less than 12 %. The simulation results of the axial view of normalized PSF coincide better with the experiment than the lateral one, which is supposedly influenced by the difficulties to account in simulation parameters of apodization, focusing, and other ultrasound beamforming measures that are taken by the scanner. The FWHM estimates in the lateral direction are according to the practical estimates with a discrepancy of less than 16 %.
2. The echoscopy simulation shows that the artery model represents A, B, and M-mode image structure like *in vivo* artery wall. The evaluated simultaneous radial and longitudinal motion of the virtually scanned 3D structure over a single pulse is visually almost indistinguishable from the generated motion pattern.

3. The results demonstrate that the variety of accuracy evaluation parameters for radial and longitudinal motion detection are capable to access error as well as evaluate the dissimilarities between estimated and theoretical motion signals.
4. The results demonstrate that the variety of slope profiles of radial and longitudinal motions that defines different elasticity tissues may be used for the differentiation of healthy volunteers and at-risk patients.
5. The results indicate that the proposed parametrization of radial motion signals is efficient for the differentiation of healthy volunteers and at-risk patients, i.e., the proposed parameters have the diagnostic ability to diagnose patients with and without the atherosclerosis.

4. GENERAL CONCLUSIONS

1. Literature review has shown that the atherosclerosis is a chronic disease of the arterial wall that is not noticeable until the atherosclerotic plaques build up. However, it has been proven that significant changes in the mechanical properties of arterial walls (i.e., longitudinal and radial motion of the arterial wall) occur much earlier than the anatomical changes (i.e., IMT). The clinical investigations have linked longitudinal motion of the CCA to the risk factors and CVDs and have shown a relationship between arterial stiffness, CVDs, and the decrease in longitudinal motion. A number of motion tracking algorithms are proposed for radial and longitudinal motion detection. Some of them are freely or commercially available for the investigation of longitudinal motion. However, none of them are applied in clinical practice nowadays. Firstly, these methods should be carefully investigated before wide usage.
2. Virtual scanning simulation that is adequate to the physical ultrasonic scanning was developed. Digital scanning shows a good agreement with the physical one: FWHM estimates of PSF in the axial and lateral directions are according to the practical estimates with a discrepancy of less than 12 % and 16 %, correspondingly. The FWHM of the beam in the elevation plane was 1.21 mm in the physical echoscopy, while in the digital elevation phantom simulation, it was 1.38 mm.
3. A 3D artery model that is capable to reproduce the biomechanical behavior of human CCA for the simulation of US RF signals was created. The echoscopy simulation shows that the artery model represents A, B, and M-mode image structure like *in vivo* artery wall. The evaluated simultaneous radial and longitudinal motion of the virtually scanned 3D structure over a single pulse is visually almost indistinguishable from the generated motion pattern.
4. The accuracy of the proposed motion detection algorithms, using simulated CCA US RF signals, was investigated. The results demonstrate that the variety of accuracy evaluation parameters for radial and longitudinal motion detection are capable to access error as well as evaluate the dissimilarities between estimated and theoretical motion signals. The median values of MAE were found to be lower than 25 μm when the OpenOpticalFlow method was investigated for both radial and longitudinal motion detection.
5. The capability to differentiate arteries by motion slope profiles was investigated. There is a good match between theoretical and estimated slope profiles of radial motion in the surrounding tissues, while the estimated profiles of longitudinal motion had a bias relative to the theoretical ones in the surrounding tissues. The results demonstrate that a variety of slope profiles of radial and longitudinal motions that defines different elasticity tissues may be used for the differentiation of healthy volunteers and at-risk patients.

6. The US RF data from healthy volunteers and patients at increased risk of CVD group was collected; the motion parameters of two different populations were calculated, and those parameters' diagnostic ability to diagnose patients with and without the atherosclerosis was evaluated. The highest sensitivity of the proposed time and frequency domain parameters has displacement, i.e., 0.77, and spectral spread, i.e., 0.86. The velocity and spectral centroid are assigned as parameters with the highest specificity, resulting in 0.88 and 0.71, correspondingly.

SANTRAUKA

Įvadas

Širdies ir kraujagyslių ligos (ŠKL) yra pagrindinė žmonių mirties priežastis visame pasaulyje. Kasmet nuo šių ligų miršta vis daugiau žmonių nei nuo kitų ligų. 2019 m., kada paskutinį kartą buvo skaičiuota pasaulio statistika, pasaulyje nuo ŠKL mirė 18,6 milijono žmonių, kas atitinka 17,1 % padidėjimą per pastarąjį dešimtmetį [1]. 42,1 % mirčių pagrindinė priežastis, priskiriama ŠKL, buvo koronarinė širdies liga [1], o aterosklerozė yra pagrindinė šios ligos priežastis. Prognozuojama, kad iki 2030 m. mirtys nuo ŠKL pasaulyje pasieks 23,6 milijono [2]. Insultas, vienas iš kelių galimų ŠKL pasekmių, yra antroji mirtingumo ir šeštoji ilgalaikės negalios priežastis [3,4]. Todėl širdies ir kraujagyslių sistemos ligų prognozavimas, norint efektyviai gydyti pacientus, yra pagrindinė visuomenės sveikatos problema[5,6,7,8,9]. Aterosklerozė, užslėptas, patologinis mechanizmas, yra lėtinė ir sisteminė kraujagyslių liga, dažnai vadinama „tyliuoju žudiku“, nes jos progresavimas ir raida yra nepaprastai sudėtingi ir gana nenuspėjami, lemiantys nepaprastai daug mirtimi pasibaigiančių atvejų, įvykusių be jokio įspėjamojo ženklo[10]. Apskritai, aterosklerozinіai pažeidimai ilgainiui yra nepastebimi, tačiau bendrieji šios ligos požymiai išryškėja tik prasidėjus komplikacijoms, tokioms kaip *intima-media* komplekso sustorėjimas, spindžio susiaurėjimas ar trombozė ir (arba) elastingumo sumažėjimas [11]. Aterosklerozė sukelia periferinių arterijų ligas, insultą, širdies priepuolius, ir visa tai vadinama ŠKL, o miokardo infarktas ir insultas apibūdinami kaip paskutinė aterosklerozės stadija [12].

Arterijos standumas yra nepriklausomas širdies ir kraujagyslių ligų požymis, analizuojamas siekiant įvertinti ŠKL riziką [13,14,15]. Klinikinėje praktikoje dažniausiai naudojami rizikos žymenys arterijos standumui vertinti yra *intima-media* komplekso storis, pulso bangos greitis ir skersinis išsitempimas (angl. *cross-sectional* distensibility) [16,17,18,19]. Deja, bet šių tradicinių rizikos žymenų, kaip atrankos testo, klinikinis potencialas tebėra ribotas [20]. Sunku įvertinti ŠKL riziką pacientams iki 50 metų, ypač jei nėra specifinių, individualių ŠKL rizikos veiksnių ar anamnezės. Todėl yra sudėtinga įvertinti ligos išsivystymo tikimybę ir prireikus pradėti gydymą vaistais [13].

Nepaisant to, yra įrodyta, kad mechaniniai pokyčiai, t. y. išilginis ir skersinis arterijos sienelės judėjimas, atsiranda daug anksčiau nei reikšmingi arterijos sienelės anatominiai pokyčiai, t. y. *intima-media* komplekso sustorėjimas [12]. Skersinis judėjimas yra parametras, apibūdinantis arterijų sienelių mechanines savybes, ir pastaraisiais metais buvo plačiai ištirtas. Tampantis informatyviu, neinvaziniu parametru, skersinis judesys padeda ištirti ŠKL ir nustatyti arterijų sienelių elastingumą. Išilginis judesys tokio pripažinimo nesulaukė, priešingai nei skersinis arterijos sienelės judėjimas. Palyginti su skersiniu judesiu, buvo manoma, kad išilginis judesys širdies ciklo metu yra neryškus. Tačiau naudojant šiuolaikinius ultragarsinius skenerius buvo pastebėta, kad širdies ciklo metu *intima-media* kompleksas juda ne tik skersine, bet ir išilgine kryptimi [21,22]. Taip pat buvo pastebėta, kad skersinio ir išilginio arterijos sienelės judesio amplitudės yra vienodos ir siekia maždaug vieną milimetrą [23]. Be to, klinikiniai tyrimai susiejo bendrosios miego arterijos išilginį

judesį su rizikos veiksniais ir ŠKL [24,25]. Ankstesni tyrimai parodė ryšį tarp arterijos standumo, ŠKL ir išilginio judesio sumažėjimo [12]. Nors ir išilginio judesio amplitudė yra susijusi su ŠKL, veiksniai, lemiantys išilginio judesio fazes, lieka nežinomi [16].

ŠKL rizikos vertinimo kontekste arterijos audinio judėjimas širdies ciklo metu yra svarbus, nes mechaninė deformacija atspindi kraujagyslių elastingumą ir yra atvirkščiai susijusi su arterijos standumu, kaip nepriklausomu sergamumo ir mirtingumo rodikliu [26]. Arterijos audinio judėjimas širdies ciklo metu susideda iš skersinio (arterijos sienelės judėjimo statmeno kraujotakai), išilginio (*intima-media* komplekso judesio lygiagrečiai kraujo tėkmei) judesių ir žiedinio įtempio. Taikant keletą judesio sekimo metodų, arterinio audinio judėjimas iš ultragarsinių radiodažninių signalų ar vaizdų sekų buvo išanalizuotas ir apibendrintas Rizi ir kt. [27].

Šiuo metu esamus ultragarsinės elastografijos metodus galima suskirstyti į dvi pagrindines grupes pagal išmatuojamą fizinį dydį: 1) įtempių vizualizavimas, 2) šlyties bangos vizualizavimas [28]. Abi šios metodų grupės naudoja išorinį spaudimo šaltinį. Nepaisant to, vidinis deformacijų šaltinis, arba vadinamasis endogeninis judesys, kurį sukelia širdies plakimas ir kraujagyslių veikla, gali būti naudojamas elastingumui matuoti [29,30,31].

Metodai, pagrįsti endogeniniu judesio detektavimu, klinikinėje praktikoje šiuo metu nėra taikomi. Pirma, šie metodai turėtų būti kruopščiai išstudijuoti ir ištirti. Dėl to būtų galima naudoti kompiuterinį ultragarsinį vizualizavimą ultragarsiniams radiodažniniams signalams ar B režimo vaizdams simuliuoti naudojant tam skirtus algoritmus. Populiariausi simuliavimo programinės įrangos paketai [32,33,34] yra CREANUIS [35] (paremtas Chochlovo, Zabolotskajos ir Kuznecovo lygtimi), skirtas netiesiniam sklidimui ir harmoniniam vizualizavimui simuliuoti, ir Field II [36] (pagrįstas Huygenso principu ir hibridiniu skaitmeniniu-analitiniu metodu), kuris įgijo platų pritaikomumą nuo modelio paskelbimo 1991 m. [37] ir programinės įrangos paketo 1996 metais [38]. Field II populiarumas yra dėl didelio lankstumo pritaikyti šią simuliuoti skirtą programą plačiam spektrui keitiklių, spindulio formavimo pasirinkimo ir vaizdavimo pasirinkimo galimybių. Tai vis dar galingas ir besivystantis įrankis, skirtas įvairiems skenavimo ir fokusavimo būdams simuliuoti, taip pat, kaip ir visam echoskopijos mechanizmui, įskaitant sklaidą audiniuose ir organuose [39]. Nors yra daug Field II pritaikymų, aprašytų begalėje straipsnių, tačiau tik keliose publikacijose kalbama apie kiekybinį simuliavimo ir eksperimento palyginimą įvertinant neapibrėžtis [40,41].

Miego arterijos sienelės judesys buvo modeliuojamas daugelio autorių. Gemignani ir kt. [42] simuliavo skersinį judesį kaip pjūklo funkciją, o Solomon ir kt. [43] kaip trikampio funkciją. Kaip skelbia Deng ir kt. [44], jie pasiūlė bendros miego arterijos geometrinį modelį, kur dinaminis atspindėtuvų modelis yra sukonstruojamas keičiant atspindėtuvų padėtį pagal sintezuotą pulso bangą. Pastaroji apskaičiuojama pagal kraujagyslės sienelės *in vivo* radiodažninius signalus naudojant 1D normalizuotos kryžminės koreliacijos algoritmą, paremtą aido sekimu. Judėjimui skersine kryptimi Hu ir kt. [45] pasiūlė izotropinį pulso modelį, kurio elastingumas apibūdinamas ryšiu tarp skersinio poslinkio ir kraujo spaudimo. Tačiau nė viename iš

ankstesnių tyrimų nenagrinėjamas išilginis arterijos judėjimas kartu su skersinio ir išilginio judesių slopimu gilyn į audinius. Tai padarė Stoitsis ir kt. [46], simuliuodami skersinį judėjimą kaip impulso funkciją, kurios parametrų vertės buvo nustatytos remiantis eksperimentais su *in vivo* duomenimis. Išilginis judesys buvo modeliuojamas kaip sinuso funkcija, nes nėra galutinės informacijos apie šio judesio matematinį modeliavimą. Remiantis panašiu *in vivo* tyrimu, taip pat buvo įtraukta skersinio ir išilginio judesių amplitudės erdvinė priklausomybė, kuri yra nepriklausoma nuo ašinės padėties.

Išilginis judesys, naujas, neinvazinis elastingumo matavimo parametras, vis dar nėra iki galo išnaudotas vertinant širdies ir kraujagyslių riziką, todėl jis turi daug potencialo. Be to, kompiuteriniam ultragarsiniam vizualizavimui turi būti atliekamas kiekybinis simuliavimo ir eksperimento palyginimas įvertinant neapibrėžtis prieš simuliuojant ultragarsinius radiodažnius signalus ar B skenavimo vaizdus, siekiant sukurti endogeninio judesio detektavimo metodus. Visi šie faktai kelia mokslinę-technologinę problemą ir darbo hipotezę.

Mokslinė-technologinė problema ir hipotezė

Metodai, paremti endogeniniu judesio detektavimu, šiuo metu nėra taikomi klinikinėje praktikoje. Pirmiausia, prieš pradedant šiuos metodus plačiai naudoti, jie turi praeiti tris „žingsnius“, tai: 1) metodo testavimas *in silico*, siekiant suprasti, sukurti ir patikrinti metodą, 2) bandymai *in vitro*, siekiant optimizuoti, dar kartą patikrinti ir patvirtinti bandymų rezultatus, ir galiausiai 3) atestacija *in vivo*, siekiant patikslinti ir patvirtinti siūlomo metodo patikimumą. Taigi, egzistuoja neišspręsta mokslinė problema: kaip nustatyti judesio sekimo algoritmų tikslumą prieš taikant metodus, paremtus endogeninio judesio sekimu, klinikinėje praktikoje?

Darbinė hipotezė teigia, kad kompiuterinis ultragarsinis vizualizavimas ir skaitmeninis 3D arterijos modelis gali būti naudojami nustatant judesio sekimo algoritmų tikslumą detektuojant audinių endogeninius mikroposlinkius, daugiausia sukeliamus kraujo pulsacija kraujagyslėse, kurie yra susiję su audinių elastingumo (ar standumo) įvertinimu ir ankstyva aterosklerozės diagnostika. Darbinė hipotezė yra patvirtinta skersiniam ir išilginiam judesiui detektuoti skirtų judesio sekimo metodų tikslumo tyrimo rezultatais.

Tyrimo objektas

Tyrimas pagrįstas bendrosios miego arterijos sienelės judesio simuliavimo algoritmų, skirtų ankstyvai aterosklerozės diagnostikai, kūrimu ir tyrimu.

Darbo tikslas

Šios daktaro disertacijos darbo tikslas yra sukurti ir ištirti ultragarsiniais radiodažniniais signalais paremtus algoritmus bendrosios miego arterijos sienelės judesių simuliavimui, susijusiam su ankstyva aterosklerozės diagnostika.

Tikslui pasiekti iškelti darbo uždaviniai

1. Sukurti ir ištirti virtualų skenavimo simuliavimą, atitinkantį fizinį ultragarsinį skenavimą.
2. Sukurti 3D arterijos modelį, gebantį atkurti žmogaus bendrosios miego arterijos biomechaninę elgseną ir tinkamą ultragarsiniams radiodažniniams signalams simuliuoti.
3. Ištirti ir įvertinti siūlomų judesio detektavimo algoritmų tikslumą naudojant simuliuotus bendrosios miego arterijos ultragarsinius radiodažninius signalus.
4. Ištirti galimybę diferencijuoti arterijas pagal judesio slopimo profilius.
5. Surinkti sveikų savanorių ir pacientų, kuriems yra padidėjusi rizika susirgti širdies ir kraujagyslių ligomis, ultragarsinius radiodažninius duomenis, ištirti ir palyginti judesio parametrus tarp dviejų skirtingų grupių.

Mokslinis naujumas

Šioje daktaro disertacijoje buvo atliktas kiekybinis skiriamumo neapibrėžčių, kylančių taikant skaitmeninį linijinį skenavimo simuliavimą naudojant Field II, vertinimas ir jų palyginimas su fizinio fantomo skenavimo rezultatais. Tai leidžia daryti išvadas apie kiekybines taško sklaidos funkcijos ir skiriamumo elevacijos plokštumoje neapibrėžtis naudojant standartinius fantomus.

Buvo sukurtas dinaminis 3D arterijos modelis, gebantis atkurti realistiškus ir dinaminius pulsuojančios žmogaus arterijos, apsuptos viskoelastinio audinio, radiodažninius signalus.

Praktinė darbo vertė

Kiekybinis ultragarsinis vizualizavimas leidžia simuliuoti neapdorotus radiodažninius signalus, atitinkančius tuos, kurie gaunami realaus ultragarsinio skenavimo metu.

Pasiūlytas dinaminis 3D arterijos modelis leidžia simuliuoti 3D deformacijos elastografiją, kurti ir verifikuoti elastografijos algoritmus, 3D elastografijos eksperimentus ir galimybių studijas.

Šioje disertacijoje pateikti metodai buvo sukurti ir taikyti gavus šio projekto paramą: Lietuvos mokslo tarybos finansuojamas mokslininkų grupių projektas *Ultragarsinės radiodažninės deformacinės elastografijos algoritmų tyrimas* (ELASTUS) – Nr. S-MIP-19-8, 2019-2022 m.

Ginti teikiami teiginiai

1. Sukurtas virtualus skenavimo simuliavimas, atitinkantis fizinį ultragarsinį skenavimą. Skaitmeninis skenavimas rodo gerą sutapimą su fiziniu: neatitikimas tarp taško sklaidos funkcijų pločių pusės lygyje ašine ir šonine kryptimis yra atitinkamai mažesnis nei 12 % ir 16 %.
2. Buvo sukurtas 3D arterijos modelis, gebantis atkurti žmogaus bendrosios miego arterijos biomechaninę elgseną ir tinkamas ultragarsiniams radiodažniniams signalams simuliuoti. Echoskopijos simuliavimas rodo,

kad arterijos modelis atvaizduoja A, B ir M režimo vaizduose arterijos struktūrą, tokią kaip ir *in vivo* arterijos sienelė. Įvertinti vienalaikiai, virtualiai nuskenuotos 3D struktūros skersinis ir išilginis judesiai vizualiai beveik nesiskiria nuo sugeneruoto judesio šablono.

3. Ištirtas siūlomų judesio detektavimo algoritmų tikslumas naudojant simuliuotus bendrosios miego arterijos ultragarsinius radiodažninius signalus. Rezultatai rodo, kad skersinių ir išilginių judesių detektavimo tikslumui vertinti skirtų parametrų įvairovė gali įvertinti ne tik klaidą, bet ir skirtumus tarp apskaičiuotų ir teorinių judesio signalų.
4. Ištirta galimybė diferencijuoti arterijas pagal judesio slopimo profilius. Rezultatai rodo, kad skersinių ir išilginių judesių slopimo profilių įvairovė, apibrėžianti skirtingo elastingumo audinius, gali būti naudojama sveikiems tiriamiesiems ir rizikos grupei priklausantiems pacientams diferencijuoti.
5. Surinkti sveikų savanorių ir pacientų, kuriems yra padidėjusi rizika susirgti širdies ir kraujagyslių ligomis, ultragarsiniai radiodažniniai duomenys, apskaičiuoti dviejų skirtingų populiacijų judesio parametrai ir įvertinta šių parametrų diagnostinė geba diagnozuoti, ar pacientai serga ateroskleroze, ar ne. Didžiausiu jautrumu iš pasiūlytų laiko ir dažnio srities parametrų pasižymėjo poslinkis, t. y. 0,77, ir spektrinė sklaida, t. y. 0,86. Greitis ir spektrinis centroidas priskirti kaip parametrai, pasižymintys didžiausiu specifiškumu, ir atitinkamai lygūs 0,88 ir 0,71.

Rezultatų aprobavimas

Disertacijoje pateikti rezultatai buvo publikuoti devyniuose mokslo darbuose, iš kurių penki straipsniai buvo paskelbti užsienio leidyklų leidžiamuose Mokslinės informacijos instituto pagrindinio sąrašo leidiniuose, turinčiuose citavimo indeksą. Rezultatai buvo pristatyti dviejose tarptautinėse ir vienoje nacionalinėje mokslinėje konferencijoje: *World Congress on Medical Physics and Biomedical Engineering* (IUPESM 2018), 2019 *IEEE International Ultrasonics Symposium* (IUS), ir Bioateitis: gamtos ir gyvybės mokslų perspektyvos 2019. 2020 m. gauta Lietuvos mokslo tarybos skirta stipendija. 2019 ir 2020 m. buvo gautos KTU skirtos doktorantų skatinamosios stipendijos už pasiekimus.

Disertacijos struktūra

Disertaciją sudaro įvadas, trys skyriai, baigiamosios išvados, santrauka, literatūros sąrašas, autoriaus publikacijų ir konferencijų sąrašas bei du priedai. Darbą sudaro 152 puslapių, 54 paveikslai, 4 lentelės, 21 formulė ir 175 literatūros šaltiniai. Darbo turinys yra išdėstytas taip: pirmame skyriuje aprašoma bendrosios miego arterijos anatomija ir histologija, išilginis arterijos sienos judėjimas, pasiūlyti skaitmeniniai arterijų modeliai, atitinkamas realios ultragarsinės echoskopijos simuliavimas ir arterijos sienelės judesio sekimo algoritmai. Antrame skyriuje pateikiamas ultragarsinis bendrosios miego arterijos tyrimas, išvystytas fizinio ultragarsinio skenavimo skaitmeninis simuliavimas ir verifikavimas, sukurtas skaitmeninis arterijos modelis ir išplėtoti ultragarsinių radiodažninių signalų

apdorojimo algoritmai. Trečiame skyriuje pateikiami eksperimentiniai modeliavimo, judesio detektavimo tikslumo ir skersinio *in vivo* judesio parametrizavimo rezultatai. Ketvirtas skyrius skirtas baigiamosioms išvadoms.

1. BENDROSIOS MIEGO ARTERIJOS JUDESIŲ IR JUDESIO SEKIMO METODŲ APŽVALGA

Bendroji miego arterija yra kaklo srityje ir patenka į miego arterijos trikampį, kurį riboja priekinis galvos sukamojo raumens kraštas, užpakalinis dvipilvio raumens pilvelis ir viršutinis mentinio poliežuvio raumens pilvelis [47].

Bendrosios miego arterijos sienelė sudaryta iš trijų sluoksnių (žr. 1.1 pav.) [17,50]:

1. vidinio sluoksnio, vadinamo *tunica intima*.
2. vidurinio sluoksnio, vadinamo *tunica media*.
3. išorinio sluoksnio, vadinamo *tunica adventitia*.

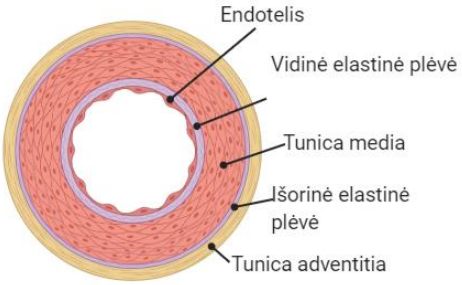

1.1 pav. Bendrosios miego arterijos struktūra

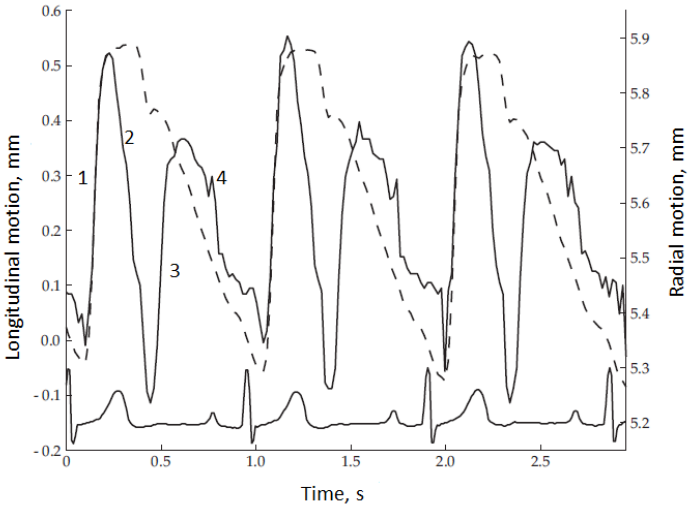

1.2 pav. Išilginio judesio (—), diametro kitimo (---) sąsaja su elektrokardiograma. Išilginio judesio būsena širdies ciklo metu pažymėta skaičiais (1,2,3,4). Išilginio judesio ir diametro pokyčio amplitudės yra tokios pačios. Tačiau, vis dar esant sistolei, išilginis judesys pasižymi aiškiu judesiu atgal (2) ir diastolės metu judesiu į priekį (3). Adaptuota iš [21]

Sistolės metu iš skilvelių išstumiamas kraujas ištempia kraujagyslių sieneles, o diastolės metu tamprios kraujagyslių sienelės pastumia kraują į periferiją ir sugrįžta į pradinę būseną. Nors skersinis arterijų išsiplėtimas sukelia pulsuojantį kraujo srautą,

dauguma arterijų (pakinklinė arterijos, žastinė, miego) juda išilgai lygiagrečiai su kraujo srautu, kuris apibūdina kraujagyslių elastingumą.

Dvikryptis *intima-media* komplekso išilginis judėjimas pastebimas širdies ciklo metu (žr. 1.2 pav.). Sistolės pradžioje *intima-media* kompleksas juda kraujo srauto kryptimi (1). Vėliau, vis dar esant sistolei, šio komplekso judėjimas vyksta prieš kraujo srauto kryptį (2). *Intima-media* kompleksas dar kartą juda į priekį diastolės metu (3) ir galiausiai grįžta į pradinę padėtį (4).

Cinthio ir kt. [21] kartu su Nillson ir kt. [51] paskelbė, kad arterijos sienelės *adventitia* sluoksnio išilginio judesio šablonas tas pats, tačiau judesio dydis yra mažesnis nei *intima-media* komplekso, kas parodė anksčiau nežinomą ryškų šlyties įtempį, taigi šlyties deformaciją, vykstančią pačioje arterijos sienelėje.

Vėliau šis fenomenas Zahnd ir kt. [52] buvo pavadintas išilgine kinetika (LOKI), kai širdies ciklo metu *intima-media* kompleksas juda *adventitia* sluoksnio atžvilgiu lygiagrečiai su kraujo srautu, ir tai sukelia arterijų sienelių šlyties deformaciją (žr. 1.3 pav.). Dėl to pastebimas šlyties įtempis ir šlyties deformacija tarp *intima-media* komplekso ir *adventitia* sluoksnio. Tyrimai parodė, kad arterijų standumą ir širdies bei kraujagyslių rizikos veiksnių buvimą atspindi išilginės kinetikos parametras [21,52].

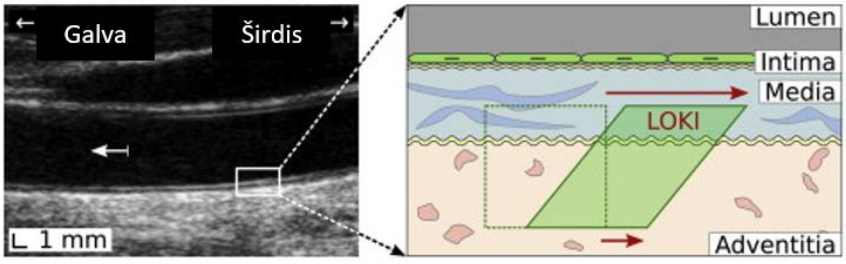

1.3 pav. Išilginis *in vivo* sveikos bendrosios miego arterijos ultragarsinis B-režimo vaizdas (*kairėje*). Balta rodyklė vaizduoja kraujo tėkmės kryptį. Išilginė kinetika, įvykstanti arterijos sienelėje širdies ciklo metu (*dešinėje*). Atkreipkite dėmesį, kad audinio judėjimo šablonas širdies ciklo metu yra daugiafazis ir dvikryptis. Šaltinis: Zahnd ir kt. [52]

Miego arterijos sienelės judesys buvo modeliuojamas daugelio autorių. [42][43][44][45]. Tačiau nė viename iš ankstesnių tyrimų nenagrinėjamas išilginis arterijos judėjimas kartu su skersinio ir išilginio judesių slopimu gilyn į audinius. Tai padarė Stoitsis ir kt. [46] simuliuodami skersinį judėjimą kaip impulso funkciją, kurios parametrų vertės buvo nustatytos remiantis eksperimentais su *in vivo* duomenimis. Išilginis judesys buvo modeliuojamas kaip sinuso funkcija, nes nėra galutinės informacijos apie šio judesio matematinį modeliavimą. Remiantis panašiu *in vivo* tyrimu, taip pat buvo įtraukta erdvinė skersinio ir išilginio judesių amplitudes priklausomybė, kuri yra nepriklausoma nuo ašinės padėties.

Kadangi skaitmeninė simuliacija tampa vis svarbesnė ultragarsinio vizualizavimo ir elastografijos raidai, vis dėlto problema yra kiekybinis neapibrėžtumų, susijusių su simuliavimo proceso komponentais, įvertinimas. Be to, kiekybinis simuliavimo palyginimas su eksperimentiniu skenavimu, įskaitant skiriamosios gebos analizę ašine, šonine ir elevacijos kryptimis, tebėra ribotas.

Skersiniam ir išilginiam judesiui detektuoti siūlomi blokų tapatinimo, optinės tėkmės, požymių atitikimo algoritmai. Kai kurie iš jų yra laisvai (CAROLAB [133]) ar komerciškai (MyLab [133]) prieinami išilginiam judesiui tirti. Bet šiuo metu nė vienas iš jų netaikomas klinikinėje praktikoje. Pirmiausia šie metodai turėtų būti detaliai ištirti prieš juos pradedant plačiai naudoti.

2. PLĖTOJAMI ARTERIJOS IR APLINKINIŲ AUDINIŲ PULSAVIMO SIMULIAVIMO METODAI BEI JUDESIO DETEKTAVIMO TIKSLUMO VERTINIMAS

2.1. Bendrosios miego arterijos ultragarsinis tyrimas

Bendrosios miego arterijos skenavimas buvo atliekamas „Ultrasonix SonixTouch“ echoskopu („Analogic Ultrasound“, Kanada) naudojant linijinę gardelę. Pagrindiniai ultragarsinio keitiklio ir duomenų surinkimo parametrai buvo tokie: bangų dažnis 13,3 MHz, fokusavimo atstumas 1,5 cm, skenavimo gylis 2,5 cm, kadrų dažnis 52 Hz, kadrų skaičius 629, vaizdą sudarančių echoskopinių linijų skaičius 640, skenavimo sektorius 50 %, radiodažninio signalo diskretizavimas 40 MHz, ultragarso bangų greitis – 1540 m/s.

Trisdešimt jaunų sveikų savanorių (dvidešimt viena moteris, devyni vyrai) ir dvidešimt aštuoni vyresni, rizikos grupei sirgti širdies ir kraujagyslių ligomis priklausantys pacientai (dešimt moterų, aštuoniolika vyrų) buvo įtraukti į tyrimą. Ultragarsinių radiodažninių signalų ir B režimo vaizdų sekos buvo surinktos Lietuvos sveikatos mokslų universiteto ligoninėje Kauno klinikose, Kardiologijos skyriuje, 2018 m. gegužės–spalio mėnesiais. Tyrimai atlikti gavus Kauno regioninio biomedicininių tyrimų etikos komiteto bioetikos leidimą (2018-08-02, No. BE-2-51, Kaunas, Lietuva).

Du kardiologai atliko bendrosios miego arterijos skersinio ir išilginio judesių ultragarsinių radiodažninių signalų ir B režimo vaizdo sekų registravimą. Išilginių ir skersinių judesių bent per du širdies ciklus registravimas buvo atliekamas 2–3 cm nuo bifurkacijos. Siekiant išvengti judesio artefaktų, ultragarsinis keitiklis buvo įtvirtintas į stacionarų laikiklį, o duomenų registravimo metu pacientų buvo prašoma sulaikyti kvėpavimą apie 10–15 sekundžių [16,19,21,25]. Galiausiai visos sekos buvo saugomos skaitmeniniu būdu ir perkeltos į kompiuterį toliau analizuoti naudojant MATLAB R2018b („The MathWorks“, Inc., Natick, JAV). Duomenų kokybiškumo įvertinimas buvo atliktas remiantis vienos ultragarsinės echoskopinės eilutės atvaizdavimu M-režime (žr. 2.1 pav.), kai aiškiai matosi, kuris laiko intervalas yra sugadintas judesio artefaktų, kuris intervalas yra kokybiškas ir kiek pastarajame intervale yra pilnų pasikartojančių širdies ciklų.

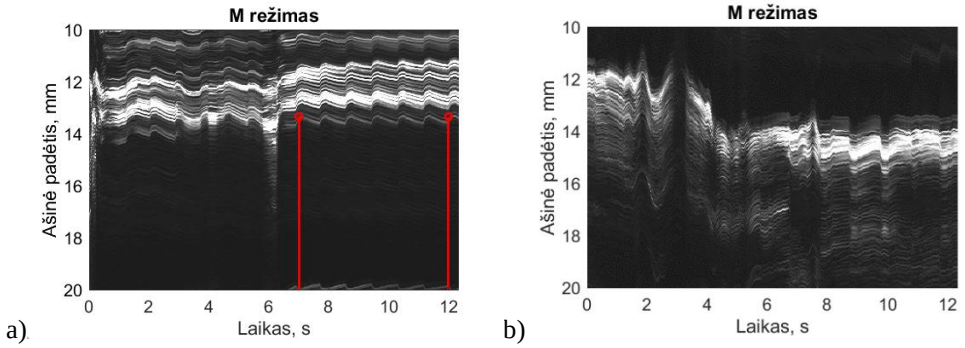

2.1 pav. Bendrosios miego arterijos aukštos kokybės duomenų (a) palyginimas su žemos kokybės duomenimis (b). Raudonais žymekliais (a) pažymėtas laiko intervalas, kuris buvo naudojamas tolimesnei analizei

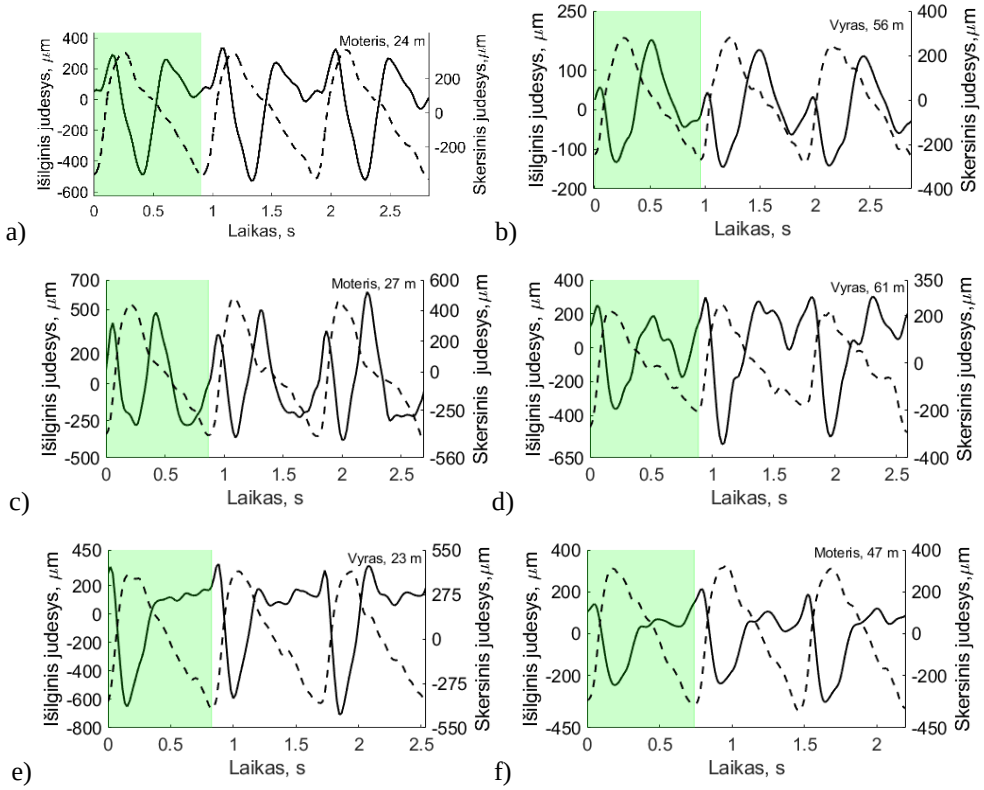

2.2 pav. *In vivo* skersinis (*punktyrinė linija*) ir išilginis (*ištisinė linija*) bendrosios miego arterijos judesiai skirtingo amžiaus tiriamiesiems, parodant skirtingus išilginio judesio šablonus: a), c), e) jaunas tiriamasis, b), d), f) rizikos grupės pacientas. Žaliai pažymėti periodai buvo naudojami modeliuojant arterijos ir audinių pulsaciją

Po vizualinės užregistruotų duomenų patikros aštuoni sveiki savanoriai ir keturi rizikos grupės pacientai nebuvo įtraukti į tyrimą, o kiekvieno tiriamojo kokybiniai laiko intervalai rankiniu būdu buvo atrikti tolesnei analizei atlikti.

Surinkti *in vivo* duomenys buvo apdoroti CAROLAB programa, kuri įvertino išilginį bei skersinį arterijos judesius. Įvertintuose judesio signaluose rankiniu būdu buvo pažymėti trys vienas po kito sekantys širdies ciklai (žr. 2.2 pav.). Tačiau tik vienas širdies ciklas buvo naudojamas modeliuojant judesį, ypač kai kiti periodai yra kvaziperiodiniai su širdies ciklu.

2.2. Fizinio ultragarsinio skenavimo skaitmeninio simuliavimo modeliavimas ir verifikavimas

Skaitmeninis keitiklis buvo modeliuojamas Field II programa [36,142] Siekiant gauti adekvatumą tarp eksperimento ir simuliavimo rezultatų, buvo identifikuojami fizinio ultragarsinio skenerio ir keitiklio parametrai ir suvedami į Field II programą (žr. 2.1 lentelę).

2.1 lentelė. Virtualaus skenavimo Field II parametrai

Parametrai	Vertės
Gardelės tipas	Linijinė
Keitiklio centrinis dažnis	5 MHz
Elementų skaičius	128
Elementų žadinimas	Dviejų periodų sinusinis signalas modeliuotas Hanning-o funkcija
Elemento aukštis	4 mm
Elemento plotis	0.279 mm
Tarpas tarp elementų	0.025 mm
Atstumas tar elementų centrų	0.304 mm
Elemento sub-dalinimas x-kryptimi	1
Elemento sub-dalinimas x-kryptimi	9
Elevacijos linzės fokusas	16 mm
Fokusas	15.5 mm
F-skaičius išsiuntime	3
F-skaičius priėmime	1.7
Apodizavimas	Hanningo funkcija
Diskretizacimo dažnis	40 MHz
Bangų greitis	1540 m/s
Nuo dažnio priklausantis slopinimas	0.5 dB/cm/MHz@ 3.5MHz

Norint tinkamai atlikti ultragarsinės skaitmeninės echoskopijos simuliavimą, reikia kiekybiškai įvertinti ir palyginti ją su fizine echoskopija. Ultragarsinio spindulio skiriamoji geba buvo vertinta pagal tris matmenis: ašinę, skersinę kryptis ir

ultragarsinio spindulio plotį. Taško sklaidos funkcijos plotis pusės lygyje buvo naudojamas vertinant skirtumą tarp fizinio ir skaitmeninio skenavimų.

Siekiant turėti vienodą B režimo vaizdo formavimą tiek fizinio, tiek skaitmeninio skenavimų metu, buvo pasirinkta vaizdo formavimą sudaryti iš radiodažninių signalų gaubtinės radimo ir log-suspaudimo nuo 0 iki -70 dB.

Eksperimento metu buvo naudojami du ATS „Laboratories Inc.“ fiziniai fantomai: 1. „Model 549 General & Small Parts“ fantomas [144] ašinei ir šoninei skiriamajai gebai, bei 2. „Model 538NH Beam Profile & Slice Thickness“ fantomas [145] spindulio pločiui elevacijos kryptimi įvertinti.

Modeliuojant skaitmeninius fantomus, 3D koordinačių sistemoje buvo nurodomos atspindėtuvų koordinatės, atspindėjimo amplitudės ir visą fantomą sudarančių atspindėtuvų skaičius. Atspindėtuvų skaičius skaitmeninių fantomų tūryje buvo nustatytas proporcingai išmatuotai fizinio ultragarsinio keitiklio skiriamumo celei [41] ir skaitmeninio fantomo tūriui. Atspindėtuvai buvo atsitiktinai paskirstę fantomo tūryje, amplitudės buvo pasiskirsčiusios pagal Gauso funkciją. Siekiant sumodeliuoti visiškai nusistovėjusį interferencijos rezultatą, atspindėtuvų skaičius skiriamumo celėje buvo lygus 10 [41,148,149]. Norint turėti adekvačias atspindžio signalo amplitudes simuliuojamame vaizde, modeliuojamų objektų (vielučių, plokštumos) amplitudės buvo normuojamos atitinkamai pagal realaus B režimo vaizdo fono atspindėtuvų amplitudes.

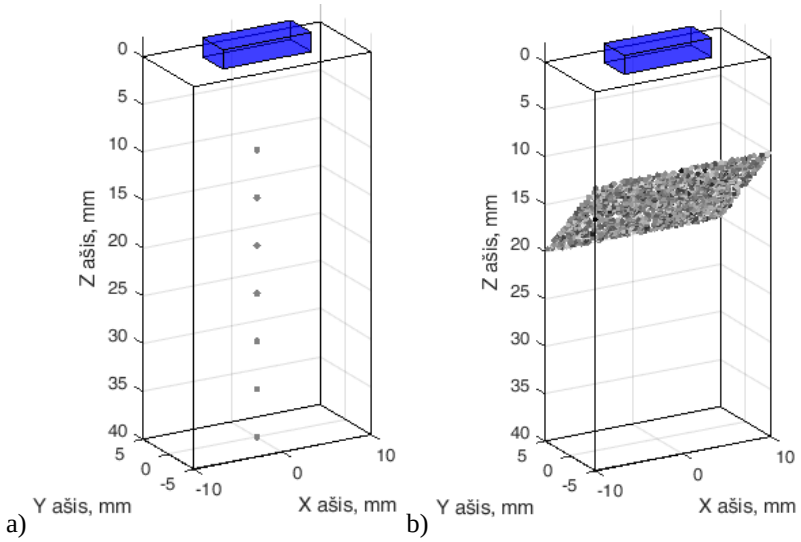

2.3 pav. Skaitmeninių fantomų konfigūracija: a) vielučių, b) spindulio pločio. Fantomų viršuje pažymėti stačiakampiai gretasieniai žymi skaitmeninio ultragarsinio keitiklio poziciją

2.3. Skaitmeninis arterijos modelis

Apibendrinta simuliavimo algoritmo eiga, pavaizduota 2.4 pav., parodo įvesties ir išvesties parametrus ir išryškina algoritmo gebėjimą modifikuoti įvesties parametrus, siekiant jį pritaikyti konkrečiai simuliavimo užduočiai.

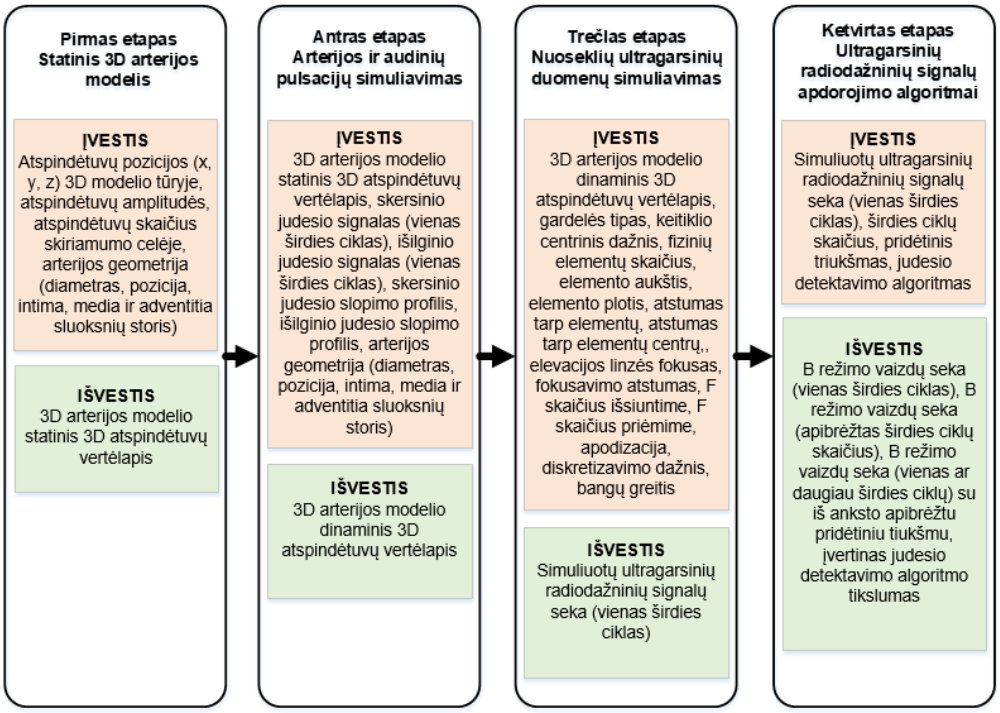

2.4 pav. Apibendrinta simuliavimo algoritmo eiga

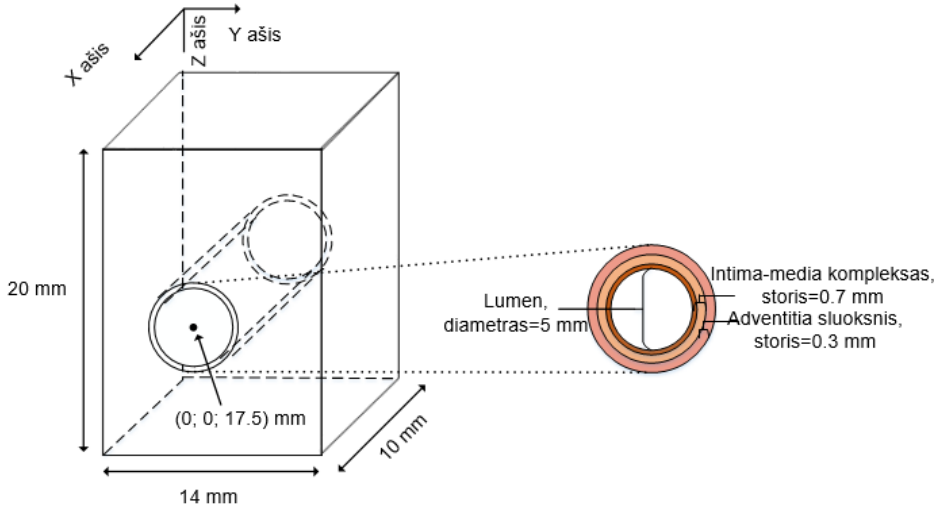

2.5 pav. Apibendrinta arterijos modelio geometrija

Pirmame etape arterija modeliuojama statiniu atspindėtuvų pasiskirstymu pagal *in vivo* arterijos geometriją, matmenis ir padėtį. Skaitmeninė arterija modeliuojama kaip trys koncentriniai vamzdžiai, kurie atitinka tris arterijos sienelės sluoksnius (žr. 2.5 pav.).

Modeliuojant skaitmeninę arteriją, 3D koordinačių sistemoje nurodomos atspindėtuvų koordinatės, atspindėjimo amplitudės ir visą modelį sudarančių atspindėtuvų skaičius. Atspindėtuvų koordinatės ir skaičius parinkti pagal metodiką, aprašytą 2.2 poskyryje, o atspindėtuvų amplitudės apskaičiuotos pagal realų bendrosios miego arterijos B-režimo ultragarsinį vaizdą. 3D arterijos modelio 3D atspindėjimo vertėlapis pateiktas 2.6 paveiksle.

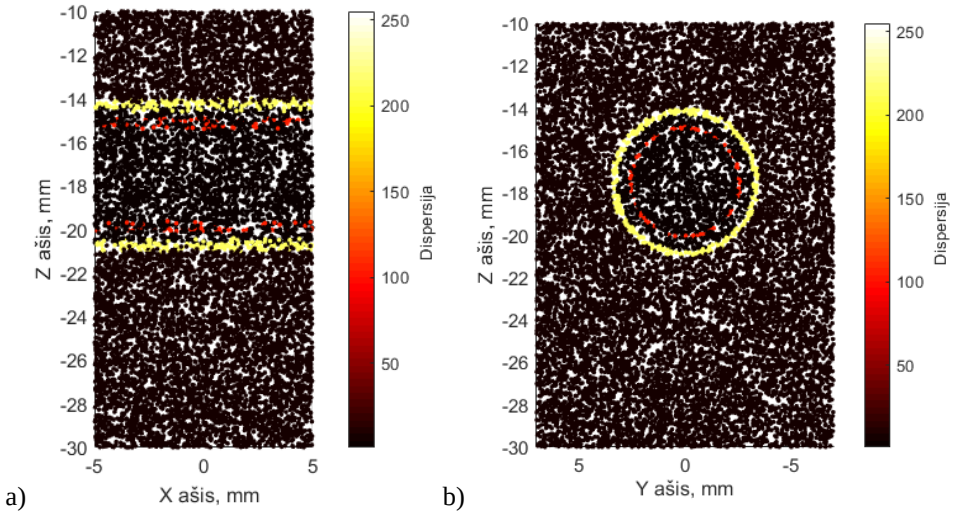

2.6 pav. 3D atspindėtuvų vertėlapis, atvaizduojantis arterijos modelį iš skirtingų projekcijų: a) išilginė, b) ašinė

Antrame etape statinis arterijos modelis modifikuojamas į dinaminį naudojant *in vivo* skersinius ir išilginius judesius (žr. 2.1 poskyris) 3D pasiskirsčiusiems arterijos atspindėtuvams. Simuliuoti pasirinktų parametrų vertės pateiktos 2.2 lentelėje.

2.2 lentelė. Arterijos modelio judesio modeliavimo parametrai

	Sveiki savanoriai	**Rizikos grupės pacientai**
Judesio signalo forma	žr. 2.2 pav. a), c), e)	žr. 2.2 pav. b), d), f)
Skersinių ir išilginių judesių amplitudės, µm	1000; 750; 500	750; 500; 250
Skersinio judesio slopimas b_1	0,17	0,26
Išilginio judesio slopimas b_2	1,08	1,62
Iš viso:	9 atvejai	9 atvejai

Kiekvienas arterijos ir jį supančių audinių pulsavimo simuliavimo žingsnis pateiktas funkcinėje schemoje 2.7 paveiksle.

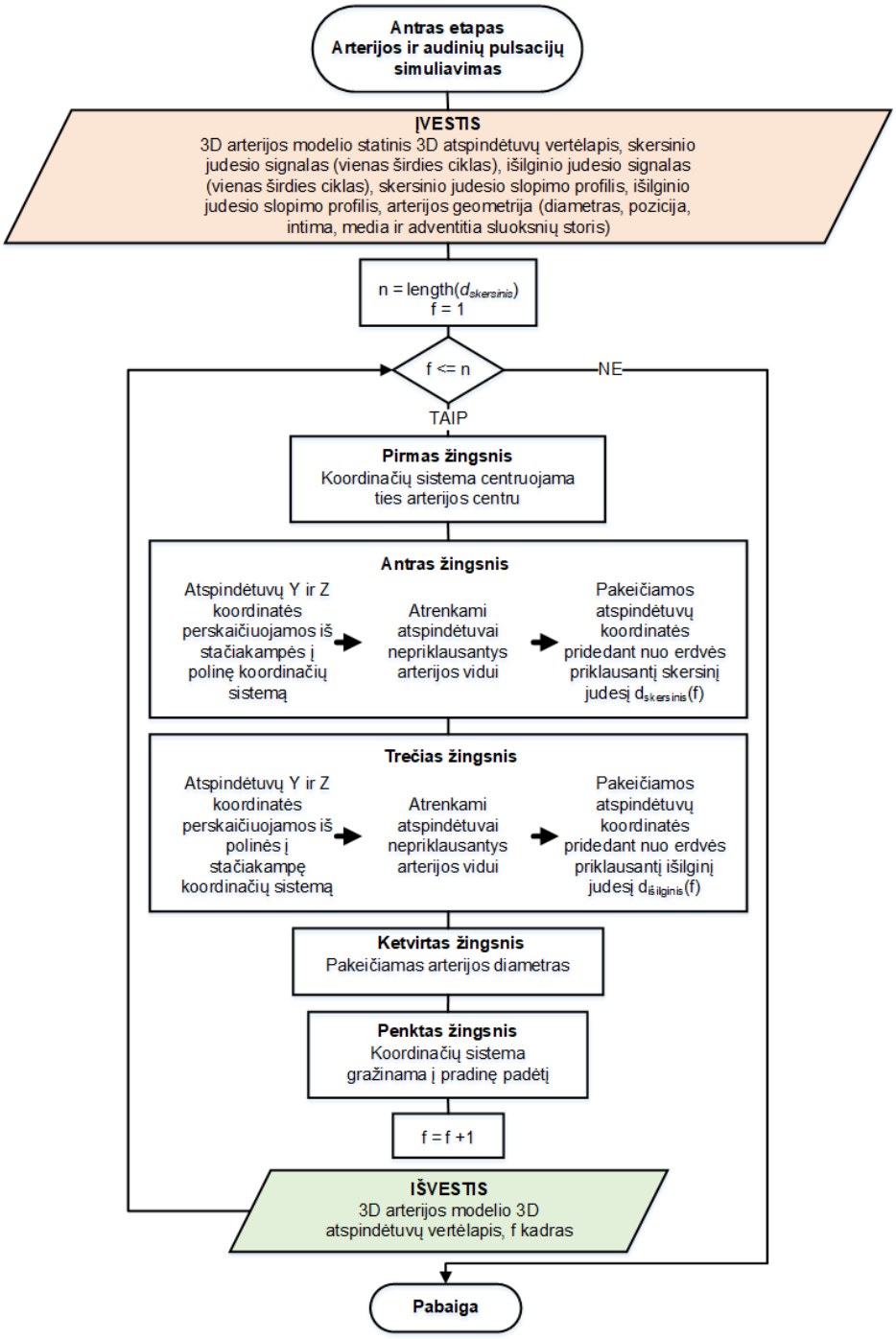

2.7 pav. Funkcinė antro etapo schema simuliuojant kompleksinę arterijos ir audinių pulsaciją. Čia *f* atitinka šiuo metu analizuojamą kadro skaičių judesio signale ir *n* – bendrą tokių kadrų skaičių

Judantys atspindėtuvai buvo naudojami vieno širdies ciklo ultragarsinių radiodažninių signalų sekai simuliuoti (trečias etapas).

Ketvirtame etape buvo atliekamas simuliuotų ultragarsinių radiodažninių signalų apdorojimas, judesio įvertinimas, judesio detektavimo rezultatų palyginimas su arterijos ir aplinkinių audinių pulsacijos atraminiais duomenimis, nustatytais antrame etape, ir santykinės judesio detektavimo klaidos įvertinimas. Judesiui detektuoti pasirinkta naudoti du algoritmus: 1. 1D kros-koreliacijos ir parabolinės interpoliacijos, 2. atviros prieigos „OpenOptikalFlow“ programą. Paklaidai tarp apskaičiuoto ir atraminio judesio įvertinti pasirinktas vidutinės absoliutinės paklaidos įvertis. Judesio detektavimo tikslumas buvo vertinamas vidurinėje echoskopavimo linijoje, esant įvairioms ašinėms padėtims (žr. 2.8 pav.), t. y. pradedant nuo 11 mm kas 1 mm iki 29 mm.

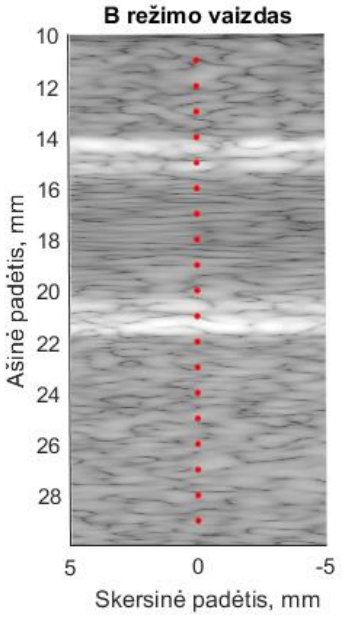

2.8 pav. Simuliuotas arterijos modelio B režimo vaizdas su pažymėtais raudonais taškais, kuriuose vertintas judesio aptikimo algoritmų tikslumas

Slopimo profilių vertinimas buvo atliktas su visais modeliuojamų duomenų atvejais. Vidutinės slopimo profilių vertės ir standartiniai nuokrypiai buvo apskaičiuoti kiekvienai iš anksto pasirinktai ašinei padėčiai (žr. 2.8 pav.).

2.4. Ultragarsinių radiodažninių signalų apdorojimo algoritmai

Atsikartojantys poslinkių signalo periodai buvo nustatomi skaičiuojant antrąją judesio signalo išvestinę (pagreičio signalą) ir ieškant pikų, nutolusių ne mažesniu nei 1 sekundės laiko atskaitos intervalu, kurių minimalus piko aukštis būtų 1/3 maksimalios pagreičio signale esančios vertės. Judesio signalas nuo pirmojo iki paskutiniojo pagreičio signale rasto piko buvo sudalytas į periodus, kurie sulygiuoti pagal diastolės momentus. Visų periodų ilgis buvo lygus trumpiausiam judesio signale

esančiam periodo ilgiui. Koreliuojantys periodai rasti skaičiuojant koreliacijos koeficientą tarp periodų ir taikant 0,95 slenkstį. Rasti koreliuojantys periodai vidurkinami laike ir gaunamas vidutinis judesio signalo periodas. Taikant Yule-Walker metodą, randamas judesio periodo spektras. Vidutiniam judesio periodui ir jo spektrui parametrizuoti buvo pasirinkti laiko ir dažnio srities parametrai, kurie pateikti 2.3 lentelėje.

2.3 lentelė. Laiko ir dažnio srities parametrai vidutinio judesio periodo signalui ir jo spektrui parametrizuoti

Laiko srities parametrai	**Dažnio srities parametrai (ribose nuo 0 Hz iki 10 Hz)**
• Širdies ritmas	• Spektrinis centroidas
• Judesio amplitudė	• Spektrinis sklaida
• Greičio amplitudė	• Spektrinis asimetrija
• Pagreičio amplitudė	• Spektrinis ekscesas

3. REZULTATAI

3.1. Skenavimo modelio pritaikymas fizinei taško sklaidos funkcijai

Modeliavimo adekvatumas priklauso nuo simuliuojamo ultragarso impulso formos atitikties eksperimentiškai išmatuotam impulsui. Tarpusavyje lygindami eksperimentinio ir simuliuojamo aido impulsų formą ir spektrus esant ultragarso bangos atspindžiui nuo vielutės, esančios 15 mm atstumu nuo keitiklio, matome santykinai gerą sutapimą (koreliacijos koeficientas tarp eksperimento ir simuliacijos aido impulsų yra 0,91, tarp spektrų – 0,98), juolab kad rezultatui įtakos turi ultragarso bangos difrakcija ir kiti sklidimo efektai.

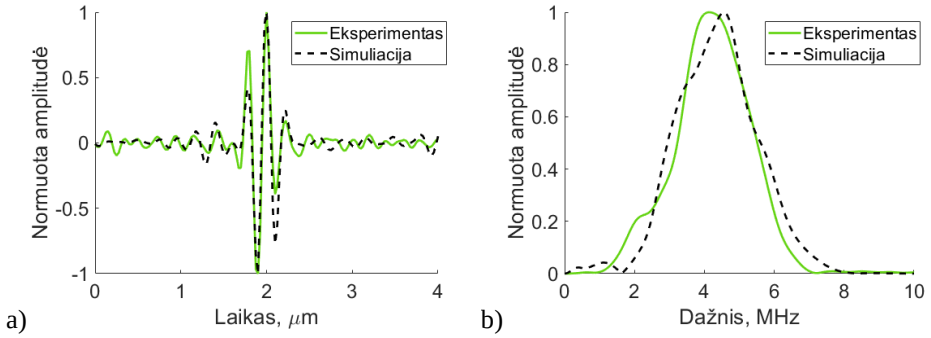

a) b)

3.1 pav. Eksperimento ir simuliacijos palyginimas: a) aido impulso signalai, atsispindėję nuo 15 mm gylyje esančios vielutės (ašinis vaizdas), b) aido impulso signalų spektrai

Kiekybiškai vertinant taško sklaidos funkcijos plotį gauta, kad vidutinė santykinė paklaida tarp eksperimento ir simuliavimo pagal ašinę ir skersinę skiriamąją gebą atitinkamai yra 11,6 % ir 15,2 % (žr. 3.1 lentelę).

3.1 lentelė. Eksperimento ir simuliavimo palyginimas

Eksperimentas				Simuliavimas					
Ašinė padėtis, mm	Skersinė padėtis, mm	Ašinė skyra, mm	Skersinė skyra, mm	Ašinė padėtis, mm	Skersinė padėtis, mm	Ašinė skyra, mm	Skersinė skyra, mm	**Ašinės skyros santykinė paklaida, %**	**Skersinės skyros santykinė paklaida, %**
9,8	-0,13	0,23	0,80	10,3	0,00	0,26	1,01	13,0	26,3
15,3	0,06	0,24	1,02	15,4	0,00	0,27	1,05	12,5	2,9
20,1	0,06	0,25	1,18	20,4	0,00	0,27	1,03	8,0	12,7
25,2	0,00	0,26	1,37	25,4	0,00	0,27	1,16	3,8	15,3
30,1	-0,06	0,24	1,46	30,4	0,00	0,29	1,29	20,8	11,6
35,6	-0,06	0,26	1,69	35,3	0,00	0,29	1,31	11,5	22,5
						Vidurkis, %		**11,6**	**15,2**

3.2 pav. parodyta, kad normuotos taško sklaidos funkcijos ašinis vaizdas geriau sutampa su eksperimentu nei šoninio vaizdo atveju. Tam įtakos turi sunkiai įvertinami apodizacijos, fokusavimo ir kiti ultragarso difrakcijos efektai.

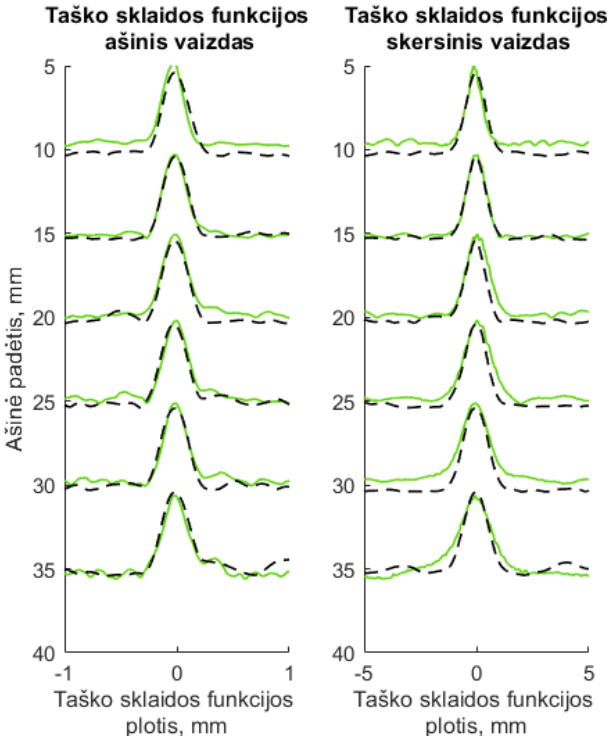

3.2 pav. Taško skaidos funkcijos pločio ašine ir skersine kryptimis palyginimas: ištisinė linija – eksperimentas, punktyrinė linija – simuliavimas. Taško skaidos funkcijos amplitudės normuotos nuo 0 iki 5

Ultragarsinio spindulio plotis pusės lygyje elevacijos plokštumoje (žr. 3.3 pav.) echoskopijos atveju buvo 1,21 mm, o simuliavimo atveju 1,38 mm.

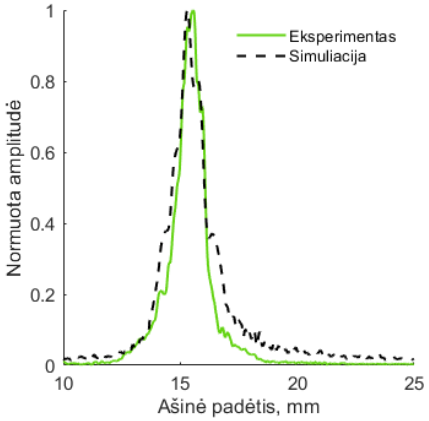

3.3 pav. Echoskopija ir simuliavimo elevacijos skiriamosios gebos palyginimas pagal iš šono vidurkintas skenavimo linijas

3.2. Arterijos modelio simuliuotų ultragarsinių radiodažninių signalų ir vaizdų rezultatai

Tarpusavyje lyginant eksperimentinius ir simuliuotus duomenis (žr. 3.4 pav.) gauta, kad A režimo atveju abiem atvejais aiškiai matyti aido impulsai nuo *lumen-intima* ir *media-adventitia* ribų, o B režimo atvejais arterijos sienelės matosi kaip dviguba linija. Taigi arterijos modelis pasižymi *in-vivo* arterijos sienelei būdinga struktūra.

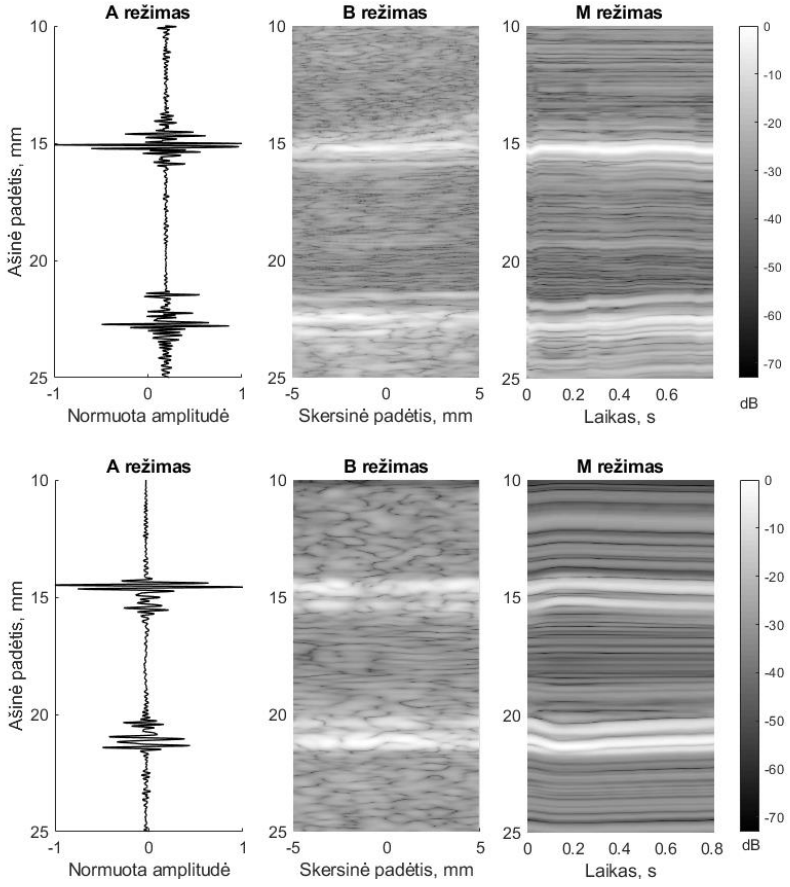

3.4 pav. Radiodažninių signalų formos palyginimas (A režimas, f_1 kadras, skersinė padėtis 0 mm), B režimo vaizdas (f_1 kadras), judesys laike (M režimas): a) *in vivo* atvejis (23 metų moteris, judesio amplitudė nenormuota), b) simuliuotas atvejis (23 metų moteris, judesio amplitudė normuota į 1 mm)

M režimo atveju pastebime arterijos modelio judėjimą pagal užduotą skersinio judesio signalą. Gauta, kad tiek apatinė, tiek viršutinė arterijos modelio sienelės juda pagal tą pačią judesio formą, tik priešingu ženklu. *In-vivo* atveju tokio vienodo abiejų sienelių judėjimo nematyti. Greičiausiai ultragarsinis keitiklis registravimo metu nebuvo visiškai tinkamai laikytas ties arterijos centru ir 90 laipsnių kampu į arteriją.

Taip pat neatmetama galimybė, kad registravimo metu ultragarsinis keitiklis buvo spaudžiamas į kaklą, ir tai neleido viršutinei arterijos sienelei judėti tokiu pat dėsniu, kaip apatinei.

Dinaminis 3D arterijos modelis turi panašius skersinių ir išilginių judesių šablonus, amplitudę ir slopimą gilyn į audinius, palyginti su teoriniais judesiais (žr. 3.5 pav.), nors apskaičiuota judesių amplitudė yra šiek tiek mažesnė nei teorinė.

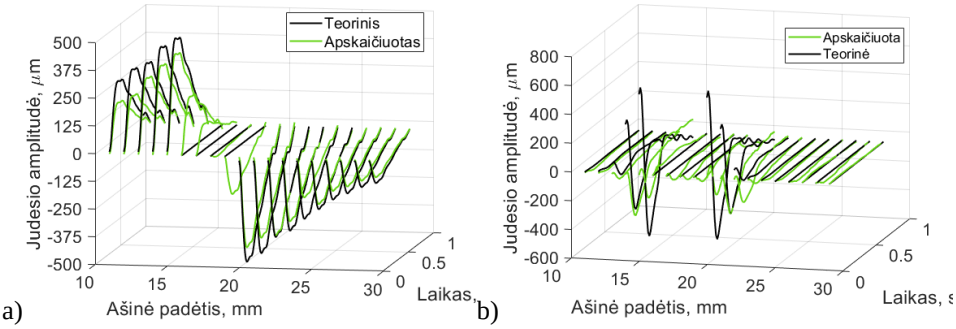

3.5 pav. Viršutinės ir apatinės arterijos sienelių ir aplinkinių audinių judesiai detektuoti su „OpenOpticalFlow“ algoritmu, 23 metų moteris: a) 1 mm amplitudės teorinis ir apskaičiuotas skersinis judesys, b) 1 mm amplitudės teorinis ir apskaičiuotas išilginis judesys

3.3. Skersinio ir išilginio judesių detektavimo metodų tikslumo tyrimo rezultatai

Vidutinės absoliutinės paklaidos analizė parodė, kad didelių klaidų pasitaiko, kai skersiniam judesiui aptikti naudojamas 1D kros-koreliacijos metodas, o judesio amplitudė buvo didesnė nei 0,75 mm (žr. 3.6 pav., a). Dideles paklaidas lėmė tai, kad tarpkadrinis judėjimas buvo didesnis nei ketvirtadalis bangos ilgio, dėl ko egzistuoja tikimybė nustatyti klaidingą koreliacijos piką, o tai lemia dideles dvireikšmiškumo klaidas. Nepaisant to, nustatyta, kad, esant didelėms skersinio judesio amplitudėms, medianinės vidutinės absoliutinės paklaidos vertės buvo mažesnės nei 25 µm tiriant „OpenOpticalFlow“ metodą.

Tiriant „OpenOpticalFlow“ metodo galimybę detektuoti išilginį judesį gauta, kad medianinės vidutinės absoliutinės paklaidos vertės yra mažesnės nei 25 µm (žr. 3.6 pav., b). Vertinant vidutinės absoliutinės paklaidos vidurkio vertes gauta, kad jos yra apie 50 µm ir turi tendenciją mažėti, kai detektuojama judesio amplitudė mažėja.

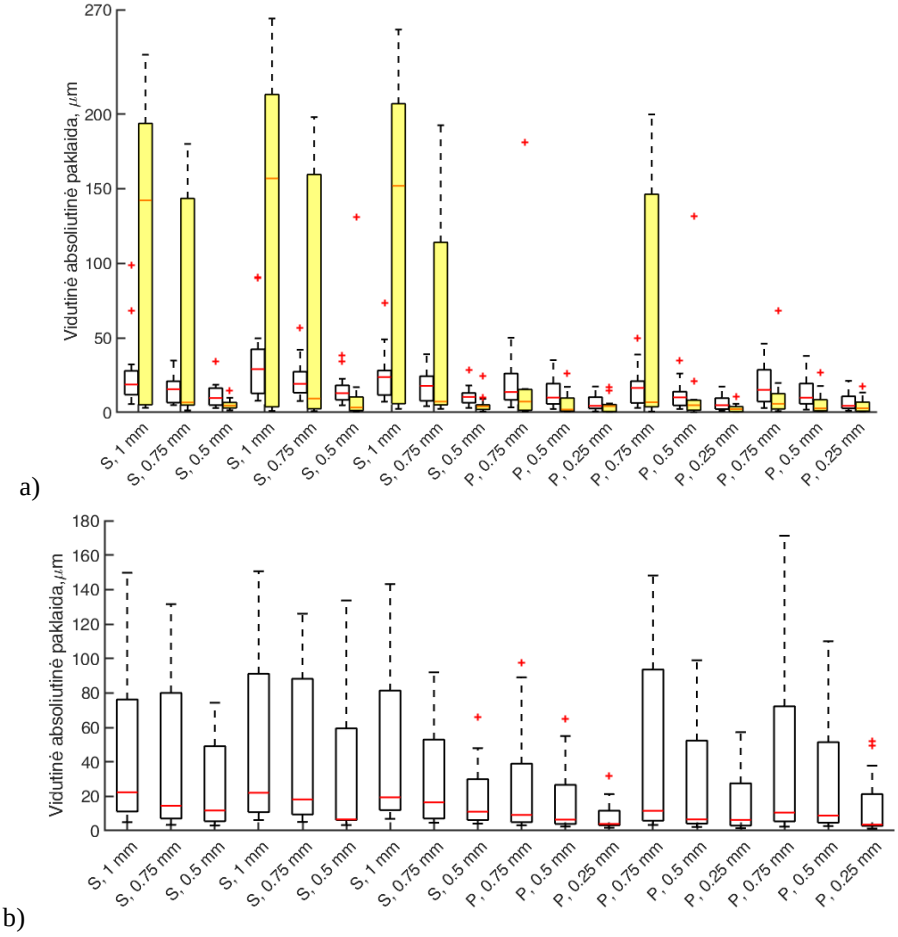

3.6 pav. Stačiakampės vidutinės absoliutinės paklaidos diagramos, vaizduojančios paklaidas, įvertintas vidurinėje skenavimo linijoje, pradedant nuo 11 mm kas 1 mm iki 29 mm) (n=19): a) skersinio judesio detektavimas, b) išilginio judesio detektavimas. Baltos ir geltonos stačiakampės diagramos atitinkamai yra 1D kros-koreliacijos ir „OpenOpticalFlow“ algoritmai. Medianinės vertės vaizduojamos horizontaliomis raudonomis linijomis, riktai − raudonais +. S – sveikas savanoris, P – rizikos grupės pacientas

3.4. Skersinių ir išilginių judesių teorinių ir apskaičiuotų slopimo profilių palyginimas

Atliekant arterijos apatinės sienelės ir aplinkinių audinių skersinių ir išilginių judesių amplitudės erdvinės priklausomybės palyginimą tarp teorinių ir apskaičiuotų verčių gauta, kad teorinis ir apskaičiuotas skersinio judesio slopimo profiliai aplinkiniuose audiniuose gerai sutampa (žr. 3.7 pav., a). Tačiau tokio gero sutapimo arterijos sienelėje nematyti. Tai galėjo nutikti dėl nepakankamo iš anksto pasirinktų taškų skaičiaus arterijos sienelėje, kuriuose buvo vertinamas slopimo profilis.

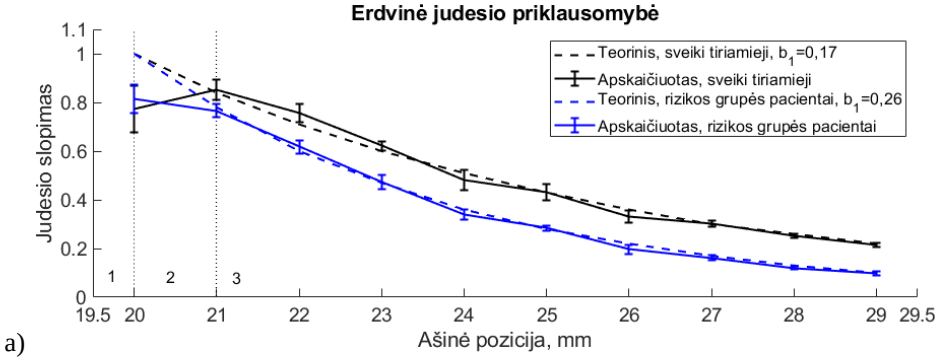

a)

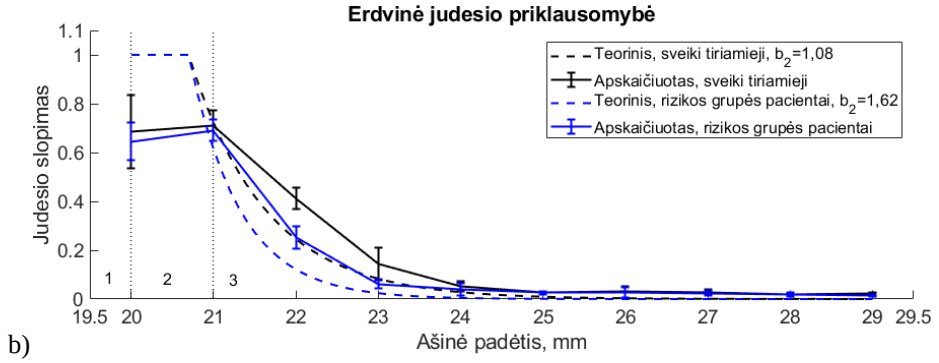

b)

3.7 pav. Teorinių ir apskaičiuotų („OpenOpticalFlow“ algoritmas) skersinių ir išilginių judesių priklausomybės nuo ašinės padėties palyginimas: a) skersinių judesių slopimas arterijos sienelėje ir aplinkiniuose audiniuose, b) išilginių judesių slopimas arterijos sienelėje ir aplinkiniuose audiniuose. Vidurkiai (n=9) ir standartiniai nuokrypiai (n=9) vaizduoja apskaičiuotas slopimo profilių vertes kiekvienai pasirinktai ašinei pozicijai. Skaičiai 1, 2, 3 atitinkamai nurodo arterijos vidų, arterijos sienelę ir aplinkinius audinius

Toks pats iš anksto parinktų taškų skaičius buvo naudojamas išilginio judesio slopimo profiliui įvertinti arterijos sienelėje. Čia matomas dar didesnis teorinių ir apskaičiuotų slopimo profilių neatitikimas (žr. 3.7 pav., a). Be to, apskaičiuoti išilginio judesio profiliai yra prasislinkę, palyginti su teoriniais aplinkinių audinių slopimo profiliais. Nepaisant teorinių ir apskaičiuotų judesio slopimo profilių neatitikimo, ypač išilginio judesio atveju, sveiki tiriamieji ir rizikos grupės pacientai gali būti diferencijuojami pagal skersinių ir išilginių judesių slopimo profilius.

3.5. *In vivo* skersinio judesio signalų parametrų nustatymo rezultatai

Lyginant laiko srities parametrus ir remiantis plotu po ROC kreive (S_{ROC}), kuris yra apie 0,8 (žr. 3.8 pav., b, c ir d), nustatyta, kad poslinkio, greičio ir pagreičio parametrai geba diferencijuoti sveikus savanorius ir rizikos grupės pacientus.

Dažnio srities parametrų (žr. 3.9 pav.) analizė parodė, kad diferencijuoti dviejų tiriamųjų grupes galima pagal spektrinį centroidą, spektrinę sklaidą, spektrinę sklaidą ir spektrinį ekscesą, nes S_{ROC} atitinkamai yra 0,69; 0,73; 0,79 ir 0,79.

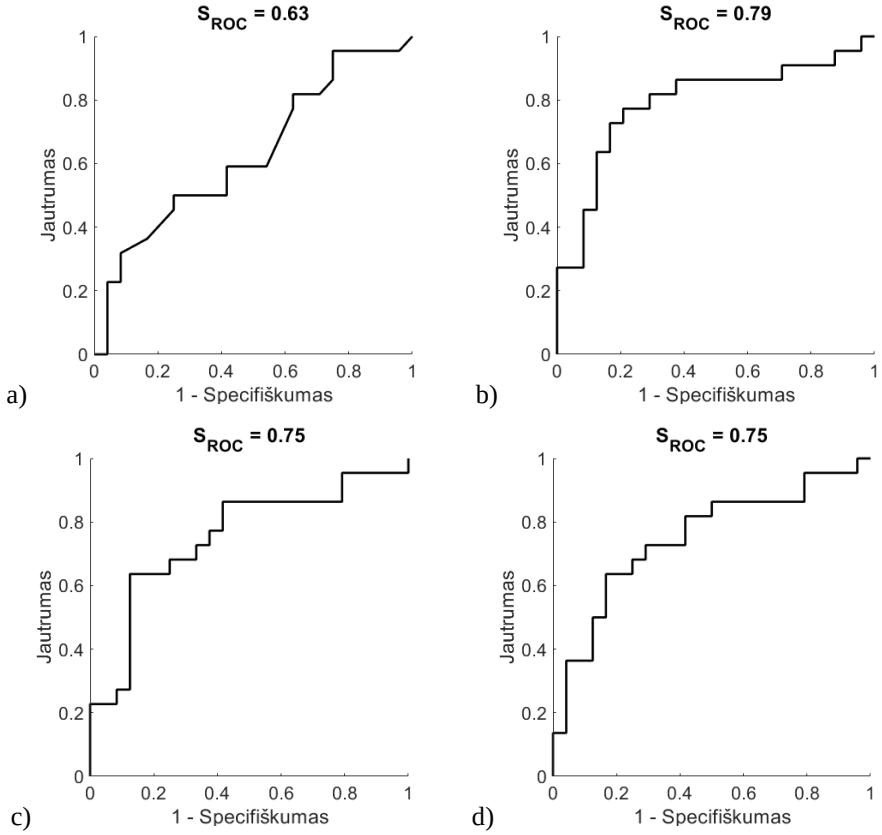

3.8 pav. ROC kreivės: a) širdies ritmo, b) poslinkio, c) greičio, d) pagreičio parametrų, vertinant jų diagnostinę vertę nustatant aterosklerozę

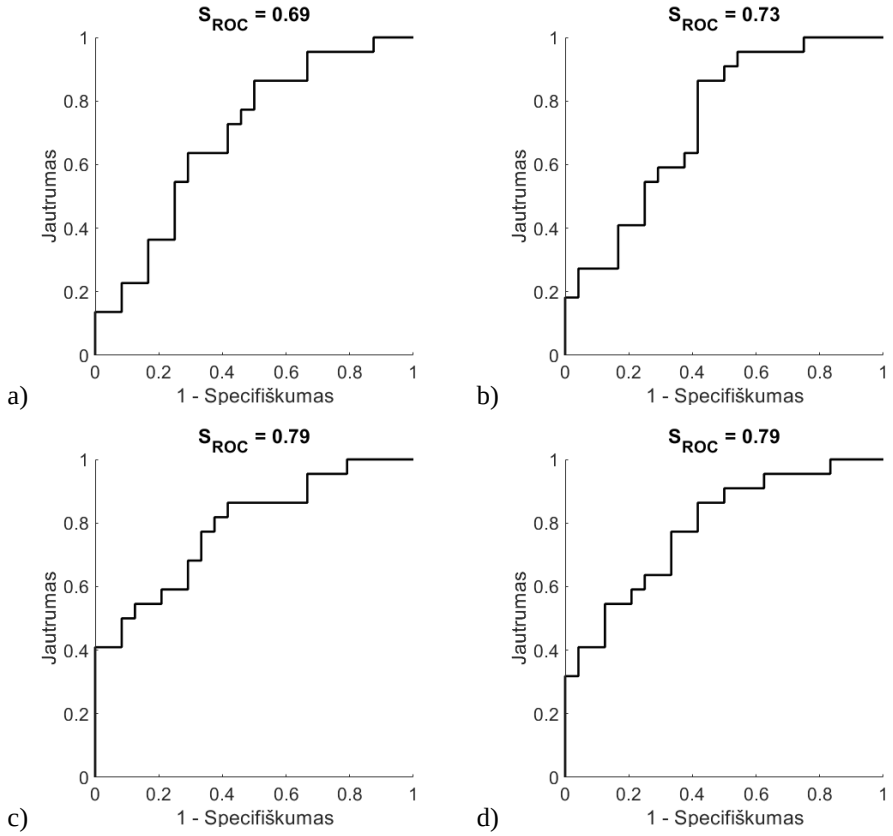

3.9 pav. ROC kreivės: a) spektrinio centroido, b) spektrinės sklaidos, c) spektrinės asimetrijos, d) spektrinio ekscesо parametrų, vertinant jų diagnostinę vertę nustatant aterosklerozę

Didžiausiu jautrumu pasižymėjo poslinkis (jautrumas=0,77) ir spektrinė sklaida (jautrumas=0,86). Greitis ir spektrinis centroidas priskirti kaip parametrai, turintys didžiausią specifiškumą, vertės atitinkamai yra 0,88 ir 0,71 (žr. 3.2 lentelę).

3.1 lentelė. Laiko ir dažnio srities parametrų diagnostinė vertė diferencijuojant sveikus savanorius nuo rizikos grupės pacientų

		Jautrumas	**Specifiškumas**
Laiko srities parametrai	Širdies ritmas, DPM	0,50	0,63
	Poslinkis, µm	**0,77**	0,79
	Greitis, µm/s	0,64	**0,88**
	Pagreitis, µm/s^2	0,73	0,71
Dažnio srities parametrai	Spektrinis centroidas, Hz	0,64	**0,71**
	Spektrinė sklaida	**0,86**	0,58
	Spektrinė asimetrija	0,77	0,67
	Spektrinis ekscesas	0,77	0,67

Baigiamosios išvados

1. Literatūros analizė parodė, kad aterosklerozė yra lėtinė arterijos sienelių liga, kuri nėra pastebima tol, kol nesusiformuoja aterosklerozinės plokštelės. Tačiau įrodyta, kad reikšmingi arterijos sienelių mechaninių savybių pokyčiai, t. y. išilginis ir skersinis arterijos sienelių judėjimas, įvyksta daug anksčiau, nei atsiranda anatominių pokyčių, t. y. *intima-media* komplekso sustorėjimas. Klinikiniai tyrimai bendrosios miego arterijos išilginį judesį susiejo su rizikos veiksniais ir ŠKL bei parodė ryšį tarp arterijos standumo, ŠKL ir išilginio judesio sumažėjimo. Skersiniam ir išilginiam judesiui detektuoti yra pasiūlyta keletas judesio sekimo algoritmų. Kai kurie iš jų yra laisvai ar komerciškai prieinami išilginiam judesiui tirti. Bet šiuo metu nė vienas iš jų nėra taikomas klinikinėje praktikoje. Pirmiausia šie metodai turi būti kruopščiai ištirti prieš juos pradedant plačiai naudoti.
2. Sukurtas virtualaus skenavimo simuliavimas, atitinkantis fizinį ultragarsinį skenavimą. Skaitmeninis skenavimas rodo gerą sutapimą su fiziniu: neatitikimas tarp taško sklaidos funkcijų pločių pusės lygyje ašine ir šonine kryptimis yra atitinkamai mažesnis nei 12 % ir 16 %. Elevacijos plokštumoje spindulio plotis pusės lygyje fizinės echoskopijos metu buvo 1,21 mm, o skaitmeninio skenavimo – 1,38 mm.
3. Sukurtas 3D arterijos modelis, gebantis atkurti žmogaus bendrosios miego arterijos biomechaninę elgseną ir tinkamas ultragarsiniams radiodažniniams signalams simuliuoti. Echoskopijos simuliavimas rodo, kad arterijos modelis atvaizduoja A, B ir M režimo vaizduose arterijos struktūrą, tokią kaip ir *in vivo* arterijos sienelė. Įvertinti vienalaikiai, virtualiai nuskenuotos 3D struktūros skersinis ir išilginis judesiai vizualiai beveik nesiskiria nuo sugeneruoto judesio šablono.
4. Ištirtas siūlomų judesio detektavimo algoritmų tikslumas naudojant simuliuotus bendrosios miego arterijos ultragarsinius radiodažninius signalus. Rezultatai rodo, kad skersinių ir išilginių judesių detektavimo tikslumui vertinti skirtų parametrų įvairovė gali įvertinti ne tik klaidą, bet ir skirtingumą tarp apskaičiuotų ir teorinių judesio signalų. Nustatyta, kad, tiriant „OpenOpticalFlow“ metodą skersiniam ir išilginiam judesiui detektuoti, vidutinės absoliutinės paklaidos medianinės vertės buvo mažesnės nei 25 μm.
5. Ištirta galimybė diferencijuoti arterijas pagal judesio slopimo profilius. Teorinis ir apskaičiuotasis skersinio judesio slopimo profiliai aplinkiniuose audiniuose gerai sutampa, tačiau išilginio judesio profiliai aplinkiniuose audiniuose yra prasislinkę, palyginti su teoriniais profiliais aplinkiniuose

audiniuose. Rezultatai rodo, kad skersinių ir išilginių judesių slopimo profilių įvairovė, apibrėžianti skirtingo elastingumo audinius, gali būti naudojama sveikiems tiriamiesiems ir rizikos grupei priklausantiems pacientams diferencijuoti.

6. Surinkti sveikų savanorių ir pacientų, kuriems yra padidėjusi rizika susirgti širdies ir kraujagyslių ligomis, ultragarsiniai radiodažniniai duomenys, apskaičiuoti dviejų skirtingų populiacijų judesio parametrai ir įvertinta šių parametrų diagnostinė geba diagnozuoti, ar pacientai serganateroskleroze, ar ne. Didžiausiu jautrumu iš pasiūlytų laiko ir dažnio srities parametrų pasižymėjo poslinkis, t. y. 0,77, ir spektrinė sklaida, t. y. 0,86. Greitis ir spektrinis centroidas priskirti kaip parametrai, pasižymintys didžiausiu specifiškumu, ir atitinkamai lygūs 0,88 ir 0,71.

REFERENCES

1. VIRANI, S.S.et al. Heart Disease and Stroke Statistics—2021 Update: A Report From the American Heart Association. In *Circulation* [online]. 2021. Vol. 143, no. 8. [accessed 2021-06-09]. Prieiga per internetą: <https://www.ahajournals.org/doi/10.1161/CIR.0000000000000950>.

2. GREENFIELD, D.M. - SNOWDEN, J.A. Cardiovascular Diseases and Metabolic Syndrome. In CARRERAS, E.et al.Sud. *The EBMT Handbook* [online]. Cham: Springer International Publishing, 2019. p. 415–420. [accessed 2021-06-09]. ISBN 978-3-030-02277-8 Available: <http://link.springer.com/10.1007/978-3-030-02278-5_55>.

3. WARD, H.et al. *Oxford Handbook of Epidemiology for Clinicians* [online]. [s.l.]: Oxford University Press ISBN 978-0-19-174077-0.

4. DONKOR, E.S. Stroke in the 21st Century: A Snapshot of the Burden, Epidemiology, and Quality of Life. In *Stroke Research and Treatment* [online]. 2018. Vol. 2018. [accessed 2020-12-22]. Available: <https://www.ncbi.nlm.nih.gov/pmc/articles/PMC6288566/>.

5. PEARSON THOMAS A.et al. AHA Guidelines for Primary Prevention of Cardiovascular Disease and Stroke: 2002 Update. In *Circulation* . 2002. Vol. 106, no. 3, p. 388–391.

6. NAGHAVI MORTEZA et al. From Vulnerable Plaque to Vulnerable Patient. In *Circulation* . 2003. Vol. 108, no. 14, p. 1664–1672.

7. SIMON ALAIN et al. Performance of Subclinical Arterial Disease Detection as a Screening Test for Coronary Heart Disease. In *Hypertension* . 2006. Vol. 48, no. 3, p. 392–396.

8. WIJEYSUNDERA, H.C. Association of Temporal Trends in Risk Factors and Treatment Uptake With Coronary Heart Disease Mortality, 1994-2005. In *JAMA* . 2010. Vol. 303, no. 18, p. 1841.

9. GOLEMATI, S.et al. Toward novel noninvasive and low-cost markers for predicting strokes in asymptomatic carotid atherosclerosis: the role of ultrasound image analysis. In *IEEE transactions on bio-medical engineering* . 2013. Vol. 60, no. 3, p. 652–658.

10. NAPOLI CLAUDIO et al. Rethinking Primary Prevention of Atherosclerosis-Related Diseases. In *Circulation* . 2006. Vol. 114, no. 23, p. 2517–2527.

11. NICOLAIDES, A.et al. Sud. *Ultrasound and Carotid Bifurcation Atherosclerosis* [online]. London: Springer-Verlag, 2012. ISBN 978-1-84882-687-8.

12. ZAHND, G.et al. Intramural shear strain can highlight the presence of atherosclerosis: A clinical in vivo study. In *2011 IEEE International Ultrasonics Symposium* . 2011. p. 1770–1773.

13. PIEPOLI, M.F.et al. 2016 European Guidelines on cardiovascular disease prevention in clinical practice: The Sixth Joint Task Force of the European Society of Cardiology and Other Societies on Cardiovascular Disease Prevention in Clinical Practice (constituted by representatives of 10 societies and by invited experts)Developed with the special contribution of the European Association for Cardiovascular Prevention & Rehabilitation (EACPR). In *European Heart Journal* . 2016. Vol. 37, no. 29, p. 2315–2381.

14. ZAHND, G.et al. Minimal-path contours combined with speckle tracking to estimate 2D displacements of the carotid artery wall in B-mode imaging. In *2011 IEEE International Ultrasonics Symposium* . 2011. p. 732–735.

15. AHLGREN, Å.R.et al. Effects of adrenaline on longitudinal arterial wall movements and resulting intramural shear strain: a first report. In *Clinical Physiology and Functional Imaging* . 2009. Vol. 29, no. 5, p. 353–359.

16. AU, J.S.et al. Carotid artery longitudinal wall motion is associated with local blood velocity and left ventricular rotational, but not longitudinal, mechanics. In *Physiological Reports* . 2016. Vol. 4, no. 14, p. e12872.

17. BAUER, M.et al. Carotid intima-media thickness as a biomarker of subclinical atherosclerosis. In *Swiss Medical Weekly* [online]. 2012. Vol. 142, no. 4344. [accessed 2020-12-21]. Available: <https://smw.ch/article/doi/smw.2012.13705>.

18. SVEDLUND, S. - GAN, L.-M. Longitudinal wall motion of the common carotid artery can be assessed by velocity vector imaging. In *Clinical Physiology and Functional Imaging* . 2011. Vol. 31, no. 1, p. 32–38.

19. ZAHND, G.et al. Evaluation of a Kalman-based block matching method to assess the bi-dimensional motion of the carotid artery wall in B-mode ultrasound sequences. In *Medical Image Analysis* . 2013. Vol. 17, no. 5, p. 573–585.

20. ZAHND, G.et al. Real-time ultrasound-tagging to track the 2D motion of the common carotid artery wall in vivo. In *Medical Physics* . 2015. Vol. 42, no. 2, p. 820–830.

21. CINTHIO, M.et al. Longitudinal movements and resulting shear strain of the arterial wall. In *American Journal of Physiology. Heart and Circulatory Physiology* . 2006. Vol. 291, no. 1, p. H394-402.

22. PERSSON, M.et al. A new non-invasive ultrasonic method for simultaneous measurements of longitudinal and radial arterial wall movements: first in vivo trial. In *Clinical Physiology and Functional Imaging* . 2003. Vol. 23, no. 5, p. 247–251.

23. CINTHIO, M.et al. Evaluation of an ultrasonic echo-tracking method for measurements of arterial wall movements in two dimensions. In *IEEE transactions on ultrasonics, ferroelectrics, and frequency control* . 2005. Vol. 52, no. 8, p. 1300–1311.

24. SVEDLUND, S.et al. Carotid artery longitudinal displacement predicts 1-year cardiovascular outcome in patients with suspected coronary artery disease. In *Arteriosclerosis, Thrombosis, and Vascular Biology* . 2011. Vol. 31, no. 7, p. 1668–1674.

25. ZAHND, G.et al. Measurement of two-dimensional movement parameters of the carotid artery wall for early detection of arteriosclerosis: a preliminary clinical study. In *Ultrasound in Medicine & Biology* . 2011. Vol. 37, no. 9, p. 1421–1429.

26. BEN-SHLOMO, Y.et al. Aortic Pulse Wave Velocity Improves Cardiovascular Event Prediction: An Individual Participant Meta-Analysis of Prospective Observational Data From 17,635 Subjects. In *Journal of the American College of Cardiology* . 2014. Vol. 63, no. 7, p. 636–646.

27. RIZI, F.Y.et al. Carotid Wall Longitudinal Motion in Ultrasound Imaging: An Expert Consensus Review. In *Ultrasound in Medicine & Biology* . 2020. Vol. 46, no. 10, p. 2605–2624.

28. SIGRIST, R.M.S.et al. Ultrasound Elastography: Review of Techniques and Clinical Applications. In *Theranostics* . 2017. Vol. 7, no. 5, p. 1303–1329.

29. BARANAUSKAS, M.et al. Ultrasonic Assessment of the Medial Temporal Lobe Tissue Displacements in Alzheimer's Disease. In *Diagnostics* . 2020. Vol. 10, no. 7, p. 452.

30. JURKONIS, R.et al. Quantification of Endogenous Brain Tissue Displacement Imaging by Radiofrequency Ultrasound. In *Diagnostics (Basel, Switzerland)* . 2020. Vol. 10, no. 2.

31. SAKALAUSKAS, A.et al. Investigation of Radiofrequency Ultrasound-Based Fibrotic Tissue Strain Imaging Method Employing Endogenous Motion: Endogenous Motion-Based Strain Elastography. In *Journal of Ultrasound in Medicine* . 2019. Vol. 38, no. 9, p. 2315– 2327.

32. ABIR, T.A.et al. Simulation analysis on effectiveness of nonlinear ultrasound imaging using synthetic cyst phantoms. In *The 8th International Conference on Software, Knowledge, Information Management and Applications (SKIMA 2014)* . 2014. p. 1–7.

33. GARCIA, D. SIMUS: an open-source simulator for ultrasound imaging. Part I: theory & examples. In *arXiv:2102.02738 [physics]* [online]. 2021. [accessed 2021-08-02]. Available: <http://arxiv.org/abs/2102.02738>.

34. MAKŪNAITĖ, M.et al. Main Uncertainties in the RF Ultrasound Scanning Simulation of the Standard Ultrasound Phantoms. In *Sensors* . 2021. Vol. 21, no. 13, p. 4420.

35. VARRAY, F.et al. Nonlinear radio frequency image simulation for harmonic imaging – CREANUIS. In *2010 IEEE International Ultrasonics Symposium* . 2010. p. 2179–2182.

36. JENSEN, J.A. - SVENDSEN, N.B. Calculation of pressure fields from arbitrarily shaped, apodized, and excited ultrasound transducers. In *IEEE Transactions on Ultrasonics, Ferroelectrics, and Frequency Control* . 1992. Vol. 39, no. 2, p. 262–267.

37. JENSEN, J.A. A model for the propagation and scattering of ultrasound in tissue. In *The Journal of the Acoustical Society of America* . 1991. Vol. 89, no. 1, p. 182–190.

38. JENSEN, J. FIELD: A program for simulating ultrasound systems. In *Medical and Biological Engineering and Computing* . 1996. Vol. 34, p. 351–352.

39. JENSEN, J.A. Ultrasound Imaging and Its Modeling. In FINK, M.et al.Sud. *Imaging of Complex Media with Acoustic and Seismic Waves* [online]. Berlin, Heidelberg: Springer Berlin Heidelberg, 2002. p. 135–166. [accessed 2019-09-20]. ISBN 978-3-540-41667-8Available: <http://link.springer.com/10.1007/3-540-44680-X_6>.

40. MATTAUSCH, O. - GOKSEL, O. Image-Based PSF Estimation for Ultrasound Training Simulation. In TSAFTARIS, S.A.et al. Sud. *Simulation and Synthesis in Medical Imaging* [online]. Cham: Springer International Publishing, 2016. p. 23–33. [accessed 2021-05-26]. ISBN 978-3-319-46629-3Available: <http://link.springer.com/10.1007/978-3-319-46630-9_3>.

41. PHAM, A.H.et al. Simulation of ultrasound backscatter images from fish. In *Progress in Biomedical Optics and Imaging - Proceedings of SPIE* . Lake Buena Vista, Florida, 2011. p. 796152.

42. GEMIGNANI, V.et al. A System for Real-Time Measurement of the Brachial Artery Diameter in B-Mode Ultrasound Images. In *IEEE transactions on medical imaging* . 2007. Vol. 26, p. 393–404.

43. SOLOMOU, R.et al. Ultrasound Common Carotid Artery Video Simulation and Motion Analysis. In KYRIACOU, E.et al. Sud. *XIV Mediterranean Conference on Medical and Biological Engineering and Computing 2016* . Cham: Springer International Publishing, 2016. p. 347–350.

44. DENG, L.et al. Ultrasound simulation model incorporating incident and reflected wave propagations along a common carotid artery. In *Computers in Biology and Medicine* . 2019. Vol. 104, p. 267–277.

45. HU, X.et al. A dynamic ultrasound simulation of a pulsating three-layered CCA for validation of two-dimensional wall motion and blood velocity estimation algorithms. In *Medical Physics* . 2018. Vol. 45, no. 1, p. 131–143.

46. STOITSIS, J.et al. Simulating dynamic B-mode ultrasound image data of the common carotid artery. In *2008 IEEE International Workshop on Imaging Systems and Techniques* . 2008. p. 144–148.

47. STROPUS, R.et al. *Žmogaus anatomija*. 2-asis leid., patais. ir papild. Ed. Kaunas: Vitae Litera, 2005. ISBN 9955-686-00-6.

48. [Online]. 2019. [accessed 2021-02-05]. Available: <https://en.wikipedia.org/w/index.php?title=Carotid_triangle&oldid=908909556>.

49. STROPUS, R.et al. *Žmogaus anatomija*. 2nd. Ed. Kaunas: Kauno medicinos universiteto leidykla, 2008. ISBN 978-9955-15-099-2.

50. EROSCHENKO, V.P. - FIORE, M.S.H. Di *DiFiore's atlas of histology with functional correlations*. 11th ed. Ed. Philadelphia: Wolters Kluwer Health/Lippincott Williams & Wilkins, 2008. 532 p. ISBN 978-0-7817-7057-6.

51. NILSSON, T.et al. A method to measure shear strain with high spatial resolution in the arterial wall non-invasively in vivo by tracking zero-crossings of B-mode intensity gradients. In *2010 IEEE International Ultrasonics Symposium* . 2010. p. 491–494.

52. ZAHND, G.et al. Progressive Attenuation of the Longitudinal Kinetics in the Common Carotid Artery: Preliminary in Vivo Assessment. In *Ultrasound in Medicine & Biology* . 2014. Vol. 18, p. 1217–1232.

53. KĖVELAITIS, E.et al. *ŽMOGAUS FIZIOLOGIJA*. 2-oji patais. ir papild. laida. Ed. Kaunas: Kauno medicinos universiteto leidykla, 2006. ISBN 978-9955-15-091-6.

54. KOPUSTINSKAS, A. - KOPUSTINSKIENĖ, G. *Biofizika* [online]. 1. Ed. [s.l.]: KTU leidykla „Technologija", 2012. ISBN 978-609-02-0591-4.

55. LAWTON, R.W. - GREENE, L.C. Warminster, PA: US Naval and Air Development Center, 1956.

56. PATEL, D.J.et al. Aortic mechanics in the living dog. In *Journal of Applied Physiology* . 1961. Vol. 16, no. 2, p. 293–299.

57. PERSSON, M.et al. Non-invasive measurement of arterial longitudinal movement. In *2002 IEEE Ultrasonics Symposium, 2002. Proceedings.* [online]. Munich, Germany: IEEE, 2002. p. 1783–1786. [accessed 2021-05-25]. Available: <http://ieeexplore.ieee.org/document/1192644/>.

58. AHLGREN, Å.R.et al. Longitudinal displacement and intramural shear strain of the porcine carotid artery undergo profound changes in response to catecholamines. In *American Journal of Physiology-Heart and Circulatory Physiology* . 2011. Vol. 302, no. 5, p. H1102–H1115.

59. AHLGREN, Å.R.et al. Profound Increase in Longitudinal Displacements of the Porcine Carotid Artery Wall Can Take Place Independently of Wall Shear Stress: A Continuation Report. In *Ultrasound in Medicine & Biology* . 2015. Vol. 41, no. 5, p. 1342–1353.

60. BURCKHARDT, C.B. Speckle in ultrasound B-mode scans. In *IEEE Transactions on Sonics and Ultrasonics* . 1978. Vol. 25, no. 1, p. 1–6.

61. GOLEMATI, S.et al. Comparison of Block Matching and Differential Methods for Motion Analysis of the Carotid Artery Wall From Ultrasound Images. In *IEEE Transactions on Information Technology in Biomedicine* . 2012. Vol. 16, no. 5, p. 852–858.

62. CINTHIO, M.et al. Longitudinal Movement of the Common Carotid Artery Wall: New Information on Cardiovascular Aging. In *Ultrasound in Medicine & Biology* . 2018. Vol. 44, no. 11, p. 2283–2295.

63. YLI-OLLILA, H.et al. Axial and Radial Waveforms in Common Carotid Artery: An Advanced Method for Studying Arterial Elastic Properties in Ultrasound Imaging. In *Ultrasound in Medicine & Biology* . 2013. Vol. 39, no. 7, p. 1168–1177.

64. GALVÃO SCHEIDEGGER, A.P.et al. Uncertainty quantification in simulation models: a proposed framework and application through case study. In *2018 Winter Simulation Conference (WSC)* . 2018. p. 1599–1610.

65. XIAOFENG ZHAO - MCGOUGH, R.J. The Khokhlov - Zabolotskaya - Kuznetsov (KZK) equation with power law attenuation. In *2014 IEEE International Ultrasonics Symposium* . 2014. p. 2225–2228.

66. JING, Y.et al. A k-Space Method for Moderately Nonlinear Wave Propagation. In *IEEE Transactions on Ultrasonics, Ferroelectrics, and Frequency Control* . 2012. Vol. 59, no. 8, p. 1664–1673.

67. MARTIN, E.et al. Experimental Validation of k-Wave: Nonlinear Wave Propagation in Layered, Absorbing Fluid Media. In *IEEE Transactions on Ultrasonics, Ferroelectrics, and Frequency Control* . 2020. Vol. 67, no. 1, p. 81–91.

68. TREEBY, B.E.et al. Modelling elastic wave propagation using the k-Wave MATLAB Toolbox. In *2014 IEEE International Ultrasonics Symposium* [online]. Chicago, IL, USA: IEEE, 2014. p. 146–149. [accessed 2020-08-21]. Available: <http://ieeexplore.ieee.org/document/6931789/>.

69. GU, J. - JING, Y. Modeling of wave propagation for medical ultrasound: a review. In *IEEE Transactions on Ultrasonics, Ferroelectrics, and Frequency Control* . 2015. Vol. 62, no. 11, p. 1979–1992.

70. DU, Y.et al. Angular spectrum approach for fast simulation of pulsed non-linear ultrasound fields. In *2011 IEEE International Ultrasonics Symposium* . 2011. p. 1583–1586.

71. GAO, H.et al. Comparison of the performance of different tools for fast simulation of ultrasound data. In *Ultrasonics* . 2012. Vol. 52, no. 5, p. 573–577.

72. JENSEN, J.et al. Optimized Plane Wave Imaging for Fast and High-Quality Ultrasound Imaging. In *IEEE Transactions on Ultrasonics, Ferroelectrics, and Frequency Control* . 2016. Vol. 63, no. 11, p. 1922–1934.

73. HU, X.et al. Assessment of Homodyned K Distribution Modeling Ultrasonic Speckles from Scatterers with Varying Spatial Organizations. In *Journal of Healthcare Engineering* . 2017. Vol. 2017, p. 1–14.

74. ZHOU, Z.et al. A Review of Ultrasound Tissue Characterization with Mean Scatterer Spacing. In *Ultrasonic Imaging* . 2017. Vol. 39, no. 5, p. 263–282.

75. MATTAUSCH, O. - GOKSEL, O. Image-Based Reconstruction of Tissue Scatterers Using Beam Steering for Ultrasound Simulation. In *IEEE Transactions on Medical Imaging* . 2018. Vol. 37, no. 3, p. 767–780.

76. ZHANG, L.et al. A high-frequency, high frame rate duplex ultrasound linear array imaging system for small animal imaging. In *IEEE Transactions on Ultrasonics, Ferroelectrics, and Frequency Control* . 2010. Vol. 57, no. 7, p. 1548–1557.

77. DENG, Y.et al. On System-Dependent Sources of Uncertainty and Bias in Ultrasonic Quantitative Shear-Wave Imaging. In *IEEE Transactions on Ultrasonics, Ferroelectrics, and Frequency Control* . 2016. Vol. 63, no. 3, p. 381–393.

78. DEI, K. - BYRAM, B. A Robust Method for Ultrasound Beamforming in the Presence of Off-Axis Clutter and Sound Speed Variation. In *Ultrasonics* . 2018. Vol. 89, p. 34–45.

79. GHOLAMPOUR, A.et al. A robust approach to apodization design in phased arrays for ultrasound imaging. In *Ultrasonics* . 2017. Vol. 76, p. 10–18.

80. FERNANDEZ, A.T.et al. Synthetic Elevation Beamforming and Image Acquisition Capabilities Using an 8 × 128 1.75D Array. In . 2003. Vol. 50, no. 1, p. 18.

81. CHEN, T.K.et al. Improvement of Freehand Ultrasound Calibration Accuracy Using the Elevation Beamwidth Profile. In *Ultrasound in Medicine & Biology* . 2011. Vol. 37, no. 8, p. 1314–1326.

82. PARK, Y.et al. Improvement of the Radiation Beam Profile of a Medical Ultrasonic Transducer. In *The Journal of the Acoustical Society of Korea* . 2015. Vol. 34, no. 4, p. 264–273.

83. HASHEMI, H.S. - RIVAZ, H. Global Time-Delay Estimation in Ultrasound Elastography. In *IEEE Transactions on Ultrasonics, Ferroelectrics, and Frequency Control* . 2017. Vol. 64, no. 10, p. 1625–1636.

84. MARION, A. - VRAY, D. Toward a real-time simulation of ultrasound image sequences based on a 3-D set of moving scatterers. In *IEEE Transactions on Ultrasonics, Ferroelectrics, and Frequency Control* . 2009. Vol. 56, no. 10, p. 2167–2179.

85. SCHLAIKJER, M.et al. Simulation of RF data with tissue motion for optimizing stationary echo canceling filters. In *Ultrasonics* . 2003. Vol. 41, no. 6, p. 415–419.

86. GOKSEL, O.et al. Simulation of Ultrasound Radio-Frequency Signals in Deformed Tissue for Validation of 2D Motion Estimation with Sub-Sample Accuracy. In *2007 29th Annual International Conference of the IEEE Engineering in Medicine and Biology Society* [online]. Lyon, France: IEEE, 2007. p. 2159–2162. [accessed 2019-09-20]. Available: <http://ieeexplore.ieee.org/document/4352750/>.

87. GENNISSON, J.-L.et al. Ultrasound elastography: Principles and techniques. In *Diagnostic and Interventional Imaging* . 2013. Vol. 94, no. 5, p. 487–495.

88. GOLEMATI, S.et al. Carotid artery wall motion estimated from b-mode ultrasound using region tracking and block matching. In *Ultrasound in Medicine & Biology* . 2003. Vol. 29, no. 3, p. 387–399.

89. GOLEMATI, S.et al. Ultrasound-Image-Based Cardiovascular Tissue Motion Estimation. In *IEEE Reviews in Biomedical Engineering* . 2016. Vol. 9, p. 208–218.

90. GASTOUNIOTI, A.et al. Carotid artery wall motion analysis from B-mode ultrasound using adaptive block matching: *in silico* evaluation and *in vivo* application. In *Physics in Medicine and Biology* . 2013. Vol. 58, no. 24, p. 8647–8661.

91. GASTOUNIOTI, A.et al. Comparison of Kalman-filter-based approaches for block matching in arterial wall motion analysis from B-mode ultrasound. In *Measurement Science and Technology* . 2011. Vol. 22, no. 11, p. 114008.

92. ALBINSSON, J.et al. Improved Tracking Performance of Lagrangian Block-Matching Methodologies Using Block Expansion in the Time Domain: In Silico, Phantom and in Vivo Evaluations. In *Ultrasound in Medicine & Biology* . 2014. Vol. 40, no. 10, p. 2508–2520.

93. GAO, Z.et al. Carotid Artery Wall Motion Estimated from Ultrasound Imaging Sequences Using a Nonlinear State Space Approach. In OURSELIN, S.et al.Sud. *Medical Image Computing and Computer-Assisted Intervention - MICCAI 2016* . Cham: Springer International Publishing, 2016. p. 98–106.

94. GAO, Z.et al. Motion Tracking of the Carotid Artery Wall From Ultrasound Image Sequences: a Nonlinear State-Space Approach. In *IEEE transactions on medical imaging* . 2018. Vol. 37, no. 1, p. 273–283.

95. GAO, Z.et al. Robust estimation of carotid artery wall motion using the elasticity-based state-space approach. In *Medical Image Analysis* . 2017. Vol. 37, p. 1–21.

96. TAT, J.et al. Reduced common carotid artery longitudinal wall motion and intramural shear strain in individuals with elevated cardiovascular disease risk using speckle tracking. In *Clinical Physiology and Functional Imaging* . 2017. Vol. 37, no. 2, p. 106–116.

97. ZAHND, G.et al. Longitudinal Displacement of the Carotid Wall and Cardiovascular Risk Factors: Associations with Aging, Adiposity, Blood Pressure and Periodontal Disease Independent of Cross-Sectional Distensibility and Intima-Media Thickness. In *Ultrasound in Medicine & Biology* . 2012. Vol. 38, no. 10, p. 1705–1715.

98. ALBINSSON, J.et al. Iterative 2D Tissue Motion Tracking in Ultrafast Ultrasound Imaging. In *Applied Sciences* . 2018. Vol. 8, no. 5, p. 662.

99. LOPATA, R.G.P.et al. Performance Evaluation of Methods for Two-Dimensional Displacement and Strain Estimation Using Ultrasound Radio Frequency Data. In *Ultrasound in Medicine & Biology* . 2009. Vol. 35, no. 5, p. 796–812.

100. SHI, H. - VARGHESE, T. Two-dimensional multi-level strain estimation for discontinuous tissue. In *Physics in Medicine and Biology* . 2007. Vol. 52, no. 2, p. 389–401.

101. ZAHND, G.et al. Dynamic Block Matching to assess the longitudinal component of the dense motion field of the carotid artery wall in B-mode ultrasound sequences — Association with coronary artery disease. In *Medical Physics* . 2018. Vol. 45, no. 11, p. 5041–5053.

102. HORN, B.K.P. - SCHUNCK, B.G. Determining optical flow. In *Artificial Intelligence* . 1981. Vol. 17, no. 1, p. 185–203.

103. HEIN, I.A. - O'BRIEN, W.D. Current time-domain methods for assessing tissue motion by analysis from reflected ultrasound echoes-a review. In *IEEE Transactions on Ultrasonics, Ferroelectrics, and Frequency Control* . 1993. Vol. 40, no. 2, p. 84–102.

104. MURRAY, V.et al. An AM-FM model for Motion Estimation in Atherosclerotic Plaque Videos. In *2007 Conference Record of the Forty-First Asilomar Conference on Signals, Systems and Computers* . 2007. p. 746–750.

105. SALLES, S.et al. Real time US-tagging combined with phase-based optical flow applied to 2D motion estimation of the carotid artery wall. In *2012 IEEE International Ultrasonics Symposium* . 2012. p. 1185–1188.

106. STOITSIS, J.et al. Analysis and quantification of arterial wall motion from B-mode ultrasound images - comparison of block-matching and optical flow. In *2005 IEEE Engineering in Medicine and Biology 27th Annual Conference* . 2005. p. 4469–4472.

107. SCARAMUZZINO, S.et al. Longitudinal Motion Assessment of the Carotid Artery Using Speckle Tracking and Scale-Invariant Feature Transform. In *Annals of Biomedical Engineering* . 2017. Vol. 45, no. 8, p. 1865–1876.

108. IDZENGA, T.et al. Enhancing the performance of lateral shear strain estimation by using 2-D strain imaging. In *IEEE transactions on ultrasonics, ferroelectrics, and frequency control* . 2014. Vol. 61, no. 5, p. 756–764.

109. SHI, H.et al. Preliminary in vivo atherosclerotic carotid plaque characterization using the accumulated axial strain and relative lateral shift strain indices. In *Physics in medicine and biology* . 2008. Vol. 53, no. 22, p. 6377–6394.

110. KASAI, C.et al. Real-Time Two-Dimensional Blood Flow Imaging Using an Autocorrelation Technique. In *IEEE Transactions on Sonics and Ultrasonics* . 1985. Vol. 32, no. 3, p. 458–464.

111. FEKKES, S.et al. Simultaneous Vascular Strain and Blood Vector Velocity Imaging Using High-Frequency Versus Conventional-Frequency Plane Wave Ultrasound: A Phantom Study. In *IEEE Transactions on Ultrasonics, Ferroelectrics, and Frequency Control* . 2018. Vol. 65, no. 7, p. 1166–1181.

112. HASEGAWA, H. - KANAI, H. Simultaneous imaging of artery-wall strain and blood flow by high frame rate acquisition of RF signals. In *IEEE Transactions on Ultrasonics, Ferroelectrics, and Frequency Control* . 2008. Vol. 55, no. 12, p. 2626–2639.

113. PERROT, V.et al. Simultaneous pulse wave and flow estimation at high-framerate using plane wave and transverse oscillation on carotid phantom. In *2017 IEEE International Ultrasonics Symposium (IUS)* . 2017. p. 1–4.

114. PERROT, V.et al. Simultaneous Tissue and Flow Estimation at High Frame Rate Using Plane Wave and Transverse Oscillation on in Vivo Carotid. In *2018 IEEE International Ultrasonics Symposium (IUS)* . 2018. p. 1–4.

115. JENSEN, J.A. - MUNK, P. A new method for estimation of velocity vectors. In *IEEE Transactions on Ultrasonics, Ferroelectrics, and Frequency Control* . 1998. Vol. 45, no. 3, p. 837–851.

116. HASEGAWA, H. - KANAI, H. Phase-sensitive lateral motion estimator for measurement of artery-wall displacement- phantom study. In *IEEE Transactions on Ultrasonics, Ferroelectrics, and Frequency Control* . 2009. Vol. 56, no. 11, p. 2450–2462.

117. SALLES, S.et al. 2-D arterial wall motion imaging using ultrafast ultrasound and transverse oscillations. In *IEEE Transactions on Ultrasonics, Ferroelectrics, and Frequency Control* . 2015. Vol. 62, no. 6, p. 1047–1058.

118. SUMI, C. Displacement vector measurement using instantaneous ultrasound signal phase-multidimensional autocorrelation and Doppler methods. In *IEEE Transactions on Ultrasonics, Ferroelectrics, and Frequency Control* . 2008. Vol. 55, no. 1, p. 24–43.

119. XUNCHANG CHEN et al. Lateral speckle tracking using synthetic lateral phase. In *IEEE Transactions on Ultrasonics, Ferroelectrics, and Frequency Control* . 2004. Vol. 51, no. 5, p. 540–550.

120. YOUSEFI RIZI, F.et al. Study of the effects of age and body mass index on the carotid wall vibration: extraction methodology and analysis. In *Proceedings of the Institution of Mechanical Engineers. Part H, Journal of Engineering in Medicine* . 2014. Vol. 228, no. 7, p. 714–729.

121. RIZI, F.Y.et al. Measuring the effect of aging on vibrations of the carotid artery wall using empirical mode decomposition method. In *Journal of Medical Signals and Sensors* . 2014. Vol. 4, no. 1, p. 27–34.

122. ZAMBACEVIČIENĖ, M. - JURKONIS, R. RF Ultrasound Based Longitudinal Motion Estimation of Carotid Artery Wall: Feasibility Study. In LHOTSKA, L.et al. Sud. *World Congress on Medical Physics and Biomedical Engineering 2018* [online]. Singapore: Springer Singapore, 2019. p. 253–257. [accessed 2021-02-04]. ISBN 978-981-10-9037-0Available: <http://link.springer.com/10.1007/978-981-10-9038-7_47>.

123. HASEGAWA, H. - KANAI, H. Improving accuracy in estimation of artery-wall displacement by referring to center frequency of RF echo. In *IEEE Transactions on Ultrasonics, Ferroelectrics, and Frequency Control* . 2006. Vol. 53, no. 1, p. 52–63.

124. HASEGAWA, H. - KANAI, H. Modification of the phased-tracking method for reduction of artifacts in estimated artery wall deformation. In *IEEE Transactions on Ultrasonics, Ferroelectrics, and Frequency Control* . 2006. Vol. 53, no. 11, p. 2050–2064.

125. HASEGAWA, H. - KANAI, H. Reduction of influence of variation in center frequencies of RF echoes on estimation of artery-wall strain. In *IEEE Transactions on Ultrasonics, Ferroelectrics, and Frequency Control* . 2008. Vol. 55, no. 9, p. 1921–1934.

126. MIYAJO, A.et al. Comparison of ultrasonic motion estimators for vascular applications. In . 2019.

127. MIYAJO, A. - HASEGAWA, H. Comparison of method using phase-sensitive motion estimator with speckle tracking method and application to measurement of arterial wall motion. In *Japanese Journal of Applied Physics* . 2018. Vol. 57, no. 7S1, p. 07LF11.

128. LIEBGOTT, H.et al. PSF dedicated to estimation of displacement vectors for tissue elasticity imaging with ultrasound. In *IEEE Transactions on Ultrasonics, Ferroelectrics, and Frequency Control* . 2007. Vol. 54, no. 4, p. 746–756.

129. BASARAB, A.et al. Phase-based block matching applied to motion estimation with unconventional beamforming strategies. In *IEEE Transactions on Ultrasonics, Ferroelectrics, and Frequency Control* . 2009. Vol. 56, no. 5, p. 945–957.

130. PERROT, V.et al. Video Magnification Applied in Ultrasound. In *IEEE Transactions on Biomedical Engineering* . 2019. Vol. 66, no. 1, p. 283–288.

131. SVEDLUND, S. - GAN, L. Longitudinal common carotid artery wall motion is associated with plaque burden in man and mouse. In *Atherosclerosis* . 2011. Vol. 217, no. 1, p. 120–124.

132. ZHANG, L.et al. Evaluation of carotid artery elasticity changes in patients with type 2 diabetes. In *Cardiovascular Diabetology* . 2014. Vol. 13, no. 1, p. 39.

133. ZAHND, G.et al. CAROLAB A platform to analyze carotid ultrasound data. In *2019 IEEE International Ultrasonics Symposium (IUS)* . 2019. p. 463–466.

134. ZAHND, G.et al. A Fully-Automatic Method to Segment the Carotid Artery Layers in Ultrasound Imaging: Application to Quantify the Compression-Decompression Pattern of the Intima-Media Complex During the Cardiac Cycle. In *Ultrasound in Medicine & Biology* . 2017. Vol. 43, no. 1, p. 239–257.

135. GASTOUNIOTI, A.et al. CAROTID – A web-based platform for optimal personalized management of atherosclerotic patients. In *Computer Methods and Programs in Biomedicine* . 2014. Vol. 114, no. 2, p. 183–193.

136. JURKONIS, R.et al. *Virtual instrument for ultrasound signal sampling and formation of B-scan image of eye (in Lithuanian)*. 2009.

137. Valstybinė ligonių kasa - Širdies ir kraujagyslių ligų prevencijos programa. In [online]. [accessed 2021-01-25]. Available: <http://www.vlk.lt/veikla/veiklos-sritys/prevencines-programos/sirdie-ir-kraujagysliu-ligu-prevencijos-programa>.

138. ALTY, J. - HOEY, E. *Practical Ultrasound: An Illustrated Guide, Second Edition*. [s.l.]: CRC Press, 2013. 298 p. ISBN 978-1-4441-6829-7.

139. AU, J.S.et al. An assessment of intra-individual variability in carotid artery longitudinal wall motion: recommendations for data acquisition. In *Physiological Measurement* . 2018. Vol. 39, no. 9, p. 09NT01.

140. MAKŪNAITĖ, M.et al. Ultrasonic Parametrization of Arterial Wall Movements in Low- and High-Risk CVD Subjects. In *Applied Sciences* . 2019. Vol. 9, no. 3, p. 465.

141. PEIKARI, M.et al. Effects of ultrasound section-thickness on brachytherapy needle tip localization error. In *Medical image computing and computer-assisted intervention: MICCAI .. International Conference on Medical Image Computing and Computer-Assisted Intervention* . 2011. Vol. 14, no. Pt 1, p. 299–306.

142. JENSEN, J.A. FIELD: A Program for Simulating Ultrasound Systems. In *10th Nordicbaltic Conference on Biomedical Imaging, Vol. 4, Supplement 1, Part 1:351–353* . 1996. p. 351–353.

143. Transducer Specification Sheet Ultrasound 2009. In *Scribd* [online]. [accessed 2021-01-29]. Available: <https://www.scribd.com/document/428987879/Transducer-Specification-Sheet-Ultrasound-2009>.

144. General & Small Parts Phantom. In *CIRS* [online]. [accessed 2021-01-18]. Available: <http://www.cirsinc.com/products/ultrasound/ats-urethane/general-small-parts-phantom/>.

145. Beam Profile & Slice Thickness Phantom. In *CIRS* [online]. [accessed 2021-01-18]. Available: <http://www.cirsinc.com/products/ultrasound/ats-urethane/beam-profile-slice-thickness-phantom/>.

146. GOLDSTEIN, A. - MADRAZO, B.L. Slice-thickness artifacts in gray-scale ultrasound. In *Journal of clinical ultrasound: JCU* . 1981. Vol. 9, no. 7, p. 365–375.

147. SKOLNICK, M.L. Estimation of ultrasound beam width in the elevation (section thickness) plane. In *Radiology* . 1991. Vol. 180, no. 1, p. 286–288.

148. CHAU, T.et al. SIMULATION OF ULTRASOUND IMAGE FROM CT-IMAGE DATA. In *Southeast Asian journal of Sciences* . 2013. Vol. 2, p. 11–18.

149. TUTHILL, T.A.et al. Deviations from Rayleigh statistics in ultrasonic speckle. In *Ultrasonic Imaging* . 1988. Vol. 10, no. 2, p. 81–89.

150. JENSEN, J. Linear description of ultrasound imaging systems. In [online]. 2001. [accessed 2021-01-21]. Available: </paper/Linear-description-of-ultrasound-imaging-systems-Jensen/69b07f6ffe22b26640a8ee113c270ddf5c0c6e2e>.

151. NILSSON, T.et al. Methods for measurements of the longitudinal movement and the shear-induced longitudinal elastic modulus of the arterial wall. In *2009 IEEE International Ultrasonics Symposium* . 2009. p. 317–320.

152. MAKŪNAITĖ, M.et al. Ultrasonic mapping of endogenous motion in brain tissue. In *2019 IEEE International Ultrasonics Symposium (IUS)* . 2019. p. 2408–2411.

153. LIU, T. OpenOpticalFlow: An Open Source Program for Extraction of Velocity Fields from Flow Visualization Images. In *Journal of Open Research Software* . 2017. Vol. 5, no. 1, p. 29.

154. JIANG, J. - PENG, B. Ultrasonic Methods for Assessment of Tissue Motion in Elastography. In *Ultrasound Elastography for Biomedical Applications and Medicine* [online]. [s.l.]: John Wiley & Sons, Ltd, 2018. p. 35–70. [accessed 2021-02-01]. ISBN 978-1-119-02152-0Available: <https://onlinelibrary.wiley.com/doi/abs/10.1002/9781119021520.ch4>.

155. ALBINSSON, J.et al. A combination of parabolic and grid slope interpolation for 2D tissue displacement estimations. In *Medical & Biological Engineering & Computing* . 2017. Vol. 55, no. 8, p. 1327–1338.

156. CÉSPEDES, I.et al. Methods for estimation of subsample time delays of digitized echo signals. In *Ultrasonic Imaging* . 1995. Vol. 17, no. 2, p. 142–171.

157. DEBELLA-GILO, M. - KÄÄB, A. Sub-pixel precision image matching for measuring surface displacements on mass movements using normalized cross-correlation. In *Remote Sensing of Environment* . 2011. Vol. 115, no. 1, p. 130–142.

158. NOBACH, H. - HONKANEN, M. Two-dimensional Gaussian regression for sub-pixel displacement estimation in particle image velocimetry or particle position estimation in particle tracking velocimetry. In *Experiments in Fluids* . 2005. Vol. 38, no. 4, p. 511–515.

159. SUN, C. Fast optical flow using 3D shortest path techniques. In *Image and Vision Computing* . 2002. Vol. 20, no. 13, p. 981–991.

160. BUDIDHA, K. - KYRIACOU, P.A. Photoplethysmography for Quantitative Assessment of Sympathetic Nerve Activity (SNA) During Cold Stress. In *Frontiers in Physiology* [online]. 2019. Vol. 9. [accessed 2021-02-04]. Available: <https://www.frontiersin.org/articles/10.3389/fphys.2018.01863/full>.

161. ELGENDI, M.et al. Detection of a and b waves in the acceleration photoplethysmogram. In *Biomedical Engineering Online* . 2014. Vol. 13, p. 139.

162. YLI-OLLILA, H.et al. Principal Component Analysis of the Longitudinal Carotid Wall Motion in Association with Vascular Stiffness: A Pilot Study. In *Ultrasound in Medicine & Biology* . 2016. Vol. 42, no. 12, p. 2873–2886.

163. SEMMLOW, J.L. - GRIFFEL, B. *Biosignal and medical image processing*. Third edition. Ed. Boca Raton: CRC Press, Taylor & Francis Group, CRC Press is an imprint of the Taylor & Francis Group, an Informa business, 2014. 607 p. ISBN 978-1-4665-6736-8.

164. YLI-OLLILA, H.et al. New indices of arterial stiffness measured from longitudinal motion of common carotid artery in relation to reference methods, a pilot study. In *Clinical Physiology and Functional Imaging* . 2016. Vol. 36, no. 5, p. 376–388.

165. TAIVAINEN, S.H.et al. Interrelationships between indices of longitudinal movement of the common carotid artery wall and the conventional measures of subclinical arteriosclerosis. In *Clinical Physiology and Functional Imaging* . 2017. Vol. 37, no. 3, p. 305–313.

166. QORCHI, S.et al. *Extraction of characteristic patterns from carotid longitudinal kinetics*. 2017.

167. Spectral Descriptors - MATLAB & Simulink. In [online]. [accessed 2021-08-02]. Available: <https://www.mathworks.com/help/audio/ug/spectral-descriptors.html#mw_rtc_SpectralDescriptorsExample_88BF6489>.

168. MITCHELL GARY F.et al. Changes in Arterial Stiffness and Wave Reflection With Advancing Age in Healthy Men and Women. In *Hypertension* . 2004. Vol. 43, no. 6, p. 1239–1245.

169. ZAMBACEVIČIENĖ, M.et al. RF Ultrasound Based Estimation of Pulsatile Flow Induced Microdisplacements in Phantom. In LHOTSKA, L.et al. Sud. *World Congress on Medical Physics and Biomedical Engineering 2018* . Singapore: Springer, 2019. p. 601–605.

170. GAO, Z.et al. Motion Estimation of Common Carotid Artery Wall Using a H ∞ Filter Based Block Matching Method. In NAVAB, N.et al. Sud. *Medical Image Computing and Computer-Assisted Intervention – MICCAI 2015* . Cham: Springer International Publishing, 2015. p. 443–450.

171. YLI-OLLILA, H.et al. Transfer Function Analysis of the Longitudinal Motion of the Common Carotid Artery Wall. In *Frontiers in Physiology* [online]. 2016. Vol. 7. [accessed 2021-04-27]. Available: <https://www.frontiersin.org/articles/10.3389/fphys.2016.00651/full>.

172. TAT, J.et al. Carotid Atherosclerotic Plaque Alters the Direction of Longitudinal Motion in the Artery Wall. In *Ultrasound in Medicine & Biology* . 2016. Vol. 42, no. 9, p. 2114–2122.

173. RIBBERS, H.et al. Noninvasive two-dimensional strain imaging of arteries: validation in phantoms and preliminary experience in carotid arteries in vivo. In *Ultrasound in Medicine & Biology* . 2007. Vol. 33, no. 4, p. 530–540.

174. LIEBGOTT, H.et al. Transverse oscillations for tissue motion estimation. In *Physics Procedia* . 2010. Vol. 3, no. 1, p. 235–244.

175. HASEGAWA, H. Phase-Sensitive 2D Motion Estimators Using Frequency Spectra of Ultrasonic Echoes. In *Applied Sciences* . 2016. Vol. 6, no. 7, p. 195.

A LIST OF PUBLICATIONS RELATED TO THE DOCTORAL DISSERTATION

Publications indexed in the Web of Science with impact factor

1. **Makūnaitė, Monika**; Jurkonis, Rytis; Lukoševičius, Arūnas; Baranauskas, Mindaugas. Main uncertainties in the RF ultrasound scanning simulation of the standard ultrasound phantoms // *Sensors*. Basel : MDPI. ISSN 1424-8220. 2021, vol. 21, iss. 13, art. no. 4420, p. 1-23. DOI: 10.3390/s21134420. [Science Citation Index Expanded (Web of Science); Scopus; DOAJ] [IF: 3,576; Q1]
2. Rizi, Fereshteh Yousefi; Au, Jason; Yli-Ollila, Heikki; Golemati, Spyretta; **Makūnaitė, Monika**; Orkisz, Maciej; Navab, Nassir; MacDonald, Maureen; Laitinen, Tiina Marja; Behnam, Hamid; Gao, Zhifan; Gastounioti, Aimilia; Jurkonis, Rytis; Vray, Didier; Laitinen, Tomi; Sérusclat, André; Nikita, Konstantina S.; Zahnd, Guillaume. Carotid wall longitudinal motion in ultrasound imaging: an expert consensus review // *Ultrasound in medicine & biology*. Oxford: Elsevier. ISSN 0301-5629. eISSN 1879-291X. 2020, vol. 46, iss. 10, p. 2605-2624. DOI: 10.1016/j.ultrasmedbio.2020.06.006. [Science Citation Index Expanded (Web of Science); Scopus; MEDLINE] [IF: 2,514; Q1]
3. Baranauskas, Mindaugas; Jurkonis, Rytis; Lukoševičius, Arūnas; **Makūnaitė, Monika**; Matijošaitis, Vaidas; Gleiznienė, Rymantė; Rastenytė, Daiva. Ultrasonic assessment of the medial temporal lobe tissue displacements in Alzheimer's disease // *Diagnostics*. Basel: MDPI AG. ISSN 2075-4418. 2020, vol. 10, iss. 7, art. no. 452, p. 1-14. DOI: 10.3390/diagnostics10070452. [Science Citation Index Expanded (Web of Science); Scopus; DOAJ] [IF: 3,110; Q1]
4. Jurkonis, Rytis; **Makūnaitė, Monika**; Baranauskas, Mindaugas; Lukoševičius, Arūnas; Sakalauskas, Andrius; Matijošaitis, Vaidas; Rastenytė, Daiva. Quantification of endogenous brain tissue displacement imaging by radiofrequency ultrasound // *Diagnostics*. Basel: MDPI. ISSN 2075-4418. 2020, vol. 10, iss. 2, art. no. 57, p. 1-16. DOI: 10.3390/diagnostics10020057. [Science Citation Index Expanded (Web of Science); Scopus; DOAJ] [IF: 3,110; Q1]
5. **Makūnaitė, Monika**; Jurkonis, Rytis; Rodriguez-Martinez, Alberto; Jurgaitienė, Rūta; Semaška, Vytenis; Mėlinytė, Karolina; Kubilius, Raimondas. Ultrasonic parametrization of arterial wall movements in low- and high-risk CVD subjects // *Applied sciences*. Basel: MDPI. ISSN 2076-3417. 2019, vol. 9, iss. 3, art. no. 465, p. 1770-1773. DOI: 10.3390/app9030465. [Science Citation Index Expanded (Web of Science); Scopus; DOAJ] [IF: 2,474; Q2]

Publications indexed in the Web of Science without impact factor

1. **Makūnaitė, Monika**; Jurkonis, Rytis; Matijošaitis, Vaidas; Rastenytė, Daiva. Ultrasonic mapping of endogenous motion in brain tissue // *2019 IEEE international ultrasonics symposium (IUS)*, Glasgow, Scotland, October 6-9, 2019. Piscataway, NJ: IEEE, 2019. ISBN 9781728145976. eISBN 9781728145969. ISSN 1948-5719. p. 2408-2411. DOI: 10.1109/ULTSYM.2019.8925971.
2. **Zambacevičienė, Monika**; Jurkonis, Rytis; Gelman, Sigita; Sakalauskas, Andrius. RF ultrasound based estimation of pulsatile flow induced microdisplacements in phantom // *IFMBE proceedings: World congress on medical physics and biomedical engineering 2018*, June 3-8, 2018, Prague, Czech Republic / L. Lhotska, L. SukupovaIgor, I. Lacković, G.S. Ibbott (eds.). Singapore: Springer, 2018. ISBN 9789811090349. eISBN 9789811090356. ISSN 1680-0737. eISSN 1433-9277. 2018, vol. 68, iss. 1, p. 601-605. DOI: 10.1007/978-981-10-9035-6_112.
3. **Zambacevičienė, Monika**; Jurkonis, Rytis. RF ultrasound based longitudinal motion estimation of carotid artery wall: feasibility study // *IFMBE proceedings: World congress on medical physics and biomedical engineering 2018*, June 3-8, 2018, Prague, Czech Republic / L. Lhotska, L. SukupovaIgor, I. Lacković, G.S. Ibbott (eds.). Singapore : Springer, 2018. ISBN 9789811090370. eISBN 9789811090387. ISSN 1680-0737. eISSN 1433-9277. 2018, vol. 68, iss. 2, p. 253-257. DOI: 10.1007/978-981-10-9038-7_47.

Reports in the national conferences

1. **Makūnaitė, Monika**. Išilginis miego arterijos sienelės judesys ankstyvai aterosklerozei diagnozuoti // *Bioateitis: gamtos ir gyvybės mokslų perspektyvos: 12-oji jaunųjų mokslininkų konferencija*, 2019 m. gruodžio 11 d.: programa ir pranešimų santraukos. Kaunas : Lietuvos sveikatos mokslų universitetas. 2019, p. 21-22. [M.kr.: T 001]

List of the attended conferences

1. **Makūnaitė, Monika**. Išilginis miego arterijos sienelės judesys ankstyvai aterosklerozei diagnozuoti. In *Bioateitis: gamtos ir gyvybės mokslų perspektyvos*, Kaunas, Lithuania, December 11, 2019.
2. **Makūnaitė, Monika**; Jurkonis, Rytis; Matijošaitis, Vaidas; Rastenytė Daiva. Ultrasonic mapping of endogenous motion in brain tissue. In 2019 IEEE International Ultrasonics Symposium (IUS), Glasgow, Scotland, October 6-9, 2019.
3. **Zambacevičienė, Monika**; Jurkonis, Rytis; Gelman, Sigita; Sakalauskas, Andrius. RF ultrasound based estimation of pulsatile flow induced microdisplacements in phantom. In *World congress on medical physics and*

biomedical engineering (IUPESM 2018), Prague, Czech Republic, June 3-8, 2018.

4. **Zambacevičienė, Monika**; Jurkonis, Rytis. RF ultrasound based longitudinal motion estimation of carotid artery wall: feasibility study. In *World congress on medical physics and biomedical engineering* (IUPESM 2018), Prague, Czech Republic, June 3-8, 2018.

APPENDIX A1

Table A1.1. Wall motion extraction techniques based on the B-mode ultrasound imaging (chronological order), adapted from [27]

Study	Technique	Data	Accuracy evaluation	
			Criteria	Score
Golemati et al. (2003)[88]	BM	11 symptomatic patients, 9 asymptomatic patients	No quantitative evaluation of accuracy	-
Persson et al. (2003)[22]	Echo tracking	1 healthy volunteer	No quantitative evaluation of accuracy	-
Cinthio et al. (2005)[23]	Echo tracking	1 healthy volunteer, 1 agar phantom	Mean differences compared with two high-resolution triangulation lasers	Longitudinal: 5.9 ± 40.5 μm Radial: 28.5 ± 19.5 μm
Stoitsis et al. (2006)[106]	BM and OF	10 healthy volunteers	Cross-correlation coefficient between BM and OF	Longitudinal: 0.32 ± 0.39 mm Radial: 0.72 ± 0.22 mm
Gastounioti et al. (2011)[91]	BM + Kalman filtering as an adaptive strategy with (a) updating of reference block and (b) updating of displacements	5 young healthy volunteers (age: 25–32), 4 elderly healthy volunteers (age: 44–73)	Tracking accuracy compared with conventional BM	Adaptive BM minimized the warping index and yielded average displacement error reductions of 24 % with respect to BM. The estimation bias reduction of 30 % with respect to BM Jitter over varying center frequencies reduction of 64 % with respect to BM
Zahnd et al. (2011)[25]	Multi-BM ruled by a deformable	26 young healthy volunteers,	Qualitative evaluation only (visual	-

	skeleton model	26 elderly diabetic patients	control by two experts)	
Golemati et al. (2012)[61]	Comparison of several existing methods: OF, WLSOF, BM, ABMM	Real image template and Field II	Average warping indices between OF, WLOF, BM, and ABMM	WLSOF: 105 µm ABMM: 120 µm BM: 405 µm OF: 694 µm
Salles et al. (2012)[105]	Phase-based OF	1 healthy volunteer	Qualitative evaluation only	-
Zahnd et al. (2012)[97]	Multi-BM guided by contour segmentation	126 indigenous Australians with periodontal disease, 27 healthy age- and sex-matched Caucasian controls	Qualitative evaluation only (visual control by two experts)	-
Zahnd et al. (2013)[19]	Kalman-based BM	57 young healthy volunteers, 25 diabetic patients	Average absolute error (±SD) from manual reference tracings	Longitudinal = 20 ± 19 µm Radial = 84 ± 107 µm
Gastounioti et al. (2013)[90]	Adaptive BM	40 patients, 1 *in silico* phantom	Tracking accuracy compared with the conventional BM	Adaptive BM algorithm, yielding a 47 % increase in accuracy with respect to the conventional BM
Yli-Ollila et al. (2013)[63]	BM + luminance optimization	19 healthy volunteers	Reproducibility	Cronbach's α coefficient: 0.59–0.97
Albinsson et al. (2014)[92]	Lagrangian BM	20 healthy volunteers, 1 simulated (Field II [Jensen 1996]), 1 *in silico* phantom	Absolute tracking error compared with Cinthio et al. (2005)	*In silico*: Improvement of tracking accuracy (mean = 48 %, $p < 0.005$) Phantom: Improvement of tracking accuracy (mean = 43 %, $p < 0.01$)

				In vivo: Reduction of block size with similar tracking performance (mean = 19 %, $p < 0.01$)
Gao et al. (2015)[170]	BM + H_∞ filter	50 patients	Mean absolute tracking difference compared with the manual annotations	Mean absolute estimation error: Longitudinal: 96 μm, Radial: 46 μm
Salles et al. (2012)[105]	Phase-based BM	1 simulated RF clip (Field II), 10 healthy volunteers	Mean absolute amplitude difference, evaluated on a numerical phantom	Longitudinal: 9.9 ± 7.9 μm Radial: 4.2 ± 3.4 μm
Yli-Ollila et al. (2016)[171]	Transfer function analysis	19 healthy volunteers	Reproducibility	Longitudinal: Cronbach's α coefficient: 0.59–0.97 Radial: Cronbach's α coefficient, 0.68–0.93
Tat et al. (2016)[172]	Multi-BM	23 healthy volunteers, 12 patients	Not specified	-
Gao et al. (2017)[95]	Elasticity-based state-space approach	37 healthy volunteers, 103 patients	Correlation coefficient (r) and RMSE against manual tracings	Radial: $r = 0.9897$ RMSE = 25.98 μm Longitudinal: $r = 0.9536$ RMSE = 142.82 μm
Scaramuzzino et al. (2017)[107]	Automatic detection and matching of multiple salient points + scale-invariant feature transform	1 *in silico* phantom, 18 healthy volunteers, 16 patients	Accuracy, Average absolute error (±SD), Maximum variation, Coefficient, Correlation coefficient	*In silico* *Intima–media* complex: 23 ± 15 μm *Adventitia*: 19 ± 18 μm *In vivo* *Intima–media* complex: 9.5 (variation coefficient, over 5 repeated measures) Adventitia: 13.8 % (variation coefficient, over 5 repeated measures)

				Compared with the visual assessment performed by 2 physicians, $r = 0.7$
Gao et al. (2017)[94]	Non-linear state space with a time-variant control signal based on the mathematical model of the carotid dynamics	30 simulated sequences, 22 healthy volunteers, 81 patients	Intraclass correlation	*In silico* Accuracy 0.1161–0.1260 mm *In vivo* *Longitudinal* Intraclass correlation ≥ 0.9948 95 % CI = 0.8871 mm *Radial* Intraclass correlation ≥ 0.9966 95 % CI = 0.4159 mm
Zahnd et al. (2018)[101]	Dynamic BM	62 elderly patients at high cardiovascular risk	Average absolute error (±SD) from manual reference tracings	150 ± 163 µm
Albinsson et al. (2018)[98]	Parabolic sub-sample and grid slope sub-sample interpolation for 2-D BM	1 healthy volunteer, 1 phantom, 1 *in silico* simulation (Field II)	Absolute sub-sample estimation errors	Reduced by 24 % on phantom data Reduced by 15 % on *in silico* data

BM = block matching; OF = optical flow; WLSOF = weighted least-squares optical flow; ABMM = affine block motion model; RMSE = root mean square error; SD = standard deviation; CI = confidence interval.

Table A1.2. Wall motion extraction techniques based on the RF ultrasound signals (chronological order), adapted from [27]

Study	**Technique**	**Hardware, format of RF data**	**Data**	**Performance**
Ribbers et al. (2007)[173]	Cross-correlation	$f_r = 25$ Hz $f_s = 39$ MHz $f_c = 11$ MHz 15-6 L linear array Philips Sonos 7500 real-time 3-D echo scanner B	1 physical phantom, 12 patients	No quantitative analysis of the *in vivo* results was performed

Zahnd et al. (2015)[20]	Local phase-based OF (Basarab et al. 2009[129])	$f_r = 91$ Hz $f_s = 50$ MHz $fc = 4$ MHz, fs50 MHz, ULA-OP research scanner	20 young healthy volunteers, 6 elderly patients	Longitudinal: 98 ± 84 μm Radial: 55 ± 44 μm
Salles et al. (2015)[117]	Transverse oscillations (Liebgott et al. 2010[174])	$f_r = 10$ kHz $f_c = 5$ MHz $f_s = 40$ MHz L14-5 W/60 array Ultrasonix SonixTouch US system (Richmond, BC, Canada)	3 artery numerical phantoms	Mean axial error: 4.2 ± 3.4 μm Mean lateral errors: 9.9 ± 7.9 μm Stiffness of the 3 vessel phantom walls that were investigated was estimated with an average relative error of 2.2 %
Hasegawa (2016)[175]	Phase tracking with frequency spectra	$f_r = 1302$ Hz $f_s = 31.25$ MHz $f_c = 7.5$ MHz Linear array PU-0558 Ueda Japan Radio (scanner RSYS0002, Microsonic, Tokyo, Japan)	1 phantom	Bias error 1-D: $R_a = 11.5$ %, $L_o = 2.0$ % Bias error 2-D: $R_a = 3.0$ %, $L_o = 2.0$ %
Zambacevičienė and Jurkonis (2019)[122]	Phase correlation and sub-sample algorithm	$f_r = 52$ Hz $f_s = 40$ MHz $f_c = 14$–5 MHz Linear array Scanner Ultrasonix SonixTouch	1 phantom	NRMSE of detected motion amplitude: 0.21–0.41 μm Coefficient of correlation = 0.95–0.98 in case of any determined longitudinal motion function when the phase correlation, sub-pixel algorithm, and additional filtering were used
Miyajo and Hasegawa (2018)[127]	Matching performed in 2-D Fourier domain	Scanner α-10 Aloka $f_r = 3472$ Hz $f_s = 40$ MHz $f_c = 10$ MHz	1 phantom, 1 healthy volunteer	Bias error and SD in lateral velocity estimates: 0.048 and 0.282 mm/s

Perrot et al. (2018)[130]	Video magnification	f_r = 2500 Hz f_s = 25 MHz f_c = 5 MHz Linear array L7-4 (Scanner Verasonics Inc., Redmond, WA, USA) Reconstruction technique: Stolts	8 healthy volunteers	Motion magnification by a factor of 1000

RF = radiofrequency; OF = optical flow; NRMSE = normalized root mean square error; fr = frame rate; fs = sample frequency; fc = center frequency.

APPENDIX A2

Radial motion estimated by 1D cross-correlation and evaluation of the mean absolute error (MAE), normalized root-mean-square error (NRMSE), and Pearson correlation coefficient between the estimated and theoretical radial motion. Radial motion map in scanning plane with preselected five points from where the estimated motion is taken and depicted together with the theoretical radial motion. There, the vertical dashed line corresponds to the time of the moment of maximal theoretical displacement. At this time moment, a radial motion map is depicted. Finally, MAE, NRMSE, and Pearson correlation coefficient are evaluated in the midline of the motion map at different axial positions, i.e., starting from 11 mm every 1 mm to 29 mm. Inter-frame radial displacements are accumulated relative to the first frame, resulting in radial motion. The white areas in the motion map correspond to the regions where inter-frame motion is higher than a quarter of the wavelength, and there exists a probability to identify false correlation peak, resulting in large tracking errors that are known as “peak hopping” errors.

27 years old female, theoretical radial motion peak-to-peak amplitude is 1 mm

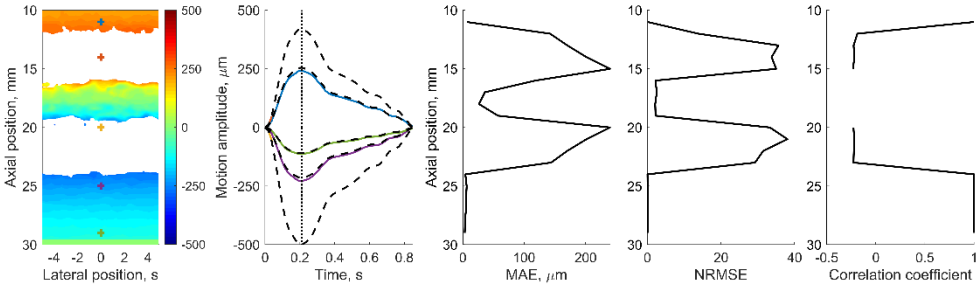

27 years old female, theoretical radial motion peak-to-peak amplitude is 0.75 mm

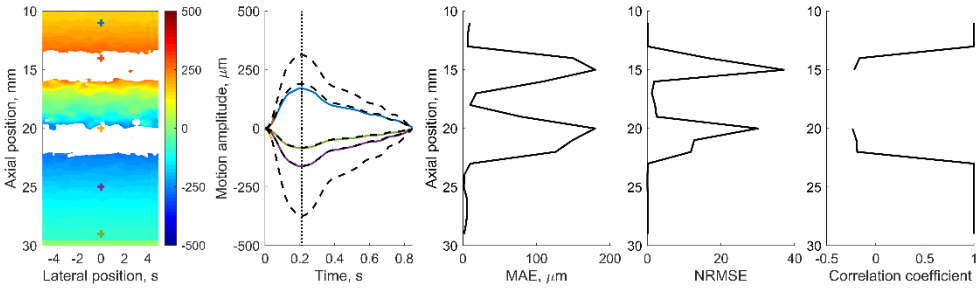

27 years old female, theoretical radial motion peak-to-peak amplitude is 0.5 mm

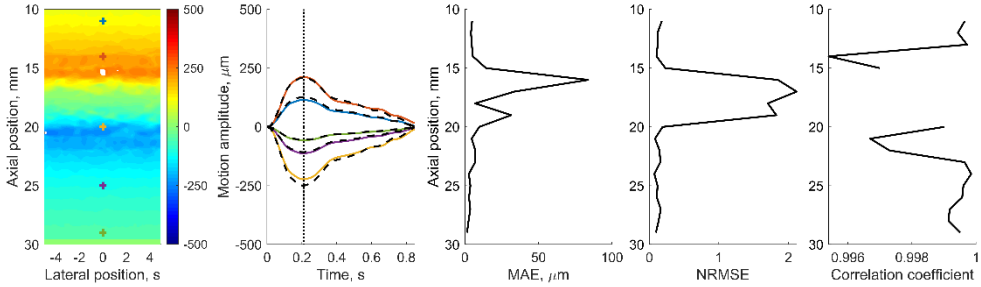

23 years old male, theoretical radial motion peak-to-peak amplitude is 1 mm

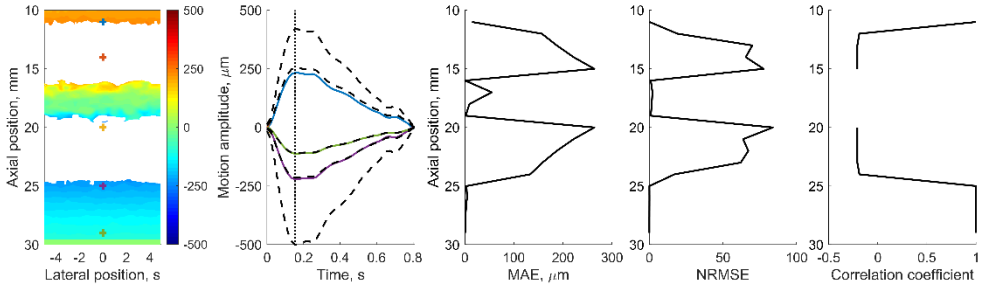

23 years old male, theoretical radial motion peak-to-peak amplitude is 0.75 mm

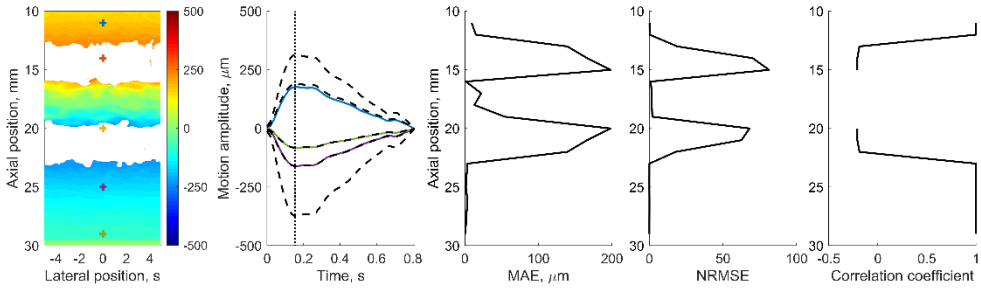

23 years old male, theoretical radial motion peak-to-peak amplitude is 0.5 mm

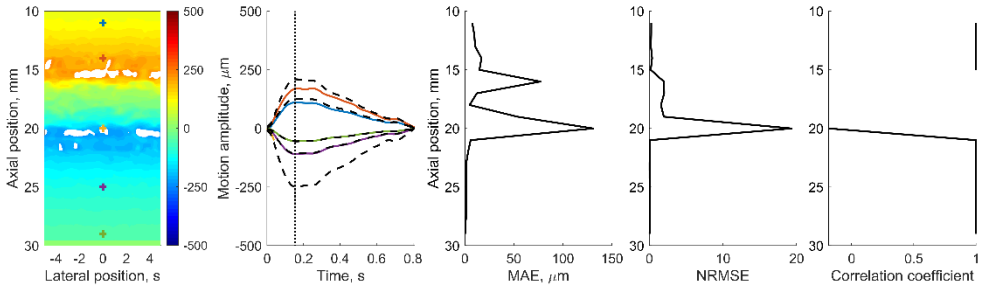

24 years old female, theoretical radial motion peak-to-peak amplitude is 1 mm

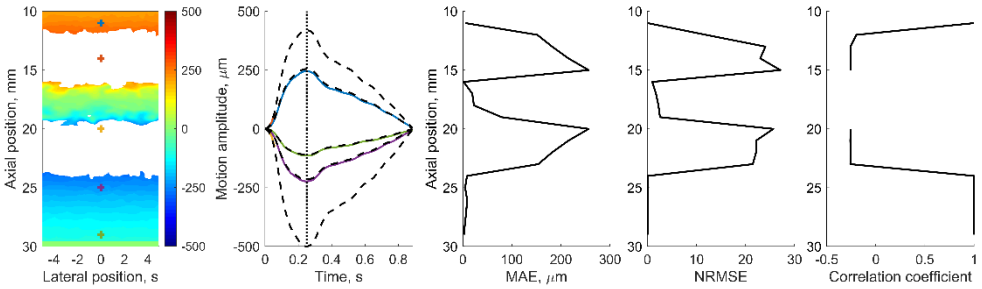

24 years old female, theoretical radial motion peak-to-peak amplitude is 0.75 mm

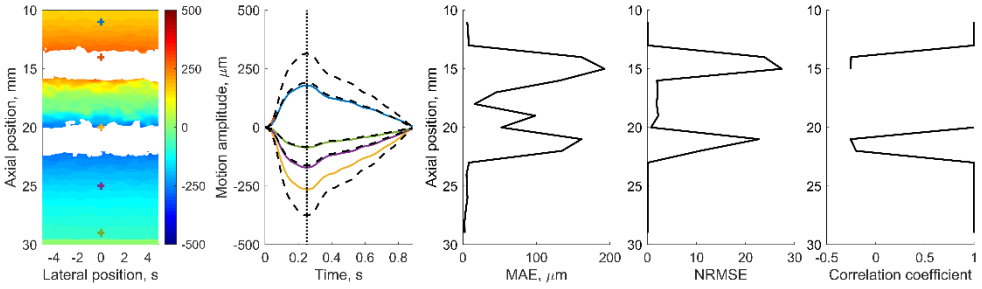

24 years old female, theoretical radial motion peak-to-peak amplitude is 0.5 mm

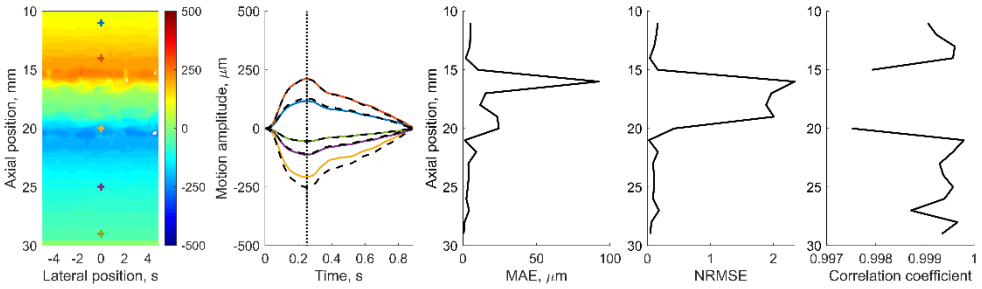

56 years old male, theoretical radial motion peak-to-peak amplitude is 0.75 mm

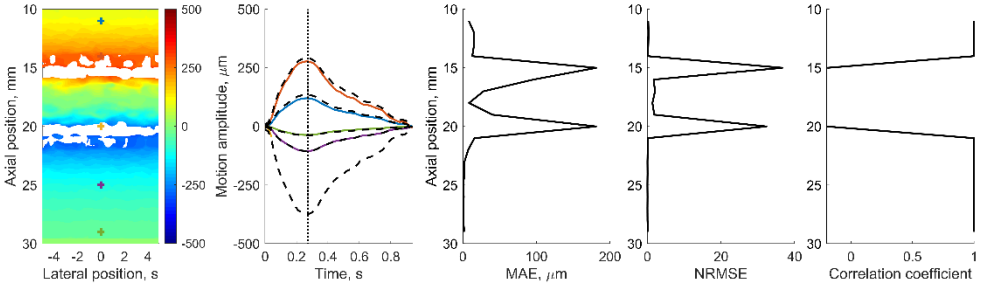

56 years old male, theoretical radial motion peak-to-peak amplitude is 0.5 mm

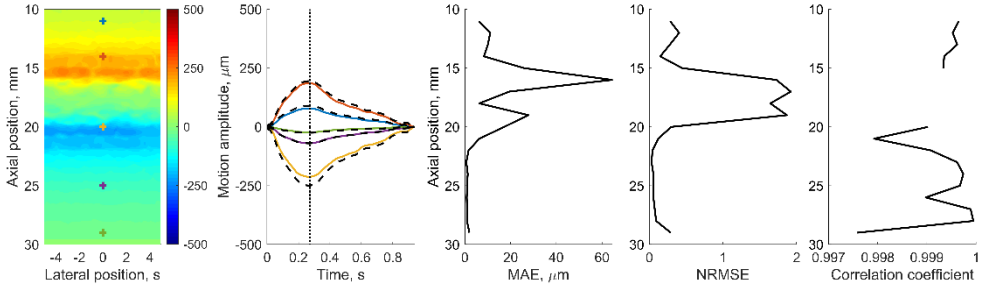

56 years old male, theoretical radial motion peak-to-peak amplitude is 0.25 mm

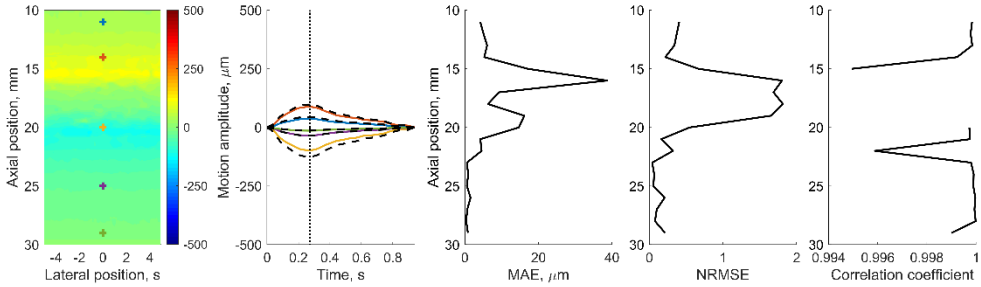

61 years old male, theoretical radial motion peak-to-peak amplitude is 0.75 mm

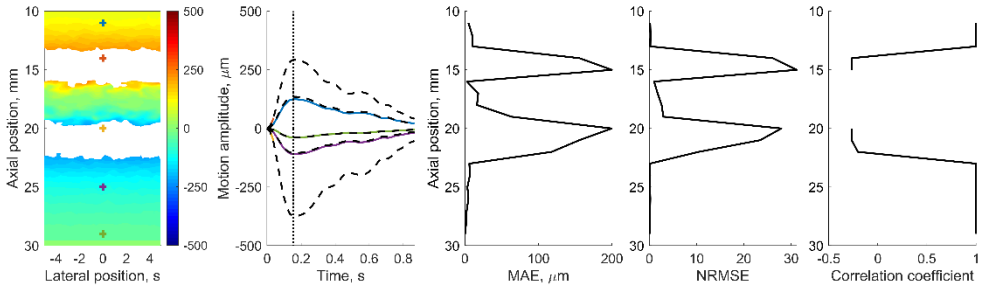

61 years old male, theoretical radial motion peak-to-peak amplitude is 0.5 mm

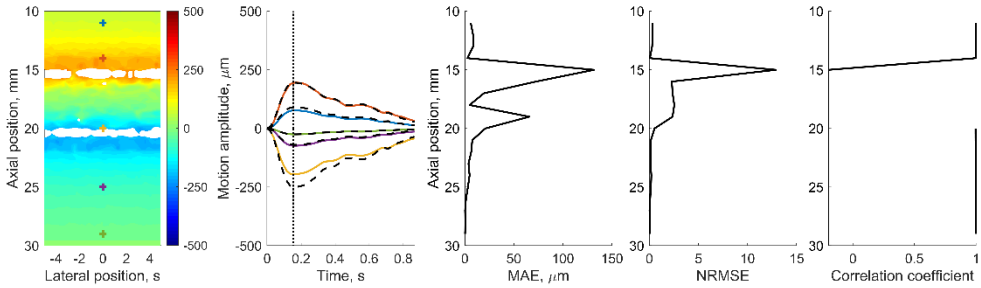

61 years old male, theoretical radial motion peak-to-peak amplitude is 0.25 mm

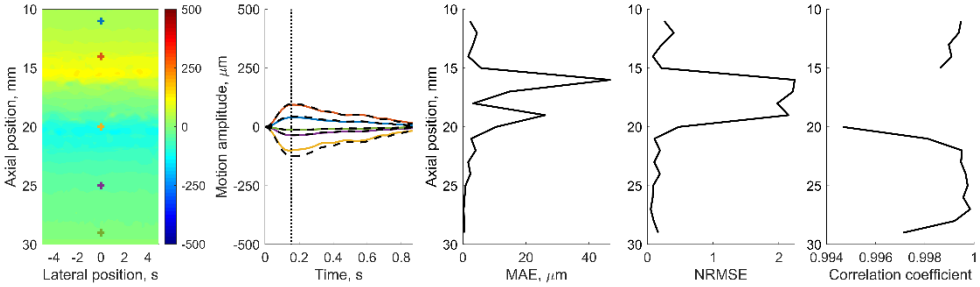

47 years old male, theoretical radial motion peak-to-peak amplitude is 0.75 mm

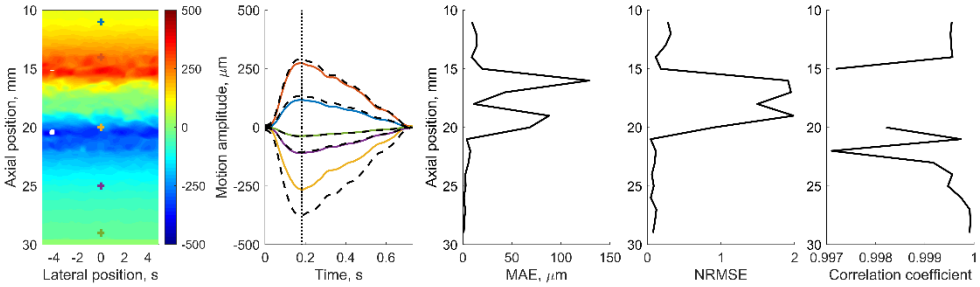

47 years old male, theoretical radial motion peak-to-peak amplitude is 0.5 mm

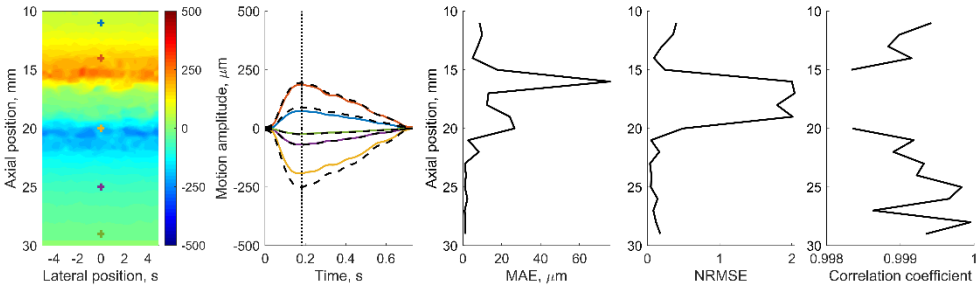

47 years old male, theoretical radial motion peak-to-peak amplitude is 0.25 mm

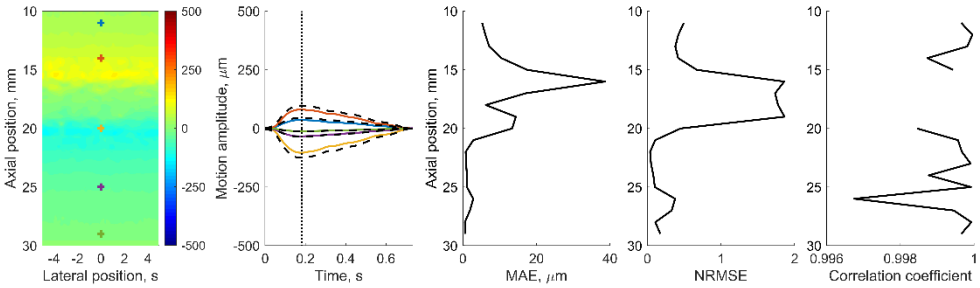

Radial motion estimated by OpenOpticalFlow and evaluation of the mean absolute error (MAE), normalized root-mean-square error (NRMSE), and Pearson correlation coefficient between the estimated and theoretical radial motion. Radial motion map in scanning plane with preselected five points from where the estimated motion is taken and depicted together with the theoretical radial motion. There, the vertical dashed line corresponds to the time of the moment of maximal theoretical displacement. At this time moment, a radial motion map is depicted. Finally, MAE, NRMSE, and Pearson correlation coefficient are evaluated in the midline of the motion map at different axial positions, i.e., starting from 11 mm every 1 mm to 29 mm. Inter-frame radial displacements are accumulated relative to the first frame, resulting in the radial motion.

27 years old female, theoretical radial motion peak-to-peak amplitude is 1 mm

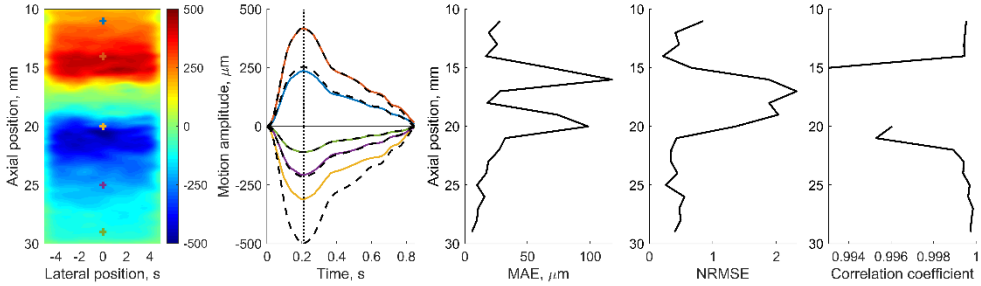

27 years old female, theoretical radial motion peak-to-peak amplitude is 0.75 mm

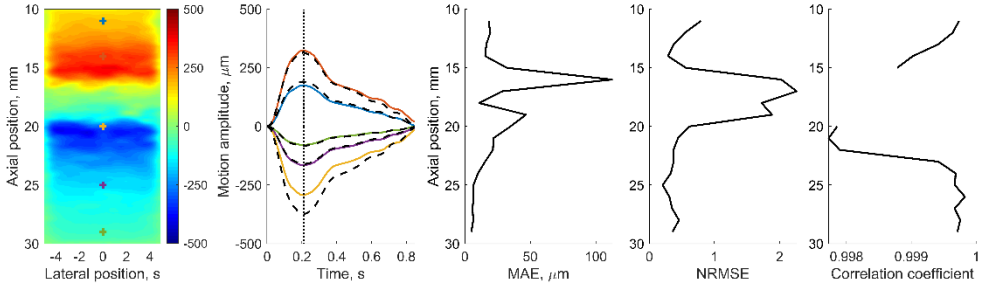

27 years old female, theoretical radial motion peak-to-peak amplitude is 0.5 mm

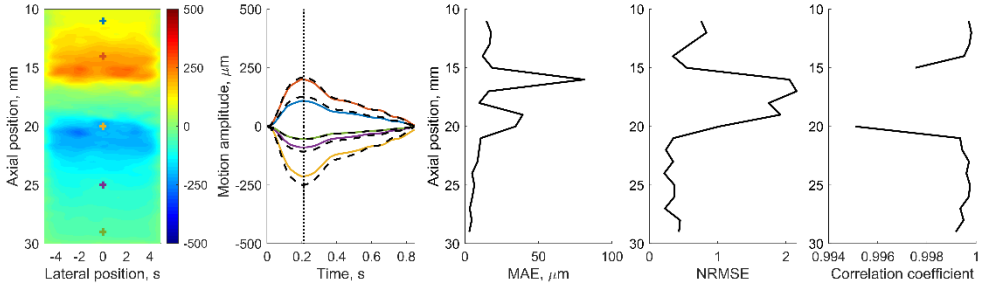

23 years old male, theoretical radial motion peak-to-peak amplitude is 1 mm

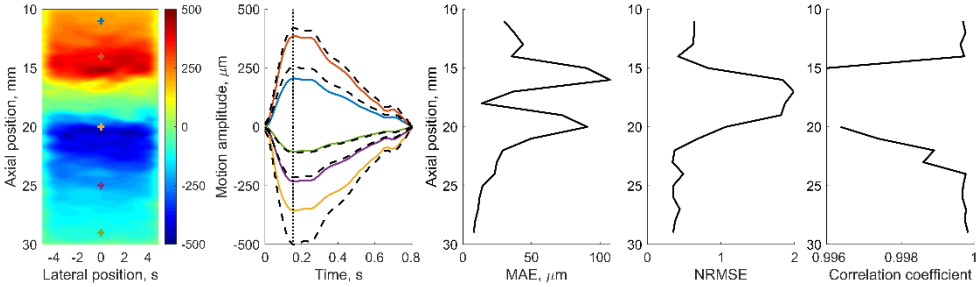

23 years old male, theoretical radial motion peak-to-peak amplitude is 0.75 mm

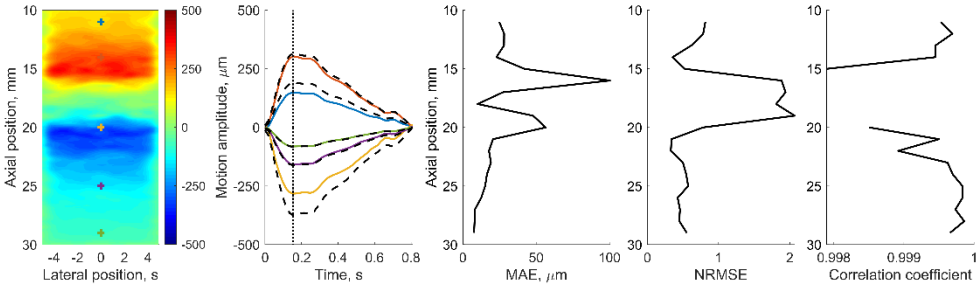

23 years old male, theoretical radial motion peak-to-peak amplitude is 0.5 mm

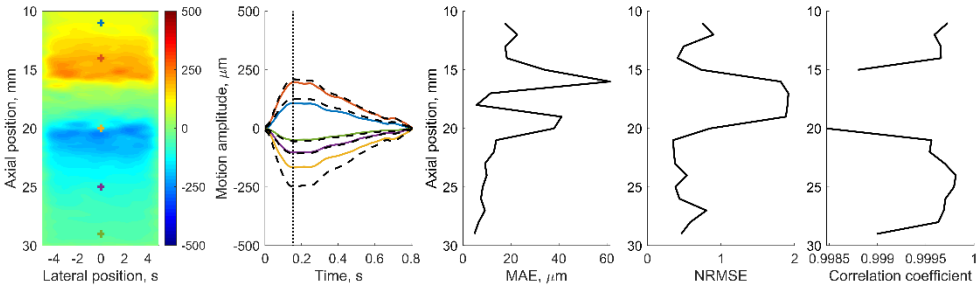

24 years old female, theoretical radial motion peak-to-peak amplitude is 1 mm

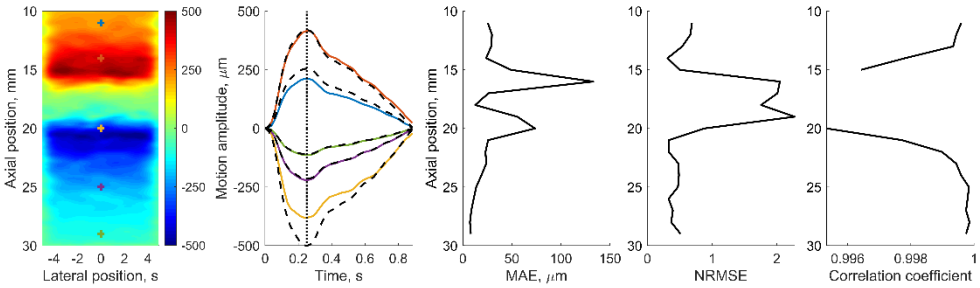

24 years old female, theoretical radial motion peak-to-peak amplitude is 0.75 mm

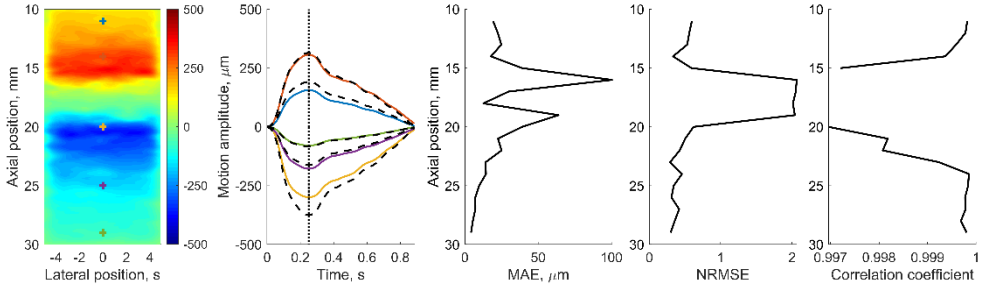

24 years old female, theoretical radial motion peak-to-peak amplitude is 0.5 mm

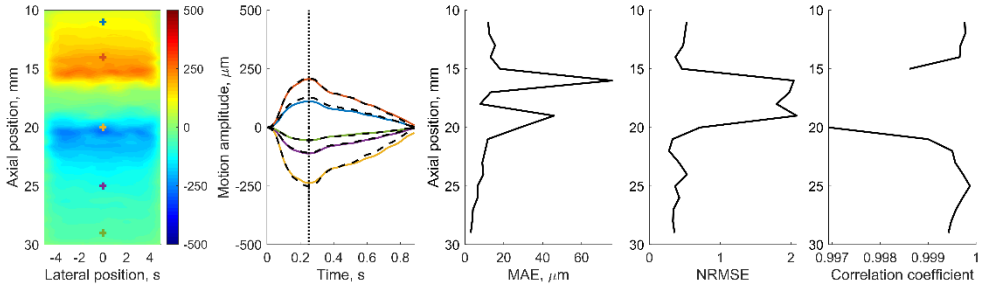

56 years old male, theoretical radial motion peak-to-peak amplitude is 0.75 mm

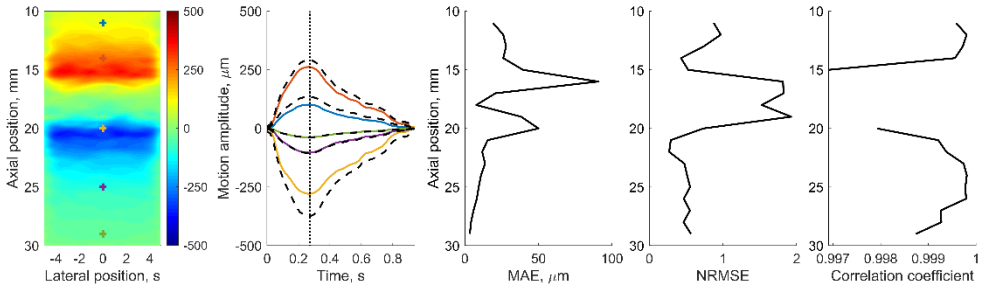

56 years old male, theoretical radial motion peak-to-peak amplitude is 0.5 mm

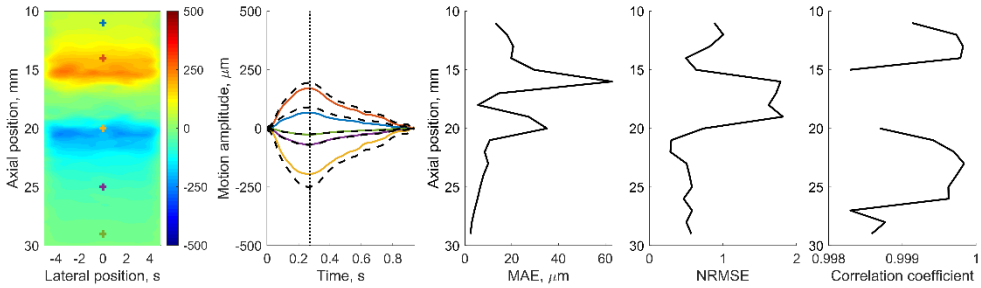

56 years old male, theoretical radial motion peak-to-peak amplitude is 0.25 mm

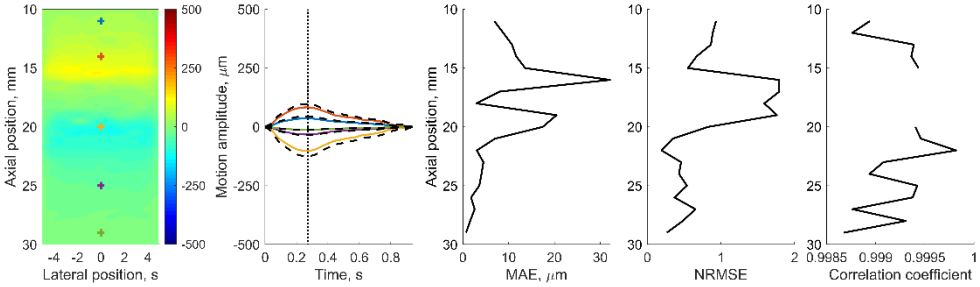

61 years old male, theoretical radial motion peak-to-peak amplitude is 0.75 mm

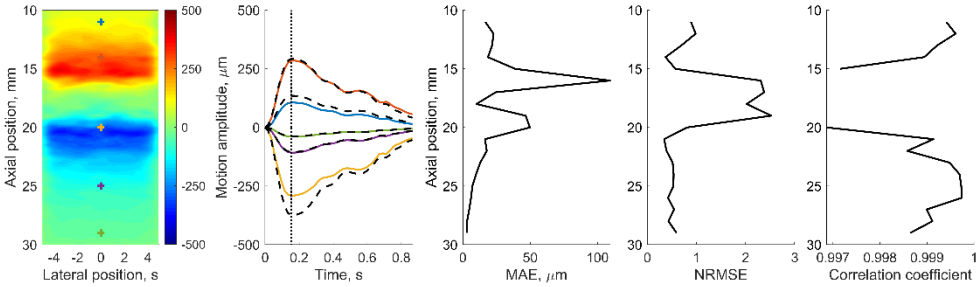

61 years old male, theoretical radial motion peak-to-peak amplitude is 0.5 mm

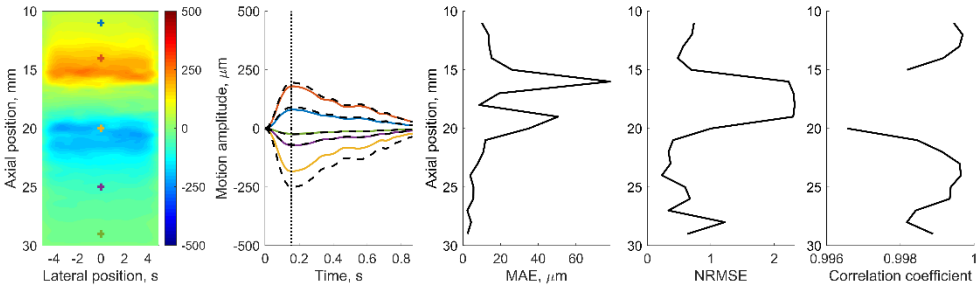

61 years old male, theoretical radial motion peak-to-peak amplitude is 0.25 mm

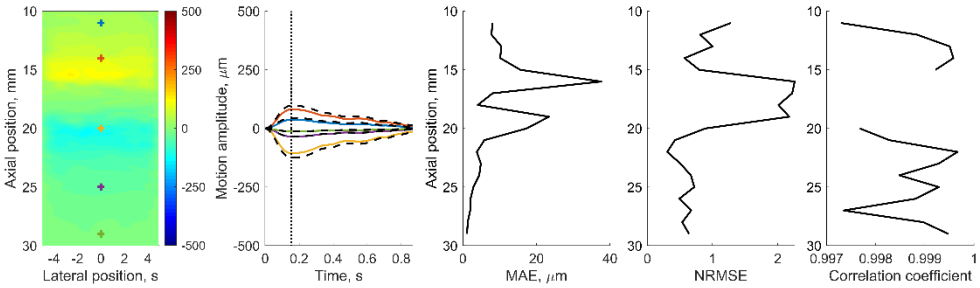

47 years old male, theoretical radial motion peak-to-peak amplitude is 0.75 mm

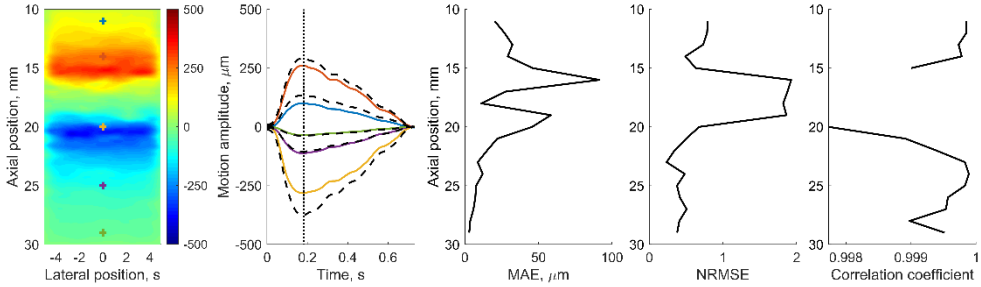

47 years old male, theoretical radial motion peak-to-peak amplitude is 0.5 mm

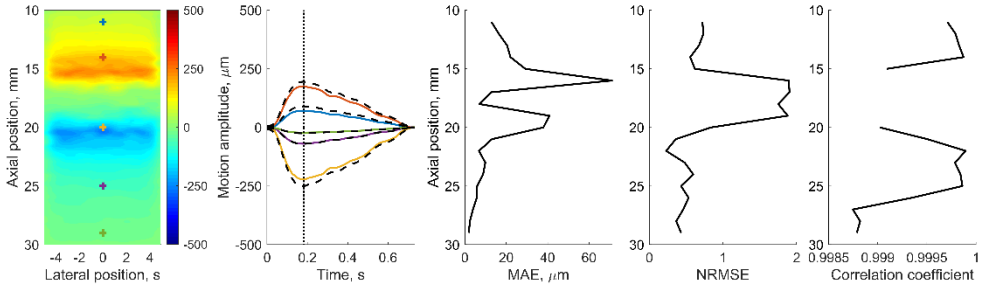

47 years old male, theoretical radial motion peak-to-peak amplitude is 0.25 mm

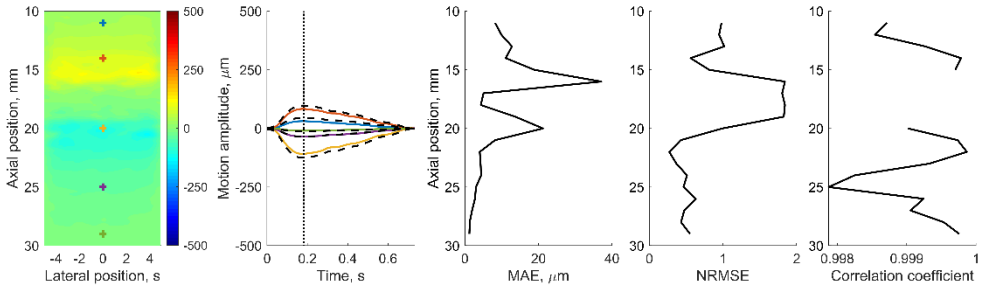

Longitudinal motion estimated by OpenOpticalFlow and evaluation of the mean absolute error (MAE), normalized root-mean-square error (NRMSE), and Pearson correlation coefficient between the estimated and theoretical longitudinal motion. Longitudinal motion map in scanning plane with preselected three points from where the estimated motion is taken and depicted together with the theoretical longitudinal motion. There, the vertical dashed line corresponds to the time of the moment of maximal positive theoretical displacement. At this time moment, a longitudinal motion map is depicted. Finally, MAE, NRMSE, and Pearson correlation coefficient are evaluated in the midline of the motion map at different axial positions, i.e., starting from 11 mm every 1 mm to 29 mm. Inter-frame longitudinal displacements are accumulated relative to the first frame, resulting in the longitudinal motion.

27 years old female, theoretical longitudinal motion peak-to-peak amplitude is 1 mm

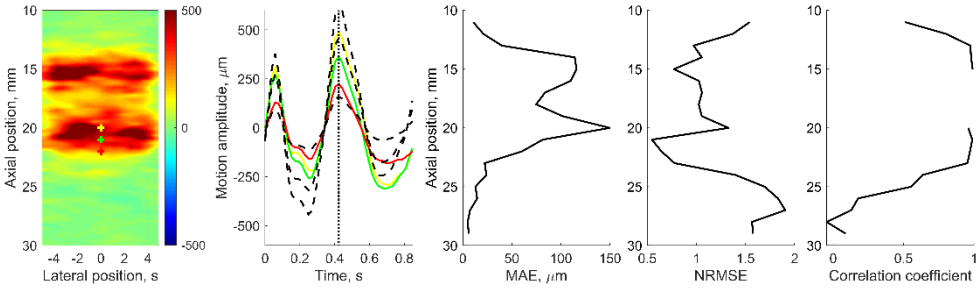

27 years old female, theoretical longitudinal motion peak-to-peak amplitude is 0.75 mm

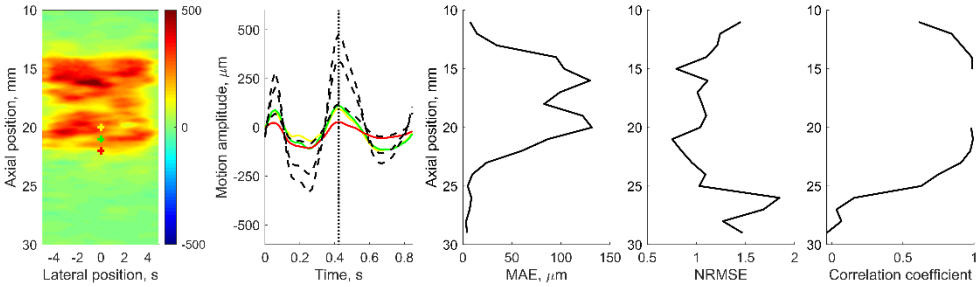

27 years old female, theoretical longitudinal motion peak-to-peak amplitude is 0.5 mm

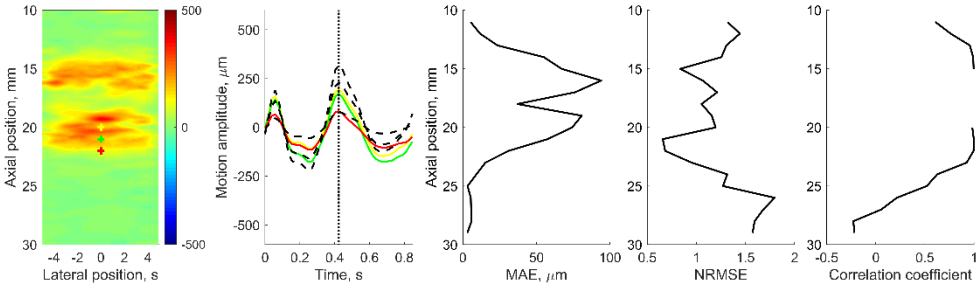

23 years old male, theoretical longitudinal motion peak-to-peak amplitude is 1 mm

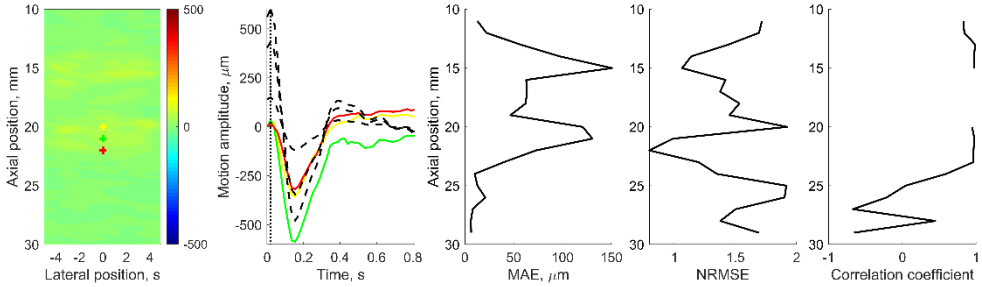

23 years old male, theoretical longitudinal motion peak-to-peak amplitude is 0.75 mm

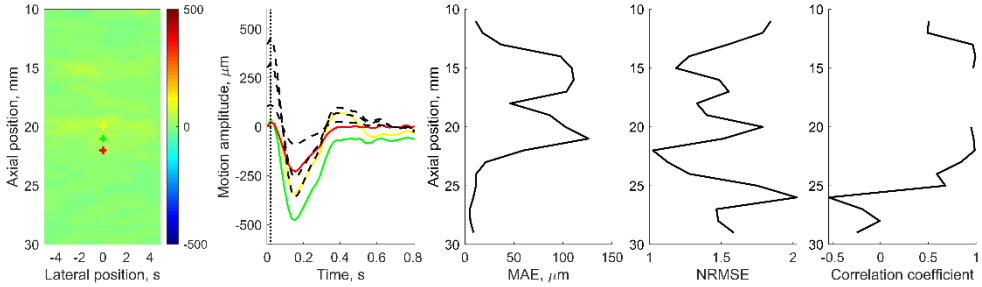

23 years old male, theoretical longitudinal motion peak-to-peak amplitude is 0.5 mm

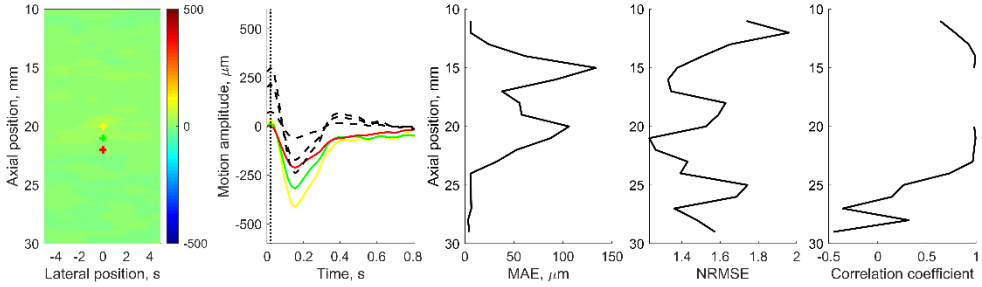

24 years old female, theoretical longitudinal motion peak-to-peak amplitude is 1 mm

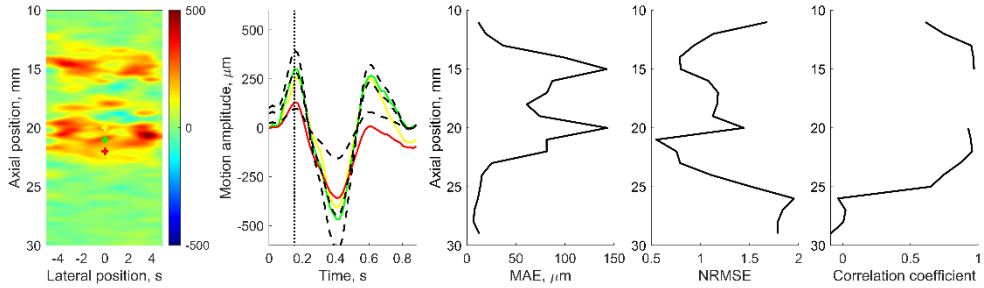

24 years old female, theoretical longitudinal motion peak-to-peak amplitude is 0.75 mm

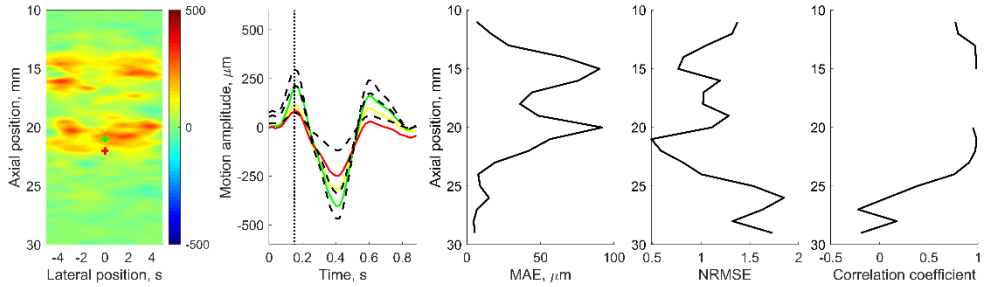

24 years old female, theoretical longitudinal motion peak-to-peak amplitude is 0.5 mm

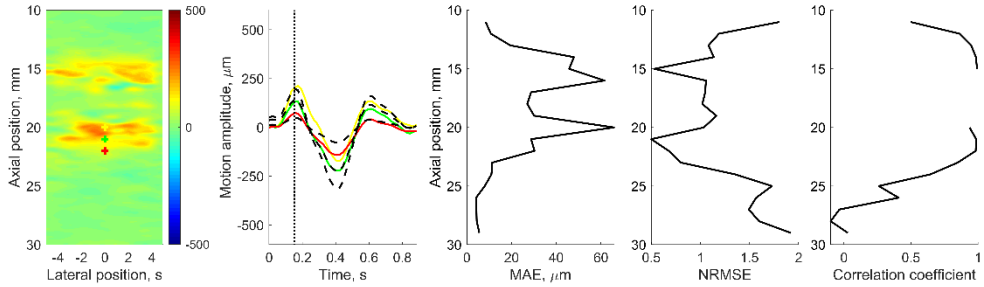

56 years old male, theoretical longitudinal motion peak-to-peak amplitude is 0.75 mm

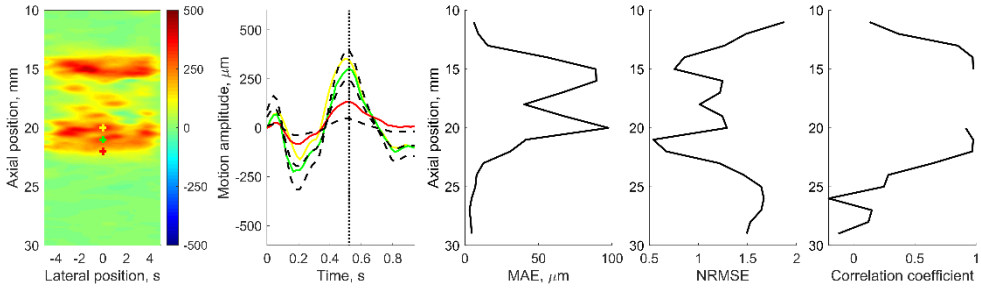

56 years old male, theoretical longitudinal motion peak-to-peak amplitude is 0.5 mm

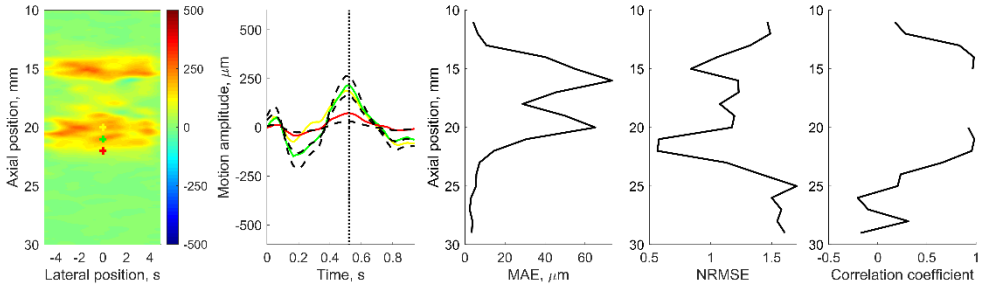

56 years old male, theoretical longitudinal motion peak-to-peak amplitude is 0.25 mm

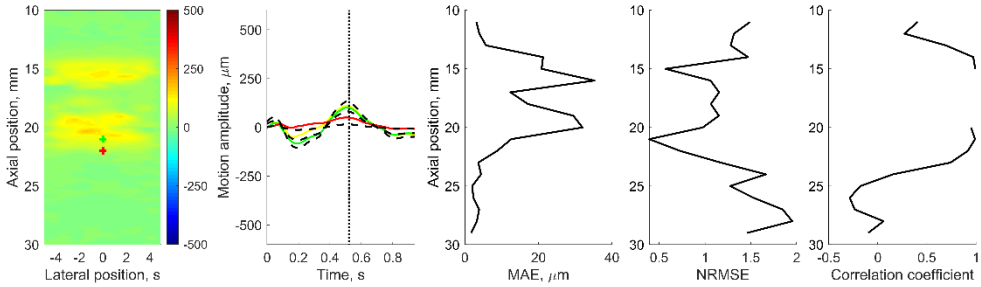

61 years old male, theoretical longitudinal motion peak-to-peak amplitude is 0.75 mm

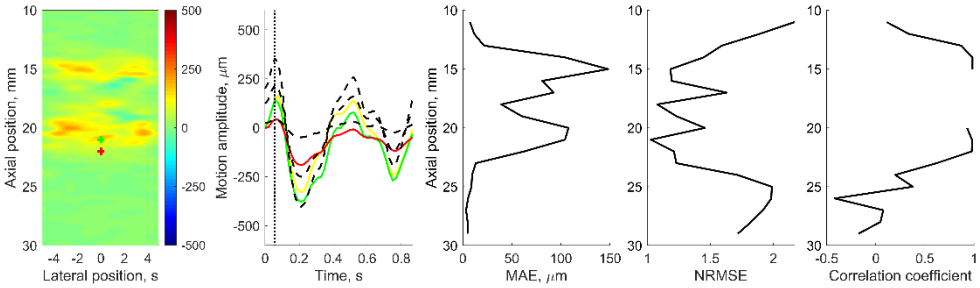

61 years old male, theoretical longitudinal motion peak-to-peak amplitude is 0.5 mm

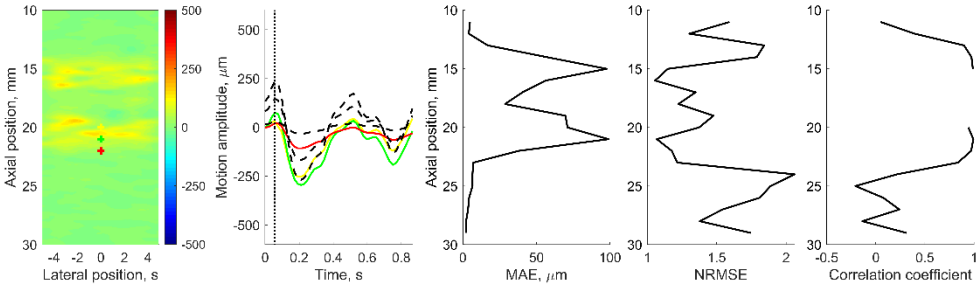

61 years old male, theoretical longitudinal motion peak-to-peak amplitude is 0.25 mm

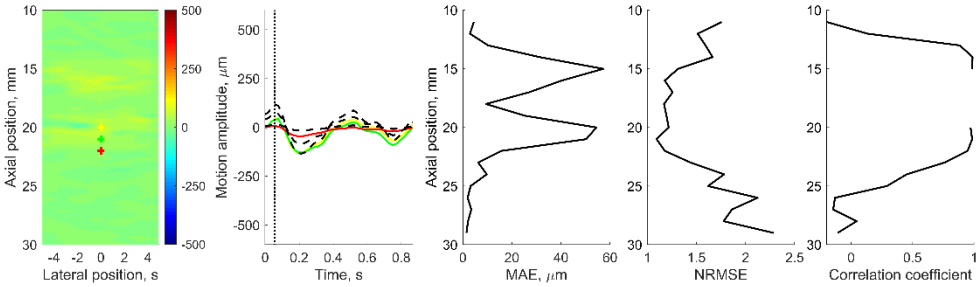

47 years old male, theoretical longitudinal motion peak-to-peak amplitude is 0.75 mm

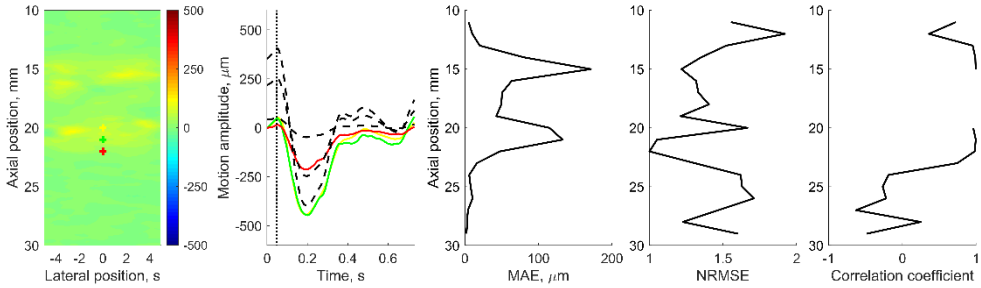

47 years old male, theoretical longitudinal motion peak-to-peak amplitude is 0.5 mm

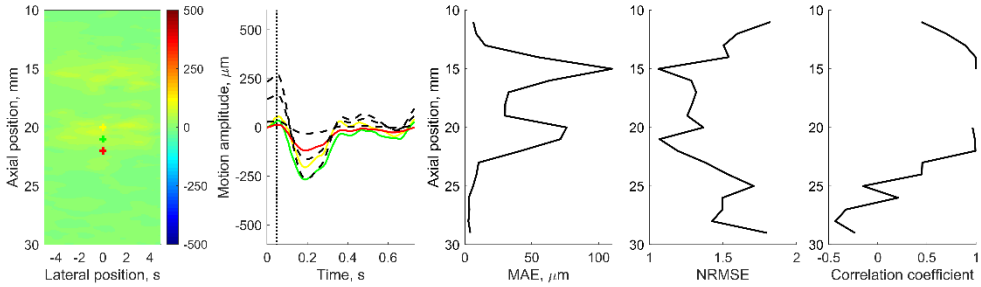

47 years old male, theoretical longitudinal motion peak-to-peak amplitude is 0.25 mm

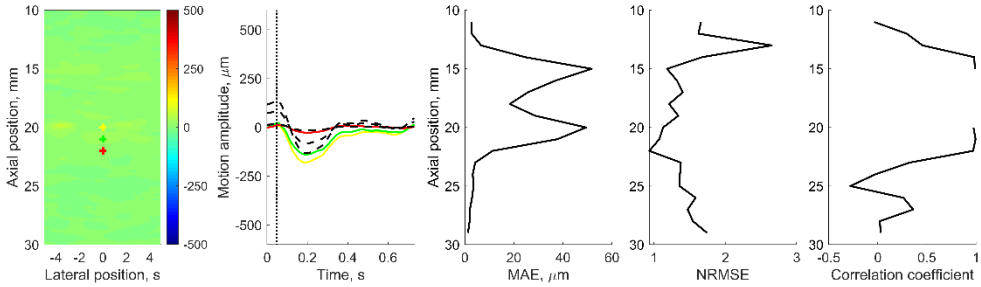

UDK 616.13-004.6-073(043.3)

SL 344. 2021-*-*, * leidyb. apsk. l. Tiražas 16 egz. Užsakymas * .

Išleido Kauno technologijos universitetas, K. Donelaičio g. 73, 44249 Kaunas

Spausdino leidyklos „Technologija“ spaustuvė, Studentų g. 54, 51424 Kaunas